Shielding material selection for the disposal of radioactive waste from ^{99}Mo production

TD Gwayisa

orcid.org/0000-0002-3038-0978

Dissertation accepted in partial fulfillment of the requirements for the degree *Master of Engineering in Nuclear Engineering* at the Potchefstroom Campus North-West University, South Africa

Supervisor:	Mr T.J. van Rooyen
Co-Supervisor:	Prof D.E. Serfontein
Graduation Date:	May2022
Student Number:	16067525

Declaration

I, the undersigned, hereby declare that the work contained in this dissertation entitled,

Shielding material selection for the disposal of radioactive waste from ^{99}Mo production

is my own, original work. I understand what plagiarism is and am aware of the University's rules and policies in this regard. I did not refer to work of current or any previous students. Where other people's work has been used (either from a printed source, Internet, or any other source), this has been properly acknowledged and referenced.

_____

Thato Gwayisa

Date: 10 December 2021

Abstract

This study focuses on the radiation shielding performance of 4 types of concrete for the storage, road transport and final disposal of cemented intermediate-level liquid (radioactive) waste generated during the production of fission-based Mo-99, i.e. $(n, f)^{99}$Mo, in concrete drums.

There is a large and growing worldwide demand for the medical radionuclide ^{99m}Tc. However, this isotope has a short half-life of only ~6 hours, so that the delay between its production and arrival at remote users, will cause most of the activity to be lost through radioactive decay. However, ^{99m}Tc has a longer-lived precursor, ^{99}Mo with a half-life that is 11 times longer than that of ^{99m}Tc, so that it is far more practical to produce ^{99}Mo and then deployed it in a ^{99}Mo-^{99m}Tc generator from which the short-lived medical radionuclide ^{99m}Tc is eluted at nuclear medicine clinics. When a fission-based process is used to produce ^{99}Mo, the product is almost carrier-free; such high specific activity (HSA) ^{99}Mo is, internationally, in high demand as a longer-lived precursor for ^{99m}Tc. The production of $(n, f)^{99}$Mo is by the irradiation of fissile target plates in a research reactor. HALEU (High-Assay Low Enrichment Uranium) target plates are irradiated for as long as 200 hours. After discharge and initial cooling, the target plates are dissolved via alkaline digestion. Iodine and molybdenum are chemically separated from the solute. The combined activity yield of the 2 medically useful and marketable fission products — ^{99}Mo and ^{131}I — from the fission of the uranium isotope ^{235}U, is in the order of 10 %, i.e. the other 90 % of the fission products constitute radioactive waste. The waste from the chemical processing of irradiated fissile target plates in an isotope production nuclear reactor, naturally separates into 3 streams: (1) high-level solid uranic residue, (2) intermediate-level liquid waste (ILLW) and (3) gaseous radionuclides. The high activity ILLW is first held in retention tanks for circa 90 days, and are then mixed with cement powder and vermiculite and agitated. The resulting cementitious slurry is transferred into 100-litre stainless-steel drums placed inside large concrete drums. The cementation process solidifies and immobilises the liquid radioactive waste. The concrete drums are placed in interim on-site storage; as soon as radiological acceptance criteria are met, these drums are transported by road to the national radioactive waste disposal site, for disposal in near-surface trenches.

This study presents a literature review of radioactive waste management, focusing on the immobilisation of ILLW via cementation and the combination of an engineered barrier system and a natural barrier system for disposal. The physics theory of the attenuation of ionising photons is presented and a simple but robust recipe is derived.

The dimensions of the concrete drums are fixed, but there is freedom for optimising the concrete material in a quest for lower transmitted dose rates, as well as the possibility of loading higher initial activities of radioactive waste per drum. This research project therefore quantifies the relative abilities of 4 types of concrete, as shielding material for the large concrete drums in which the cemented liquid radioactive waste is disposed. The 4 types of concrete options that are investigated for their abilities to reduce transmitted dose-rates, are (1) ordinary concrete (the baseline case), (2) magnetite concrete, (3) hematite concrete and (4) barite concrete.

Design-basis values for (1) the fissile isotope content and uranium vector in target plates, (2) fission power per target plate assembly and (3) irradiation time in the core of an isotope production reactor, were defined. To evaluate the radiation shielding performance of the concrete types, radionuclide activities and the resulting photon emission source terms must first be quantified. Codes in the SCALE 6.2.4 code system along with its nuclear data, were used to quantify the source term in the ILLW for a number of discrete times after the end of the irradiation of the target plates in the reactor. Problem-specific, self-shielded 1-group ORIGEN cross-sections were prepared with a long run of the SCALE sequence, T6-DEPL. These cross-section sets were prepared to allow subsequent fast analyses with the SCALE code ORIGEN. A SCALE ORIGEN calculation model was used to model the irradiation, cooling, chemical partition of the elements during chemical processing, which separates the liquid waste from the solid residue. This ORIGEN calculation model was also used to follow the isotopic evolution of the source term in the intermediate-level liquid radioactive waste in discrete time steps up to 10 years.

Calculation models of the 4 concrete drum types, each containing source terms representing different cooling times, were developed for the Monte Carlo radiation transport code MCNP6.2. The contact dose rates on the outer surface of the drums, as well as the Transport Index (TI) dose rate at a distance of 1 m from the drums, were quantified at different decay times of the cemented ILLW. Dose-rate fields were quantified around a single drum as well as at a perimeter fence around a rectangular array of drums were calculated. The shielding performance, i.e. the ability to reduce the transmitted dose rate, of all 4 concretes were measured against the reference case of no shielding. The dose rate reduction performance of the 3 high-density shielding concretes, are also expressed relative to the performance of ordinary concrete. A notable finding was that a shielding wall has to be constructed around the decay yard; such a design was developed. Another investigation concerned the required burial depth of the drums in the trenches. A conservative calculation model was developed and used to arrive at a safe burial depth for the drums.

Conclusions are that barite concrete has the best dose rate reduction performance, but that hematite concrete may be the preferred material choice, based on its complete local supply chain as well as operational experience with constructing durable hematite concrete drums that can survive long road journeys without cracking. Both these high-density concretes offer significant dose rate reduction advantages over ordinary concrete.

Keywords: Fission-produced Mo-99, radioactive waste, intermediate-level liquid waste, fissile target plate, irradiated target plate, source term, waste immobilisation, cementation, waste disposal, concrete, radiation shielding, dose rate, waste acceptance criteria, SCALE, ORIGEN, MCNP

Table of Contents

Declaration ..... **ii**

Abstract ..... **iii**

Table of Contents ..... **vi**

List of Figures ..... **xvii**

List of Tables ..... **xxiii**

Abbreviations and special nomenclature ..... **xxvi**

Hyphenation ..... **xxxvii**

A note regarding the use of units in this work ..... **xxxvii**

The terms fluence and fluence-rate ..... **xxxvii**

1. Introduction **39**

1.1 Prelude 39

1.2 The demand for high specific activity ^{99}Mo 39

1.2.1 ^{99}Mo-^{99m}Tc generators 39

1.2.2 The production of ^{99}Mo 39

1.2.3 Targeted radiopharmaceuticals and the need for high specific activity (HSA) ^{99}Mo 40

1.2.4 The impossible quest: Producing high specific activity (HSA) ^{99}Mo via a non-fission process 40

1.2.5 The large radioactive waste of a fission-based production route for ^{99}Mo 41

1.3 Fission-produced medical radionuclides: ^{99}Mo and ^{131}I 41

1.4 Radioactive waste from fission-produced ^{99}Mo....42

1.5 Disposal of cemented liquid radioactive waste from fission-produced ^{99}Mo, in concrete drums....44

1.5.1 Selection of concrete drum material....44

1.5.2 Feasibility of computational shielding studies....45

1.6 Natural background dose rate, dose limits, dose constraints and demarcation criteria for radiological zoning....45

1.7 Transport of radioactive material....46

1.8 Economic reasons for this investigation....47

1.9 Research purpose and research problem....47

1.10 Research objectives....48

1.11 Research hypothesis....48

1.12 Research methodology....50

1.13 Organisation of this dissertation....51

2. Radiation shielding materials against photon-dominated radioactive sources such as ILLW....55

2.1 Introduction....55

2.2 Dose attenuation factor (DAF) — a criterion for judging the efficacy of radiation shielding....55

2.3 Review: Radiation physics principles for the shielding of packages of radioactive material that are dominated by the emission of ionising photons....57

2.3.1 Ionising photons....57

2.3.2 Atomic physics mechanisms for the attenuation of ionising photons....57

2.3.3 Energy dependence of photon interaction cross-sections for PEA, CS and PP....60

2.3.4 Energy range of dominance: PEA, CS and PP....62

2.3.5 Radiation physics “recipe” for selecting optimal shielding materials against ionising radiation 63
2.3.6 Linear attenuation coefficients for barite concrete and ordinary concrete 65
2.3.7 Formulation of the first fundamental principle of photon shielding 68
2.3.8 Biological hazardousness of ionising photons as a function of photon energy 69
2.3.9 Formulation of the second fundamental principle of photon shielding and shield optimisation 71
2.3.10 Tenth-value thicknesses (TVTs) of shielding materials against important radioisotopes 71
2.4 Review: Natural abundance of the chemical elements in the crust of the earth; Minerals suited for the manufacture of high-density shielding concrete 73
2.4.1 The natural abundance of the chemical elements in the crust of the earth 73
2.4.2 Minerals suited for the manufacture of high-density shielding concretes 75
2.4.3 Economic process for the selection of radiation shielding materials 76
2.4.4 The need for high-density shielding concretes 77
2.4.5 Iron ore production in South Africa 77
2.4.6 Magnetite ore; magnetite concrete 78
2.4.7 Hematite ore; hematite concrete 78
2.4.8 Barite ore; barite concrete 79
2.5 Radiation shielding concretes: Benefits and composition 80
2.5.1 Attractiveness of concrete as radiation shielding material 80
2.5.2 Elemental composition: Ordinary concrete (ORD-CRT) 81
2.5.3 Elemental composition: Magnetite concrete 82
2.5.4 Elemental composition: Hematite concrete (HEM-CRT) 83
2.5.5 Elemental composition: Barite concrete 84
2.6 Summary and conclusions 86

3. Radioactive waste classification, conditioning, immobilisation, shielding, storage and disposal 87

3.1 Introduction 87

3.2 Radioactivity in a cosmological context 87

3.3 Literature review: The IAEA's classification of radioactive waste types 88

3.3.1 Radioactive waste categories 88

3.3.2 Low and Intermediate-Level Waste, Short-Lived (LILW-SL) 89

3.3.3 Low-Level Waste, Short-Lived (LLW-SL) 90

3.3.4 Intermediate-Level Waste, Short-Lived (ILW-SL) 90

3.3.5 HLW: High-Level Waste 90

3.4 Literature review: Clearance levels for the clearance of radioactive material 91

3.4.1 Clearance levels: IAEA 91

3.4.2 Clearance levels: Nuclear Industry Safety Directors Forum (NISDF, 2017) 93

3.4.3 Radionuclide content of one drum filled with cemented liquid radioactive waste from the fission-based production of ^{99}Mo, in the light of clearance levels 95

3.5 Literature review: Radioactive waste management technology for ILLW 99

3.5.1 Introduction 99

3.5.2 General overview of radioactive waste management 99

3.5.3 Classification of radioactive waste 99

3.5.4 Monographs on the management of radioactive waste from the production of ^{99}Mo 101

3.5.5 Portland cement 102

3.5.6 Geopolymer cement 103

3.5.7 Concretes 103

3.5.8 Ordinary concrete 104

3.5.9 Ageing and deterioration of reinforced concrete structures such as drums for ILLW 104
3.5.10 Concretes based on geopolymer cement as binder-hardener 106
3.5.11 Concrete as a secondary barrier for the disposal of ILW 106
3.5.12 Shielding efficacy of high-density shielding concretes 107
3.5.13 Availability of high-grade iron ores in South Africa, for the manufacture of high-density shielding concrete 110
3.5.14 Engineered radiation safety system for radioactive waste 110
3.5.15 Immobilisation technologies for radioactive waste 110
3.5.16 Conditioning and immobilisation of radioactive waste; the concept wasteform 111
3.5.17 Engineered barrier system (EBS) and natural barrier system (NBS) 112
3.5.18 Engineered radionuclide containment barriers: ILLW 112
3.5.19 Cementation of intermediate-level radioactive waste; Immobilisation of radioactive waste via cementation 113
3.5.20 Selection and design of radioactive waste repositories 121
3.5.21 Clays in radioactive waste management 122
3.5.22 Future impact of low and intermediate-level radioactive waste on humans and the environment 122
3.5.23 Road transport of radioactive material 123
3.5.24 Gap analysis 124
3.6 Road transport and disposal of concrete Radioactive waste drums 125
3.7 Summary and perspective 126

4. Liquid radioactive waste from chemically processed irradiated target plates 127

4.1 Introduction 127
4.2 An isotope production reactor that produces ^{99}Mo as a fission product 127

4.3 Irradiation of target plates in the research reactor 129
4.4 Elemental and isotopic composition of LEU_{20} target plates (TP_LEU_{20}) 130
4.5 LEU_{20} target plates: Uranium vector and mass-loading 131
4.6 Burnup of the IHM in the target plates 132
4.7 Nuclear fission 133
4.7.1 The energetic driving force behind nuclear fission: Binding energy per nucleon 133
4.7.2 Fission cross-sections: Fissile vs fissionable isotopes 134
4.7.3 Neutron spectrum in the fissile layer on the irradiated target plates 137
4.8 Fission products produced by fission 140
4.8.1 Fission product yield 140
4.8.2 Understanding the radioactivity of fission fragments and fission products 141
4.9 Evolution of activities of radionuclides during and after target plate irradiation 145
4.10 Three waste streams from fission-based production of ^{99}Mo 147
4.10.1 Target plate dissolution and chemical processing 147
4.10.2 Solid residue from irradiated target plates 147
4.10.3 Intermediate-level liquid (radioactive) waste (ILLW) 148
4.10.4 Future economic values of radioactive waste from fission-produced ^{99}Mo 148
4.10.5 Gaseous radioactive waste from fission-produced ^{99}Mo 148
4.11 Production, cementation and drumming of intermediate-level liquid waste (ILLW) 149
4.12 Specific research objectives 151
4.12.1 Introduction 151
4.12.2 Problem statement 151
4.12.3 General research goals 152
4.12.4 Specific research objectives 153

5. Calculation models and results 156

5.1 Process timeline: ILLW from fission-^{99}Mo production 156

5.2 Engineering specifications of tanks for ILLW and concrete drums for cemented ILLW 157

5.3 Calculation models: SCALE TRITON T6-DEPL and ORIGEN 157

5.4 Partitioning of chemical species between the solid and liquid radioactive waste streams during the chemical processing of ITPs 158

5.5 Liquid radioactive waste from (n,f) ^{99}Mo production: Activity and dominant radionuclides 158

5.5.1 Radionuclide inventory per concrete waste drum, after 1 yr, 5 yrs and 10 yrs 158

5.5.2 The long hauliers: Radionuclide inventory per concrete drum, after 10^4 years 162

5.5.3 Graphic summary: Isotopic evolution of activity per drum 163

5.6 Photon emission source term from ILLW from (n,f) ^{99}Mo production 164

5.6.1 Energy spectrum 164

5.6.2 Lowering of the high energy component of the photon emission spectrum from ILLW 166

5.7 MCNP calculation models: Graphical representations 167

5.7.1 Calculation model: Single drum 167

5.7.2 Calculation model: Drum array in the “decay yard” 170

5.8 Calculated dose rates for a single, stand-alone concrete drum containing cemented ILLW from (n,f) ^{99}Mo production 171

5.8.1 Design of the computational experiment 171

5.8.2 Dose rates for case NoShield (single drum) 171

5.8.3 Dose rates for case ORD-CRT (case 1drum) 173

5.8.4 Dose rates for case MAG-CRT (case 1drum) 174

5.8.5 Dose rates for case HEM-CRT (case 1drum) 175

5.8.6 Dose rates for case BAR-CRT (case 1drum) 176

5.8.7 Shielding performance of MAG-CRT, HEM-CRT and BAR-CRT relative to ORD-CRT (stand-alone drum) 177

5.8.8 Transportability of individual drums in terms of radiological criteria 178

5.8.9 Shielding factors achieved with different concrete types 180

5.9 Improved performance of high-density shielding concretes at longer decay times 183

5.10 Depth dose curves for different concrete compositions 183

5.11 Calculated dose rates at the fence around the "decay yard" for an array of 5 × 11 = 55 drums containing cemented ILLW from (n, f) ^{99}Mo production 187

5.12 Contour plots of the dose-rate fields around single and multiple concrete drums containing cemented ILLW 193

5.13 Investigation of the shielding effect of a concrete shielding wall of different thicknesses, around the decay yard 197

5.14 Required burial depth of concrete drums holding ILLW, in trenches at the disposal site 202

5.14.1 Research objective RO$_{12}$ 202

5.14.2 MCNP calculation model: Trench filled with buried drums 203

5.14.3 MCNP-generated plots of calculation models: Trench filled with buried drums 203

5.14.4 Results of dose rate calculations: concrete drums with radioactive waste buried in a trench at a disposal site 205

5.14.5 Documentation of calculation model and results: Drums with radioactive waste, buried in a trench 209

5.15 Tenth-value thickness (TVT) values for high-density shielding concretes 209

5.15.1 Additional TVT information 209

5.15.2 Explanation of the apparent anomaly in calculated TVT values for the shielding of ^{60}Co by hematite and barite concrete 210

6. Summary and conclusions 212

6.1 Meeting of research objectives....212
6.2 Statistical validity of results....212
6.3 Verification and validation of results....212
6.4 Concrete type(s) to be used for drums housing cemented liquid radioactive waste from a fission-based ^{99}Mo production process....212
6.4.1 Ordinary concrete: a mediocre shielding material....212
6.4.2 Magnetite concrete: an unnecessary choice in SA....213
6.4.3 Best selection: Barite concrete or hematite concrete?....213
6.5 Importance and applicability of this study....214
6.6 Potential further work in the field of the characterisation, immobilisation, shielding, storage, transport and disposal of radioactive waste....214

Annexure A: The isotope production reactor and the target plate assemblies for fission-based radionuclide production....216

A.1 Reactor core layout....216
A.2 Core and fuel parameters....217
A.3 Fuel assemblies....217
A.4 Target plate (TP) assemblies for radionuclide production....221

Annexure B: Calculation models: SCALE T6-DEPL, SCALE ORIGEN and MCNP6....222

B.1 Calculation models....222
B.2 Transport-depletion (T-DEPL): Neutron transport and burnup/depletion calculation sequences in the SCALE system....222
B.3 SCALE 6.2.4 TRITON T6-DEPL calculation model for a LEU_{20} TP_7 target plate assembly....224

B.4 SCALE 6.2.4 ORIGEN calculation model for the irradiation of 42 individual LEU_{20} target plates and the production of circa 35 litres of ILLW — intermediate-level liquid waste 230

B.4.1 The SCALE 6.2.4 code ORIGEN 230

B.4.2 The ORIGEN calculation model 231

B.4.3 Material feed during the alkaline digestion of the ITPs 234

B.4.4 Partitioning of chemical species between solid and liquid waste streams: retained fractions during processing 235

B.5 The Monte Carlo method 239

B.5.1 Introduction 239

B.5.2 Examples of Monte Carlo processes 240

B.5.3 Monte Carlo sampling techniques for discrete stochastic variables 241

B.5.4 Extension to continuous probability density functions 245

B.6 How the code MCNP is used to calculate dose rates around packages of radioactive material 246

B.6.5 Operator form of the Boltzmann transport equation (BTE) 246

B.6.6 Deterministic and stochastic radiation transport codes 247

B.6.7 MCNP calculation models: Overview 247

B.7 MCNP calculation model: Single concrete drum with cemented liquid radioactive waste 256

B.7.1 The code MCNP 256

B.7.2 Statistical validity of computed dose rates 258

B.7.3 MCNP calculation model: Single concrete drum 258

B.8 MCNP calculation model: Array of 11 x 5 concrete drums in the "decay- yard" 261

Bibliography 265

List of Figures

Figure 2-1: A general source-shield concept 56

Figure 2-2: Regions in the (E_γ; Z) plane where different photon interaction mechanisms dominate — PEA, CS and PP 60

Figure 2-3: Photon energy domains where PEA ("PE" in the graph), CS or PP dominates, in the case of the material Pb (Z(Pb) = 82) 61

Figure 2-4: Important photon interaction mechanisms and their cross-sections for Fe 62

Figure 2-5: Linear interaction coefficients for photon interactions in ordinary concrete (ORD-CRT) and barite concrete (BAR-CRT) 66

Figure 2-6: Ratio between the linear interaction coefficients for photon interactions in barite concrete and ordinary concrete 67

Figure 2-7: The fluence-rate to dose-rate response function R(E) for ionising photons (ICRU, 2020) 70

Figure 2-8: Periodic Table of the elements 74

Figure 2-9: Abundance of the elements in the earth's crust 74

Figure 2-10: Magnetite ore 78

Figure 2-11: Hematite ore — note the reddish hue 79

Figure 2-12: Crushed high-grade barite ore at a barite mine 80

Figure 3-1: Conceptual illustration of the IAEA's classification scheme for radioactive waste (IAEA, 2009a: 7) 88

Figure 4-1: Layout of the core of the research and isotope production reactor that produces ^{99}Mo in target plates, via fission 128

Figure 4-2: The curve of binding energy per nucleon, *BE(A),* is seen to peak in the region of ^{56}Fe, where it is significantly higher than for heavy nuclei such as ^{235}U and ^{238}U 133

Figure 4-3: Cross-sections for the neutron-induced fission of ^{235}U and ^{238}U 135

Figure 4-4: Animation of the fission of the ^{235}U nucleus 136

Figure 4-5: Energy spectrum of prompt fission neutrons emitted when 235U undergoes neutron-induced fission 138

Figure 4-6: The neutron energy spectrum inside the target plates 139

Figure 4-7: The fission product yields when the fissile isotope ^{235}U is fissioned by thermal neutrons 140

Figure 4-8: Fission-product yields $Y_{FP}(A)$ as a function of the mass number of the fission products, for thermal neutron-induced fission of ^{235}U 141

Figure 4-9: A colour-coded chart of the nuclides 142

Figure 4-10: A 3D plot of the chart of the nuclides, showing the "valley of β-stability" amidst the surrounding "hills of β-instability"; in the far distance, the steep peak of α-instability can be discerned 143

Figure 4-11: Animation of the concept "valley of β-stability" 144

Figure 4-12: Activities of the radionuclides ^{99}Mo, ^{131}I and ^{137}Cs in the modelled process mass, as a function of time; the initial irradiation phase has a duration of 200 h, i.e. 8.333 days..... 146

Figure 5-1: The total activity of all the radionuclides in the liquid radioactive waste from fission-produced ^{99}Mo, as well as the combined activity of the radionuclide ^{137}Cs plus its progeny nuclide, ^{137m}Ba, as a function of cooling time 163

Figure 5-2: The combined activity of the radionuclide pair, ^{137}Cs and ^{137m}Ba, relative to the total activity of all radionuclides in the ILLW, as a function of time 164

Figure 5-3: Photon emission spectra for liquid radioactive waste produced from the production of (n,f)^{99}Mo 165

Figure 5-4: Photon emission spectra for liquid radioactive waste produced from the production of (n,f)^{99}Mo, on linear-linear scales, for decay times of 1 yr, 5 yrs and 10 yrs..... 166

Figure 5-5: Side-view of a large high-density concrete drum containing cemented ILLW 168

Figure 5-6: Top view of a concrete drum filled with radioactive waste, with 2 circumferential calculational detectors — one for the calculation of the contact dose rate (CDR) and the other to calculate the TI 169

Figure 5-7: Array of 5 × 11 = 55 concrete drums filled with cemented liquid radioactive waste, arrayed on a concrete slab in a "decay yard" 170

Figure 5-8: Contact dose-rates on an individual concrete drum containing cemented ILLW, as a function of elapsed time 179

Figure 5-9: Transport Index (TI) for the concrete drums containing cemented ILLW, as a function of elapsed time..... 180

Figure 5-10: Shielding factor for different concrete drum materials, as a function of elapsed time, relative to the case of no shielding material 181

Figure 5-11: The shielding factors achieved with BAR-CRT, HEM-CRT and MAG-CRT, relative to ORD-CRT, at discrete cooling times of the cemented ILLW from ^{99}Mo production by a fission process..... 182

Figure 5-12: Dose rates as a function of the radius, for cemented ILLW in concrete drums with 4 different compositions 184

Figure 5-13: Radial dependence of the shielding factors of BAR-CRT and HEM-CRT relative to ORD-CRT, inside and around BAR-CRT and HEM-CRT drums containing cemented ILLW 186

Figure 5-14: Dose rates at the perimeter fence around an array of 5×11=55 concrete drums containing cemented ILLW from the fission-based production of ^{99}Mo, for distinct concrete types, as a function of the decay time of the ILLW 190

Figure 5-15: Shielding factors, evaluated at the perimeter fence around a 5×11=55 array of concrete drums containing cemented ILLW, as a function of elapsed time — shielding ability of 4 concrete types relative to the reference case of NoShield — no shielding 191

Figure 5-16: Relative shielding factors, evaluated at the perimeter fence around a 5×11=55 array of concrete drums containing cemented ILLW, as a function of elapsed time — shielding ability of MAG-CRT, HEM-CRT and BAR-CRT relative to ORD-CRT 192

Figure 5-17: Relative shielding factors, evaluated at the perimeter fence around a 5×11=55 array of concrete drums containing cemented ILLW, as a function of elapsed time — shielding ability of BAR-CRT relative to MAG-CRT and HEM-CRT..... 193

Figure 5-18: Dose-rate field through and a single drum filled with radioactive waste, which rests on a large concrete slab 194

Figure 5-19: Dose-rate for the “decay yard” where an array of 11×5 drums is stored..... 195

Figure 5-20: Dose rates in the decay yard when cemented ILLW is placed in a 21×5 array of unshielded 100-litre stainless-steel drums 196

Figure 5-21: Contour plot of the shielding effect of a shielding wall around the perimeter of the decay yard — the wall is 270 cm high and 60 cm thick. 198

Figure 5-22: Influence of skyshine on dose rates beyond a 240 cm high perimeter shielding wall around the decay yard, for 2 wall thicknesses 199

Figure 5-23: Ability of a shielding wall around the periphery of the decay yard, to lower dose rates 201

Figure 5-24: An MCNP geometry plot of the side-view (i.e. x-z view) of an 11×11×3 square-pitched array of radioactive waste drums buried in a trench at a disposal site; the modelled thickness of the soil overburden in this diagram is 2.35 m 204

Figure 5-25: A top view (i.e. x-y view) of 11×11 concrete drums filled with radioactive waste, in a trench at a disposal site 205

Figure 5-26: Side-view (x-z plot) of dose rates around waste drums buried in a trench (logarithmic dose-rate axis) 206

Figure 5-27 Side-view (x-z plot) of dose rates around waste drums buried in a trench (linear dose-rate axis) 206

Figure 5-28: Dependence of the surface dose rate directly above buried radioactive waste drums, on the thickness of soil covering to topmost row of underground drums; there are 11×11×3 = 363 radioactive waste drums in the trench, each drum filled with the design-basis source term at a decay time of 1 year 208

Figure 6-1: Top view of the core layout of the MTR 216

Figure 6-2: Single fuel plate in a fuel assembly used in the IPR 218

Figure 6-3: An x-y view at the active part of a fuel assembly used in the IPR 219

Figure 6-4: Axial view of a fuel assembly in the IPR 220

Figure 6-5: Photos of a fuel assembly for the MTR 221

Figure 6-6: Top view of the geometry of the SCALE-6.2.4 TRITON T6-DEPL calculation model of one central target plate assembly, surrounded by 8 fuel assemblies in the reactor core 228

Figure 6-7: Side-view of a TP_7 target plate assembly surrounded by fuel assemblies; the active height of a target plate is only 18 cm whereas the active height of a FA is 59.37 cm 229

Figure 8: Probabilities of photon interaction types 243

Figure 9: Normalised cumulative probability distribution function for photon interaction type at a given incident photon energy 244

Figure 6-10: The fluence-rate to dose-rate response function R(E) for ionising photons (ICRU, 2020) 264

List of Tables

Table 2-1: Photon energy regions where the 3 principal interaction mechanisms, PEA, CS and PP, will be dominant for materials in common shielding concretes 63

Table 2-2: The 3 principal interaction mechanisms of ionising photons, and their linear interaction coefficients $\mu = N\sigma$ 64

Table 2-3: Tenth-value thickness (TVT) for combinations of radionuclides and shielding materials 71

Table 3-1: Unconditional clearance levels for radionuclides, according to (IAEA, 1996) 91

Table 3-2: Clearance levels for selected radionuclides, for the re-use of metallic items 93

Table 3-3: Expected radionuclide content of one drum filled with cemented liquid radioactive waste from fission process production of ^{99}Mo, at the 10-year mark since target plate processing 97

Table 4-1: Inventory of radioactive noble gases in one irradiated TP_7 assembly, quantified 7 days after end-of-irradiation 149

Table 5-1: Process timeline for high-activity liquid waste stream from the production of fission-based ^{99}Mo 156

Table 5-2: Radionuclides having the highest activities in the ILLW from chemically processed irradiated fissile target plates, evaluated at cooling times of 1 yr, 5 yrs and 10 yrs 159

Table 5-3: Long-haulier radionuclides in the ILLW — {Nuclide; Activity} matrix after 10^4 years 162

Table 5-4: Percentage photons emitted at $E_\gamma \geq 1$ MeV in ILLW from fission-produced ^{99}Mo 166

Table 5-5: Colour-coding convention used to guide the eye in the presentation of the shielding abilities of ordinary concrete (ORD-CRT), magnetite concrete (MAG-CRT), hematite concrete (HEM-CRT) and barite concrete (BAR-CRT) 171

Table 5-6: Dose rates in the complete absence of shielding concrete, calculated for one stand-alone drum containing ILLW from an $(n,f)^{99}Mo$ production process 172

Table 5-7: Concrete drums for ILLW from an $(n,f)^{99}Mo$ production process: Dose rates for ordinary concrete (ORD-CRT) 173

Table 5-8: Concrete drums for ILLW from an $(n,f)^{99}Mo$ production process: Radiological performance of magnetite concrete (MAG-CRT) drums; shielding factors are relative to case NoShield..... 174

Table 5-9: Concrete drums for ILLW from an $(n,f)^{99}Mo$ production process: Dose rates for hematite concrete (HEM-CRT)..... 175

Table 5-10: Concrete drums for ILLW from an $(n,f)^{99}Mo$ production process: Dose rates for barite concrete (BAR-CRT) 176

Table 5-11: The improved photon shielding performance of (1) magnetite concrete (MAG-CRT), (2) hematite concrete (HEM-CRT) and (3) barite concrete (BAR-CRT), relative to ordinary concrete (ORD-CRT) as material for a drum containing ILLW from $(n,f)^{99}Mo$ production, i.t.o. contact dose rates (CDRs) 177

Table 5-12: The improved photon shielding performance of (1) magnetite concrete (MAG-CRT), (2) hematite concrete (HEM-CRT) and (3) barite concrete (BAR-CRT), relative to ordinary concrete (ORD-CRT) as material for a drum containing ILLW from $(n,f)^{99}Mo$ production, i.t.o. Transport Index (TI) 177

Table 5-13: Calculated average dose rates at the perimeter fence around an array of $5 \times 11 = 55$ drums in a “decay yard” 187

Table 5-14: The relative merit of using the 3 types of high-density concrete, relative to using ordinary concrete, for 55 drums arrayed in the decay yard 188

Table 5-15: The relative merits of using high-grade heavy concretes, relative to lower-grade heavy concretes, for 55 drums arrayed in the decay yard 188

Table 5-16: Tenth-value thickness (TVT) for combinations of radionuclides and shielding materials; TVT values for 3 high-density shielding concrete formulations are included 210

Table 6-1: Some key parameters of the isotope production reactor used to produce ^{99}Mo via a fission process 217

Table 6-2: Initial material composition of the 42 TPs 233

Table 6-3: Retained fractions, i.e. partition fractions of chemical elements for the selection of the liquid waste pathway in the generation of ILLW from fission-produced ^{99}Mo 236

Abbreviations and special nomenclature

SI *(Système International d'Unités)* abbreviations for units as well as standard notations for isotopes, chemical elements and molecules are used in this work. Other abbreviations and special nomenclature are listed below.

A

α .....Alpha-particle

a.....Annum (year)

A .....Activity (context)

A .....Atomic mass, i.e. $A = Z + N$ (context)

AC .....Actinide

ACE.....A Compact ENDF

ALARA.....As Low As Reasonably Achievable

AP .....Activation Product

ARP.....Automated Rapid Processing

B

BAR-CRT .....Barite Concrete

BC .....Barite Concrete

BE .....Binding Energy

BU .....Burnup

BWR .....Boiling Water Reactor

C

CA .....Control Assembly

CDR .....Contact Dose-Rate

CENTRM.....Cross-section processing routine in SCALE

CISSTD.....Characterisation, Immobilisation, Shielding, Storage, Transport and Disposal

CRAM.....Chebyshev Rational Approximation Method

CRT-BAR.....Barite concrete

CRT-HEM .....Hematite concrete

CRT-MAG.....Magnetite concrete

CRT-ORD.....Ordinary concrete

CS .....Compton Scattering

CSA.....Calcium Sulfo-Aluminate

CVCS .....Chemical and Volume Control System

D

d.....Day

D.....Dose

$\dot{D}$.....Dose rate

DAF.....Dose Attenuation Factor

DBST .....Design-Basis Source Term

DIPR .....Dedicated Isotope Production Reactor

DM .....Drum Material

DR .....Dose Rate

E

E .....Energy

EBS .....Engineered Barrier System

ENDF .....Evaluated Nuclear Data File

ENDF/B .....Evaluated Nuclear Data File, type B

ENDF/B-8.0 .....Evaluated Nuclear Data File, type B, release 8.0 (example)

ERSS .....Engineered Radiation Safety System

EW .....Exempt Waste

$(E_g; Y_g)$.....{Energy, Yield} matrix or probability density function

$(E_g; Y_g(t_d))$.....{Energy, Yield} matrix or probability density function at decay time t_d

F

f .....Fission

FA.....Fuel Assembly

FDR.....Fence Dose-Rate

FFA .....Fuel Follower Assembly

FoS .....Factor of Safety

FP .....Fission Product

FRDRCF .....Fluence-Rate to Dose-Rate Conversion Factor

G

γ .....Gamma-photon, i.e. ionising photon

Ga.....Giga-annum, i.e. a billion years, i.e. 10^9 years

GPC.....Geopolymer cement

GW.....Gigawatt

GWD.....Gigawatt-day

H

h.....Hour

HALEU.....High-Assay Low Enrichment Uranium

HC.....Hematite Concrete

HEM-CRT.....Hematite Concrete

HEU .....High Enrichment Uranium

HLW.....High-Level Waste

HSA.....High Specific Activity

I

IAEA.....International Atomic Energy Agency

ICRP.....International Commission on Radiological Protection

ICRU.....International Commission on Radiation Units and Measurements

IFHM.....Initial Fissile Heavy Metal

IHM.....Initial Heavy Metal

ILLW.....Intermediate-Level Liquid Waste

ILLW[$(n,f)^{99}$Mo] .....Intermediate-Level Liquid Waste from the fission-based production of ^{99}Mo

ILW .....Intermediate-Level Waste

IP .....Intellectual Property

IPR .....Isotope Production Reactor

ITP.....Irradiated Target Plate

J

JANIS.....JAva-based Nuclear Information Software — a GUI to access and plot data in ENDF/B and other nuclear data collections

L

LANL.....Los Alamos National Laboratories

LCS .....Low Carbon Steel

LEMS .....Liquid Effluent Management Services

LEU .....Low Enrichment Uranium

LEU_{20}.....Low Enrichment Uranium that contains 19.75 % enriched uranium

LLW .....Low-Level Waste

LILW.....Low and Intermediate-Level Waste

LILW-LL.....Low and Intermediate-Level Waste, Long-Lived

LILW-SL.....Low and Intermediate-Level Waste, Short-Lived

LODE.....Linear Ordinary Differential Equation

LSA .....Low Specific Activity

LTS.....Long-Term Storage

LW-ITP .....Liquid Waste from Irradiated Target Plates

LWR.....Light Water Reactor

M

MAG-CRT .....Magnetite Concrete

MC .....Magnetite Concrete

MCNP .....Monte Carlo N-Particle

MTR.....Materials Testing Reactor

MW .....Megawatt

MWD .....Megawatt-day

N

n .....Neutron

N .....Nuclide (context)

N .....Number of neutrons in the nucleus (context)

$(N_i; A_i)$.....{Nuclide, Activity} matrix

$(N_i; A_i(t_d))$.....{Nuclide, Activity} matrix at decay time t_d

NBDR .....Natural Background Dose-Rate

NBS.....Natural Barrier System

$(n, f)^{99}\mathrm{Mo}$ .....Fission-produced, i.e. reactor-produced $^{99}\mathrm{Mo}$

NFY.....Neutron-induced Fission Yield

NNR .....National Nuclear Regulator

NORM.....Normally Occurring Radioactive Material

NORM-E.....Enhanced activity NORM

NORM-L.....Low activity NORM

NoShield .....Absence of radiation shielding (context)

NPP .....Nuclear Power Plant

NRC .....Nuclear Regulatory Commission (USA)

NRWDI .....National Radioactive Waste Disposal Institute

NSD .....Near-Surface Disposal

O

OC .....Ordinary Concrete

ODE .....Ordinary Differential Equation

OPC.....Ordinary Portland Cement

ORD-CRT .....Ordinary Concrete

ORIGEN .....Oak Ridge Isotope GENerator — an activation & depletion code in SCALE

ORNL.....Oak Ridge National Laboratory

P

PC.....Portland Cement

PDR.....Photon dose rate

PEA .....Photo-Electric Absorption

PP .....Pair Production

PWM.....Predisposal Waste Management

PWR.....Pressurised Water Reactor

R

ρ .....Mass-density

R.....Radius (meaning depends on the context)

R.....Response (meaning depends on the context)

$\Re_\gamma(E)$.....The response function, which figures in a real linear functional of the form

$$R = \langle \varphi_\gamma, \Re_\gamma \rangle$$

which mathematically converts or maps the photon fluence function $\varphi_\gamma(E)$ to photon effective dose; the fluence-rate to dose-rate (conversion) function

RCC.....Right Circular Cylinder

RHS.....Right Hand Side

RO .....Reverse Osmosis (meaning depends on context)

RO .....Research Objective (meaning depends on context)

RP.....Radiation Protection

RS.....Radiation Safety

RSICC.....Radiation Safety Information Computational Center

RW .....Radioactive Waste

S

s.....Second

SA .....South Africa

SDEF.....Source Definition

SDR.....Surface Dose Rate

SF .....Shielding Factor

SFY .....Spontaneous Fission Yield

SOC.....State-Owned Company

SR.....Solid Residue

SR-ITP .....Solid Residue from Irradiated Target Plates

SRITP[$(n,f)^{99}$Mo] ....Solid Residue from Irradiated Target Plates used to produce $(n,f)^{99}$Mo

SS .....Stainless-Steel

SS-304L .....Stainless-Steel 304L

SS-316L .....Stainless-Steel 316L

ST.....Source Term

T

TEM .....Tissue-Equivalent Material

TEM-DET .....Tissue-Equivalent Material Detector

TI.....Transport Index

TP.....Target Plate (generic)

TP_1.....An individual Target Plate

TP_7.....Target Plate assembly with 7 individual TPs

TPT .....Transport

TRITON.....SCALE calculational sequence for transport-depletion calculations

U

U-Al .....Uranium-Aluminium alloy

US .....United States (of America)

USA.....United States of America

USD.....US Dollar

V

VLLW .....Very Low-Level Radioactive Waste

W

WAC.....Waste Acceptance Criteria

X

XS .....Cross-Section

Y

Y .....Yield

Z

Z .....Atomic number, i.e. the number of protons in the nucleus of an element

ZAID.....$ZAID = 1000 \times Z + A$ for general radiation transport; simplified to $ZAID = 1000 \times Z$ for low-energy photon and electron transport

Hyphenation[1]

Hyphens are used as sparingly as possible, and are mainly used to prevent ambiguity and "reader overload". Hyphenation is used to guide the eye during the conceptual parsing of multi-noun word clusters ("pileups"). For example: the hyphenation in "fluence-rate to dose-rate conversion factor" lends clarity, but non-hyphenated forms "dose rate" and "fluence rate" are used whenever there is no clustering-related potential for confusion. In other words, this apparent "inconsistency" is deliberate and functional. Hyphens are deployed electively to visually link closely related concepts together, to add clarity to multi-noun word clusters.

A note regarding the use of units in this work[2]

Practically all radiation transport codes use the centimetre-gram-second (CGS) system of units. The radiation transport codes used in this work — MCNP and the SCALE system — use the unit cm for length and gram for mass. To avoid confusion, this work therefore freely uses the CGS unit system and expresses the dimensions of radiation shields in the unit cm, fluence-rate in the units $\mathrm{cm}^{-2}.\mathrm{s}^{-1}$, fluence in the unit cm^{-2} and mass-density in the units $\mathrm{g\ cm}^{-3}$. The standard engineering practice of reporting the dimensions of structures and components in the unit mm is typically not followed in this work.

The terms fluence and fluence-rate[3]

Both the International Commission on Radiological Protection (ICRP) and the International Commission on Radiation Units & Measurements (ICRU) do not permit the use of the term "flux" for the quantity $\varphi = Nv$ where N is the number of moving, free (i.e. unbound) particles per unit volume, and v is the velocity of these particles — see e.g. ICRP (2007) and ICRU (2011). These 2 authoritative international commissions enforce the use of the terms **fluence rate** for φ and **fluence** for the time-integral $\Phi = \int_0^\infty \varphi(t)\, dt$. Because this work deals with radiation protection and radiation

[1] Note: This paragraph was formulated and added by the study supervisor, TJvR.

[2] Note: This paragraph was formulated and added by the study supervisor, TJvR.

[3] Note: This paragraph was formulated and added by the study supervisor, TJvR.

dose — quantities for which the ICRP and ICRU act as international custodians — the terminology recommended by these 2 commissions will be used.

1. Introduction

1.1 Prelude

This chapter introduces a broad outline of the technological background, the research problem, the general purpose of the research and a preliminary formulation of general research objectives. A research hypothesis is also formulated.

1.2 The demand for high specific activity ^{99}Mo

1.2.1 ^{99}Mo-^{99m}Tc generators

A highly sought-after radionuclide with many nuclear medicine applications, is ^{99m}Tc (technetium-99m). This radionuclide has a half-life of only 6.0067 hours, which is too short for product delivery journeys that last more than a few hours. Affluent countries can afford to place particle accelerators that directly produce the desired therapeutic radionuclide ^{99m}Tc, close to several major medical centres. Less affluent countries have to produce the precursor isotope of ^{99m}Tc, namely ^{99}Mo, and deploy ^{99}Mo-^{99m}Tc generators to produce ^{99m}Tc. The isotope ^{99}Mo has a half-life of 65.976 hours (2.7472 days) which is 11 times longer than that of ^{99m}Tc; the ^{99}Mo serves as a longer-lived supply-reservoir for its shorter-lived daughter radionuclide, ^{99m}Tc. The activity of ^{99m}Tc grows in to be in good equilibrium with that of its precursor, ^{99}Mo, within less than 2 days. At a nuclear medicine centre, the required activity of ^{99m}Tc is eluted from the generator; a ^{99}Mo-^{99m}Tc generator has a service life of approximately 10 days. References that discuss ^{99}Mo-^{99m}Tc generators are (Elliott, 1994), (Knapp & Mirzadeh, 1994), (Eckelman, 2009), (GE Healthcare, 2014) and (Van So Le, 2014).

1.2.2 The production of ^{99}Mo

We now consider two research reactor based methods of producing the radionuclide ^{99}Mo; this nuclide can be produced via e.g.:

- The irradiation of natural molybdenum (^{nat}Mo) or molybdenum enriched in the isotope ^{98}Mo, in the core of a research reactor, to produce ^{99}Mo via neutron activation.

- Fissioning fissile actinide nuclei such as ^{235}U in fissile target plates that are irradiated inside a nuclear reactor.

The fission reaction $^{235}_{92}\mathrm{U}(n,f)$ delivers a large ensemble of fission products, from which ^{99}Mo can be separated to deliver an almost carrier-free ^{99}Mo product at a high specific activity (HSA). The specific activity of ^{99}Mo is $\frac{A(^{99}\mathrm{Mo})}{m(\mathrm{Mo})}$, i.e. the activity A of ^{99}Mo divided by $m(\mathrm{Mo})$ i.e. the combined masses of all isotopes of Mo that are present in the product.

The production of ^{99}Mo via the fissioning of fissile actinides is denoted as an $(n,f)^{99}$Mo process.

1.2.3 Targeted radiopharmaceuticals and the need for high specific activity (HSA) ^{99}Mo

Before use in a patient, most medical radionuclides, including ^{99m}Tc, are chemically bound to a targeting vector, i.e. a molecule with a selective affinity for targeted tissue such as e.g. a cancerous tumour or a site of local inflammation or infection. This organic chemistry step is easier to perform if the activity of ^{99m}Tc per unit mass of saline eluate obtained from a ^{99}Mo-^{99m}Tc generator, is high. Conventional alumina-based elution systems in ^{99}Mo-^{99m}Tc generators are strongly dependent on the specific activity of ^{99}Mo, and a decreased specific activity will increase the required size of the elution column in the generator and ultimately decrease the concentration of the medical radionuclide, ^{99m}Tc, in the saline eluate. The lower the ^{99m}Tc activity per unit mass of saline eluate, the more difficult it is to chemically bind an adequate activity of ^{99m}Tc in targeted radiopharmaceuticals (Brown *et al.*, 2021).

1.2.4 The impossible quest: Producing high specific activity (HSA) ^{99}Mo via a non-fission process

An important principle is that conventional chemical separation techniques are practically incapable of distinguishing between isotopes of the same chemical element, i.e. chemical techniques are unable to e.g. enrich ^{99}Mo out of an ensemble of many isotopes of the element Mo. The same is true for other isotopes of, e.g., iodine.

If ^{nat}Mo is irradiated in a typical isotope production reactor (IPR), in an attempt to produce ^{99}Mo via neutron activation, then investigations with high-fidelity calculation models (Van Rooyen, 2020a)

indicate that a typical activity per unit mass of ^{99}Mo in chemically purified, extracted molybdenum will be in the order of 3.5E10 Bq/g, i.e. approximately 1 Ci/g.

If, on the other hand, fissile target plates with LEU_{20} (low enrichment uranium-containing approximately 20% ^{235}U in the uranium) are irradiated for 200 hours in an isotope production reactor (IPR) to produce ^{99}Mo via a fission-based process, SCALE ORIGEN calculations (Van Rooyen, 2020a) indicate that the activity per unit mass of the desired radionuclide ^{99}Mo in chemically purified, extracted Mo, will be in the order of 2.3E15 Bq/g, which is almost 5 decimal orders of magnitude higher (i.e. better) than that of ^{99}Mo produced by the neutron activation reaction $^{nat}\mathrm{Mo}(n,\gamma)$ in an IPR core. The general finding is that ^{99}Mo from a $^{nat}\mathrm{Mo}(n,\gamma)$ or $^{98}\mathrm{Mo}(n,\gamma)$ process, will be an inferior, low specific activity (LSA) product, whereas $(n,f)^{99}$Mo will be a superior, high specific activity (HSA), almost carrier-free product for deployment in ^{99}Mo-^{99m}Tc generators.

The conclusion is that the production of high specific activity ^{99}Mo via non-fission processes is difficult, if not impossible, so that there is an enduring need to use fission-produced ^{99}Mo (Mirzadeh *et al.*, 2011), especially in countries where nuclear medicine centres do not have on-site or near-site isotope production cyclotrons for the direct production of the short-lived ^{99m}Tc.

1.2.5 The large radioactive waste of a fission-based production route for ^{99}Mo

A fission-based production route for ^{99}Mo produces a large ensemble of undesired radioactive fission products — less than 10 % of the fission products are medically useful while the remainder is unwanted, radioactive byproducts. This means that the production of HSA ^{99}Mo via a fission process, leads to the parallel production of a large inventory of unwanted fission-products which constitute radioactive waste.

1.3 Fission-produced medical radionuclides: ^{99}Mo and ^{131}I

The easiest way to ensure a steady and dependable supply of the short-lived medical radioisotope ^{99m}Tc at hospitals and clinics, is to produce its longer-lived precursor, ^{99}Mo, which has a half-life of 65.976 hours, i.e. 2.749 days (Soppera *et al.*, 2013). The ^{99}Mo is then packaged in a ^{99}Mo-^{99m}Tc generator from which the desired medical radionuclide, ^{99m}Tc, can be eluted at clinics (Ahmad, 2011; Ahmad *et al.*, 2014). The latter radioisotope is then, typically, chemically bound to a targeting "vector" such as a monoclonal antibody, via an intermediate ligand (Jansen *et al.*, 2010). The "vector" is a molecule with a selective affinity for the targeted tissue, which leads to a selective, i.e. targeted delivery

of the radiopharmaceutical to targeted sites in the body (Kozempel *et al.*, 2018). The ability to elute and deploy ^{99m}Tc is most efficient when the ^{99}Mo in the generator is of high specific activity (HSA), i.e. the masses of other, undesired isotopes of Mo must be significantly less than the mass of ^{99}Mo in the generator (Tomar *et al.*, 2010).

High specific activity ^{99}Mo is produced with relative ease using a fission-based process (NEA, 2016), i.e. $(n, f)^{99}$Mo. Target plate (TP) assemblies that contain enriched uranium are irradiated in a high fluence-rate, φ_n, of thermalised neutrons, in a research reactor. The fissile uranium isotope, ^{235}U undergoes fission, and the desired radionuclide ^{99}Mo forms an economically viable fraction of the fission products. The ^{99}Mo-^{99m}Tc generators have useful service lives of circa 10 days after delivery at clinics.

The production of $(n, f)^{99}$Mo is most conveniently performed in research reactors, where it is relatively easy to load and unload target plate assemblies. If a research reactor is used almost exclusively for radionuclide production, it is designated as a Dedicated Isotope Production Reactor (DIPR).

Another fission product of interest to nuclear medicine is ^{131}I, which can, just as ^{99}Mo, be produced from the fission of ^{235}U. Quantified at a time circa 1 day after the removal of irradiated target plates from the reactor core, the activity of ^{99}Mo is circa 8.2 % of the total activity of all fission products, while that of ^{131}I amounts to circa 1.6 % of the combined activity of all fission products. (A "cooling" time of circa 24 hours is required before chemical processing of irradiated target plates can begin, because the initial heating power in irradiated TPs is excessively high (Van Rooyen & Adetula, 2018).) There is a lower clinical demand for ^{131}I than for ^{99}Mo, so that ^{99}Mo represents at least 95 % of the useful radionuclides produced by fission; therefore the name — $(n, f)^{99}$Mo — for this fission-based production route mentions only ^{99}Mo. It should be noted that high quality, HSA ^{131}I can also be produced via a non-fission route by irradiating a tellurium target in a research reactor (Fllaoui *et al.*, 2016; Haffner *et al.*, 2019; Van Rooyen, 2020b).

1.4 Radioactive waste from fission-produced ^{99}Mo

It is seen that the combined activity of medically useful radionuclides accounts for only 10 % (8.2 % ^{99}Mo plus 1.6 % ^{131}I) of the total inventory of fission products produced by irradiating fissile target material in fission reactors (activities are quantified 24 hours after the discharge of ITPs). All other

radionuclides from this process are presently viewed as radioactive waste, i.e. a liability that has to be disposed, at a significant cost.

There are 3 radioactive waste streams from the chemical processing of irradiated target plates: (1) solid uranic residue, (2) liquid waste as well as (3) gaseous waste, i.e. fission-gases such as radionuclides of krypton and xenon (IAEA, 1998). The actinides as well as some fission products with low solubility in the alkaline sodium hydroxide TP dissolution process, remain as insoluble "filter cake" i.e. solid residue (SR), formally referred to as SR-ITPs — solid residue from irradiated target plates. Other fission products show a chemical preference for the liquid waste stream. Most radionuclides partition between the solid and liquid pathways (IAEA, 1998), with reasonably consistent partition fractions, also called retention fractions. Because the chemical properties of different isotopes of a given element are essentially identical, the partition fractions are specified to codes such as the SCALE code ORIGEN (ORNL, 2020) or the UKAEA's code FISPACT-II (Sublet *et al.*, 2017) on a per-element basis, by specifying 2-column $(E; PF)$ partition fraction matrices, where E designates the element and PF the partition fraction for that element. The numerical values of the partition fractions for the generation of intermediate-level liquid (radioactive) waste (ILLW) from $(n, f)^{99}\mathrm{Mo}$ production, are discussed and presented in more detail from page 235 in Annexure B. These partition or retention factors are averages for the specific chemical processing technology employed at a specific facility. The liquid radioactive waste is accumulated and allowed to "cool off" for circa 3 months (90 days, i.e. approximately 0.25 years) before being mixed into a cemented slurry, which is transferred into 100-litre stainless-steel drums inside large concrete drums. These inner SS-304L drums typically have wall thicknesses of 3 mm, and serve as a durable, corrosion-resistant barrier to slow down any egress of radionuclides. The cementation matrix, the inner SS-304L drum and the outer concrete drum, serve as engineered barriers designed to immobilise the radionuclides for several centuries.

Radioactive waste that:

- has a high activity per unit mass,
- contains significant activities of radio nuclides with $T_{½} > 30$ yrs,
- contains negligible quantities of actinides, and
- generates a negligible heating power,

is classified as intermediate-level radioactive waste (ILW) (IAEA, 2009a). In liquid radioactive waste from $(n, f)^{99}\mathrm{Mo}$ production, the radionuclide $^{137}\mathrm{Cs}$ is notably present (see Figure 5-2 on page 164)

and becomes dominant (relative to other radionuclides) within approximately 5 years after waste production. This radioactive waste stream lies at the boundary between low-level (radioactive) waste (LLW) and intermediate-level (radioactive) waste (ILW) because the half-life of ^{137}Cs is almost exactly 30 years (Stewart *et al.*, 2013). This waste is presently classified as LILW-SL — Low and Intermediate-Level (radioactive) Waste, with an activity dominated by short-lived radionuclides — that is suitable for disposal in concrete drums, in near-surface trenches at the approved disposal facility. Whereas dry Very Low-Level (radioactive) Waste (VLLW) and LLW may be drummed in painted mild steel drums with metal wall thicknesses at or below 2 mm, the disposal of this LILW-SL is in stainless-steel drums embedded inside concrete drums. Because the radionuclide of principal concern is ^{137}Cs, the wasteform and waste package must be designed to survive predictably intact to circa 20 half-lives this nuclide, i.e.

$$20 \times 30 \text{ yrs} = 600 \text{ yrs}.$$

All Low and Intermediate-Level (radioactive) Waste (LILW) that is produced in a moist, wet or liquid form, requires cementation to immobilise the radionuclides in a chemically stable and durable solid matrix. Radioactive waste conditioning by cementation falls under the radioactive waste management category of predisposal operation (PDO). The 3 engineered barriers in this wasteform are, therefore (1) the cemented, solidified, immobilised waste matrix, (2) the stainless-steel drum and (3) the thick concrete drum.

1.5 Disposal of cemented liquid radioactive waste from fission-produced ^{99}Mo, in concrete drums

1.5.1 Selection of concrete drum material

The large concrete drums containing cemented liquid radioactive waste from fission-produced ^{99}Mo, must conform to dimensions approved by the nuclear safety regulator and radioactive waste disposal institutes, to allow for the optimal filling of trenches dug for drum disposal at disposal sites for radioactive waste. In other words, the outer dimensions of the drums used for the disposal of cemented liquid waste from target plate dissolution and chemical processing, are prescribed, but there is room for investigating different types of concrete as drum material, i.e. shielding material. Put in another way: the outer dimensions of the drums are fixed but the material composition of the drum's shielding material is open to investigation and optimisation.

In this work, the abilities of 4 different types of concrete are investigated computationally. These 4 concrete types are:

- Ordinary concrete (ORD-CRT)
- Magnetite concrete (MAG-CRT)
- Hematite concrete (HEM-CRT)
- Barite concrete (BAR-CRT).

1.5.2 Feasibility of computational shielding studies

Before circa 1975, relying only on computations for a study of the abilities of different concretes to shield radioactive material, would have been a "hard sell" to a safety regulator, because computers, radiation transport codes, as well as radiation interaction data, were all in underdeveloped, immature states. Today (2021), computers, radiation transport codes, as well as atomic and nuclear interaction data, have reached a level of maturity and reliability that allows the nuclear industry to rely almost completely on "computational experiments" for "virtual commissioning" of radiation shielding designs. Nuclear and radiation safety regulators are comfortable with this philosophy and practice, provided that (1) the design-basis source term and material compositions are realistic-conservative and (2) calculations are carried out within a quality management system where results are subjected to formal verification and validation (V&V) "reality checks".

1.6 Natural background dose rate, dose limits, dose constraints and demarcation criteria for radiological zoning

The average annual dose of ionising radiation to a person living on the surface of planet earth, is around 2.5 mSv (ICRP, 2007). If we deduct radon-related dose from this, we are left with around 1 mSv per annum. Dividing this dose by the number of hours in 1 year, leads to the result that the average natural background dose-rate (NBDR) on the surface of the earth[4] is in the order of 0.11 μSv/h, i.e. 1.1E-4 mSv/h, i.e.

$$NBDR \approx 0.11\ \mu\text{Sv h}^{-1} \tag{1-1}$$

[4] Note: The study supervisor (TJvR) was involved with such measurements for 16 years (1990 – 2006).

because $1.0\,\frac{\text{mSv}}{\text{yr}} \approx 0.11\,\frac{\mu\text{Sv}}{\text{h}}$.

The average dose limit for occupational exposure is an effective dose of 20 mSv per year (ICRP, 2007). For members of the public, this limit is 1 mSv per year (ICRP, 2007), with the understanding that no single facility or site may contribute more than $1/3$ of this limit. All nuclear and radiation facilities therefore work with the operational constraint that the most highly exposed member of the public may not receive more than 0.3 mSv i.e. 300 μSv per annum from practices (IAEA, 2014a).

Most operators of nuclear and radiation facilities classify areas where dose rates from ionising radiation may exceed approximately 1 μSv/h, i.e. 1.0E-3 mSv/h, as controlled radiation areas and place these under access control, signposting and radiological surveillance. At the Koeberg NPP this value is low and prudent, namely $0.5\ \mu\text{Sv/h}$ (Van Rooyen, 2019a) i.e. only 5 times higher than the NBDR. At [facility name omitted] this dose rate criterion for areas that do not require radiological demarcation somehow remained stuck — since approximately the 1970s — at the unusually high value of 2.5 μSv/h (Van der Merwe, 2017) which is 25 times higher than the NBDR and 5 times higher than the norm for radiological area demarcation used at the Koeberg PWR.

1.7 Transport of radioactive material

Any package containing radioactive material, e.g. a concrete drum containing radioactive waste, becomes eligible for road transport once the peak contact dose-rate (CDR) on its external surface drops to a value below 2 mSv/h, and its Transport Index (TI) is below 10. In SI units, this acceptance criterion on the TI means that the peak dose-rate at a distance of 1 m from the external surface of the drum, may not exceed 0.1 mSv/h. To qualify for road transport, both the above criteria have to be met — the limit on the peak contact dose-rate, as well as the limit on the TI. The maximum acceptable TI value on a package that may be transported by road, is almost 1000 times higher than the NBDR. The maximum allowed contact dose-rate (CDR) on the surface of a package that qualifies as transportable by road, is close to 20,000 times higher than the NBDR. More information about the regulations that govern the safe transport of radioactive material, as well as references, are presented in § 3.5.23 on page 123.

1.8 Economic reasons for this investigation

The specific economic driving forces for the investigation presented in this work, are as follows. If concrete compositions can be identified that reduce the transmitted dose rates to values several times lower than the dose attenuation factor achieved with the same thickness of ordinary concrete, (1) a significantly higher activity of radionuclides may be loaded per drum, and/or (2) the waiting time between the filling of the drum and its shipment from the waste producer to the waste repository can be reduced significantly, thereby lowering the number of drums that need to be procured to dispose of a given activity, as well as lowering the number of drums in on-site interim storage. Radioactive waste disposal institutes typically charge a "flat rate" per concrete drum (as well as a large penalty for drums that do not have standardised dimensions). The higher the dose attenuation factor of the fixed-thickness concrete wall of a drum, the more activity can be disposed of per drum, and the fewer drums would be required for radioactive waste disposal, i.e. disposal costs will be lowered. Even if the activity loading per drum remains constant, the waiting time before a drum becomes transportable will be lowered by using a drum material with superior shielding properties. (See 3.5.23 on page 123 for the radiological acceptance criteria that apply to the shipment (e.g. road transport) of radioactive material.) If drums are filled at a fixed rate, and the use of high-density shielding concrete reduces the required on-site, predisposal storage time from e.g. 15 years to 1 year, it follows that up to 15 times fewer drums will have to be held in on-site interim storage, which will be of considerable practical benefit to the waste producer.

1.9 Research purpose and research problem

The purpose of the research reported here is the quantification of the relative abilities of different concrete compositions for concrete drums for the storage, transport and disposal of intermediate level radioactive waste (ILW), to reduce the dose rate outside the drums. Practical problems that have led to this research are economic: The disposal of intermediate-level radioactive waste in large concrete drums, is expensive because (1) the unit cost of a drum is high, (2) road transport of drums over the approximately 1200 km that separates the waste generator site and the disposal facility, is costly and (3) the disposal charge per drum is high and continually escalating. If radioactive waste disposal drums manufactured from concrete having a low shielding factor SF are used, a limited amount of activity can be disposed of in a single drum, and a large number of drums will have to be used, stored, transported and disposed of, i.e. the aggregated cost will be high. If concrete materials with better shielding factors SF are used, more activity can be disposed of per drum, or drums can be shipped to

the disposal site sooner, i.e. fewer drums will have to be stored by the waste producer. These benefits will translate into economic savings.

The production of medical radionuclides should not be based on a foundation of generating present income at the cost of neglected and unfunded future liabilities. In other words, radioactive waste disposal should be planned, financed, engineered and managed in a manner that will minimise detriment and cost.

1.10 Research objectives

The general research objective in this dissertation is to quantify the performance of 4 different concrete compositions as shielding drum material for the storage, transport and disposal of intermediate-level liquid (radioactive) waste (ILLW) from irradiated target plates used to produce fission-produced ^{99}Mo, i.e. $(n,f)^{99}$Mo. The concrete types under investigation are listed in § 1.5.1 on page 44. A more specific, detailed set of step-by-step research objectives can only be formulated after an extensive survey of the scientific literature. Such detailed research objectives are therefore presented in § 4.12 which starts on page 151.

1.11 Research hypothesis

The research hypothesis is as follows:

Intermediate-level liquid (radioactive) waste is disposed of in concrete drums of given dimensions. Because concrete drum dimensions such as height, diameter and the wall thickness of the concrete, are "locked-in" design facets, the performance of the concrete shielding drums containing cemented ILW from fission-based radionuclide production, can only be improved by increasing the shielding factor (SF) presented by a given, fixed thickness of concrete shielding material. The category of ionising radiation from ILLW that is responsible for practically all radiation dose outside the drums, is ionising photons. It is a well-known fact that the ability of a material to attenuate ionising photons within the energy range emitted by ILW from $(n,f)^{99}$Mo production, i.e. the shielding factor (SF) presented by a given thickness of shielding material, generally increases as a function of (1) the atomic number Z of the chemical elements in, and (2) the mass-density ρ of, the shielding material. (These principles of the shielding of ionising photons are presented in § 2.2 which starts on page 55.)

In ordinary concrete, the dominant elements are O ($Z(\mathrm{O}) = 8$), Si ($Z(\mathrm{Si}) = 14$) plus some Ca ($Z(\mathrm{Ca}) = 20$). Ordinary concrete typically contains around 53 % O, 34 % Si 3 % Al and 4.5 % Ca. This means that ordinary concrete is a low-Z shielding material; furthermore, its mass-density is typically below 2.4 $\mathrm{g\,cm^{-2}}$, i.e. mediocre. In magnetite concrete, the silicon dioxides in fine and coarse aggregate used in ordinary concrete, are substituted by magnetite ore fine and coarse aggregates. Magnetite is an iron oxide, i.e. the ore will contain a significant fraction of the higher-Z element Fe ($Z(\mathrm{Fe}) = 26$). A typical magnetite concrete will contain a minimum of 35% Fe by mass. Hematite concrete uses fine and coarse materials from hematite ore, which is even richer in Fe than magnetite ore, and a typical hematite concrete will contain a minimum of 45 % Fe by mass. In the making of barite concrete, the fine and coarse material (sand & gravel) used in ordinary concrete, are replaced with fine and coarser material from barite ore, which typically contains 90 % or more $\mathrm{BaSO_4}$ (barium sulphate). A typical barite concrete will contain a minimum of 45% Ba by mass. Barium is attractive because it has a high atomic number of $Z(\mathrm{Ba}) = 56$.

By using high-density shielding concretes such as magnetite or hematite concrete, which contains a high proportion of the element Fe ($Z(\mathrm{Fe}) = 26$), or barite concrete, which contains a significant fraction of the element Ba ($Z(\mathrm{Ba}) = 56$), the average Z-value of the shielding material is increased, as is its mass-density ρ. By virtue of $\boxed{Z \uparrow}$ and $\boxed{\rho \uparrow}$, it is hypothesised that $\boxed{\mathrm{SF} \uparrow}$, i.e. using shielding materials with higher average atomic numbers and higher mass-densities will improve shielding factors favourably, relative to the baseline case of ordinary concrete. This will open the door to the economic benefits listed in § 1.8 on page 47. The above expectation of quantitative shielding performance can be formulated as $\boxed{\left\{\begin{matrix}\boxed{Z \uparrow} \\ \boxed{\rho \uparrow}\end{matrix}\right\} \Rightarrow \boxed{\mathrm{SF} \uparrow}}$.

Based on the Z-values of the elements in the different concretes being investigated, the mass fractions of the elements having $Z > 20$ in these concretes, and the typical mass-densities ρ of high-density shielding concretes, it is hypothesised that, for a given radioactive source term and a fixed concrete drum wall thickness, the shielding factors (SFs) will be related as per Eq. (1-2),

$$\boxed{\mathrm{SF(BAR\text{-}CRT)}} > \boxed{\mathrm{SF(HEM\text{-}CRT)}} > \boxed{\mathrm{SF(MAG\text{-}CRT)}} > \boxed{\mathrm{SF(ORD\text{-}CRT)}}. \qquad (1\text{-}2)$$

The above formulation of the research hypothesis means that barite concrete is expected to perform best, hematite second best, magnetite concrete third best and ordinary concrete the worst.

The null-hypothesis can be formulated as "heavy shielding concretes, i.e. high-density concretes, will not reduce transmitted dose-rates to lower values than is obtained with the use of ordinary concrete". The alternative hypothesis is that "heavy shielding concretes will reduce transmitted dose-rates to significantly lower values than is obtained with the use of ordinary concrete". In this work, the null-hypothesis will be shown to be false, i.e. the alternative hypothesis will be accepted. The alternative hypothesis can be summarised as $\left\{\boxed{Z \uparrow}\right\} \Rightarrow \boxed{\text{SF} \uparrow}$.

1.12 Research methodology

The research methodology that is followed to reach the research objectives, is the following multi-step process:

1. Perform an extensive literature survey in order to become familiar with, and to summarise, present best practices regarding the immobilisation, shielding, storage, transport and disposal (CISSTD) of intermediate-level liquid (radioactive) waste (ILLW).

2. Define a conservative yet realistic design-basis source term for the radionuclide loading that enters into a single concrete drum earmarked for disposal, in terms of (1) the number of chemically processed irradiated target plates, (2) target plate power, (3) irradiation time and (4) the partition factors encountered in the separation chemistry that produces the ILLW from $(n, f)^{99}$Mo production.

3. Use a calculation model developed for the ORIGEN code in the SCALE 6.2.4 (ORNL, 2020) computational system, to quantify the design-basis source term as a {nuclide, activity matrix} i.e. $[N_i; A_i(t)]$ matrix, where N_i is the identity of radionuclide i and $A_i(t)$ is its activity at time t.

4. In the above calculation model, instruct the code ORIGEN to use the radiation emission nuclear database in SCALE 6.2.4 to convert the $[N_i; A_i(t)]$ matrix to an {photon energy, photon emission yield} i.e. an $[E_g; Y_g(t)]$ photon emission matrix, where E_g denotes the energy and Y the emission yield, with $g = 1, \dots G$ being the index of the multigroup partition of the photon energy variable. The $[N_i; A_i(t)]$ matrix and the derived $[E_g; Y_g(t)]$ matrix jointly constitute the "source term" of the package of radioactive material at a number of discrete times t. To

ensure good accuracy, partition the photon energy range $[0.001\ \text{MeV}; 20\ \text{MeV}]$ into $G = 290$ energy groups (which is specified to the SCALE code ORIGEN).

5. Use the $[E_g; Y_g(t_d)]$ radiation emission source-terms obtained from the ORIGEN calculation model, at a number of selected decay times, t_d, in MCNP6.2 (LANL, 2018) calculation models to quantify the dose rate field around a single drum as well as an array of drums, for the four concrete compositions as well as for the reference case of unshielded drums. This serves to quantify dose rates for comparison with regulatory limits, demarcation criteria and acceptance criteria, and also serves to quantify shielding factors SF that are achieved, so that the different concrete shielding materials can be compared.

6. Test the research hypothesis and accept either the null-hypothesis or the alternate hypothesis. (It will only be necessary to resort to the use of formal inferential statistics to choose between the null-hypothesis and the alternate hypothesis, if there is any evidence that the effect size and the statistical spread in results make the use of inferential statistics necessary. If the effect size exceeds the statistical uncertainty by orders of magnitude, there is no need for using formal inferential statistics.)

7. Arrange the shielding performance of the different concrete compositions, from best to worst.

8. Recommend the most practical concrete composition for concrete drums containing ILLW, based on a balanced consideration of (1) shielding efficacy, (2) cost, (3) the availability of a local supply chain in Southern Africa as well as (4) the ethical principle of sourcing materials locally to stimulate the Southern African economy.

1.13 Organisation of this dissertation

This dissertation is organised into 6 chapters and 2 annexures.

Chapter 1 (which starts on page 39) paints a picture of the societal, medical and technological backdrop and motivation for this study. The production of a medical radionuclide that is in high demand world-wide, depends largely on a fission-based production process that produces a high quantity of radio-active waste. The level of radioactivity as well as the emission characteristics and half-lives of the radionuclides present in the intermediate-level liquid (radioactive) waste (ILLW) from the $(n, f)^{99}\text{Mo}$ production process, requires several centuries of adequate confinement as well as radiation shielding

during, the latter especially during storage and transport to the disposal site. Four candidate concrete types are introduced and the research objectives are formulated

Chapter 2 (which starts on page 55) focuses on the cost-effective radiation shielding of radioactive sources that are dominated by the emission of ionising photons, as is the case with ILLW. *Metrics of merit* for radiation shielding materials are formulated: the dose attenuation factor (DAF) as well as the shielding factor (SF). The radiation physics theory about the relative performance of the elements of the Periodic Table against photon-dominated sources of ionising radiation, is reviewed. To design radiation shielding based on effective, available, affordable and benign materials, the natural abundance and safety of different raw materials that can be used as aggregate for producing concrete shielding drums, are reviewed. Two elements in the Periodic Table that have atomic numbers $Z > 20$, are earmarked as being abundant and affordable: Fe and Ba. The mineral forms in which these elements are available in nature, are identified and are screened for chemical stability and low toxicity. Four candidate radiation shielding concrete formulations are identified as viable and worthy of further investigation.

Chapter 3 (which starts on page 87) deals with the classification, conditioning, immobilisation, shielding, storage, transport and disposal of radioactive waste, in particular ILLW from the fission-based production of medical radionuclides. The main literature review of this study is concentrated in Chapter 3. First, an overview of the IAEA's classification system for radioactive waste, is presented. Next, the concept clearance level is introduced and 2 sets of currently implemented clearance levels are given. The radioactive content of the immobilised waste matrix under assessment is measured against current clearance levels and it is shown that the radioactive waste has to be immobilised in a durable wasteform and placed inside engineered and natural barriers for at least 600 years; this requirement necessitates the use of a cementation matrix inside an inner stainless-steel drum, which is embedded inside an outer concrete drum; this entire waste package is disposed in near-surface trench disposal at an arid waste disposal site. A selection of published literature dealing with the classification, immobilisation, shielding, storage and disposal of radioactive waste, is reviewed. The radioactive waste conditioning technology of immobilisation via cementation, is discussed. An overview of cement and concrete types and aggregates used in ordinary and high-density shielding concretes, are presented. Concepts such as wasteform and engineered barrier system, are discussed. Attention is also focused on the use of clays placed around packages of disposed radioactive material, as a secondary engineered barrier that will serve to further adsorb and immobilise any radioactive material that may begin to leach out of the wasteform after e.g. a century post disposal. The road

transport of concrete radioactive waste drums is discussed in the context of international radiological safety criteria. Upon the completion of the literature survey, gaps that presented themselves are identified, with the aim of addressing these deficiencies in the dissertation.

Chapter 4 (which starts on page 127) deals primarily with the source term in the ILLW studied in this work. The technical concept "source term" involves the {Nuclide, Activity} i.e. $[N_i; A_i(t)]$ matrix in the ILLW and the consequent radiation emission {Energy, Yield} matrix, i.e. $[E_g; Y_g(t)]$ matrix representing the spectral detail of radiation emission. Conceptual details about the irradiation of target plates in a research reactor is presented, with the aim to define a conservative yet realistic design-basis source term $[E_g; Y_g(t)]$. The process of nuclear fission is presented. The yield of fission products and the reason for the radioactivity of fission products, are discussed. The 3 radioactive waste streams inherent in $(n, f)^{99}\mathrm{Mo}$ production, are presented. Some predisposal waste management process detail for the ILLW is presented, including cementation, drumming and on-site interim storage of the waste drums. Enough background and foundational concepts have been introduced at this stage, to progress to the formulation of a formal list of research objectives, in their final, detailed form.

Chapter 5 (which commences on page 156) introduces calculation models developed for the 2 major codes that were used in this study. Computed results are presented, discussed and explained. The performance of the 4 candidate concrete types for a single drum of radioactive waste, as well as for an array of drums standing in the "decay yard" at the production facility, are quantified and discussed. One finding is that the decay yard requires a shielding wall around its perimeter, and a calculation model is used to arrive at a viable design for such a wall. A range of graphs and contour plots are used to summarise the results. The question about the minimum burial depth of the drums in the trenches at the disposal site, is answered using a calculation model along with an imposed constraint on the surface dose rate. Finally, tenth-value thickness (TVT) values for 3 high-density shielding concretes are quantified for the shielding of a selection of important radionuclides.

A short Chapter 6 (page 212) summarises the overall research findings and highlights how the research objectives were met. The winner of the contest for "best shielding concrete" is announced, but another concrete type is recommended as a more practical solution in the light of local availability of raw materials as well as cost. Finally, the value added by this research and dissertation is highlighted.

Annexure A (starting on page 216) presents detail about a typical research reactor and target plate technology used to produce $(n, f)^{99}\mathrm{Mo}$. Design detail as well as proprietary chemical processing detail are deliberately omitted, to protect Intellectual Property (IP).

Annexure B (page 222) presents technical detail regarding codes and calculation models developed for and used in, this study; it serves as a repository for technical detail that is considered too detailed to warrant inclusion within the main body of this document.

2. Radiation shielding materials against photon-dominated radioactive sources such as ILLW

2.1 Introduction

This chapter presents a literature survey regarding the shielding of radioactive sources that are dominated by the emission of ionising photons. The survey is presented in several sections.

1. The concepts dose attenuation factor (DAF) and shielding factor (SF) are introduced in § 2.2; these quantities are used as metrics of merit for assessing and comparing the performance of radiation shielding structures such as concrete drums and walls.

2. Literature reviewed in § 2.3 brings the fundamental physics principles that underly the shielding of ionising photons into focus and shows how these can be used to design optimised radiation shielding around intense sources of ionising photons, such as e.g. ILLW.

3. The short survey in § 2.4 focuses on identifying readily available chemical elements and affordable minerals that are suited for use in concretes with radiation shielding applications in the disposal of radioactive waste such as ILLW, which contains high activities of nuclides that emit ionising photons.

4. In § 2.5 the four concrete compositions that will be assessed for their shielding performance for ILLW, are specified.

2.2 Dose attenuation factor (DAF) — a criterion for judging the efficacy of radiation shielding

Radioactive waste that contains a high activity of radionuclides and a high activity per unit mass, typically require shielding to make storage areas radiologically acceptable and to enable the road transport and final disposal of the radioactive waste. It is necessary to develop metrics of merit for the radiological benefit of layers and structures that perform a radiation shielding function. Two such metrics of shielding performance are developed here: the dose attenuation factor (DAF) and the shielding factor (SF). These metrics will be used extensively in the reporting of results in Chapter 5.

Consider the general source-shield structure shown in Figure 2-1. Ionising radiation is incident on the shield, and the transmitted dose rate at a point of interest, x, is $\dot{D}(x)$.



Figure 2-1: A general source-shield concept

For a given shielding application, a given material configuration of radiation shielding material around a source of ionising radiation, is characterised by a dose attenuation factor (DAF), defined in Eq. (2-1). Here the literal subscript WS means "with shield" while NS means "no shield".

$$\begin{aligned} DAF(x) &= \frac{\text{Transmitted dose-rate at position } x, \text{with the shield in place}}{\text{Transmitted dose-rate at position } x, \text{without the shield in place}} \\ &= \frac{\dot{D}(x) \text{ with the shield in place}}{\dot{D}(x) \text{ without the shield in place}} \\ &= \frac{\dot{D}_{WS}(x)}{\dot{D}_{NS}(x)} \end{aligned} \tag{2-1}$$

In Eq. (2-1), the point x is located on the opposite side of the shield compared to the source, as is seen in Figure 2-1, i.e. $DAF(x)$ relates to the transmitted dose rate. If a radiation shield imparts e.g. $DAF = \frac{1}{150}$ to a system, this implies that the radiation shield decreases the transmitted dose-rate to a value $\frac{1}{150}$ of what the radiation level would have been at the measurement position x, in the absence of the radiation shield. In different terms, if $DAF = \frac{1}{n}$, this means that we are gaining a radiological shielding factor of $SF = \frac{1}{DAF}$ by deploying the shielding. The simple reciprocal relationship between the shielding factor (SF) and the dose attenuation factor (DAF) is given in Eqs. (2-2) and (2-3).

$$DAF = \frac{1}{SF} \tag{2-2}$$

and

$$SF = \frac{1}{DAF}. \tag{2-3}$$

Let $\dot{D}_{NS}$ signify the dose rate at a position of interest such as inside a given calculational detector, when there is no shielding material, (this usually means that only air is present; NS = "no shield"). Let $\dot{D}_{WS}$ signify the dose rate at the same position when an engineered radiation shield is in place (WS = "with shield"). Then the definition for the dose attenuation factor can be expressed as in Eq. (2-4)

$$DAF = \frac{\dot{D}_{WS}}{\dot{D}_{NS}} \tag{2-4}$$

while the shielding factor SF, which is the reciprocal of the DAF, can be written as Eq. (2-5)

$$SF = \frac{\dot{D}_{NS}}{\dot{D}_{WS}}. \tag{2-5}$$

If radiation shielding imparts a shielding factor of e.g. $SF = 150$ to a system, this makes the workplace a factor 150 times safer compared to the case where no shielding is used.

2.3 Review: Radiation physics principles for the shielding of packages of radioactive material that are dominated by the emission of ionising photons

2.3.1 Ionising photons

In the disciplines of atomic and nuclear physics, a distinction is made between X-rays and γ-rays. For the purposes of radiation shielding, this distinction is usually irrelevant, so that the term ionising photon is used instead. When the symbol γ is used in this work, it signifies any ionising photon, irrespective of whether this photon originated in an atomic process (as an X-ray photon) or a nuclear process (i.e. as a gamma-photon).

Research objective RO_1, which is formulated on page 153, is the need to present a clear formulation of the radiation physics principles that underlie the optimisation of radiation shielding for radiation sources that are dominated by the emission of ionising photons.

2.3.2 Atomic physics mechanisms for the attenuation of ionising photons

In the energy range of ionising photons emitted by the radionuclides in liquid radioactive waste from a fission process, practically all photons will be produced at energies lower than circa 5 MeV — see

e.g. Figure 5-3 on page 165 as well as Table 5-4 on page 166. In this energy range, 3 photon interaction mechanisms are dominant: photo-electric absorption (PEA), Compton scattering (CS) and pair production (PP). These 3 interaction types will now be discussed.

Photo-electric absorption (PEA)

Photo-electric absorption (PEA) involves the total absorption of the incident photon by the electrons of the atom. The atomic electrons do not interact with the incident photon as free electrons, but as bound electrons; PEA is a reaction between the incident ionising photon and the entire atom (Shultis & Faw, 2000:44). The incident photon is absorbed, and the energy that is imparted to the atom causes the emission of a so-called photo-electron. From the principle of conservation of total energy, it follows that the energy of the emitted photo-electron will be lower than that of the incident photon that had been absorbed in PEA. For photon interactions with materials with $Z \leq 60$, PEA is dominant in the energy range below typically 0.5 MeV (see Figure 2-2 on page 60). The energies of emitted photo-electrons will typically be in the energy range below 0.1 MeV, and for such low-energy electrons, the formation of bremsstrahlung photons is practically irrelevant i.t.o. energy and yield. When the vacancy left by the emission of the photo-electron is filled with an electron from an outer shell, either characteristic fluorescence X-rays or Auger electrons may be emitted. The penetrating abilities of characteristic fluorescence X-rays are negligibly low, and Auger electrons have such low energies that bremsstrahlung production may be ignored. Secondary ionising particles are emitted when PEA takes place, yet energy conservation considerations imply that the energies of all individual secondary photons will be far less than the energy of the original incident ionising photon. From the expression $\boxed{\mu_{PEA} \propto \rho^1 Z^3}$ in Table 2-2 on page 64, it follows that the linear interaction coefficient μ_{PEA} for the photo-electric absorption of these less energetic, secondary photons will be considerably larger than the cross-section for the photo-electric absorption of the original photon. A series of successive reactions will take place, and every PEA event in this interaction sequence will further decrease the photon energy, E_γ. Eventually, photon energies will drop into the domain where both the penetrating ability and the biological hazardousness of the photon are irrelevant.

Compton scattering

Compton scattering (CS) is an interaction of an incident photon with an individual atomic electron. The effect of CS on the energy of photons is best illustrated by presenting a numerical example. Because CS is an interaction between a photon and an independently acting electron, the numbers

quoted below are practically independent of the interacting atom. Consider e.g. a photon of incident energy $E_\gamma = 0.85$ MeV that undergoes Compton scattering with an atomic electron. It can be shown that the expectation value of the scattering angle will be $\langle\theta\rangle = 51°$ and that the expectation value of the energy of the scattered photon will be $\langle E\rangle = 0.52$ MeV (Van Rooyen, 1992). If the Compton scattered photon undergoes another CS interaction, the expectation value of the scattering angle will now be $\langle\theta\rangle = 57°$ and the expectation value of the energy of the scattered photon will be $\langle E\rangle = 0.38$ MeV (Van Rooyen, 1992). For a third CS event, $\langle\theta\rangle = 61.4°$ and $\langle E\rangle = 0.30$ MeV; for a fourth CS event, $\langle\theta\rangle = 64.6°$ and $\langle E\rangle = 0.24$ MeV. Eventually, CS will scatter the photon into the energy domain where PEA becomes the most likely photon interaction mechanism. A PDF version of a MathCAD-15 worksheet that analyses Compton scattering is embedded here (Van Rooyen, 1992):



Because CS is an interaction with an individual atomic electron and not with the atom as a whole, the linear interaction coefficient for CS is linearly proportional to ρ but is independent of Z.

Pair production (PP)

When the energy of a photon is more than twice the rest-mass energy $m_e c^2$ of an electron, i.e.

$$E_\gamma > 1.02 \text{ MeV},$$

the formation of an electron-positron pair becomes energetically possible. In pair production (PP), the incident photon disappears and in its place an electron-positron pair appears. As a result of the law on the conservation of linear momentum, pair production can only take place in the vicinity of a third particle that can recoil to take up linear momentum. This recoiling particle must have an electrical charge, and is usually an atomic nucleus. As a result of the kinetic energy absorbed by the recoil particle, the threshold for pair production is marginally larger than 1.02 MeV. Excess energy of the incident photon is shared between the kinetic energies of the positron, electron and recoiling particle.

Consider an electron-positron pair produced by pair production. The electron e^- and positron e^+ are charged particles and are slowed down by continuous Coulomb interactions in matter, as well as by the emission of bremsstrahlung photons (continuous-spectrum X-rays), in a process that can be termed radiative slowing-down. Bremsstrahlung photons will have energies far lower than that of the incident photon. When the positron had lost most of its energy, it recombines with its anti-particle, namely a

negatively charged electron. Both leptons disappear, and typically 2 annihilation photons, each of which has an energy equal to the rest-mass energy of the positron, i.e. 0.511 MeV, are produced.

Pair production is a markedly effective photon attenuation mechanism in that it is able to lower photon energies by a decimal order of magnitude or more (from e.g. 8 MeV to 0.511 MeV) in a single interaction. The exit-energy of the photons from PP events, namely 0.511 MeV, falls in the energy range where these photons will typically undergo e.g. 2 to 5 subsequent CS events before being absorbed in a PEA event. In this fashion, PP can serve as the first event in a chain of interactions that will rapidly degrade photon energies from e.g. 10 MeV to values below the threshold for ionisation, i.e. under 1 keV. When photons reach such low energies, they are highly absorbable and have lost most of their ionising nature and related biological hazard.

2.3.3 Energy dependence of photon interaction cross-sections for PEA, CS and PP

Regions in the $(E_\gamma; Z)$ plane where different photon interaction mechanisms dominate — PEA, CS and PP — are shown in Figure 2-2.

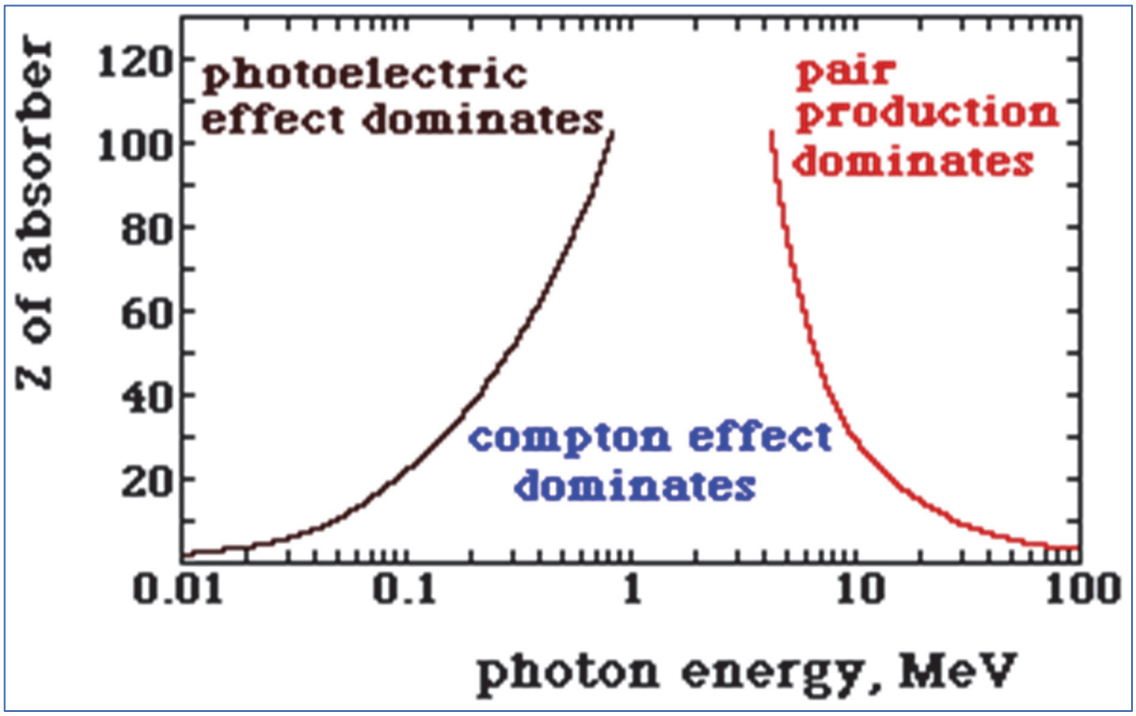


Figure 2-2: Regions in the (E_γ; Z) plane where different photon interaction mechanisms dominate — PEA, CS and PP

Figure 2-3 shows the photon energy ranges where PEA, CS or PP will dominate photon interactions, for Pb ($Z(Pb) = 82$) as the material medium.

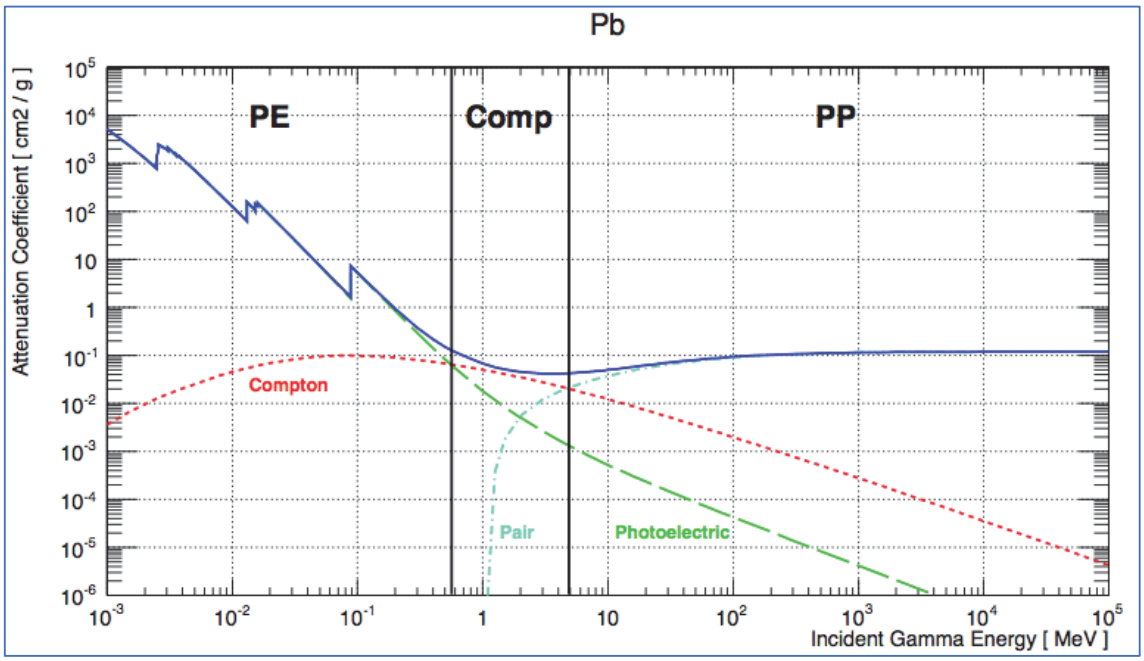


Figure 2-3: Photon energy domains where PEA ("PE" in the graph), CS or PP dominates, in the case of the material Pb (Z(Pb) = 82)

Figure 2-4 shows the 3 dominant photon interaction mechanisms for the element Fe. The data for the plot was taken from ENDF/B-7.1 in SCALE 6.2.4 by using the SCALE Fulcrum interface (ORNL, 2020).

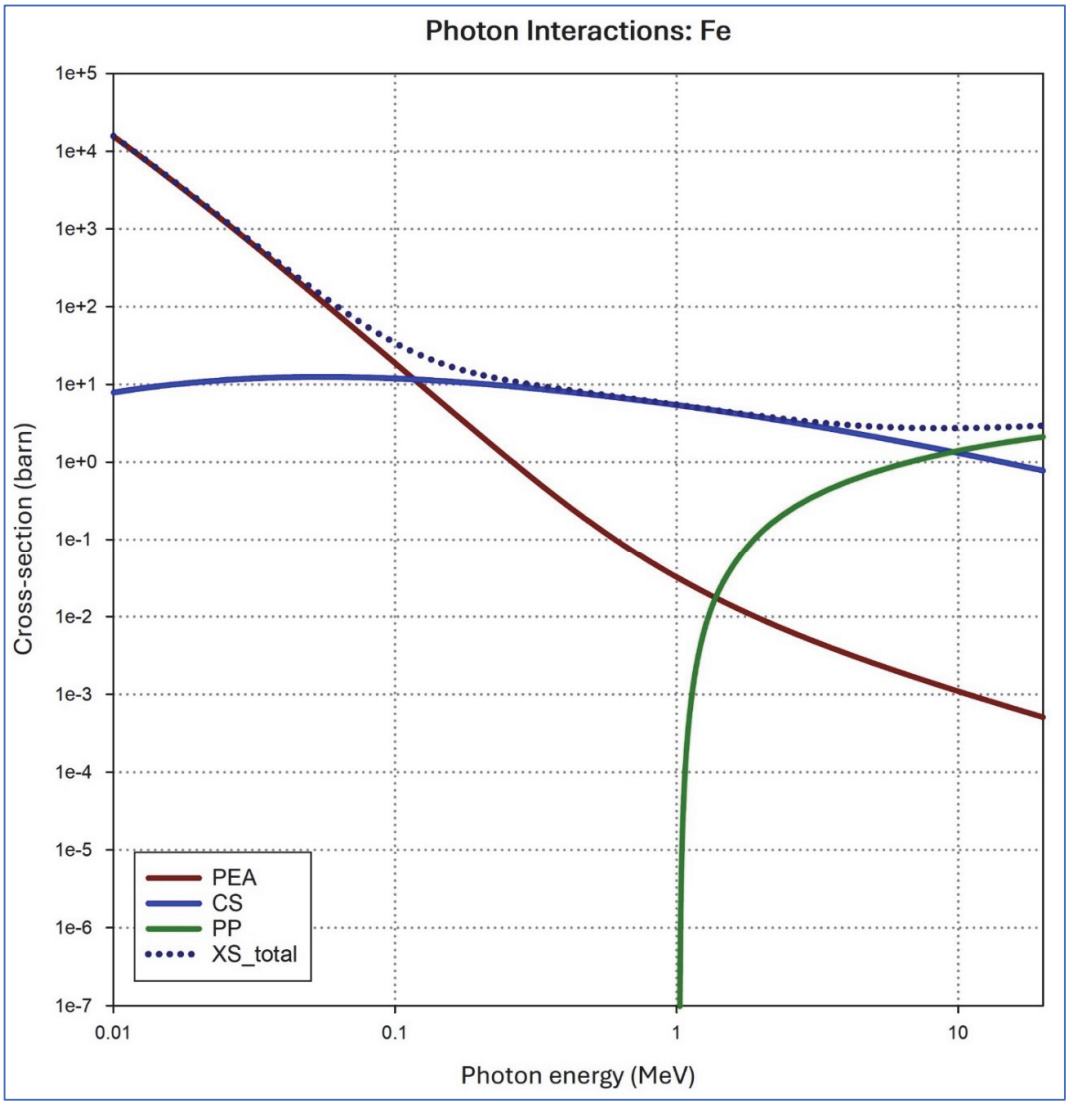


Figure 2-4: Important photon interaction mechanisms and their cross-sections for Fe

2.3.4 Energy range of dominance: PEA, CS and PP

Table 2-1 summarises the photon energy regions where the 3 principal interaction mechanisms — PEA, CS and PP — will be dominant for the chemical elements in shielding materials, including shielding concretes.

Table 2-1: Photon energy regions where the 3 principal interaction mechanisms, PEA, CS and PP, will be dominant for materials in common shielding concretes

	PEA dominant	CS dominant	PP dominant
O and Si ($Z \approx 11$) (ordinary concrete)	$E_\gamma \leq 0.06$ MeV	0.06 MeV $\leq E_\gamma \leq 20$ MeV	$E_\gamma \geq 20$ MeV
Fe ($Z = 26$) (Magnetite and Hematite concrete)	$E_\gamma \leq 0.12$ MeV	0.12 MeV $\leq E_\gamma \leq 10$ MeV	$E_\gamma \geq 10$ MeV
Ba ($Z = 56$) (Barite concrete)	$E_\gamma \leq 0.3$ MeV	0.3 MeV $\leq E_\gamma \leq 7$ MeV	$E_\gamma \geq 7$ MeV
Pb ($Z = 82$)	$E_\gamma \leq 0.6$ MeV	0.6 MeV $\leq E_\gamma \leq 5$ MeV	$E_\gamma \geq 5$ MeV

In Table 2-1 it is seen that the energy band where Compton scattering dominates, is very wide for low-Z materials such as O and Si, and becomes increasingly narrow for higher-Z materials such as Ba and Pb.

Application to photon emission spectrum of ILLW

In Table 5-4 on page 166 it is seen that practically no photons are emitted from ILLW in the high energy range where pair production will be dominant. Practically all photons are emitted in the energy range where Compton scattering, and photo-electric absorption will be dominant. An incident photon will typically undergo a number of Compton scattering interactions, followed by PEA.

2.3.5 Radiation physics "recipe" for selecting optimal shielding materials against ionising radiation

The only penetrating ionising radiation type emitted by the radionuclides in cemented LILW-SL from $(n,f)^{99}$Mo production, is ionising photons. The maximum range of any emitted electrons in the cement or concrete will be below a few mm, so that primary electrons cannot possibly traverse the concrete. All primary electrons will be slowed down and stopped inside the cemented radioactive waste matrix, the 3 mm thick stainless-steel inner drum, and the wall of the concrete drum, and will, at most, emit some low-energy bremsstrahlung photons. From the perspective of ionising radiation that contributes to the dose rate field surrounding the concrete drum, the only particle of concern is primary ionising photons.

Three important photon interaction types are possible in the energy range of photons emitted in the liquid radioactive waste: Photo-electric absorption (PEA), Compton scattering (CS) and pair production (PP) (Shultis & Faw, 2000, 2005). These photon interaction types are responsible for the attenuation, i.e. the shielding, of the emitted ionising photons. As shown above, photo-electric absorption and Compton scattering will be the 2 dominant photon interaction mechanisms, especially after the cemented ILLW had been cemented and stored for more than 1 year, when the energy spectrum $Q(E)$ of emitted photons move towards lower energies. Expressions were derived for the linear interaction coefficients of the 3 dominant photon interaction mechanisms, in materials with atomic number Z and mass-density ρ; these expressions are summarised in Table 2-2 (Van Rooyen, 2020c). The linear interaction coefficient μ is related to the interaction cross-section σ by the relationship $\mu = N\sigma$, where N is the number-density of atoms of the element per unit volume.

Table 2-2: The 3 principal interaction mechanisms of ionising photons, and their linear interaction coefficients μ = Nσ

Interaction	**Linear interaction coefficient μ**
Photo-electric absorption (PEA)	$\mu_{PEA} \propto \rho^1 Z^3$
Compton scattering (CS)	$\mu_{CS} \propto \rho^1$
Pair production (PP)	$\mu_{PP} \propto \rho^1 Z^1$

From the 3 expressions for the linear interaction coefficient μ in Table 2-2, the author (Van Rooyen, 2020c) states:

> It follows clearly […] that there exists a simple recipe for maximising the efficiency of radiation shielding against a source of ionising photons: Maximise the atomic number Z and maximise the density ρ of the shielding material.

The above "materials selection recipe" works well in the photon energy range below circa 10 MeV; at higher photon energies, the (γ, n) reaction channel opens and makes shielding material selection more complex.

A typical shielding optimisation problem has the following format: A given thickness is available for placing shielding materials. Select a durable and affordable shielding material that will maximise the shielding factor that can be achieved for this constrained material thickness. In other words, the

shielding thickness is fixed shielding material must be selected that has to minimise the transmitted dose-rate, while also being affordable, durable and non-toxic.

To test the strength of drums for the storage and disposal of radioactive waste, these drums undergo drop tests and the amount of cracking and material loss suffered during such tests, have to pass regulatory acceptance criteria (IAEA, 2018).

2.3.6 Linear attenuation coefficients for barite concrete and ordinary concrete

The US National Institute of Standards and Technology (NIST) lists mass attenuation coefficients for interaction of ionising photons with matter, for elements up to $Z = 92$ as well as a small selection of compounds. These compounds include 2 types of concrete, namely ordinary concrete and barite concrete (but not magnetite or hematite concrete); the NIST data can be found at the following URLs:

https://physics.nist.gov/PhysRefData/XrayMassCoef/ComTab/concrete.html
https://physics.nist.gov/PhysRefData/XrayMassCoef/ComTab/concreteba.html

The above atomic interaction data for ionising photons were used to produce Figure 2-5 and Figure 2-6.

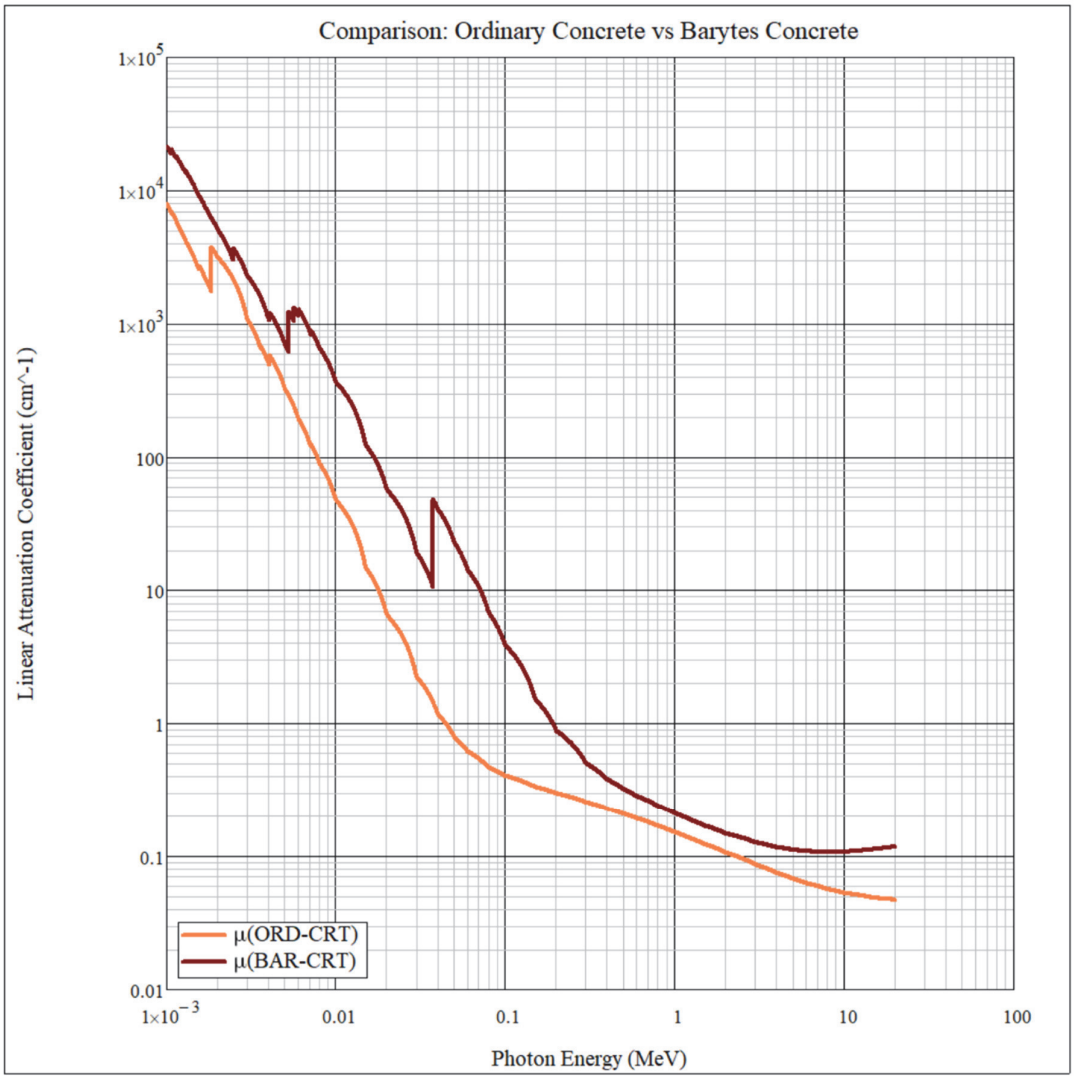


Figure 2-5: Linear interaction coefficients for photon interactions in ordinary concrete (ORD-CRT) and barite concrete (BAR-CRT)

Note that the vertical axis in Figure 2-5 is logarithmic, i.e. the ratio $\frac{\mu_{BC}(E)}{\mu_{OC}(E)}$ is not properly appreciated when looking at this figure. For this reason Figure 2-6 displays the ratio $\frac{\mu_{BC}(E)}{\mu_{OC}(E)}$ on a linear vertical axis.

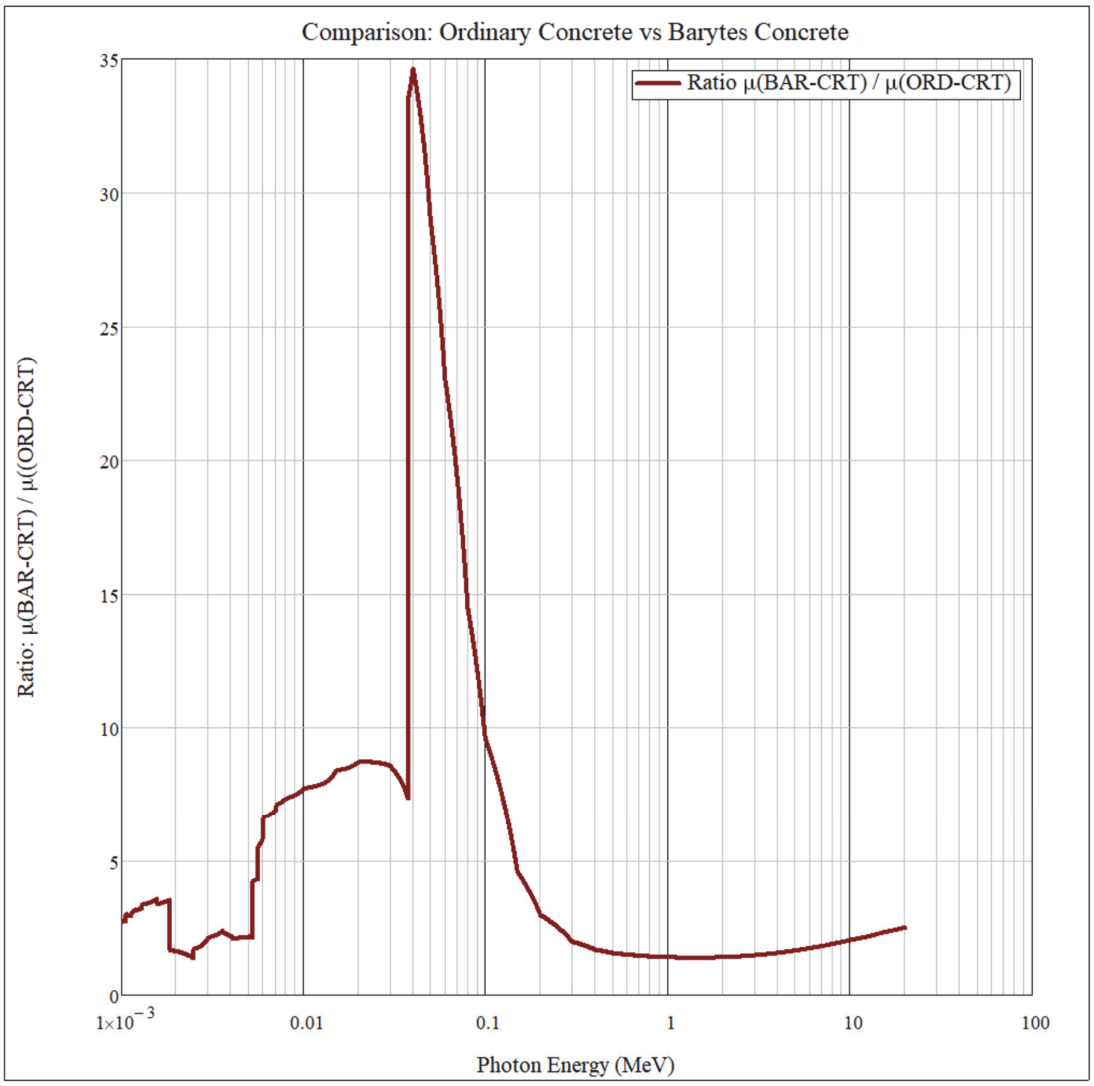


Figure 2-6: Ratio between the linear interaction coefficients for photon interactions in barite concrete and ordinary concrete

Figure 2-6 indicates that barite concrete will be significantly superior to ordinary concrete over the photon energy range $0.006\ \text{MeV} < E_\gamma < 0.14\ \text{MeV}$, and even more superior over the energy sub-interval $0.038\ \text{MeV} < E_\gamma < 0.10\ \text{MeV}$. The latter is the energy range where photo-electric absorption (PEA) is the dominant photon interaction mechanism. Over the energy range where Compton scattering dominates photon interaction, the benefit of barite concrete over ordinary concrete is quite low and close to the ratio of their mass-densities, namely $\frac{\rho_{BC}}{\rho_{OC}} = \frac{3.4}{2.3} \approx 1.45$. In other words, the ratio $\frac{\mu_{BC}(E)}{\mu_{OC}(E)}$ can be as high as 34 in the energy range where PEA dominates interaction, whereas the ratio $\frac{\mu_{BC}(E)}{\mu_{OC}(E)}$ will only range between 1.4 and 1.7 over the higher energy range $0.5\ \text{MeV} < \text{E}_\gamma < 5\ \text{MeV}$. Note

from Figure 5-3 on page 165 that the radioactive waste that has to be shielded in the present study, barely emits any notable ionising photons at energies above 1 MeV. Figure 5-3 also indicates that the fraction of ionising photons emitted at higher energies will decrease as the radioactive waste "ages", i.e. the photon emission spectrum will shift more and more into the energy range where the ratio $\frac{\mu_{BC}(E)}{\mu_{OC}(E)}$ will be above 5, so that the difference in the abilities of barite and ordinary concrete to attenuate the dose rate, will increase as the radioactive waste ages.

In summary: Based on published atomic interaction data for photons, for barite and ordinary concrete, it is clear that $SF(\text{BAR-CRT}) > SF(\text{ORD-CRT})$ and that this will become more pronounced at longer decay times.

2.3.7 Formulation of the first fundamental principle of photon shielding

Of the 3 dominant photon interaction mechanisms, it is specifically PEA that will absorb photons, i.e. lower the fluence rate ϕ_γ. Figure 2-4 on page 62 shows that the cross-section $\sigma_{PEA}(E)$ for PEA is a monotonically decreasing function of increasing photon energy, i.e. $\sigma_{PEA}(E)$ is a monotonically increasing function of decreasing photon energy. The lower the photon energy, E_γ, therefore, the higher will be the reaction rate of a photon interaction mechanism that will decrease the fluence rate $\varphi_\gamma(E)$ of ionising photons.

The relationship between the fluence rate $\varphi(E)$ and the effective dose rate $\dot{D}$ is given in Eq. (2-7) on page 69 and is $\dot{D} = \langle \mathfrak{R}_\gamma, \varphi \rangle$, where $\mathfrak{R}_\gamma$ denotes the fluence-rate to dose-rate response function (see Figure 2-7) and the inner product brackets denote integration over the continuous variables of phase space (Van Rooyen, 2020c).

Based on the above analysis, the first fundamental principle of photon shielding can now be formulated. Because PEA interactions will absorb photons and thereby lower φ and because the cross-section $\sigma_{PEA}(E)$ for PEA increases at lower energies, it is important to select a shielding material that will maximise PEA interactions. In the fundamental expression

$$\dot{D} = \langle \mathfrak{R}_\gamma, \varphi \rangle$$

this will lower $\dot{D}$ by lowering φ. As summarised in Table 2-2, it is known that the linear interaction coefficient μ_{PEA} has the approximate dependence on ρ and Z: $\mu_{PEA} \propto \rho^1 Z^3$, i.e. μ_{PEA} is maximised by maximising the mass-density ρ and, more importantly, the atomic number Z of shielding materials. The practical implementation of the quest to lower the photon dose rate $\dot{D}_\gamma$ by lowering the photon

fluence-rate φ_γ, is therefore to maximise ρ and, more importantly, Z. This first fundamental principle of photon shielding can be expressed symbolically as in Eq. (2-6) (Van Rooyen, 2020c). In Eq. (2-6), the greater importance of maximising Z is conveyed by selective boldfacing.

$$\left\{\begin{matrix}\boxed{\rho \uparrow} \\ \boxed{\boldsymbol{Z} \uparrow}\end{matrix}\right\} \Rightarrow \boxed{\text{PEA} \uparrow} \Rightarrow \boxed{\varphi_\gamma \downarrow} \Rightarrow \boxed{\dot{D}_\gamma \downarrow} \tag{2-6}$$

The practical implementation of Eq. (2-6) is to use materials rich in e.g. Ba ($Z = 56$), Pb ($Z = 82$) and depleted uranium (DU) ($Z = 92$) in photon shielding applications. These materials are excellent at absorbing ionising photons, thereby lowering the fluence rate and, as a result, also the dose rate.

2.3.8 Biological hazardousness of ionising photons as a function of photon energy

The biological hazardousness of ionising photons depends on their energy. This is quantified in the fluence-rate to dose-rate response function, $\mathfrak{R}_\gamma(E)$, which is shown in Figure 2-7, which is based on the latest work (ICRU, 2020) of the International Commission on Radiological Protection (ICRP) and the International Commission on Radiation Units & Measurements (ICRU). In Figure 2-7, the unit of the fluence-rate to dose-rate response function, $\mathfrak{R}_\gamma(E)$, is $\frac{Sv/h}{\text{cm}^{-2}\ \text{s}^{-1}}$ i.e. it relates a given fluence rate of ionising photons, $\varphi(E)$ to the effective dose rate (i.e. the "whole body" dose rate), $\dot{D}$. The relationship between the fluence rate $\varphi(E)$ and the effective dose rate $\dot{D}$ is given in Eq. (2-7),

$$\dot{D} = \langle \mathfrak{R}_\gamma, \varphi \rangle \tag{2-7}$$

where the inner product brackets denote integration over the continuous variables of phase space (Van Rooyen, 2020c).

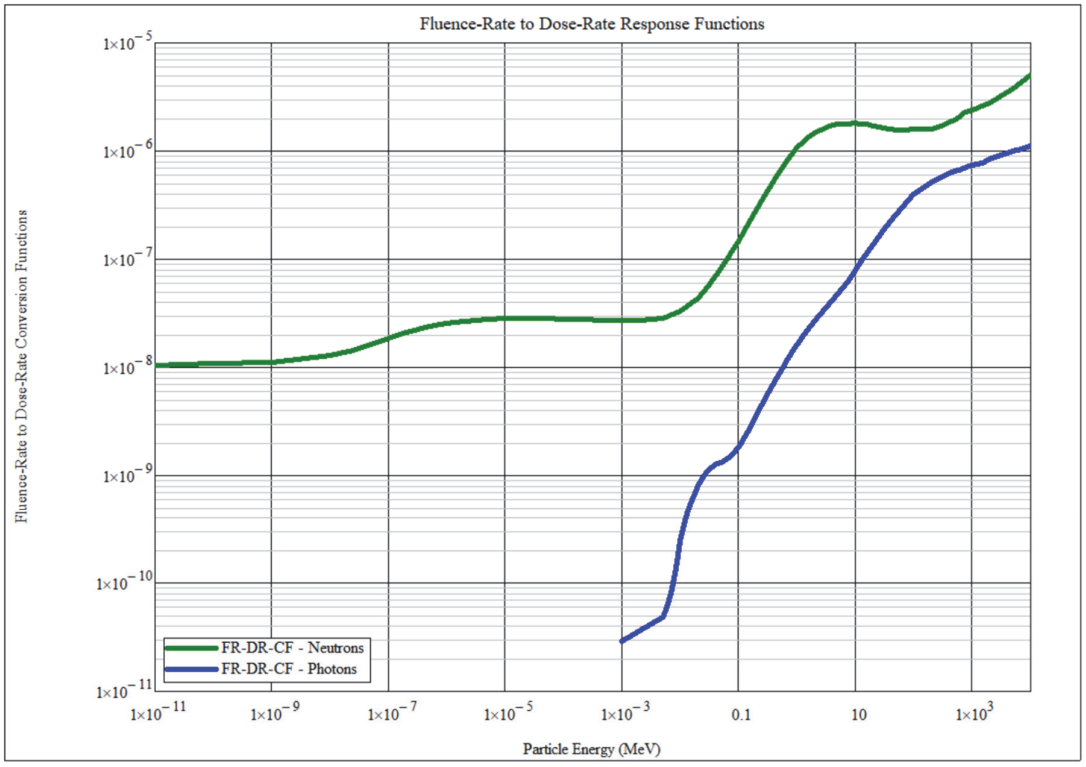


Figure 2-7: The fluence-rate to dose-rate response function R(E) for ionising photons (ICRU, 2020)

Figure 2-7 shows that, from 1 keV to 10^4 MeV, the biological hazardousness of a given fluence rate of ionising photons is a monotonically increasing function of the energy of the incident photon. Conversely, as photon energy decreases, the same photon fluence rate will become biologically less hazardous. Some numerical examples based on (ICRU, 2020) are (Van Rooyen, 2020c):

- $\frac{R_\gamma(E_\gamma=0.5\text{ MeV})}{R_\gamma(E_\gamma=5.0\text{ MeV})} = \frac{1}{5.4}$
- $\frac{R_\gamma(E_\gamma=0.1\text{ MeV})}{R_\gamma(E_\gamma=10\text{ MeV})} = \frac{1}{42.6}$.

Lowering photon energy from 5 MeV to 0.5 MeV will decrease their biological hazardousness by a factor of 5.4, and lowering E_γ from 10 MeV to 0.1 MeV will decrease their biological hazardousness by a factor of 42.6, for a constant fluence rate φ.

2.3.9 Formulation of the second fundamental principle of photon shielding and shield optimisation

Based on the foregoing analysis, the second fundamental principle of photon shielding can now be formulated. Because the dosimetric response function of ionising photons, $\mathfrak{R}_\gamma(E)$ is a monotonically decreasing function of decreasing photon energy, E_γ, shielding materials that have a high ability to lower photon energy must be used, because photons will be biologically less hazardous, i.e. contribute a lower effective dose $\dot{D}$, when their energies E_γ are lowered. Photons interact and undergo a reduction in energy E_γ via 3 principal interaction mechanisms — PP, CS and PEA. As summarised in Table 2-2, it is known that these 3 photon interactions and hence their contributions to the lowering of photon energies E_γ, are (in general) maximised by maximising the density ρ and the atomic number Z of shielding materials. The practical implementation of the quest to lower the photon dose rate by lowering photon energies, is therefore to select shielding materials that will maximise ρ and Z. This fundamental principle of photon shielding can be expressed symbolically as in Eq. (2-8) (Van Rooyen, 2020c).

$$\left\{\begin{matrix}\boxed{\rho\uparrow}\\ \boxed{Z\uparrow}\end{matrix}\right\} \Rightarrow \boxed{E_\gamma\downarrow} \Rightarrow \boxed{\mathfrak{R}_\gamma\downarrow} \Rightarrow \boxed{\dot{D}_\gamma\downarrow} \qquad (2\text{-}8)$$

2.3.10 Tenth-value thicknesses (TVTs) of shielding materials against important radioisotopes

The tenth-value thickness (TVT) is defined as the thickness of a shielding material for a given radionuclide source, that will decrease the transmitted dose-rate by a factor 10. Van Rooyen (2018) used the code MCNP6.2 to calculate tenth-value thicknesses of combinations of several important shielding materials and radionuclides; these TVT values are summarised in Table 2-3 (Van Rooyen, 2018a).

Table 2-3: Tenth-value thickness (TVT) for combinations of radionuclides and shielding materials

Material	Mass-density ρ ($\mathrm{g\ cm^{-3}}$)	Tenth-value thickness for radionuclide (cm)		
		^{60}Co	^{137}Cs	^{192}Ir
Tungsten-alloy	17.4	2.5	1.4	1.7

Material	Mass-density ρ ($\mathrm{g\ cm^{-3}}$)	Tenth-value thickness for radionuclide (cm)		
		^{60}Co	^{137}Cs	^{192}Ir
$\left\{\begin{matrix}\mathrm{W} & 94\ \% \\ \mathrm{Ni} & 3\ \% \\ \mathrm{Cu} & 3\ \%\end{matrix}\right\}$				
Lead-alloy $\left\{\begin{matrix}\mathrm{Pb} & 95\ \% \\ \mathrm{Sb} & 4\ \% \\ \mathrm{Sn} & 1\ \%\end{matrix}\right\}$	11.0	3.7	1.9	2.0
Iron (Fe)	7.85	6.0	4.2	4.0
Aluminium (Al)	2.70	17.1	12.3	11.3
Ordinary concrete	2.30	19.4	13.9	12.8

Note that the tenth-value thicknesses (TVT) of magnetite concrete, hematite concrete and barite concrete are not present in Table 2-3. During the course of the research reported here, these "missing values" will be calculated, and Table 2-3 will be extended — refer to Table 5-16 on page 210. This identified "gap" is turned into Research Objective RO_{13} which is formulated on page 155.

The dominant radionuclide in $ILLW[(n,f)^{99}\mathrm{Mo}]$, after a number of years of decay, has been calculated to be ^{137}Cs (refer to e.g. Table 5-2 on page 159 as well as Figure 5-2 on page 164), which means that we may use the ^{137}Cs column in Table 2-3 for comparing the performance of shielding materials against $ILLW[(n,f)^{99}\mathrm{Mo}]$. It is seen that a thickness of 13.9 cm of ordinary concrete is required to lower the transmitted dose-rate from a ^{137}Cs source by a factor 10 (the definition of the concept TVT). A mere 1.9 cm of Pb or an even thinner 1.4 cm of a tungsten-alloy are capable of achieving the same dose rate attenuation factor as 13.9 cm of ordinary concrete. However, tungsten is very expensive, while lead is impractically weak and also toxic. In fact, the waste acceptance criteria of most radioactive waste disposal institutes do not accept above-trace quantities of Pb in waste packages, because Pb is chemically toxic.

From a cost perspective, concrete is an ideal material for a radioactive waste drum — it is economical, strong, durable, neutralises acids and does not corrode. However, it is clear from Table 2-3 that the radiation shielding ability of ordinary concrete is frustratingly low — for a ^{137}Cs source, a $2 \times 14\ \mathrm{cm} = 28\ \mathrm{cm}$ thickness of ORD-CRT is required to cut the transmitted dose-rate by a factor $10^2 = 100$, and a thickness of $3 \times 14\ \mathrm{cm} = 42\ \mathrm{cm}$ ORD-CRT is required to cut the transmitted dose-rate by a factor $10^3 = 1000$, for ^{137}Cs as principal source nuclide. This finding demonstrates the need

for the present investigation, namely, to quantify the improved shielding performance that can be achieved by using 3 types of high-density shielding concrete.

2.4 Review: Natural abundance of the chemical elements in the crust of the earth; Minerals suited for the manufacture of high-density shielding concrete

2.4.1 The natural abundance of the chemical elements in the crust of the earth

Can better shielding concretes than barite concrete be formulated affordably?

Figure 2-8 shows a Periodic Table of the elements, and Figure 2-9 presents quantitative information about the abundance of chemical elements in the earth's crust[5]. Note that the vertical axis has a logarithmic scale, with 3 decimal orders of difference between the major tick labels.

If one is looking for (1) available, (2) affordable and (3) non-toxic elements (4) having $Z > 26$, there is a scarcity of suitable candidates. The only viable candidates are Sr ($Z = 38$), Zr ($Z = 40$) and Ba ($Z = 56$). Ba is particularly attractive, because its Z-number is by far the highest, and because rich $BaSO_4$ (barite) deposits are readily available. The conclusion is that no affordable concrete will be better than barite concrete, in photon shielding applications. A contributing factor to the apex-position of barite concrete is that Pb is banned at radioactive waste repositories, based on its chemical toxicity. The practice of adding lead oxide, or even metallic lead shot, to heavy shielding concretes, is therefore strictly forbidden in radioactive waste disposal practices.

[5] https://en.wikipedia.org/wiki/Abundance_of_the_chemical_elements

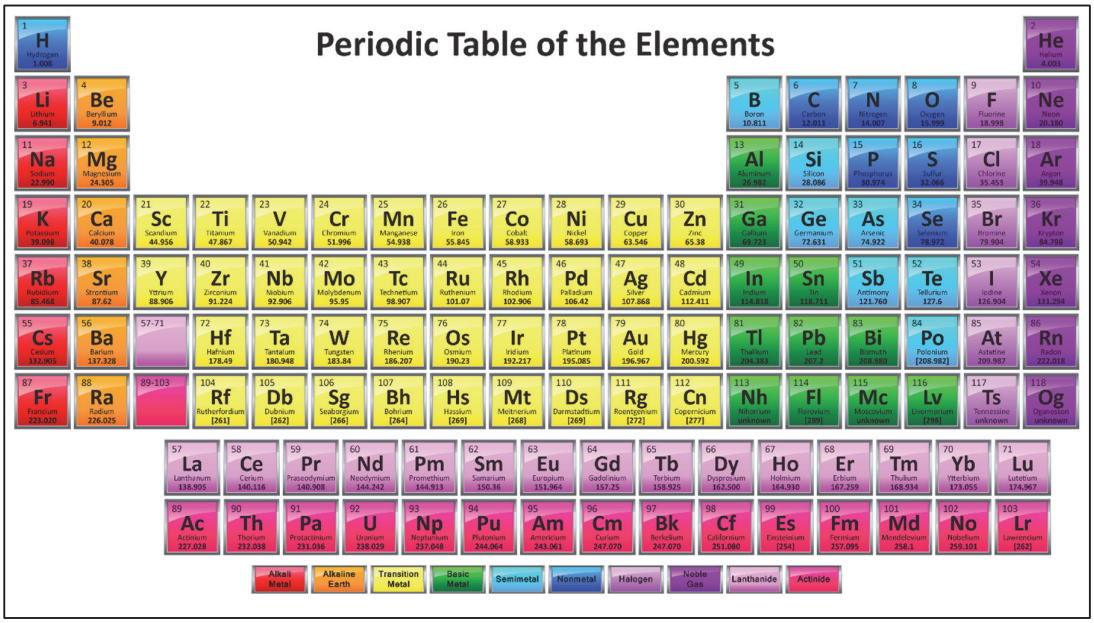


Figure 2-8: Periodic Table of the elements

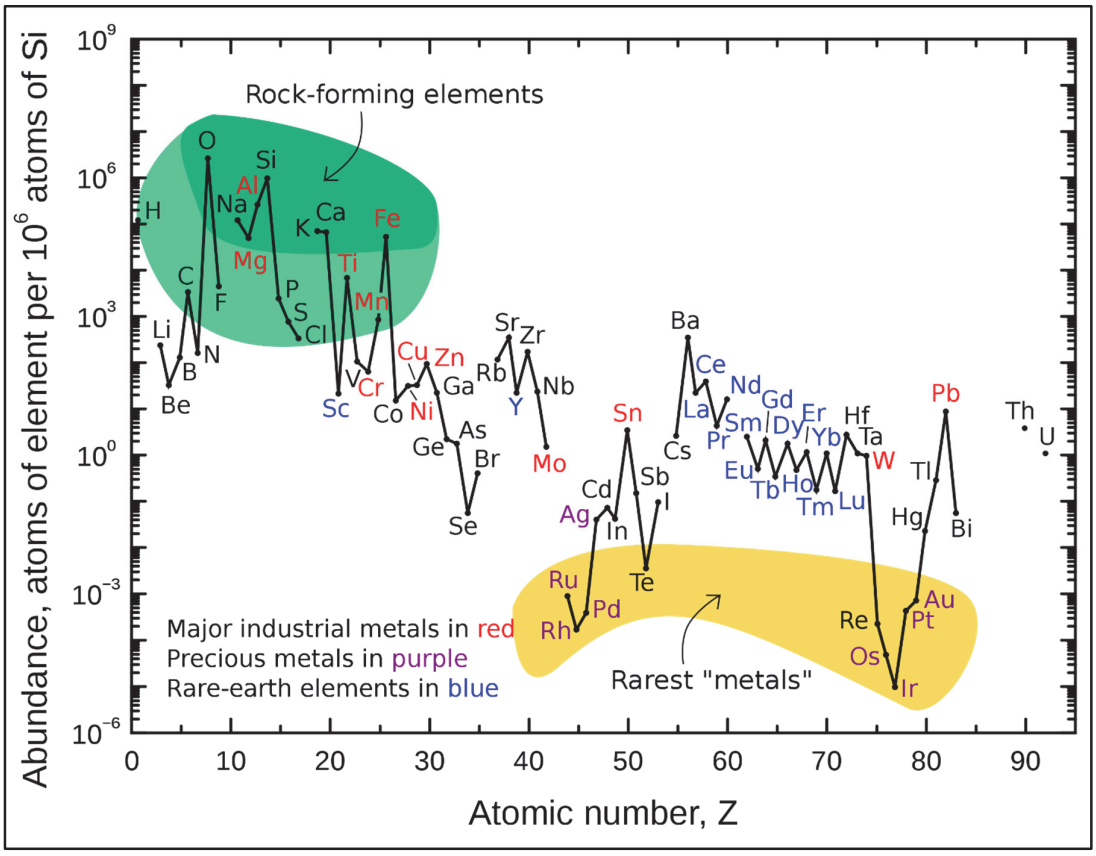


Figure 2-9: Abundance of the elements in the earth's crust

If we scour the Periodic Table for an element with an atomic number Z above 30 that is abundant, affordable and relatively non-toxic, we encounter a "great gap" between Fe ($Z = 26$) and the next suitable element, namely barium (Ba). The Z-number of Ba is 56, which will be very advantageous in shielding concretes for intense radionuclide sources dominated by the emission of ionising photons.

2.4.2 Minerals suited for the manufacture of high-density shielding concretes

Barium is found in barite deposits, which typically contains above 90 % $BaSO_4$ (barium sulphate). Barium sulphate is extremely insoluble and therefore non-toxic[6]. In Figure 2-9, the element barium ($Z(\mathrm{Ba}) = 56$) stands out as the most abundant element having $Z > 40$. Barite is also the most affordable mineral containing a high percentage of an element with $Z > 40$. It follows that there are not only physics reasons, but also economic reasons why barite concrete will be the "apex concrete" i.t.o. its ability to shield ionising photons, combined with availability, affordability and low toxicity. There is a worldwide supply chain for the mineral barite because it is used in oil well drilling for the extraction of underwater petroleum reserves.

In barite concrete, coarsely milled barite ($BaSO_4$) aggregate replaces the regular gravel coarse aggregate used in ORD-CRT, while more finely milled barite ($BaSO_4$) replaces the sand (fine aggregate) that would be used in ORD-CRT. Barite concrete typically contains 40 % to 48 % Ba by mass. Although the bulk mass-density of barite concrete is not higher than that of hematite concrete, the ability of Ba ($Z = 56$) to absorb and degrade photon energy via pair production (PP) and, especially, photo-electric absorption (PEA), is significantly better than that of Fe ($Z = 26$). This means that barite concrete will outperform HEM-CRT in the approximate photon energy range $E_\gamma < 0.5$ MeV and for $E_\gamma > 2$ MeV but will fail to outperform HEM-CRT in the approximate photon energy range $0.5\ \mathrm{MeV} < E_\gamma < 2\ \mathrm{MeV}$ where Compton scattering dominates — see the dependencies of the linear interaction coefficient μ in Table 2-2 on page 64 as well as the energy domains in Figure 2-2 on page 60 where it is shown where PEA, CS or PP dominates photon shielding in the E-Z plane.

More information on barite ore and barite concrete, is presented in § 2.4.8.

Iron ores that are rich in the element Fe, are hematite and magnetite ore. More information on magnetite and hematite ores and concretes, is presented in § 2.4.6 and § 2.4.7.

---

[6] Note by study supervisor, TJvR: Medical patients who must undergo X-ray scans of the intestines often consume as much as 100 grams of barium sulphate suspended in liquid as a so-called "barium meal" or "barium swallow" aimed at adding contrast to X-ray scans.

2.4.3 Economic process for the selection of radiation shielding materials

The logical flow for the selection of economically sensible shielding materials for nuclear reactors, particle accelerators, processing hot-cells, storage hot-cells, spent fuel transfer casks and radioactive waste disposal, proceeds as follows:

- If the radiation source is stationary, large and very intense, and there are no restrictions on the size and mass of the radiation shield, one usually defaults to the use of ordinary concrete. For example: the concrete bioshield around the reactor pressure vessel (RPV) in a containment building at a PWR power reactor, is a reinforced ordinary concrete structure designed to be thick enough to perform its shielding function, because there is no need to save space or create a mobile, transportable shield. The same holds for vaults at a particle accelerator facility.
- For low-level radioactive waste (LLW) that requires some shielding plus a more durable disposal package compared to thin-walled mild steel drums, ordinary concrete is the material of choice (Van Rooyen, 2019b).
- For concrete radioactive waste drums containing ILW, it is important to minimise the transmitted dose-rate, subject to constraints on package dimensions and mass. In such cases, the appropriate choice of material is high-density shielding concretes such as magnetite concrete, hematite concrete or barite concrete. Van Rooyen (2011) describes a radiation shielding assessment for large storage hot-cells constructed of hematite concrete.
- If space and mass are more tightly restricted, the use of a combination of steel and lead shielding may become appropriate. Example: Transport casks for the transfer of spent research reactor fuel assemblies are typically an inner stainless-steel 316L pipe and a large outer carbon-steel pipe with lead metal (Pb) cast into the space between the small and the large pipes (Adetula, 2017; Van Rooyen, 2019c). If the package must be disposed at a radioactive waste disposal site, Pb cannot be used (reason: chemical toxicity) so that steel or a special batch of very high-density concrete sandwiched between structural steel shells or plates, can be used.
- If a shielded radionuclide source or a shielded micro-reactor must be launched into space, then the mass and size of radiation shielding are subject to tight constraints, so that more expensive, strong and highly effective shielding materials have to be used. A micro-reactor for a space-station can e.g. employ borated high-density polyethylene (HDPE) along with stainless-steel and tungsten-alloy, for n/γ shielding, with the boron enriched to e.g. 80 % in the neutron-absorbing isotope, ^{10}B. For terrestrial applications, using such highly optimised but expensive

materials would be wasteful; wherever possible, concretes based on affordable mineral aggregates are preferred.

2.4.4 The need for high-density shielding concretes

Ordinary concrete serves well as a radiation shielding material in thick structures when unlimited space is available, so that shielding may be designed to be thick and heavy. Bioshields constructed from ordinary concrete are simply made as thick as is necessary to shield the radiation. However, when concrete structures have to be transported and disposed of in e.g. trench repositories, the use of ordinary concrete will lead to the need for excessively large and heavy radioactive waste drums. Instead of being able to transport e.g. 6 drums per truck to the disposal site, a large truck would only be able to load, say, 3 ordinary concrete drums; this would lead to excessive disposal costs. The use of special shielding concretes that are rich in heavy elements such as iron ($Z = 26$) and barium ($Z = 56$) would enable the producer to use significantly more compact drums, which will translate to lower overall radioactive waste disposal costs.

For the shielding of ionising photons, which dominates the emission from the liquid radioactive waste, the use of materials with higher atomic numbers Z and higher mass-densities ρ, is necessary to improve the shielding attenuation factor that can be achieved with a given thickness of concrete. The necessity to use high-Z shielding materials will be denoted symbolically as $\boxed{Z \uparrow}$, while the necessity to use shielding materials with a high mass-density ρ will be denoted symbolically as $\boxed{\rho \uparrow}$. Three readily available ores can be used to formulate and manufacture concretes that achieve the desired $\boxed{Z \uparrow}$ and $\boxed{\rho \uparrow}$: Magnetite ore, hematite ore and barite ore. The first 2 ores (magnetite and hematite) are iron ores, while barite is a barium ore.

2.4.5 Iron ore production in South Africa

The highest quality and most important iron ores for steelmaking are hematite (Fe_2O_3) and magnetite (Fe_3O_4). Hematite is the more sought-after iron ore and the preferred raw material in efficient steelmaking factories. It accounts for ~95 % of South Africa's iron ore production. Local iron ore reserves are all high-quality hematite ore, allowing the production of high-quality lump (nominally 64 % Fe) and high-grade sinter-fines (nominally 63.5 % Fe). Iron ore for the export market is produced at mines near Sishen and Kolomela, while mines at Thabazimbi supply the domestic market (Netshiozwi, 2002).

2.4.6 Magnetite ore; magnetite concrete

Magnetite is a magnetic iron ore. Its molecular formula, Fe_3O_4, can also be written as $FeO \cdot Fe_2O_3$, which consists of wüstite (FeO) and hematite (Fe_2O_3). Magnetite exhibits the strongest ferro-magnetism of all the natural minerals found on earth.

In the manufacture of magnetite concrete (MAG-CRT), crushed magnetite lump is used as coarse aggregate, while magnetite sinter-fines serve as fine aggregate (Abubakar *et al.*, 2014; Bashter *et al.*, 1997; Gunoglu & Akkurt, 2021).

Magnetite iron ore is found in South Africa, but both its availability and Fe content are lower than that of hematite ore.

Figure 2-10 shows magnetite ore — note that it is visually quite distinct from hematite ore (see Figure 2-11).



Figure 2-10: Magnetite ore

2.4.7 Hematite ore; hematite concrete

In the manufacture of hematite concrete (HEM-CRT), crushed coarse hematite lump serves as coarse aggregate, while high-grade sinter-fines serve as fine aggregate (Gencel *et al.*, 2010). Hematite concrete is often reddish to purple in hue, and therefore resembles the colour of blood (Greek: hema) —

hence the name hema-tite. Hematite iron ore is mined and beneficiated in South Africa; hematite lump, as well as hematite sinter-fines, are readily available.

Figure 2-11 shows a chunk of hematite ore.



Figure 2-11: Hematite ore — note the reddish hue

2.4.8 Barite ore; barite concrete

The weak point of the element Fe as a shielding material against ionising photons, is its "average" Z-number of only 26. In certain parts of the world, rich barite ore deposits are found; barite is an ore that contains more than 90 % of the chemical compound $BaSO_4$ (barium sulphate). The Z-number of barium is $Z = 56$, so that barite ore, i.e. $BaSO_4$, is a desirable aggregate for use in shielding concrete against ionising photons. Another positive is that $BaSO_4$ is extremely insoluble and therefore non-toxic[7], especially in the alkaline environment of cement. A negative factor is that the SO_4 anion in $BaSO_4$ is mediocre from a photon shielding perspective, because the Z-numbers of sulphur ($Z(S) = 14$) and oxygen ($Z(O) = 8$) are low.

To produce barite concrete, ordinary gravel (coarse aggregate) and sand (fine aggregate) are replaced by coarse and fine barite ore aggregates, which typically contain more than 90 % $BaSO_4$.

[7] Note by study supervisor TJvR: The extreme insolubility of barium sulphate is almost proverbial in the world of chemistry.

Barite ore is not mined in South Africa and will have to be imported from e.g. China at a cost of approximately USD 180 per tonne (2021), excluding shipment and taxation. As a result, the cost of barite concrete is expected to exceed that of hematite and magnetite concrete.

Figure 2-12 shows crushed high-grade barite ore.



Figure 2-12: Crushed high-grade barite ore at a barite mine

The mass-density of high-grade barite ore is 4.2g cm^{-3}.

2.5 Radiation shielding concretes: Benefits and composition

2.5.1 Attractiveness of concrete as radiation shielding material

Concrete is the most common shielding material against ionising radiation, in applications where the budget is tight and where large, heavy, bulky structures are acceptable. Concrete is extensively used as radiation shielding material in nuclear reactor facilities, spent nuclear fuel repositories, particle accelerator vaults, as well as mausoleums for the storage of large radioactive components removed from a nuclear power plant (Van Rooyen, 2019d). Concrete's photon attenuation properties can be tailored by controlling its elemental composition, i.e. by selecting appropriate aggregates. Moreover, concrete has a relatively low fabrication cost and can be cast in many complex forms, exhibiting good mechanical, structural and physicochemical properties. All these characteristics make concrete a suitable and widely used material for an extensive range of radiation shielding applications.

The elemental compositions of the 4 concrete types that are modelled as shielding materials radioactive waste drums for ILLW[$(n, f)^{99}$Mo], are now presented.

2.5.2 Elemental composition: Ordinary concrete (ORD-CRT)

Ordinary concrete will be used as a reference shielding material — the improved performance of specialised high-density shielding concretes will often be expressed as improvements upon the base-line shielding performance of ordinary concrete.

The US NRC requires that all shielding and dose rate calculations for ordinary concrete, related to licensing applications to the NRC, be performed for the prescribed elemental composition of NRC regulatory concrete given in material specification in Composition 2-1 (Rearden & Jessee, 2020). This is the design-basis composition of ordinary concrete in this study.

Composition 2-1: Elemental composition of regulatory concrete

```
c US NRC REGULATORY CONCRETE, Specification for low-energy P E Runs:
M3     1000    -1.0
       8000    -53.2
       11000   -2.9
       13000   -3.4
       14000   -33.7
       20000   -4.4
       26000   -1.4
```

Composition 2-1 is expressed in MCNP ZAID format: The ZA-ID (ID = identity) of a material is

$$ZAID = 1000 \times Z + A,$$

where Z is the atomic number and A the mass number. For photon-electron transport below the energy of circa 10 MeV, however, the A-number is irrelevant and then the ZAID is simply

$$ZAID = 1000 \times Z$$

i.e. only the elemental composition matters, and not the exact isotopic composition. In the above energy regime ($E < 10$ MeV), where photon interactions are usually atomic and not nuclear, the ZAID of oxygen ($Z(\mathrm{O}) = 8$) in the above specification is e.g. 8000, the ZAID for Si ($Z(\mathrm{Si}) = 14$) is 14000, the ZAID for Ca ($Z(\mathrm{Ca}) = 20$) is 20000 while the ZAID for Fe ($Z(\mathrm{Fe}) = 26$) is 26000.

From the material specification of ordinary concrete above, we see that the most abundant elements in the NRC's regulatory ordinary concrete are oxygen (53.2 % of the mass), silicon (33.7 % of the mass), calcium (4.4 % of the mass) and Al (3.4 % of the mass). Both O ($Z(\mathrm{O}) = 8$) and Si ($Z(\mathrm{Si}) = 14$)

have rather low Z-numbers, and the bulk mass-density of ordinary concrete is also low relative to e.g. steel, at circa $\rho \approx 2.3$ g cm^{-3}. Although ORD-CRT is relatively affordable and strong, it is a mediocre photon shielding material, especially when reasonably compact, transportable structures such as radioactive waste drums have to be designed. The Fe content of the NRC's regulatory ORD-CRT is very low at only 1.4 % of the bulk mass.

2.5.3 Elemental composition: Magnetite concrete

Unlike ORD-CRT, the elemental composition of MAG-CRT has not been standardised by regulators such a the NRC, probably because magnetite iron ores have different compositions. Therefore a conservative composition for MAG-CRT that contains only ~36.5 % Fe by mass, was selected. The chosen elemental composition of magnetite concrete is stipulated in Composition 2-2 and is the design-basis composition of magnetite concrete in this study. The material composition is conservative in the sense that it is judged that at least 80 % of specialised, professionally compounded magnetite concretes are expected to contain a higher mass-% of Fe and have a higher mass-density than the magnetite concrete specified in Composition 2-2. The reference work, *Compendium of Material Composition Data for Radiation Transport Modeling,* compiled and published by Pacific North-West National Laboratory (PNNL) in the USA (PNNL, 2011), specifies that most magnetite concretes will contain above 40 % Fe by mass and will have a mass-density above 3.3 g cm^{-3} . The concrete used in this study is, deliberately selected to be slightly below par i.t.o. Fe content and mass-density, and therefore shielding ability, so that computed dose rates will be conservative, i.e. dose rates will be overestimated and not underestimated.

Composition 2-2: Elemental composition of magnetite concrete, as used for computations in this study

```
c Lower-Density Magnetite Concrete, 36 % Fe; mass-density = 3.2 g/cc
M14     1000      -0.411
        8000      -44.55
        12000     -1.142
        13000     -3.849
        14000     -6.675
        16000     -0.142
        20000     -5.126
        22000     -0.933
        23000     -0.312
        24000     -0.120
        25000     -0.209
```

```
      26000     -36.53
```

From the material specification of magnetite concrete (Composition 2-2), we observe that the most abundant elements in magnetite concrete are oxygen (44.6 % of the mass), Fe (36.5 % of the mass), calcium (5.1 % of the mass), Si (6.7 % of the mass) and Al (3.9 % of the mass). The element Fe has a mid-range Z-number of $Z(\mathrm{Fe}) = 26$, while O ($Z(\mathrm{O}) = 8$), Si ($Z(\mathrm{Si}) = 14$) and Ca ($Z(\mathrm{Ca}) = 20$) have low Z-numbers. The bulk mass-density of magnetite concrete is significantly higher than that of ORD-CRT, at $\rho \approx 3.2\ \mathrm{g\ cm^{-3}}$. In view of these facts, MAG-CRT is expected to be a better shielding material against ionising photons, compared to ORD-CRT.

2.5.4 Elemental composition: Hematite concrete (HEM-CRT)

Unlike ORD-CRT, the elemental composition of HEM-CRT has not been standardised by regulators such as the NRC, probably because hematite iron ores have variable compositions[8]. Therefore a conservative composition for HEM-CRT that contains ~47.4 % Fe by mass, was selected. The chosen elemental composition of hematite concrete is stipulated in Composition 2-3 and serves as the design-basis composition of hematite concrete in this study. The material composition is conservative in the sense that it is judged that at least 80 % of specialised, professionally compounded hematite concretes are expected to contain a somewhat higher mass-% of Fe and have a higher mass-density than the hematite concrete composition specified in Composition 2-2. The reference work, *Compendium of Material Composition Data for Radiation Transport Modeling,* compiled and published by Pacific North-West National Laboratory (PNNL) in the USA (PNNL, 2011), only contains a reference composition for magnetite concrete and not for hematite concrete, because hematite ore reserves in the USA were exhausted by the effect of 2 world wars and the subsequent Cold War. The hematite concrete composition used in this study is, deliberately selected to be marginally below par i.t.o. shielding abilities, so that all results will be conservative, i.e. dose rates will be overestimated and not under-estimated.

Composition 2-3: Elemental composition of hematite concrete, as used for computations in this study

```
c High-Density Hematite Concrete Composition, 47 % Fe; mass-density = 3.5
g/cc
```

[8] In some countries, hematite iron ores were almost completely depleted during World War 2 and the first decades of the subsequent cold war, for the manufacture of armaments. The only remaining iron ores in these parts of the world, are magnetite ores.

```
M10     1000      -0.311
        8000      -36.05
        12000     -0.934
        13000     -2.449
        14000     -3.396
        16000     -0.142
        20000     -7.132
        22000     -1.443
        23000     -0.311
        24000     -0.170
        25000     -0.229
        26000     -47.44
```

From the material specification of hematite concrete (Composition 2-3), we observe that the most abundant elements in hematite concrete are Fe (47.4 % of the mass), oxygen (36.1 % of the mass), calcium (7.1 % of the mass), Si (3.4 % of the mass) and Al (2.5 % of the mass). The element Fe has an average Z-number of $Z(\mathrm{Fe}) = 26$, while O ($Z(\mathrm{O}) = 8$), Si ($Z(\mathrm{Si}) = 14$) and Ca ($Z(\mathrm{Ca}) = 20$) have low Z-numbers. The bulk mass-density of the design-basis hematite concrete is significantly higher than that of ORD-CRT, at $\rho \approx 3.5\ \mathrm{g\ cm^{-3}}$. In view of these facts, hematite concrete is expected to be a better shielding material against ionising photons, compared to ordinary concrete.

2.5.5 Elemental composition: Barite concrete

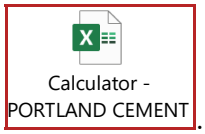
The weak point of the element Fe as a shielding material against ionising photons, is its "average" Z-number of 26. In certain parts of the world, there are very rich barite ore deposits; barite is an ore that contains more than 90 % of the chemical compound $\mathrm{BaSO_4}$. The Z-number (i.e. the atomic number or the number of protons in the nucleus, or the number of bound orbital electrons in a neutral atom) of barium (Ba) is $Z(\mathrm{Ba}) = 56$, so that barite i.e. $\mathrm{BaSO_4}$ ore is in principle, a desirable aggregate for shielding concrete against photon sources.

Unlike ORD-CRT, the elemental composition of BAR-CRT has not been standardised by regulators such as the NRC, because barite ores have variable compositions. Therefore a composition for BAR-CRT that contains 80 % $\mathrm{BaSO_4}$, 16 % cement and 4 % water by mass, and has a bulk mass-density of $3.4\ \mathrm{g\ cm^{-2}}$ was selected. A simple EXCEL-based "calculator" was used to calculate the compositions

of mixtures of ores and cement; this EXCEL spreadsheet[9] is embedded here:



This worksheet uses quantities calculated with the following cement composition calculator[10]:



The elemental composition of barite concrete is presented in Composition 2-4. This is the design-basis composition of barite concrete in this study.

Composition 2-4: Elemental composition of barite concrete, as used for computations in this study

```
c Barite Concrete (rho = 3.4 g/cc)
M03   1000      -00.448
      8000      -31.127
      11000     -00.119
      12000     -00.193
      13000     -00.423
      14000     -01.720
      16000     -10.993
      19000     -00.133
      20000     -07.662
      26000     -00.112
      56000     -47.071
```

From the material specification of barite concrete (Composition 2-4), it is observed that the most abundant elements in typical barite concrete are Ba (circa 47 % by mass), oxygen (circa 31 % by mass), sulphur (circa 11 % by mass) and calcium (circa 7.7 % by mass). The dominant element in barite concrete, Ba, has an above-average Z-number of $Z(\mathrm{Ba}) = 56$, while O ($Z(\mathrm{O}) = 8$), S ($Z(\mathrm{S}) = 16$) and Ca ($\mathrm{Z(Ca)} = 20$) have low or unremarkable Z-numbers. The bulk mass-density of typical barite concrete is significantly higher than that of ORD-CRT, at approximately $\rho \approx 3.4\ \mathrm{g\ cm^{-3}}$. In view of these facts, barite concrete is expected to be a significantly better shielding material against ionising

[9] EXCEL worksheet developed by study supervisor, TJvR.

[10] EXCEL worksheet developed by study supervisor, TJvR.

photons, compared to ordinary concrete. It is also expected that it will prove to be the best performing photon shielding material in the calculational experiments that will be performed in this work.

The reference work, *Compendium of Material Composition Data for Radiation Transport Modeling,* compiled and published by Pacific North-West National Laboratory (PNNL) in the USA (PNNL, 2011), presents essentially the same composition and mass-density for barite concrete as Composition 2-4. The barite concrete composition used in this study is therefore not conservative but is accurately representative of the performance of real-world barite concrete. In the formulation of magnetite and hematite concretes, the composition of the beneficiated magnetite and hematite coarse and fine aggregates will show a larger variation than will be observed for barite aggregate. Barite concrete is a highly specialised product and is almost always formulated and mixed by professional concrete suppliers.

2.6 Summary and conclusions

It has been shown that materials with good shielding properties against ionising photons must have high atomic numbers Z and high mass-densities ρ. Two relatively abundant chemical elements that are found in ores that are non-soluble, abundant and benign from a toxicity perspective, are Fe and Ba. The element Fe is found in magnetite and hematite iron ores, while the element Ba is found in barite ores. These ores can be used to formulate magnetite concrete, hematite concrete and barite concrete. In South Africa, high-grade hematite ore reserves are available so that hematite will be the iron ore of choice locally, for the manufacture of shielding concretes based on iron ore. In parts of the world where high-grade hematite ores have been depleted, processed magnetite ore can be used as aggregate in high-density shielding concrete.

3. Radioactive waste classification, conditioning, immobilisation, shielding, storage and disposal

3.1 Introduction

This chapter deals with the following topics:

1. The international classification system for radioactive waste.
2. Clearance levels and derived design-basis lifetime criteria for disposal packages for radioactive waste.
3. A literature review of technologies for radioactive waste management, in particular immobilisation. Cement and concrete technologies are briefly reviewed and the ageing of reinforced concrete structures such as concrete drums for ILLW[$(n, f)^{99}$Mo], are reviewed.
4. A literature review of the use of specialised high-density shielding concretes.
5. As a by-product of the literature review, the vocabulary of radioactive waste management will be learned and incorporated into this manuscript.
6. The road transport of packages of radioactive material.
7. Based on the literature review, gaps that have to be addressed, are identified and are eventually built into the research objectives for this project.

3.2 Radioactivity in a cosmological context

According to present cosmological models, the entire earth is composed of originally highly radioactive material produced in stellar nucleosynthesis and neutron star mergers. This radioactive material had "cooled" for at least 4.6 Ga (a Ga is a giga-annum, i.e. a billion years, i.e. 10^9 years). Since the discovery that (1) nuclear energy is several million times more concentrated than chemical energy, and that (2) nuclear reactions can be used to produce valuable therapeutic and diagnostic radio-nuclides, technologies have been developed that produce substantial amounts of radioactive by-products. We do not have the luxury of "waiting another 4.6 billion years", i.e. radioactive waste

management programmes must be developed to keep the environment safe, to minimise the negative impact of human-produced radionuclides on the present and future habitability of the earth's biosphere.

3.3 Literature review: The IAEA's classification of radioactive waste types

3.3.1 Radioactive waste categories

The International Atomic Energy Agency (IAEA) has developed a system for the classification of radioactive waste (IAEA, 2009a). The IAEA classification system is illustrated in Figure 3-1.

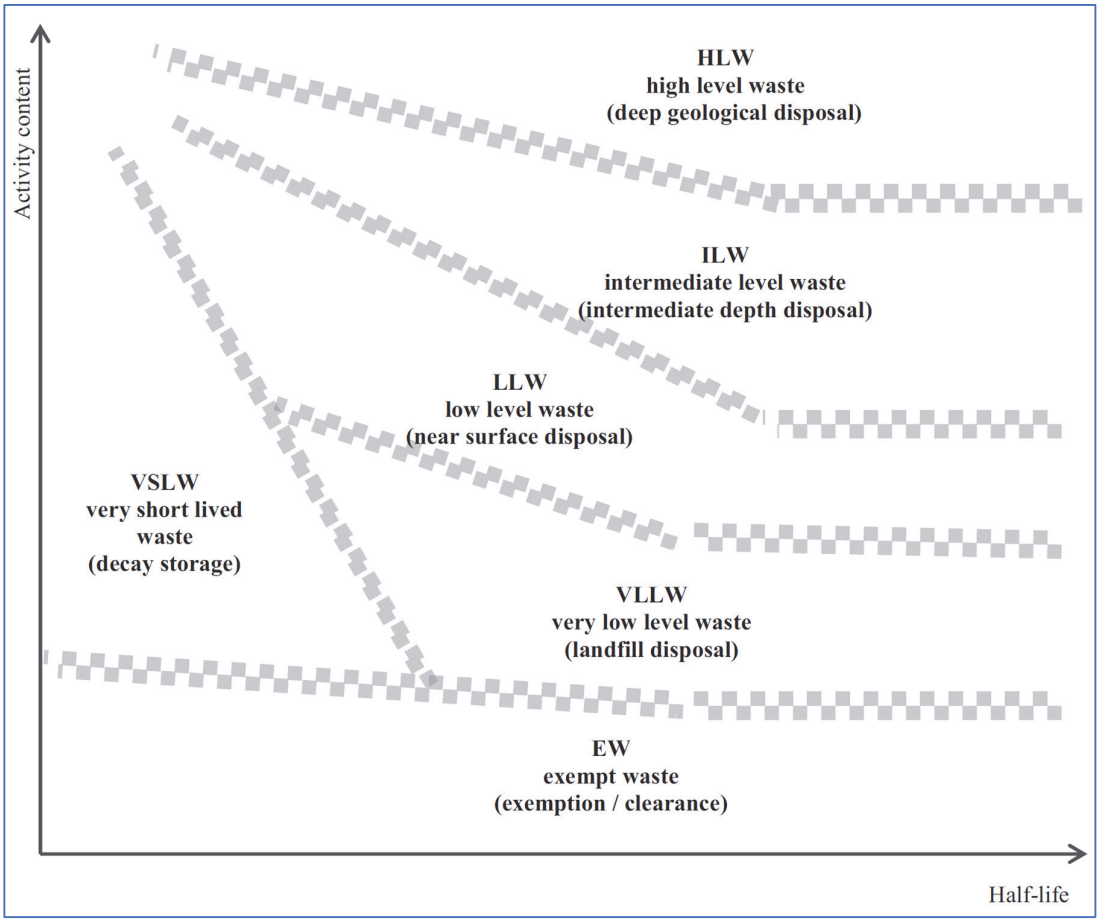


Figure 3-1: Conceptual illustration of the IAEA's classification scheme for radioactive waste (IAEA, 2009a: 7)

In Figure 3-1, the vertical axis represents the activity content of the waste while the horizontal axis represents the half-lives of the radionuclides contained in the waste. The higher the activity content

and the activity per unit mass, the greater the need to contain and immobilise the waste to isolate it from dispersal into the biosphere.

In practice, many governments and regulatory bodies use a practical adaptation of the classification system shown in Figure 3-1. This classification system is also encountered in various IAEA reports, e.g. (IAEA, 2006) and (IAEA, 2020). South Africa's National Radioactive Waste Classification System follows this scheme and defines 6 classes of radioactive waste:

1. High-Level Waste (HLW).
2. Low and Intermediate-Level Waste, Long-Lived (LILW-LL).
3. Low and Intermediate-Level Waste, Short-Lived (LILW-SL).
4. Very Low-Level Waste (VLLW).
5. NORM-L (Low activity NORM).
6. NORM-E (Enhanced activity NORM).

3.3.2 Low and Intermediate-Level Waste, Short-Lived (LILW-SL)

Low and Intermediate-Level Waste, Short-Lived (LILW-SL) is radioactive waste having an $\frac{\text{activity}}{\text{mass}}$ ratio above clearance levels, but with limited amounts of long-lived radionuclides (IAEA, 2009a). LILW-SL requires containment and isolation from the environment for up to a few hundred years; suitably robust waste packages of LILW-SL may be disposed in e.g. near-surface disposal (NSD) trenches. If radioactive waste contains high activities of short-lived radionuclides, and only very low activities of longer-lived radionuclides such as ^{99}Tc, it can still be classified as LILW-SL, despite the presence of low activities of long-haulier radionuclides.

In South Africa, the intermediate-level liquid (radioactive) waste (ILLW) generated from $(n, f)^{99}$Mo is classified as resorting under the category LILW-SL, i.e. Low and Intermediate-Level Waste, Short-Lived. In this work, the emphasis will therefore fall on this waste category.

Disposal sites for LILW-SL are typically located in arid areas where there are no notable underground aquafers at depths shallower than e.g. 200 m.

3.3.3 Low-Level Waste, Short-Lived (LLW-SL)

The category LILW-SL can be subdivided into LLW-SL and ILW-SL. The most affordable disposal package for dry, non-corrosive LLW-SL is in steel drums which are buried in relatively shallow trenches at a waste disposal site. In some cases, ordinary concrete (ORD-CRT) drums are preferred for the disposal of LLW-SL. The use of concrete drums containing an embedded, smaller stainless-steel drum, enables the radioactive waste producer to dispose of moist LLW-SL directly, without having to first dry out and condition the waste in preparation for disposal in steel drums.

3.3.4 Intermediate-Level Waste, Short-Lived (ILW-SL)

Intermediate-Level Waste of subtype Short-Lived, denoted as ILW-SL, is radioactive waste that has an $\frac{\text{activity}}{\text{mass}}$ ratio and activity content par waste package above that of LLW but contains only low activities of radionuclides having half-lives above e.g. 100 years. When produced, ILW-SL is often liquid or moist; it requires a greater degree of containment, immobilisation and isolation than that provided by near-surface disposal in thin-walled steel drums (IAEA, 2009a). ILW typically needs no provision for heat dissipation during its storage and disposal (IAEA, 2009a). This radioactive waste type requires predisposal conditioning and immobilisation such as cementation. Disposal is in concrete drums containing an embedded, smaller stainless-steel drum, with a typical wall thickness of approximately 3 mm. This inner stainless-steel drum serves as an additional, durable barrier to delay any egress of radionuclides into the environment. Concrete drums containing ILW-SL are typically buried in somewhat deeper trenches compared to the disposal of drums filled with LLW-SL. The radiation shielding ability of ORD-CRT is usually insufficient for ILW-SL so that the use of drums manufactured from high-density shielding concrete has to be considered. Placement of such waste in ORD-CRT drums will necessitate the use of either impractically huge drums, or will necessitate predisposal, on-site storage periods of more than a decade, both of which are highly undesired.

3.3.5 HLW: High-Level Waste

High-level waste (HLW) is radioactive waste with activity concentrations high enough to generate significant quantities of heat via radioactive transitions, and also contain high concentrations of long-lived radionuclides. These factors must be taken into consideration in the design of a disposal facility for HLW (IAEA, 2009a). HLW has to be disposed in deep, stable geological formations, more than a

few hundred metres below the earth's surface. HLW requires a significantly higher degree of containment, immobilisation and isolation compared to less problematic waste types (IAEA, 2009a).

In this work, the focus will be on solidified intermediate-level liquid radioactive waste, i.e. neither VLLW nor HLW will be discussed at any level of detail.

3.4 Literature review: Clearance levels for the clearance of radioactive material

The clearance levels for the clearance of radioactive material are the radionuclide activity concentration per unit mass or surface area, at which the material may e.g. be unconditionally released into the public domain with no further regulatory control.

3.4.1 Clearance levels: IAEA

The IAEA sets distinct clearance levels for different classes of radioisotopes, based on model-based radiation exposure calculations and radiological risk-assessment criteria (IAEA, 1996). Table 3-1 is a summary of information in (IAEA, 1996), showing the clearance levels of 5 categories of radionuclides. The clearance level of a radionuclide is the activity per unit mass or per unit surface area, at which the material may be released into e.g. the public domain.

Table 3-1: Unconditional clearance levels for radionuclides, according to (IAEA, 1996)

Clearance category	Clearance level — lower limit	Clearance level — upper limit	Radionuclides	Half-life
1	0.1 Bq/g	1.0 Bq/g	Na-22	2.6018 a
			Co-60	5.2712 a
			Na-24	14.957 h
			Mn-54	312.2 d
			Zn-65	243.93 d
			Nb-94	20,400 a
			Ag-110m	249.95 d
			Sb-124	60.2 d
			Cs-134	2.0652 a
			Cs-137	30.08 a
			Eu-152	13.517 a
			Pb-210	22.2 a

Clearance category	Clearance level — lower limit	Clearance level — upper limit	Radionuclides	Half-life
2	1 Bq/g	10 Bq/g	Co-58	70.86 d
			Fe-59	44.495 d
			Sr-90	28.79 a
			Ru-106	371.8 d
			In-111	2.8063 d
			I-131	8.0252 d
			Ir-192	73.83 d
			Au- 198	2.6941 d
3	10 Bq/g	100 Bq/g	Cr-51	27.701 d
			Co-57	271.7 d
			Tc-99m	6.02 h
			I-123	13.2235 h
			I-125	59.407 d
			I-129	1.57000E7 a
			Ce-144	284.91 d
			Tl-201	3.0442 d
4	100 Bq/g	1000 Bq/g	C-14	5700 a
			P-32	14.268 d
			Cl-36	3.0129994E5 a
			Fe-55	2.744 a
			Sr-89	50.563 d
			Y-90	2.6666667 d
			Tc-99	2.111E5 a
			Cd-109	1.2638189 a
5	1000 Bq/g	10,000 Bq/g	H-3	12.32 a
			S-35	87.37 d
			Ca-45	162.61 d
			Ni-63	101.2 a
			Pm-147	2.6234 a

In Table 3-1 the 5 distinct clearance categories of (IAEA, 1996) have been colour-coded to guide the eye.

From Table 3-1 it is seen that the radionuclides ^{22}Na, ^{54}Mn, ^{60}Co, ^{65}Zn, ^{94}Nb, ^{110m}Ag, ^{134}Cs, ^{137}Cs, ^{152}Eu, ^{154}Eu and ^{210}Pb are most problematic, because their clearance levels are highly restrictive; the presence of these radionuclides above activities per unit mass as low as circa 1 Bq/g, can prevent the unconditional clearance of such materials. If, e.g., the activity per unit mass of ^{60}Co or ^{152}Eu in concrete from a reactor building that is deconstructed during decommissioning, exceeds 0.1 Bq/g by more than a factor of, e.g. 2, all the concrete that exceeds the clearance level will have to be crushed and drummed in e.g. standard 200-litre waste drums, and sent to a national waste disposal facility, at considerable cost. From Table 3-1 it is also seen that less dangerous radionuclides such as ^{3}H, ^{45}Ca and ^{63}Ni, enjoy much more lenient clearance levels than the "most problematic radioisotopes" category.

3.4.2 Clearance levels: Nuclear Industry Safety Directors Forum (NISDF, 2017)

In a publication, *The UK Nuclear Industry Guide To: Clearance and Radiological Sentencing: Principles, Process and Practices* (NISDF, 2017), clearance levels for an exhaustive list of radionuclides are listed; these values are reproduced in Table 3-2. The colour-coding ranges for Table 3-2 is deliberately close to the scheme used in Table 3-1.

Table 3-2: Clearance levels for selected radionuclides, for the re-use of metallic items

Radionuclide	*Z*	*A*	Clearance levels (Bq g^{-1})
Pb-210	82	210	0.66
Co-60	27	60	1.00
Na-22	11	22	1.10
Ag-108m	47	108	1.30
Ag-110m	47	110	1.30
Nb-94	41	94	1.40
Bi-207	83	207	1.40
Cs-134	55	134	1.60
Eu-154	63	154	1.80
Eu-152	63	152	2.00
Co-56	27	56	2.10
Sc-46	21	46	3.40
Zr-95	40	95	3.60
Mn-54	25	54	3.70
Cs-137	55	137	3.70
I-129	53	129	4.00

Ta-182	73	182	4.20
Sb-124	51	124	5.10
Sb-125	51	125	5.20
Zn-65	30	65	6.30
Tb-160	65	160	7.30
Co-58	27	58	8.00
Os-185	76	185	8.70
Ir-192	77	192	9.20
Se-75	34	75	14.00
Ru-106	44	106	14.00
Cl-36	17	36	15.00
Sr-90	38	90	15.00
Sr-85	38	85	16.00
Sn-113	50	113	18.00
Co-57	27	57	30.00
Ce-139	58	139	30.00
Gd-153	64	153	31.00
Te-123m	52	123	37.00
Eu-155	63	155	41.00
Ce-144	58	144	68.00
Cd-109	48	109	91.00
I-125	53	125	130.00
W-181	74	181	140.00
Tc-97	43	97	150.00
Mo-93	42	93	170.00
Cs-135	55	135	220.00
Zr-93	40	93	290.00
Te-127m	52	127	300.00
Tl-204	81	204	310.00
Tc-97m	43	97	560.00
Tc-99	43	99	570.00
Tm-170	69	170	660.00
C-14	6	14	770.00
Y-91	39	91	810.00
Nb-93m	41	93	1000.00
Pm-147	61	147	1000.00
As-73	33	73	1100.00
Ca-45	20	45	1200.00
Fe-55	26	55	1500.00
S-35	16	35	1800.00
W-185	74	185	2000.00

Ni-63	28	63	3000.00
Sm-151	62	151	3200.00
Tm-171	69	171	3200.00
Ni-59	28	59	7100.00
Mn-53	25	53	15000.00
H-3	1	3	25000.00

The clearance level information in Table 3-2, as taken from (NISDF, 2017) is exceptionally valuable because the numerical values are directly and quantitatively derived from dosimetry models, with minimal rounding-off of numerical results, taking into account the following exposure scenarios and pathways (NISDF, 2017):

1. Skin dose from the re-use of cleared equipment.

2. Dose from inadvertent ingestion incurred during the re-use of equipment.

3. External gamma dose incurred during the re-use of cleared equipment.

4. Inhalation dose incurred during normal use of cleared equipment.

5. Inhalation dose incurred during cleaning/sanding of cleared equipment.

6. Inhalation dose incurred during repair/scrapping of cleared equipment.

Clearance level information published by other regulatory and advisory agencies typically suffers from excessive rounding-off of numerical values. The information in Table 3-2 does not suffer from such over-simplification and blunting by "category-binning", i.e. it is highly credible and quantitatively useful.

3.4.3 Radionuclide content of one drum filled with cemented liquid radioactive waste from the fission-based production of ^{99}Mo, in the light of clearance levels

Table 3-3 lists the calculated, expected radionuclide content of one drum filled with cemented liquid radioactive waste from $(n, f)^{99}$Mo production, at the 10-year mark. Values were calculated using the SCALE 6.2.4 system, using calculation models described in Annexure B which starts on page 222. Activities per unit mass were quantified for the cemented waste matrix inside the drum. The volume of the waste was taken to be 90 litres, i.e. just below the 100-litre internal volume of the inner stainless-

steel drum, and the mass-density of the cemented liquid radioactive waste was assumed to be 1.5 g cm^{-2}, i.e. considerably lower than that of ordinary concrete. Exfoliated vermiculite is added to the cementation mixture; the bulk density of this mineral is only 0.1 g cm^{-3} so that its addition is expected to lower the overall density of the cementitious matrix to below that of ORD-CRT. The lower the density of the cemented waste is assumed to be, the more conservative the calculated activities per unit mass and time to clearance parameters reported in e.g. Table 3-3 will be.

The colour-coding of the radionuclides in column 1 of Table 3-3 conform closely to the colour-coding system in Table 3-1 and Table 3-2. In column 1 of Table 3-3, radionuclides for which no published clearance levels could be found, are not colour-coded. In column 3 of Table 3-3, radionuclides for which clearance levels are exceeded at the 10-year mark since waste production, are marked in light red. Radionuclides that do not exceed clearance levels, at $T = 10$ yr since waste production, are marked in light green. Three greyed-out rows in Table 3-3 are for short-lived progeny isotopes in equilibrium with long-lived precursor isotopes, for which "time-to-clearance" information is provided for the longer-lived precursor radionuclide.

Table 3-3 contains "time to clearance" values. These values are calculated as follows. Consider a radionuclide with a given half-life and activity per unit mass. Suppose the present activity per unit mass is R_{cl} times higher than the clearance level. This means a period of time must elapse that will ensure that the activity per unit mass has diminished to the clearance level. Suppose that this radioactive transition process requires N half-lives of a radionuclide with a half-life of T_{half}. Using the definition of half-life, this means that one has to solve for N in the expression $\left(\frac{1}{2}\right)^N = \frac{1}{R_{cl}}$, which yields $N = \frac{\ln(R_{cl})}{\ln(2)}$, i.e. the time to clearance for this specific half-life is

$$T_{cl} = \left(\frac{\ln(R_{cl})}{\ln(2)}\right) T_{½}. \tag{3-1}$$

The calculation with Eq. (3-1) is performed for all radionuclides of interest in the waste, and the maximum of all the T_{cl} values for the individual radionuclides, is the required time to reach clearance levels and, therefore, the design-basis time for which the wasteform and engineered barriers must survive.

Table 3-3: Expected radionuclide content of one drum filled with cemented liquid radioactive waste from fission process production of ^{99}Mo, at the 10-year mark since target plate processing

Nuclide	Activity (Bq/drum)	Activity per unit mass (Bq/g)	Clearance level (Bq/g)	Decrease factor required	$T_{½}$ (yr)	Time to Clearance (yr)
Cs-137	6.51E+11	3.14E+06	3.7	8.50E+05	30.08064	592.5
Ba-137m	6.16E+11	2.98E+06	3.7			
Pm-147	1.65E+11	7.99E+05	1000	7.99E+02	2.62346	25.3
Y-90	6.60E+10	3.19E+05	120			
Sr-90	6.60E+10	3.19E+05	15	2.12E+04	28.79061	413.9
H-3	9.61E+09	4.64E+04	25000	1.86E+00	12.32026	11.0
Sb-125	1.72E+09	8.30E+03	5.2	1.60E+03	**2.75862**	29.4
Sm-151	1.33E+09	6.41E+03	3200	2.00E+00	**90.00192**	90.3
Pr-144	1.28E+09	6.20E+03				
Ce-144	1.28E+09	6.20E+03	68	9.12E+01	0.780058	5.1
Eu-155	1.26E+09	6.07E+03	41	1.48E+02	**4.7531**	34.3
Rh-106	4.72E+08	2.28E+03				
Ru-106	4.72E+08	2.28E+03	14	1.63E+02	**1.01795**	7.5
Te-125m	4.21E+08	2.03E+03				
Cs-134	2.67E+08	1.29E+03	1.6	8.08E+02	2.06524	19.9
Eu-154	1.22E+08	5.88E+02	1.8	3.27E+02	8.60118	71.8
Tc-99	1.10E+08	5.30E+02	570	9.30E-01		
Eu-152	8.98E+07	4.34E+02	2	2.17E+02	13.53729	105.1
Co-60	7.29E+07	3.52E+02	1	3.52E+02	5.27124	44.6
Fe-55	6.09E+07	2.94E+02	1500	1.96E-01		
Sn-121m	3.95E+07	1.91E+02				
Sn-121	3.06E+07	1.48E+02				
Pr-144m	1.23E+07	5.92E+01				
Cd-113m	5.28E+06	2.55E+01				
C-14	3.71E+06	1.79E+01	770	2.33E-02		
Zr-93	1.91E+06	9.22E+00	290	3.18E-02		
Ni-63	1.01E+06	4.87E+00	3000	1.62E-03		
Cs-135	8.54E+05	4.13E+00	220	1.88E-02		
Nb-93m	6.65E+05	3.21E+00	1000	3.21E-03		
Sn-126	5.23E+05	2.53E+00				
Sb-126m	5.23E+05	2.53E+00				
Sn-119m	1.69E+05	8.16E-01				
Se-79	1.28E+05	6.19E-01				
I-129	1.22E+05	5.89E-01	4	1.47E-01		
Sb-126	7.32E+04	3.54E-01				
Pd-107	6.63E+04	3.20E-01				

Mn-54	3.29E+04	1.59E-01	3.7	4.30E-02		
Ag-108m	2.84E+04	1.37E-01	1.3	1.06E-01		
Ag-110m	1.36E+04	6.57E-02	1.3	5.05E-02		
Ni-59	6.81E+03	3.29E-02	7100	4.63E-06		
Zn-65	3.80E+03	1.83E-02	6.3	2.91E-03		
Ag-108	2.47E+03	1.19E-02				
			Required waiting time (yr)			**592.5**

Note that published clearance levels are only available for a limited number of radionuclides, so that there are inevitable gaps in Table 3-3. "Time-to-clearance" and half-life information are only provided for radionuclides that exceed clearance levels at the $T = 10$ yr mark.

In Table 3-3, at least 14 radionuclides in the cemented ILW matrix are seen to exceed clearance levels at the 10-year mark. What is more, the activity of ^{137}Cs per unit mass in the cemented waste matrix, exceeds its clearance level by almost 6 decimal orders of magnitude; given its half-life of circa 30 years, it will take 20 half-lives, i.e. 600 years of radioactive transition- before the cemented ILW matrix would meet clearance levels for ^{137}Cs, because $\left(\frac{1}{2}\right)^{20} \approx 10^{-6}$. This analysis shows the need for immobilising the liquid radioactive waste from chemically processed irradiated target plates, in a cementitious matrix surrounded by 2 barriers — a 3 mm inner stainless-steel drum wall, plus the thick concrete wall of the radioactive waste drum. The radioactive waste matrix in the centre of the drum will only pass clearance levels after circa 600 years, i.e. the designed life-expectancy of the waste package must exceed 600 years and should be in the order of 1000 years, for a Factor of Safety (FoS).

Table 3-3 indicates that ^{137}Cs is the nuclide that dictates the design lifetime of the engineered barriers in wasteforms of ILLW$[(n,f)^{99}\text{Mo}]$.

The EXCEL spreadsheet used to calculate the required waiting time before clearance levels will be met, is embedded here:



To open the above spreadsheet, double-click its icon[11].

[11] Note by supervisor TJvR: Note that the EXCEL XLOOKUP function that is used in this EXCEL sheet, may not work in versions of Microsoft EXCEL older than circa mid-2019.

3.5 Literature review: Radioactive waste management technology for ILLW

3.5.1 Introduction

Liquid and wet LLW must be immobilised in a suitable fixation matrix so that the final waste package will meet the required criteria for final disposal in a radioactive waste repository. Cementation is an important process used for the fixation of liquid and wet radioactive waste such as liquid waste concentrates, spent ion-exchange resins and sludges. Active cement grout is also used for the fixation of low-level solid radioactive waste loaded in final packing containers. In the cementation of liquid radioactive waste, it is advantageous to incorporate exfoliated vermiculite into the cementation recipe, because it has a high ability to tightly bind ions such as e.g. cæsium cations (Cs^+).

The only immobilisation technology for radioactive waste that will receive attention in this literature review, is cementation. Glassification, vitrification and ceramic waste matrices will not be considered here.

3.5.2 General overview of radioactive waste management

Nagasaki & Nakayama (2015) presents an overview of the field of radioactive waste engineering and management, with specific application to the situation in Japan. The characterisation, treatment and final disposal of radioactive wastes, institutional systems and social issues such as inter-generational ethics, are discussed.

Raj *et al.* (2006) as well as Wattal (2013) present overviews of radioactive waste management practices in India.

Saling (2018) presents a broad overview of radioactive waste management. Like Nagasaki & Nakayama (2015), this is a textbook for postgraduate courses on radioactive waste management. The book by Saling is more practically useful than the one by Nagasaki & Nakayama.

3.5.3 Classification of radioactive waste

Hosan (2018) and (IAEA, 2009a) present the currently accepted classification system for radioactive waste. Radioactive waste is classified as follows:

Exempt waste has such low concentrations of radionuclides that it does not require requirements for radiation protection, irrespective of whether the waste is disposed of in conventional landfills or recycled. This type of waste is cleared from regulatory control (IAEA, 2009a).

Very short-lived waste (VSLW) contains only radionuclides of very short half-life with activity concentrations above exemption levels. This type of waste can be stored until the activity has fallen to below clearance levels, allowing for the cleared waste to manage as usual waste.

Very Low-Level Waste (VLLW): Considerable amounts of waste arising from the operation and decommissioning of nuclear facilities with levels of activity concentration in the region of or slightly above the margins specified for the permission of material from regulatory control (IAEA, 2009a). Waste with such a limited hazard, which is nevertheless above or close to the values for exempt waste, is called very low-level waste. A satisfactory level of safety for VLLW achieved by its disposal in engineered surface landfill type facilities. This engineered surface landfill type facility is the usual practice for hazard from some mining operations and other waste containing naturally occurring radionuclides from various operations involving minerals processing and other activities.

Low-Level Waste (LLW): Low-level waste is radioactive waste that is appropriate for near-surface disposal. This near-surface disposal option is appropriate for waste that contains radioactive material in amounts that require that robust containment and isolation for relatively short period of time up to a few hundred years.

Intermediate-level waste (ILW): This type of waste contains long-lived radionuclides in quantities that require a level of containment and separation from the biosphere that cannot be provided by near-surface disposal. Disposal in a facility at a depth ranging between e.g. 20 m and 100 m is specified as the disposal option for ILW that contains a substantial activity fraction of long-lived radionuclides with restrictive clearance levels. Disposal at such depths eliminate erosion as well as inadvertent human interruption. This eliminates the need for the continuous application of vigilant institutional controls (IAEA, 2009a).

Freiesleben (2013) discusses the final disposal of radioactive waste. The origin and properties of radioactive waste as well as the LLW, ILW and HLW classification scheme, are presented. The diverse

options for conditioning of waste of different levels of radioactivity are reviewed. Cementation is listed as a widely used method for immobilising liquid radioactive waste in a durable matrix. (The focus of the review is HLW and not the ILLW that is the focus of the present work.)

3.5.4 Monographs on the management of radioactive waste from the production of ^{99}Mo

In 1998, the International Atomic Energy Agency (IAEA, 1998) published a report on the management of radioactive waste from the production of ^{99}Mo. The report fucuses on a fission-based production process and its ILLW waste, i.e. ILLW$[(n,f)^{99}\mathrm{Mo}]$. First, the worldwide production of the radioisotope ^{99}Mo is reviewed, also production in South Africa. Based on calculations, the authors state that activation products in radioactive waste are overshadowed by fission products. One year post-irradiation, only 4 activation products formed in the irradiated target plates have non-neglible relative activities; these are ^{3}H , ^{55}Fe, ^{65}Zn and ^{60}Co. This IAEA report was written at a time when the use of high enrichment uranium (HEU) was still the norm, while the use of Low Enrichment Uranium (LEU) was novel. The IAEA notes that the use of LEU rather than HEU for ^{99}Mo production has several disadvantages on waste generation, namely:

1. Increased amounts of solid uranic waste are produced and has to be stored in highly secured storage areas.
2. Increased volume of liquid radioactive waste generation (more spent chemicals and equipment) as a result of having to process more uranium to obtain the same yield of ^{99}Mo. The amount of dissolving solution used increases by a factor of at least 3, and process equipment with larger volumes is required.
3. Increased amounts of Pu and other transuranic elements are produced; this increases the cost and difficulty of disposal.

The IAEA report (IAEA, 1998) describes the on-site processing of radioactive waste from the fission-based production of ^{99}Mo, at Necsa in South Africa as follows (IAEA, 1998:36).

> "Dissolution of irradiated target plates and purification of ^{99}Mo are carried out in lead shielded hot-cells. The radioactive xenon gas that is released during ITP dissolution is adsorbed onto standard activated carbon in stainless-steel columns. These columns are then closed off for a period long enough to allow the radioactive transition of practically all Xe radioisotopes.

Nuclides of krypton are not retained completely. Small amounts of gaseous iodine are removed from the hot cell off-gas by using suitably impregnated activated carbon filters. Hydrogen gas which is evolved during target plate dissolution is either oxidised into water by hot copper oxide, or the dissolution rate is controlled in such a way that the hydrogen concentration in the ventilation system is within safety limits. Monitoring systems for radioactive noble gases, radioactive isotopes of iodine, α-, β- and γ-emitters as well as H_2 gas, are distributed throughout the ventilation system for process control measures as well as the quantification of releases to the environment. Alkaline radioactive liquid waste is accumulated in shielded stainless-steel tanks, allowed to decay for 3 months and then immobilised in a cement-vermiculite mixture. The radioactive cemented slurry is transferred into a stainless-steel drum placed inside a high-density concrete drum container which provides the necessary radiation shielding during handling and transport to the waste repository for LILW, for burial in shallow trenches. After 6 months to 1 year, the dominant radionuclides in the ILLW is reported to be the fission products ^{137}Cs , ^{95}Zr, ^{95}Nb and ^{103}Rb".

Mushtaq *et al.* (2009) presents an overview of the management of radioactive waste from fission-produced ^{99}Mo production using LEU uranium targets and a modified CINTICHEM process. The authors point out that radioactive waste will be generated as solids, liquids, and gases, and will include material in the LLW, ILW and HLW radioactivity categories. Initial treatment of waste streams is required at the production site, prior to short-term or long-term storage, as well as final disposal. The authors point out that these waste conditioning technologies are well established and generally available in all countries with existing nuclear industries and infrastructures.

3.5.5 Portland cement

Portland cement is the most common type of cement in widespread use around the world as a basic ingredient of concrete, mortar and grout. It is a fine powder, produced by heating limestone and clay minerals in a kiln to form clinker, grinding the clinker, and adding 2 % to 3 % of gypsum (calcium sulphate). OPC, i.e. ordinary Portland cement, contains around 70 % calcium silicates (Atkins & Glasser, 1992).

Environmental concerns related to the production and use of Portland cement are the high energy consumption required to mine the raw materials and then manufacture and transport the cement, and the related air pollution, including the release of the greenhouse gas, carbon dioxide. Production of

Portland cement is estimated to contribute almost 10 % of worldwide CO_2 emissions in 2019. As a result, alternative cements such as geopolymer cements (Kim *et al.*, 2021) are under investigation for radioactive waste disposal (Cau-dit-Coumes, 2013).

3.5.6 Geopolymer cement

To protect the environment, alternatives to Portland-type cements are required. Geopolymer cement is an important alternative to Portland cement, but cannot replace it entirely. Any process waste material — such as fly-ash, granulated blast furnace slag, clay, etc., that contain aluminosilicate mineral, yield geopolymer cements when treated with alkaline aqueous solutions of e.g. NaOH or KOH (Geddes *et al.*, 2018; Kim *et al.*, 2021; Singh *et al.*, 2020).

3.5.7 Concretes

In most practical applications, cement powder is mixed with mineral aggregates for the production of concrete. Fine, millimetre-sized aggregate such as sand is mixed with cement and water to give a product termed "mortar" while mixtures of cement with both fine and coarse aggregate (e.g. sand plus gravel), plus water, are termed "concrete". The boundary between "fine" and "coarse" aggregate is circa 2 mm. A mortar made using particles smaller than 1 mm is suitable as a plaster. Any free flowing $\{\text{cement} + \text{fine particles} + \text{water}\}$ mixture is known as "grout". Cement serves as the hardening binder in grout, mortar and concrete.

Mineral aggregates are used in mortars, grouts and concretes that find application in construction, because they (1) improve the $\frac{\text{strength}}{\text{cost}}$ ratio and spread out the heat of hydration of cement over a much larger volume. If not managed, the heat of hydration could lead to excessive temperature rises, especially in large concrete masses. The aggregates also help restrain and reduce the impacts of normal physical shrinkage which occurs during the hydration and hardening of mortars and concretes.

The freshly mixed cement product — grout, mortar or concrete — usually has a period of workability lasting several hours, during which the mix remains fluid and may be emplaced by pouring or pumping. Cements and concretes are stronger when the water to cement ratio is low, and this is achieved by the use of superplasticisers.

Structural engineers often refer to concrete as "liquid rock" because it can be moulded and shaped when workable, and then sets to rock-like hardness.

3.5.8 Ordinary concrete

To manufacture ordinary concrete (ORD-CRT), sand is used as fine aggregate and ordinary gravel with sizes below circa 20 mm, is used as coarse aggregate. The chemical composition of ordinary concrete is dominated by oxygen and silicon, which typically account for more than 85 % of the mass of ORD-CRT. The sand and gravel that is used must have coarse textures to ensure strong binding. This desired texture is found in marine sand but not in desert sand, i.e. the latter is not suitable for making concrete.

3.5.9 Ageing and deterioration of reinforced concrete structures such as drums for ILLW

When steel reinforcing inside concrete begins to rust, its volume will expand by a factor of at least 4. This swelling of the corroding steel rebar causes tensile stresses within the concrete, leading to failure by spalling. In a concrete drum with a circumferential steel reinforcing mat, the outer part of the drum will crack away from the circumference of the rusting reinforcing and the drum will disintegrate, losing the outer ~25% of its thickness.

The typical pH of new concrete is around 13. At this alkaline pH, the concrete pacifies the embedded steel reinforcing and actively prevents rust. A process known as concrete carbonation causes embedded steel reinforcements to corrode, and the resulting expansion will weaken and crack the concrete, leading to spalling. Carbonation commences as soon as concrete is exposed to the atmosphere, and can advance at a typical rate of 1 mm to 5 mm per year, dependent on the concrete's porosity and permeability as well as climatic conditions. Carbonation is the most common cause of reinforcement corrosion in free-standing, above-ground structures. Carbonation can be slowed down by not exposing the concrete to water and through the (routine) application of a protective anti-carbonation coating.

Concrete carbonation is the result of an electrochemical reaction between carbon dioxide (CO_2), moisture (H_2O) and calcium hydroxide ($Ca(OH)_2$) that is present in cement, producing calcium carbonate ($CaCO_3$). The chemical reaction that replaces the alkaline $Ca(OH)_2$ with the less alkaline $CaCO_3$, lowers the alkalinity of concrete from the initial pH13 to around pH9. This hardens the concrete and increases its compressive strength, but at this reduced pH level, the protective passivation layer surrounding the reinforcing steel begins to break down, leaving the steel vulnerable to corrosion. As soon as the pH of the concrete dips to below approximately pH10.5, the corrosion of embedded steel rebar sets in. This corrosion is significantly accelerated by, especially, the presence of the chloride

anion, Cl^-, which is abundant in marine environments and atmospheres as well as in many types of brackish soils.

Rust (hydrated iron oxide) has a volume that is 4 to 6 times larger than the original steel. As the steel reinforcement rusts, it will expand, placing the concrete under tensile stress (concrete is notoriously weak under any tensile loading) which will cause the concrete to crack and spall.

The lowering of the pH of concrete is a chemical reaction of water (moisture) and atmospheric CO_2 with the concrete.

The implications of the above facts for the drums used for the storage, transport and disposal of ILLW$[(n,f)^{99}\mathrm{Mo}]$ are as follows:

1. The ingress of water into the concrete should be minimised after the initial (4-week) curing process. This means that the drums must be stored in a dry, elevated, undercover area before transport to the waste producer, at the waste producer and during road transport to the disposal site. Two years of standing outside in the decay yard exposes the drums to cycles of heat, frost and rain. Moisture can penetrate the concrete and carbonation, i.e. the loss of alkalinity will be initiated.

2. Carbonation can be prevented or halted with the application of a protective anti-carbonation coating system. This should be specified for both new and existing concrete drums. It is important to specify a coating system that provides protection against the ingress of carbon dioxide, oxygen and water, while allowing damp substrates to breathe without blistering.

3. Once the drums arrive at the disposal site, it is important that the time they spend on the surface of the terrain, exposed to the elements, must be minimised. The aim is to get the drums into the trenches and covered with soil overburden as soon as possible. Carbonation will then slow down because the disposal site is in an arid semi-desert.

4. Drums must be given an initial protective, anti-carbonation coating at the manufacturer, must be transported under protective sail cover, stored in a roofed and elevated "decay yard" where rain and floodwater cannot wet the drums. If this is not done, the drums that were exposed to regular showers of rain while being stored in an open-to-the-elements decay yard for, say, 2 years, will arrive at the disposal site pre-charged with moisture, which will then sustain the carbonation process, i.e. the loss of adequately high pH, followed by rusting of steel

reinforcing, followed by spalling. This is an example of stepping away from the short-sighted culture of generating present income at the cost of future liability.

3.5.10 Concretes based on geopolymer cement as binder-hardener

When cured at an adequately elevated temperature, concretes based on geopolymer cements develop high strength and can be used in many applications. Geopolymer cements can be formulated to cure more rapidly than Portland-based cements; some mixes gain most of their ultimate strength within 24 hours (Singh *et al.*, 2020). Strength development in concretes using geopolymer cement as binder-hardener, is generally slow under ambient temperatures; this makes heat-curing essential for gaining rapid early strength. For regular fly-ash geopolymer concrete, a 24-hour period of heating at 60–80 °C is enough to achieve sufficient strength (Singh *et al.*, 2020). Geopolymer cement that is based on fly-ash, is suitable for pre-cast concrete structures such as beams, girders, railway sleepers, wall panels, hollow core slabs, concrete pipes as well as concrete drums for wastes disposal. With heating, a concrete drum manufactured using geopolymer cement (GPC) as binder-hardener, can be ready for transport to a client within 2 days.

In practice, licensing a new concrete type for radioactive waste disposal, is a lengthy process of proving to the regulator that the new technology meets all acceptance criteria. At present, the use of Portland cement for the cementation of liquid radioactive waste, is licensed. To license concrete radioactive waste disposal drums manufactured with geopolymer cements, containing ILLW cemented with geopolymer cement, will require an extended approval and licensing campaign. As always, smaller countries should wait for such technologies to be licensed by the major role-players in the nuclear industry, and then adopt the well-proven, previously licensed technology locally.

3.5.11 Concrete as a secondary barrier for the disposal of ILW

Concrete — itself a cement product — is usually the material of choice for the secondary protection barrier between the cemented ILW and the surrounding environment (Kot'átková *et al.*, 2017)[12]. When the cemented slurry is pumped into the drum, when the drum is in on-site interim storage and when the drum is transported, the concrete also serves as radiation shielding. After disposal at a radioactive waste repository, the concrete drum wall serves as a barrier against the migration of radionuclides into the environment. Humanity has many decades of experience with the use of cements and concretes in

[12] Note that the authors of this article use the term "deposition" for "disposal".

structural engineering technology, and their durability and performance in many environments have been characterised and quantified (Glasser, 2011; Ojovan, 2011; Ojovan *et al.*, 2019). Steel reinforced concrete drums are the favoured waste package for ILW, which includes cemented ILLW. For additional radionuclide containment, the 3 mm thick wall of the embedded SS-304L drum inside the larger concrete drum, also serves a robust containment purpose. The purpose of these engineered barriers is to limit any groundwater and soil moisture ingress into the immobilised waste matrix and to serve as an additional barrier against the transport of radionuclides out of the cemented waste, into the environment. Besides radiation shielding, the functions of the concrete are to (1) block the movement of moisture, so that atomic and molecular diffusion is the only mechanism of transport of radioactive material, (2) provide strong sorption of many radionuclides, i.e. ensure low diffusion coefficients for any movement of radionuclides, and (3) provide an alkaline chemical environment around the stainless-steel inner drum as well as structural steel reinforcing embedded in the concrete, which serves as a passivation material for metallic structures contacted by the concrete (Ojovan *et al.*, 2019).

3.5.12 Shielding efficacy of high-density shielding concretes

Abdo *et al.* (2002) investigated the radiation attenuation properties for barite concrete (BAR-CRT) as a biological shield for nuclear power plants, particle accelerators, research reactors, laboratory hot-cells and a range of radiation sources. Their samples of BAR-CRT had a reported mass-density of $\rho = 3.49\ \mathrm{g\ cm^{-3}}$. This study is of limited practical use from the perspective of the shielding of radioactive waste — the authors measured the shielding properties of one particular batch of BAR-CRT, and the emphasis is on neutron shielding. They conclude that barite aggregates have advantages such as being free from deleterious substances, which react with the alkalis in Portland cement. This could contribute to the long-term chemical stability of BAR-CRT. They foresee that BAR-CRT may find many applications in a wide range of fields, including radiation shielding. Japanese sourced aggregate of barite ores was chosen to construct high-density barite concrete shielding. The barite ore contained an average of 91.9% $BaSO_4$, 2.7% SiO_2 , 1.8% Al_2O_3 and 1.7% $CaCO_3$. The remainder consisted of $MgCO_3$ and NaCl plus traces of the elements P and Fe. The specific batch of barite concrete prepared by the investigators, contained circa 82% barite ore, 12% cement and 5.3% water as well as small sprinkling of super-plasticiser to extend the duration of workability (softness) and allow water reduction without any loss of workability.

Gencel *et al.* (2010) discuss concretes containing hematite for use as shielding barriers. The article focuses on the mechanical properties rather than the radiation shielding properties of the cement. The following properties of hematite concrete are presented and discussed: compressive strength, workability, segregation, durability in freeze-thaw cycles, and concrete shrinking. The authors point out that hematite concrete may be prone to undergoing further oxidation, which can lead to the development of weak spots in the concrete.

Akkurt *et al.* (2006) investigated the shielding of ionising photons by concrete, for concretes containing different amounts of barite and normal-density aggregates. The linear attenuation coefficients (μ, unit: cm^{-1}) were measured at $E_\gamma = 0.66$ MeV and $E_\gamma = 1.33$ MeV.

Akkurt *et al.* (2010) reports measured values for the linear attenuation coefficients for concrete containing zeolite as an aggregate in different concentrations (0%,10%, 30% and 50%). They conclude that zeolite failed to improve the radiation shielding properties of concrete. Zeolites are microporous, aluminosilicate minerals commonly used as adsorbents, and have garnered a reputation as "molecular sieves". Typical zeolite has a chemical formula $\mathrm{Na_2Al_2Si_3O_{10} \cdot 2H_2O}$. The atomic numbers of all these elements in typical zeolite range between 1 and 14, and the average Z-number is in the range of only 8, i.e. low. The theoretical treatment in § 2.2 on page 55 also leads to the conclusion that the admixture of zeolite will not be able to improve the attenuation of ionising photons by concrete. The ability of a concrete to attenuate ionising photons is best improved by adding abundantly available higher-Z elements, in particular Fe and Ba, in suitable mineral forms such as hematite and barite. This is clear from Table 2-2 on page 64. Zeolite does not contain such sought-after higher-Z chemical elements.

Basyigit *et al.* (2011) present an article on experimentally determined radiation shielding abilities of heavy shielding concretes relative to ordinary concrete. The authors went to great lengths to measure the attenuation of ionising photons in different concretes, and conclude (sic!) "The experimental results on measuring the radiation shielding, the heavyweight concrete prepared with heavyweight aggregates of different mineral origin show that, are useful radiation absorbents when they used in concrete mixtures". A consideration of the theoretical treatment in § 2.2 starting on page 55, which is summarised in Table 2-2 on page 64, also point out that adding higher-Z elements such as Fe and Ba to concrete, would significantly improve the mixture's radiation shielding properties. The article by Basyigit *et al.* (2011) confirms this, but also points to a "gap" that is discernable in several published articles on concrete shielding and is formally listed in the "gaps analysis" in § 3.5.24 on page 124.

Shams *et al.* (2018) report an experimental investigation of the effect of adding barite aggregate and hematite aggregate into concrete, on the product's ability to attenuate γ-photons. The results showed that increasing the percentage of barite or hematite aggregates, increased the linear attenuation coefficient μ for γ-interaction as well as the 28-day compressive strength of the concrete product. It was found that the order of the layers in multi-layered concrete shields has no significant impact on the attenuation of γ-photons, and that a homogenous admixture of hematite and barite in concrete provided better photon attenuation properties than layering the concrete into successive barite/hematite concrete layers.

Gunoglu & Akkurt (2021) reports an investigation that showed that magnetite concrete is a better shield for ionising photons than ordinary concrete. This experimental finding confirms the theoretical treatment in § 2.2 which starts on page 55 which also concludes that the addition of higher-Z elements such as Fe ($Z = 26$), which is abundantly present in magnetite ore, will improve the concrete's γ-shielding properties.

Conclusion

After having reviewed the above literature on the formulation and selection of shielding concretes with usefully good γ-attenuation characteristics, it is concluded that several experimental investigations do not verbalise the theoretical basis that underlies the attenuation of ionising photons in the energy range under circa 10 MeV. The simple theoretical treatment in § 2.2 (which starts on page 55), points out that there exists a simple and robust recipe for maximising the shielding ability of a mixture such as a concrete, namely to (1) add high-Z chemical elements to the mixture and (2) maximise its mass-density ρ. Under the constraints of availability, affordability, long-term chemical stability and non-toxicity, this leads to the selection of hematite[13] concrete and barite concrete as the best practical radiation shielding concretes for the attenuation of the γ-radiation emitted by typical radioactive wastes. This identified gap in the literature is addressed in § 3.5.24 on page 124.

[13] Note by study supervisor TJvR: In magnetite at least 40% of Fe will initially be in the Fe^{2+} (ferro) oxidation state. Subsequent oxidation of "ferro" oxidation state Fe in magnetite concrete will form iron in the Fe^{3+} i.e. "ferri" oxidation state and this long-term oxidation of concrete constituents may affect the long-term structural performance of magnetite concrete negatively. In hematite, Fe is more fully oxidised (to the Fe^{3+} i.e. "ferri" state) than in magnetite, so that hematite concrete will display better long-term chemically stability compared to magnetite concrete.

3.5.13 Availability of high-grade iron ores in South Africa, for the manufacture of high-density shielding concrete

In an impressive MSc dissertation, Netshiozwi (2002) focuses on the geological origin of high-grade hematite ores at the Thabazimbi mine in the Limpopo Province of South Africa. This study is written from the perspective of academic geology, and the only practical implication for the present study is that hematite is, indeed, locally available for the manufacture of high-density shielding concrete.

3.5.14 Engineered radiation safety system for radioactive waste

An engineered radiation safety system (ERSS) has 3 pillars, namely:

1. A **radiation containment system** (Van Rooyen, 2020c), attenuates the flow of ionising radiation out of the radioactive material, by surrounding the source region with a radiation shielding design.

2. A **radionuclide containment system** (Van Rooyen, 2020c) serves as a material containment structure that traps and immobilises the radioactive material for a designed lifespan. This containment system is a combination of engineered barriers and natural barriers.

3. An **access control system** (Van Rooyen, 2020c) serves to keep unauthorised people (as well as higher mammals), outside radiologically controlled areas.

Higher-activity radioactive waste is placed in containers that serve a shielding function. An example is the cementation matrix and thick outer concrete drum in which ILLW is disposed. The cement matrix, stainless-steel drum and outer concrete drum also serve as a radionuclide containment system, i.e. a radioactive material containment system. Radioactive waste is stored and disposed at facilities with strict access control systems.

3.5.15 Immobilisation technologies for radioactive waste

Immobilisation of radioactive waste is achieved by its chemical incorporation into the structure of a suitable matrix — typically cement, glass or ceramic — so that the radionuclides are bound, captured, trapped and unable to escape. Encapsulation of waste is achieved by physically surrounding it in materials — typically bitumen or cement — so that it is isolated, and radionuclides are retained. Physical encapsulation is routinely applied to intermediate-level waste (ILW).

3.5.16 Conditioning and immobilisation of radioactive waste; the concept wasteform

A variety of radioactive waste conditioning technologies and related processes have been developed. Conditioning processes transform the "raw" radioactive waste into forms suitable for handling, storage, transport and disposal (Glasser, 2011). One often-used conditioning technology is cementation. Cementation is an attractively simple and affordable conditioning technology for the immobilisation of radioactive waste.

A major aim of the cementation of radioactive waste, specifically liquid radioactive waste, is the immobilisation of the radionuclides (Ojovan *et al.*, 2019). Immobilisation involves the safe embedding of radioactive waste into a matrix that drastically attenuates the rate of leakage of radionuclides into the environment. Immobilisation involves the retention of radionuclides in the solid matrix. The retention afforded by cementitious materials is attractively high because such materials have high sorption or uptake capacity (Sukhanov, 2013).

Immobilisation of radioactive wastes in a stable, solid matrix reduces the potential for migration or dispersion of radionuclides, and drastically reduces dispersal rates. The product of incorporating radioactive waste into a durable immobilisation matrix is called a wasteform. Immobilisation is the conversion of radioactive waste into a disposable wasteform via solidification, embedding and encapsulation. Immobilisation makes the handling, transportation, storage and disposal of radioactive wastes safe and, therefore, viable. Immobilisation of radioactive waste is achieved by the incorporation of the waste into the chemical and physical structure of a suitable matrix such as a cement, in which radionuclides are chemically and physically trapped, captured, retained and (almost) unable to escape. Encapsulation of waste is achieved by physically surrounding it in a multi-barrier package so that it remains isolated, and radionuclides are retained. Immobilisation (e.g. cementation), as well as physical encapsulation, is applied to ILW.

The purpose of a wasteform is to immobilise nuclear waste in a solid matrix that is chemically and physically significantly more durable and more radiation resistant than the original form of the waste (e.g. a liquid). The wasteform stabilises the waste during packaging, an interim storage period, transportation, emplacement within a geological repository, and the post-closure disposal period, i.e. the period when the disposed waste packages are no longer actively guarded and surveyed.

The immobilisation of nuclear waste is the conversion of radioactive waste into a wasteform that resists the dispersion of the radioactivity and its entry into the biosphere, for several centuries. Immobilisation involves solidification, embedding and encapsulation of the waste in order to reduce the potential for migration or dispersion of radionuclides during operational and disposal stages of the lifecycle of the radioactive waste. Immobilisation of waste radionuclides inside durable wasteform materials provides a key barrier that contributes to the overall performance of any storage and disposal system for radioactive waste. Materials for nuclear waste immobilisation constitute the core of the multi-barrier systems for the isolation of radioactive waste from the environment, aimed at ensuring long-term safety of the storage and disposal of such waste.

3.5.17 Engineered barrier system (EBS) and natural barrier system (NBS)

Within a repository for the disposal of radioactive waste, the wasteform is one part of a multi-layer engineered barrier system (EBS). During storage the wasteform is the primary barrier preventing the release of radionuclides into the environment while during post-closure disposal, the wasteform will reduce the release of radionuclides from breached and compromised containers that could result due to corrosion, earthquakes, human intrusion or other disruptive phenomena. Disposal facilities for radioactive waste are located in areas known for possessing a robust natural barrier system (NBS) against the diffusion and migration of radionuclides. The natural barrier system is based on the geochemical environment wherein the engineered barriers reside. Key elements of a natural barrier system are (1) an arid climate, (2) the absence of aquafers, (3) a very deep water-table as well as (4) a good portion of clay in the soil — clay acts as a natural immobiliser.

3.5.18 Engineered radionuclide containment barriers: ILLW

The endpoints for radioactive waste are storage and final disposal. Conditioning methods such as immobilisation and packaging in containers depend on the level of radioactivity and the halflives of waste radionuclides. Safety of storage and disposal is achieved mainly by containment. Containment deploys several barriers around the radioactive waste, aimed at restricting the release of radionuclides into the environment; this is known as the multi-barrier concept. In the case of cemented ILLW, the first 3 restricting barriers are engineered barriers, namely (1) the cement matrix, (2) the inner stainless-steel drum and (3) the outer large concrete drum. The general approach is to use more durable and reliable radionuclide retention barriers for more hazardous waste. Very low-level waste (VLLW) typically does not require immobilisation and are disposed in simple steel drums. Low and

intermediate-level waste dominated by shorter-lived radionuclides (LILW-SL) is typically immobilised using cements. Low and Intermediate-level waste that is dominated by longer-lived radionuclides (LILW-LL) has a higher activity per unit mass compared to LLW and can be immobilised using glasses, bitumen, traditional cements or geopolymer cements. Once immobilised, LILW-SL or LILW-LL can be packaged in high-integrity stainless-steel drums inside strong, thick concrete drums.

3.5.19 Cementation of intermediate-level radioactive waste; Immobilisation of radioactive waste via cementation

One of the easiest and most widely used methods for immobilising ILLW is cementation. Advantages are low cost, the simplicity of the process, and low process temperatures which eliminates the release of volatile radionuclides. Cement has high radiation stability, impact resistance and heat/fire resistance. Some of the limitations of cementation are poor compatibility with some organic materials (i.e. petroleum oils) as well as with radioactive waste having a high salt content.

Liquid and moist/wet[14] intermediate-level radioactive waste must be solidified and immobilised prior to disposal. Such conditioning of radioactive waste is classified as predisposal waste management (IAEA, 2009b). Most radioactive waste forms require predisposal waste management (PWM). The purpose of PWM is to produce waste packages suitable for storage, transportation and final disposal. Cementation is a widely applied technique for the conditioning of intermediate level radioactive wastes (ILW), including moist and liquid wastes (Sukhanov, 2013). Cementation is simple and inexpensive. Calcium silicate cements have added advantages, such as easy supply, compatibility with aqueous wastes, good self-shielding and high alkalinity, which assists with the precipitation, confining and immobilisation of many radionuclides.

Glasser (2010) presents a scholarly discussion of the use of cements in radioactive waste disposal. He notes that there is a wide range of cements, a wide range of service environments in which cement is used, as well as many different functions expected of cement. Portland cement has been widely used to encapsulate and immobilise radioactive wastes for storage, transport and as radiation shielding. Relative to other potential immobilisation matrices, cement does not only provide physical encapsulation, but also has a chemical immobilisation potential, by chemically reacting with and binding many radionuclides. The author notes that the chemical binding potential of cements is

[14] E.g., ion-exchange resins used in the chemical and volume control system at a pressurised water reactor (PWR) to purify reactor coolant.

essentially sacrificial, i.e. by binding with radionuclides, the cement matrix is weakened, and its degradation is accelerated, thus limiting the performance lifetime of the cement matrix. The author states Glasser (2010)

> The origin of the chemical binding potential of cement arises from the chemisorption on cement solids, incorporation by solid solution in cement solids and precipitation of a solubility-limiting phase or phases in a calcium-rich, high pH environment. These favourable potentials, especially pH conditioning, are, as noted, essentially sacrificial: cement must dissolve or react to maintain these conditions in the course of its service life. The immobilisation potential will also change with time, even in isolation, because cement minerals undergo internal ageing and slow reaction with other proximal materials.

The high pH of Portland cement matrices has advantages but also, disadvantages. Portland cement gives excellent protection against corrosion to embedded steel but, on the other hand, it corrodes electropositive metals such as aluminium, with the evolution of hydrogen. Formation of a high pH "plume" may also spread from the concrete to proximal materials and minerals, degrading other barriers such as bentonite and lowering the sorptive potential for radionuclides of near-field minerals (i.e. minerals closer than a few metres from the waste packages). These considerations have led to the search for alternative, lower-pH cements which are less alkaline than Portland cement. A description of some common types is given. The author concludes that the most robust of these alternative, non-PPC cement formulations are based on (1) calcium aluminate, (2) calcium sulfo-aluminate (CSA), (3) magnesium phosphate and (4) geopolymer cements.

Bart *et al.* (2012) survey the use of cement-based materials for nuclear waste storage and disposal. Particular attention is given to the use of cementation as a technique for the treatment of low- and intermediate-level radioactive wastes to achieve immobilisation. Cementation is compared to other solidification techniques. The authors stress the advantages of calcium silicate cements over other materials and discuss the long-term suitability and safety of cementitious waste forms as well as cement-based barriers such as concretes. This book also discusses the formulation and production of cement waste forms for storing radioactive waste, and assesses the potential of novel binders to enhance the conditioning of problematic radioactive wastes.

Cau-dit-Coumes *et al.*, (2009) argue persuasively that calcium sulfo-aluminate (CSA) cement blended with ordinary Portland cement is a stable binder to encapsulate low-level radioactive slurries of

complex chemistry. Pure ordinary Portland cement (OPC) failed as a binder-hardener when waste contained high concentrations of borates and phosphates.

Cau-dit-Coumes (2013) discusses alternative binders to ordinary Portland cement for radioactive waste solidification and stabilisation. It is pointed out that the common practice has been to solidify and stabilise low- and intermediate-level radioactive wastes with calcium silicate cements such as ordinary Portland cement. However, the quality of the final product may be noticeably reduced by adverse cement-waste interactions. The article reviews the potential of 3 kinds of alternative inorganic binders to treat problematic wastes; these binder-hardeners are (1) calcium aluminate and calcium sulpho-aluminate cements, (2) magnesium and calcium phosphate cements, and (3) alkali-activated binders. The potential of these cements for the conditioning of radioactive waste is discussed.

Cau-dit-Coumes (2014) discusses the role of cementation in the immobilisation and stabilisation of ILW. Collier *et al.* (2014) investigated the suitability of a supersulfated cement for nuclear waste immobilisation. The high alkalinity of Portland cement corrodes nuclear waste containing aluminium metal, leading to the evolution of free hydrogen. The authors report that that the supersulfated cement has a high potential for the immobilisation of ions that are present in radioactive waste, and that both pH and aluminium corrosion are lower than observed with the use of Portland cement. De Freitas & Al-Tabbaa (2013) report on similar investigations, namely the development of low-pH cements for immobilisation of intermediate-level radioactive waste (ILLW). They state that the low resistance to hyperalkaline pore waters compromises the suitability of Portland Cement (PC) as immobilisation cement. They also state that the manufacture of PC is responsible for significant CO_2 greenhouse gas emissions. The authors characterise the use of low-pH cements for radioactive waste immobilisation as more environmentally responsible and also report that reactive magnesium oxide and magnesium phosphate cements have important chemical stability advantages, reduced permeability and higher density relative to PC cement.

Drace & Ojovan (2011) discuss cementitious materials for radioactive waste management, in the context of an IAEA Coordinated Research Project (CRP) to investigate the behaviour and performance of cementitious materials used in radioactive waste management systems. The use of cement materials in waste packages, wasteforms and backfills are described. The following research topics receives attention: (1) cementitious materials for radioactive waste packaging, including radioactive waste immobilisation into a solid waste form, (2) emerging and alternative cementitious systems; (3) physical-chemical processes occurring during the hydration and ageing of cement matrices and their

influence on the cement matrix quality and durability; (4) methods of production of cementitious materials for immobilisation into wasteform, backfills and containers; (5) conditions envisaged in the disposal environment for packages (physical and chemical conditions, temperature variations, groundwater, radiation fields); (6) testing and non-destructive monitoring techniques for quality assurance of cementitious materials; (7) waste acceptance criteria for waste packages, waste forms and backfills; transport, long-term storage and disposal requirements; and finally (8) modelling or simulation of long-term behaviours of cementations materials used for packaging, waste immobilisation and backfilling, especially in the post-closure phase. (Drace *et al.*, 2012) also discusses the above issues.

Evans (2008) reviews the binding mechanisms of radionuclides to cement. Radionuclide solubility is one of the factors that can determine the "source term" for potential migration to the far-field (i.e. more than e.g. 5 m away from the waste package). He concludes that the mechanisms of immobilisation of radionuclides in cements need close study in order to quantify the nature of the binding. Evans' review summarises the main sorption mechanisms and then details immobilisation mechanisms for many elements. The author reports that Cs is bound best when the calcium oxide (CaO) content in the cement is high, and the Al_2O_3 and SiO_2 content is low. Also reported is that the use of zeolite as a blending material in cement has been found to cause an 80-fold reduction in the leaching of Cs from the cement. This is an important finding, i.e. the addition of not only vermiculite, but also zeolite to the cementation "recipe" deserved serious investigation by all producers of fission-based medical radionuclides, because the ILLW waste stream will invariably be dominated by ^{137}Cs within as little as 2 years after waste production — see e.g. Figure 5-1 (page 163) as well as Figure 5-2 (page 164).

Geddes *et al.* (2018) review the use of metakaolin-based geopolymers for nuclear waste encapsulation. The UK nuclear industry has a significant and challenging stockpile of nuclear wastes, and geopolymers produced from activation of the calcined clay metakaolin offer a valuable alternative to Portland cement-based systems. The characteristics of different formulations of metakaolin-based geopolymers, reacted with sodium and potassium silicate, are therefore of interest. As preliminary steps, the compressive strength and rheology of some metakaolin geopolymer grouts have been studied. The study only investigated the mechanical properties of geopolymer cements, and not any of the key performance indicators (i.e. metrics of merit) such as immobilisation parameters, and therefore has no immediate practical implications for the present study.

Glasser (2011) discusses the application of inorganic cements to the conditioning and immobilisation of radioactive wastes. The treatment is analogous to (Glasser, 2010) which had been summarised above.

Hussain & Al-Othmany (2013) focus on the treatment and conditioning of spent ion-exchange resins from nuclear power plants. Like the ILLW from ^{99}Mo production, this is a wet/moist waste that is cemented and placed inside stainless-steel drums embedded inside large, high-density concrete drums. The authors note that cementation serves to immobilise the waste while the thick high-density concrete drum provides shielding, i.e. it reduces dose rates to enable drums to be shipped to the disposal site within an acceptable short period of time after having been filled with cemented radioactive waste.

Predisposal management of radioactive waste, as the term is used by IAEA publications, covers all the steps in the management of radioactive waste from generation until its disposal, including pre-treatment, treatment and conditioning processing, storage and transport (IAEA, 2009b). The safety objective is the protection of human health, and the environment. This IAEA report sets standards and guidelines for predisposal management of radioactive waste.

There is a need for international standardisation regarding wasteforms, waste packages and waste management. An IAEA report (IAEA, 2006) deals with the development of standardised specifications for radioactive waste packages. An important task for waste management organisations is to translate general waste acceptance requirements into detailed waste package specifications. The IAEA report states that waste package specifications should be individually prepared and implemented for each type of radioactive waste package produced, considering both waste form and waste container, and should reflect specific characteristics of the waste package. Such specifications allow simpler and more accessible control and verification methods to be applied directly by the waste generators and disposal facility operators. A waste package is designed as an engineered component for ensuring the safe management of radioactive waste. Converting waste acceptance requirements into waste package specifications is, therefore, an important procedure. For near-surface disposal, the IAEA specifies that wet, moist and liquid wastes have to be conditioned by e.g. cementation in order to immobilise the radionuclides. This conditioning (i.e. solidification and immobilisation) is normally to be carried out by the waste producer, before transportation to the repository site for final disposal.

(IAEA, 2014b) is an IAEA Safety Guide for near-surface disposal of packages of radioactive waste. This Safety Guide states that near-surface disposal (NSD) is primarily suitable for waste containing mainly short-lived radionuclides (radionuclides with half-lives of less than approximately 30 years are

considered to be short-lived) and only low concentrations of long-lived radionuclides. The radionuclide ^{137}Cs, which dominates ILLW[$(n,f)^{99}$Mo], has a half-life marginally longer than 30 years, which means that such waste qualifies for near-surface disposal. Near-surface disposal refers to the emplacement of solid, or solidified, radioactive waste containing predominantly short-lived radionuclides in a disposal facility located at or near the land surface. The depth chosen for disposal, depends on the nature of the waste. An important feature of near-surface disposal is the possible need to maintain institutional control over the site for a period following closure, founded on the need to prevent disturbance of the facility and its contents unauthorised human intrusion. The concentration, immobilisation and containment of the waste and its isolation from the biosphere, is the universally accepted waste management strategy. Containment and isolation can be provided through a series of complementary barriers, e.g. the waste form itself (e.g. a cemented matrix), durable waste containers, the placement of cation absorbing bentonite clay and zeolite in direct contact with the containers before burial, and the selection of a very arid disposal site serve to prevent the release of radionuclides from the wasteform and to attenuate the migration of radioactive contaminants from the (underground) disposal location to the accessible environment. The concept of near-surface disposal covers disposal in engineered trenches or vaults, at varying depths — from a few metres to a few tens of metres — in facilities employing a variety of engineered barriers. The design lifetime of the physical and chemical containment must be long enough to last until radioactive decay has significantly reduced the hazard posed by the radioactive waste. Waste containment relates to the prevention and attenuation of the migration of radionuclides. Containment is achieved by physical barriers such as a stainless-steel drum embedded inside a concrete drum; these barriers must have low permeability to water. Chemical containment relates primarily to waterborne migration and refers to the retardation of the migration of radionuclides by the reduction of their solubility and/or by the sorption of radionuclides onto a solid, immobile substrate material. Chemical containment is typically provided by the cementation of the waste. At repositories, the prevention and limitation of the ingress of water, coupled with chemical containment inside a durable wasteform, are key determinants of the safety of near-surface disposal of radioactive waste.

(IAEA, 2019) focuses on strategy and methodology for radioactive waste characterisation. Proper control of chemical and radiochemical parameters of radioactive waste within the entire waste management life cycle, and the careful testing of the quality of final wasteforms and waste packages, are principal components of a successful waste management strategy. It is the task of the waste producer to characterise the waste before disposal will be considered. In other words, waste characterisation forms part of waste acceptance requirements for disposal — radioactive waste that

has not been characterised, may not be disposed. Characterisation is the assessment of key waste parameters, e.g. the activity of radionuclides per drum, the 2-column nuclide-activity matrix $[N_i; A_i(t)]$ in each drum, the chemical nature of the drum content, as well as the physical/mechanical properties of the wasteform. A description of the originating process that produced the waste, also forms part of the overall characterisation "data package" for the radioactive waste.

(IAEA, 2017) deals with the selection of technical solutions for the management of radioactive waste. Ionascu *et al.* (2013) focus on the chemical composition of radioactive waste and the mechanical performance of a cemented waste matrix. Jantzen *et al.* (2013) present an overview of radioactive waste conditioning, immobilisation, and encapsulation processes and technologies. Kelley (2017) presents an overview of proven technologies for the solidification of complex liquid radioactive waste. Kot'átková *et al.* (2017) present an overview of concrete and cement composites used for radioactive waste deposition. Laverov *et al.* (2012) review confinement matrices for low- and intermediate-level radioactive waste. Lee *et al.* (2019) review geopolymer technology for the solidification of ion-exchange resins that had absorbed radionuclides to ILW levels. Matsuyama *et al.* (2017) also focus on the use of geopolymer cements for the solidification of intermediate-level radioactive waste. Milestone (2006) reports on investigations of chemical reactions in radioactive waste encapsulated inside a cement matrix and states that there is a need for a "toolbox of different cement types". Chemical reactions that occur between radioactive waste and its cement matrix used for encapsulation, can compromise the integrity of the resulting wasteform. Some of the interactions that can occur within Portland cement-based systems, are discussed. The author states that, to achieve successful encapsulation of the wide range of radioactive waste types that make up the legacy wastes, i.e. historic wastes, present in the UK, a recipe toolbox or formulary of different cement systems with differing chemistries is needed, so that waste types can be matched with the most appropriate and compatible cementation systems.

Lersow & Waggitt (2019) present an overview of the disposal of all forms of radioactive waste using "geotechnical environmental structures" that will ensure long-term stable and safe storage.

In (Ojovan, 2011; Ojovan & Hyatt, 2020; Ojovan *et al.*, 2019) there are extensive treatments of materials and technologies for the conditioning and immobilisation of radioactive waste.

Ouda (2021) presents an investigation on the gamma-ray attenuation characteristics of alkali-activated concrete waste-based[15] geopolymer modified with fly-ash. This study is purely empirical and phenomenological in nature and there is no insight into the physics of photon shielding, as is presented in § 2.2 (page 55) in the present work. Bulk density, compressive strength, photon attenuation coefficients as well photon transmission factors (half-value layer thickness (HVL); tenth-value layer thickness (TVL) and mean free path length (MFP) of ionising photons in studied concrete samples were determined at different hydration times. The gamma attenuation coefficients of the blend were experimentally conducted with NaI (Tl) scintillation detector utilising ^{137}Cs and ^{60}Co sources. The author mentions that the inclusion of 15% pozzocrete fly-ash (PFA) in the geopolymer system, alkali-activated with 10% NaOH resulted in the enhancement of both physical and mechanical properties and has also improved the attenuation of gamma rays. This observation by Ouda (2021) is simple to explain, using the theory presented in § 2.2 (page 55): the fly-ash introduces higher-Z chemical elements into the concrete and may also increase its bulk density, which are factors that will improve the attenuation of ionising photons.

Rahman *et al.* (2014) is a monograph dealing with the use of cementitious materials for nuclear waste immobilisation. Sharp *et al.* (2003) review cementitious systems for the encapsulation of intermediate-level radioactive waste. Shi & Fernández-Jiménez (2006) review the stabilisation and solidification of hazardous and radioactive wastes with alkali-activated cements.

Škvára *et al.* (2008) present a historical overview of the development of geopolymer concrete. Sukhanov (2013) reviews methods and production of cementation materials for the immobilisation of specific liquid radioactive waste streams from radiochemical plants, into durable solid waste forms. Swift *et al.* (2013) discuss the use of phosphate modified calcium aluminate cement for the encapsulation and immobilisation of radioactive waste, into durable waste forms. Tan *et al.* (2019) present the comparative performance figures of cement and metakaolin-based geopolymer, for the immobilisation of strontium. The radionuclide ^{90}Sr is an abundant fission product, so that it is vital to verify that immobilisation matrices perform well in the immobilisation of the Sr^{2+} cation. Chemically, strontium mimics the nutrient calcium, so that ^{90}Sr acts as a bone-seeking radionuclide when ingested or inhaled. Its half-life is close to 29 years and in a ILLW$[(n,f)^{99}\text{Mo}]$ the presence of ^{90}Sr requires several centuries of immobilisation — see Table 3-3 on page 97.

[15] That is, the geopolymer cement contains industry waste products such as milled slags and fly-ash.

Xuequan *et al.* (1991) present an overview of radioactive waste forms based on cementation and immobilisation in alkali-activated slag cement. Zosin *et al.* (1998) present geopolymer materials based on magnesia-iron slags for the conditioning and storage of radioactive wastes. Zhou *et al.* (2006) propose a calcium sulfo-aluminate cement system as an alternative to Portland cement for the encapsulation of radioactive and other toxic waste. Yu *et al.* (2019) present the synthesis and characterisation of Mn-slag based geopolymer (MSG) for the immobilisation of cobalt. The researchers report a satisfactory degree of immobilisation of cobalt, especially when in the oxidised Co^{2+} state. A practical application of this paper to radioactive waste immobilisation would be the in-matrix retention of the radionuclide ^{60}Co — a neutron activation product that can be prevalent in specific radioactive waste streams.

Conclusion

Cementation is an established technology for the immobilisation of radioactive waste, especially moist/wet and liquid radioactive waste, into a stable and durable wasteform. The admixture of vermiculite and zeolite into the cementation "recipe" can improve the sorptive quality of the cement matrix for fission products, which are usually encountered as positively charged cations. Several articles focus on moving away from the use of Portland cement in favour of the use of geopolymer cements that use industrial waste such as slag and fly-ash. One issue is that the manufacture of Portland cement releases massive amounts of the greenhouse gas carbon dioxide, whereas the use of geopolymer cements for waste disposal would be an important step in decarbonising the radioactive waste management sub-sector within the nuclear industry.

3.5.20 Selection and design of radioactive waste repositories

The IAEA report, *Design Principles and Approaches for Radioactive Waste Repositories* (IAEA, 2020), is a valuable and comprehensive guide for the international community. The repository selection process and design process are described. The radioactive waste inventory, waste classification category and the wasteform after predisposal conditioning and packaging has to be considered. Design principles such as the requirements-driven design-basis, the multiple barrier safety concept, safe, reliable, available and maintainable technology, iteratively developed and optimised designs, maintenance of design integrity, traceable design, nuclear safeguards and security integrated design, are treated. Several examples of operational repository designs are presented, inter alia earthen trenches, near-surface engineered structures, subsurface disposal systems at intermediate depths and

disposal in deep, stable geological formations. The adaptation of existing underground facilities as well as borehole disposal are also treated.

3.5.21 Clays in radioactive waste management

Following 5 and more years of radioactive decay, cemented ILLW from fission processes is typically dominated by the radionuclide ^{137}Cs — see e.g. Figure 5-2 on page 164. Pusch (2006) presents an overview of the use of clays in radioactive waste management. Clays have high sorption coefficients for hydrated cations such as e.g. the Cs^+ cation. Packing clay in around radioactive waste packages buried in near-surface disposal trenches, will help to absorb any radioactive cations that may escape confinement after e.g. a century or more after disposal. Yıldız *et al.* (2011) focus specifically on the sorption behaviour of the Cs^+ cation in clay minerals such as bentonite and zeolite, from a radioactive waste management perspective. Sorption kinetics and thermodynamics are treated and clays such as bentonite, along with the mineral zeolite are identified as having valuable sorption properties for the Cs^+ cation. Sellin & Leupin (2013) present a review of the value of clay as an engineered barrier in radioactive waste management. From the perspective of the present investigation, it is especially the high sorptivity of clay for Cs^+ cations that is of value. The practical implication of the findings of the above researchers is that, should the natural clay content in the soil at a repository for radioactive waste disposal be low, a layer of additional clay must be placed in direct contact with the concrete waste drums when the trenches are filled.

An article by (Borai *et al.*, 2009) indicates that the placement of cation absorbing minerals such as bentonite clay and zeolite around drums of cemented radioactive waste at the time of final disposal, will assist to trap and drastically slow down the migration of cationic radionuclides of Cs, should these species escape from a disposed radioactive waste package.

3.5.22 Future impact of low and intermediate-level radioactive waste on humans and the environment

Kautsky *et al.* (2016) review the impact of low and intermediate-level radioactive waste on humans and the environment over the next one hundred thousand years. In order to assess the potential radiological risk to humans and the environment from a geological repository for radioactive waste, a safety assessment has to be performed. The release and transfer of radionuclides from the repository into the surface environment has to be quantified, and the effects in the biosphere are to be evaluated for an assessment period up to 10^5 years. Such a long projection into the future is challenging, because

assumptions about the time-dependence of surface ecosystems must be made over very long time-scales. In the safety assessment, natural variation and uncertainties in climate during the long assessment period must be captured by considering a finite set of climate cases. Where relevant, the future evolution of the landscape at the site, caused by e.g. post-glacial isostatic rebound (i.e. a slow rising of the land surface), must be modelled, and areas where modelling indicated that radionuclides could discharge into the biosphere, must be identified. Transfers of surface water and groundwater can be described with spatially distributed hydrological models. The projected release of radionuclides from the bedrock was then fed into a biosphere radionuclide transport model, simulating the transport and fate of radionuclides within and between ecosystems in the landscape. Annual radiation doses to human inhabitants were calculated by combining activity concentrations in environmental media (soil, water, air and plants) with assumptions on habits and land use of future human inhabitants. Similarly, dose rates to representative organisms of non-human biota must be calculated from activity concentrations in relevant habitats, following the ERICA methodology[16].

3.5.23 Road transport of radioactive material

The latest edition of the authoritative international regulations on the transport of radioactive material, is the IAEA's Specific Safety Requirements (SSR-6) Rev. 1: Regulations for the Safe Transport of Radioactive Material (IAEA, 2018).

In the above IAEA SSR-6, the limits on the transport index (TI) and peak surface dose rate for packages of radioactive material, are specified as follows (IAEA, 2018: 63):

> "…the TI of any package or overpack shall not exceed 10…"
>
> "…the maximum dose rate at any point on the external surface of a package or overpack shall not exceed 2 mSv/h."

The Transport Index (TI) of a package of radioactive material is the numerical value of the peak dose rate at a distance of 1 m from its external surface, expressed in the (now obsolete, non-SI) units mrem/h (milli-rem per hour). In SI units, the TI is the numerical value of the latter dose rate, expressed in the

[16] Comment by study supervisor TJvR: The ERICA assessment tool is described in **http://erica-tool.com/erica/**. It is a software system that has a structure based upon the tiered ERICA integrated approach to assessing the radiological risk to terrestrial, freshwater and marine biota. The ERICA Tool guides the user through the assessment process, recording information and decisions and allowing the necessary calculations to be performed to estimate risks to selected animals and plants. ERICA has simple embedded transport models; the transport models are taken from (IAEA, 2001).

SI units mSv/h, multiplied by 100 or, equivalently, this dose rate expressed in the SI units μSv/h, divided by 10.

Applied to the case of concrete drums containing cemented intermediate-level liquid radioactive waste, the above means that drums will become eligible for road transport once both the following requirements are met: (1) the peak contact dose-rate (CDR) on its external surface has to drop to below a value below 2 mSv/h, and (2) the Transport Index (TI) of the package has to be below 10. In SI units, this acceptance criterion on the TI means that the peak dose-rate at a distance of 1 m from the external surface of the drum, may not exceed 0.1 mSv/h.

The maximum acceptable TI value on a package that may be transported by road, is in the order of 1000 times higher than the natural background dose rate (NBDR). The maximum allowed contact dose-rate (CDR) on the surface of a package that qualifies as transportable by road, is close to 20,000 times higher than the NBDR.

3.5.24 Gap analysis

The literature survey points to the following gaps, which are marked by the symbols G_i.

G_1 In the literature review on concrete shielding, a specific gap came to light. Several studies never formulate the fundamental physics principles that determine the effective attenuation of ionising photons. This gap can be called the "lack of a clear theoretical understanding and formulation of the fundamental principles for the optimisation of shielding against ionising photons". In the present work, this gap was addressed in § 2.2 (page 55). This gap is formulated on page 153 as research objective RO1.

G_2 There is a lack of published studies that compare the radiation shielding performance of different concrete types, as shielding material for a range of generic sources of ionising photons. This gap has been addressed, at a theoretical level, in § 2.2 (starting on page 55) as well as in § 2.4 (starting on page 73). This gap is cast into the form of a series of research objectives (page 153) and is addressed in Chapter 5, which commences on page 156.

G_3 There is a lack of published studies that compare the radiation shielding properties of different concrete types, for cemented intermediate-level liquid (radioactive) waste (ILLW) radioactive waste from an $(n, f)^{99}$Mo production process. This gap will be addressed in, mainly, Chapter 5, which commences on page 156.

The 3 major gaps that have been identified and formulated, will be addressed in this study. Their integration into the research plan can be seen in the formulation of the specific list of research objectives in § 4.12, which begins on page 151.

3.6 Road transport and disposal of concrete Radioactive waste drums

Figure 39 shows 6 hematite concrete drums containing ILW, being transported to a radioactive waste disposal site. Note that a limited number of drums are transported per truck, that the drums with the lowest surface dose-rates are located closest to the truck driver, and that a distance of more than 3 m is deliberately maintained between the front drum and the driver of the vehicle.



Figure 39: Large concrete drums containing cemented liquid radioactive waste, being transported to a radioactive waste disposal site; the reddish hue of the drums is indicative of hematite concrete, which typically contains between 45 % and 55 % Fe

Figure 40 shows how concrete drums containing cemented radioactive waste, are disposed of in a trench at the disposal site.



Figure 40: A trench with concrete drums filled with low-level radioactive waste (LLW); the light grey colour of the drums indicate that the drum material is ordinary concrete

The required depth of disposal trenches for concrete radioactive waste drums, depends on whether the waste is ILW or LLW. Trenches for drums containing ILW such as cemented ILLW are typically excavated a few metres deeper than trenches for drums filled with LLW or VLLW.

3.7 Summary and perspective

In Chapter 3, a range of radioactive waste management concepts and technologies have been reviewed. Specific gaps have been identified, based on the literature study; these gaps have been incorporated into the research objectives for this study. The purpose of Chapter 4 will be to arrive at the design-basis source term per drum present in ILLW$[(n,f)^{99}\mathrm{Mo}]$.

4. Liquid radioactive waste from chemically processed irradiated target plates

4.1 Introduction

In this chapter, we first introduce the specific research reactor used to produce $(n,f)^{99}$Mo and $(n,f)^{131}$I. The irradiation of target plates containing enriched uranium is presented next. This is followed by a presentation of the chemical processing of the irradiated target plates.

4.2 An isotope production reactor that produces ^{99}Mo as a fission product

Routine production of $(n,f)^{99}$Mo is performed at a specific isotope production reactor (which will not be named here). It is a 20 MW tank-in-pool reactor of the "Oak Ridge MTR" design and uses plate-type uranium fuel that is, nominally, 19.75 % enriched in the fissile isotope ^{235}U. Nuclear fuel material with a uranium enrichment grade close to 20% is denoted as LEU_{20}. Nuclear fuel with an enrichment grade between 5 % and 20 % is known as HALEU — High-Assay Low Enrichment Uranium. The reactor's fuel is a uranium silicide dispersion which is hot-rolled in Al metal powder, and then covered by Al cladding. Aluminium alloys can be used in research reactors where the maximum cladding temperature remains reliably below circa 110 °C and the maximum bulk temperature of the coolant water in the core is below circa 75 °C. The core is surrounded on 3 sides by Be and Al reflector elements arranged in a rectangular lattice, as shown in Figure 4-1. Neutron moderation and core cooling are provided through forced convection of demineralised light water. The average in-core neutron fluence-rate that is available in isotope production positions, is approximately $\varphi_n \approx 2.8 \times 10^{14}\ \mathrm{cm^{-2}\ s^{-1}}$ (IAEA, 2003; IAEA, 2011b).

Figure 4-1 presents a top view of the layout of the core of the specific research reactor used to produce $(n,f)^{99}$Mo.

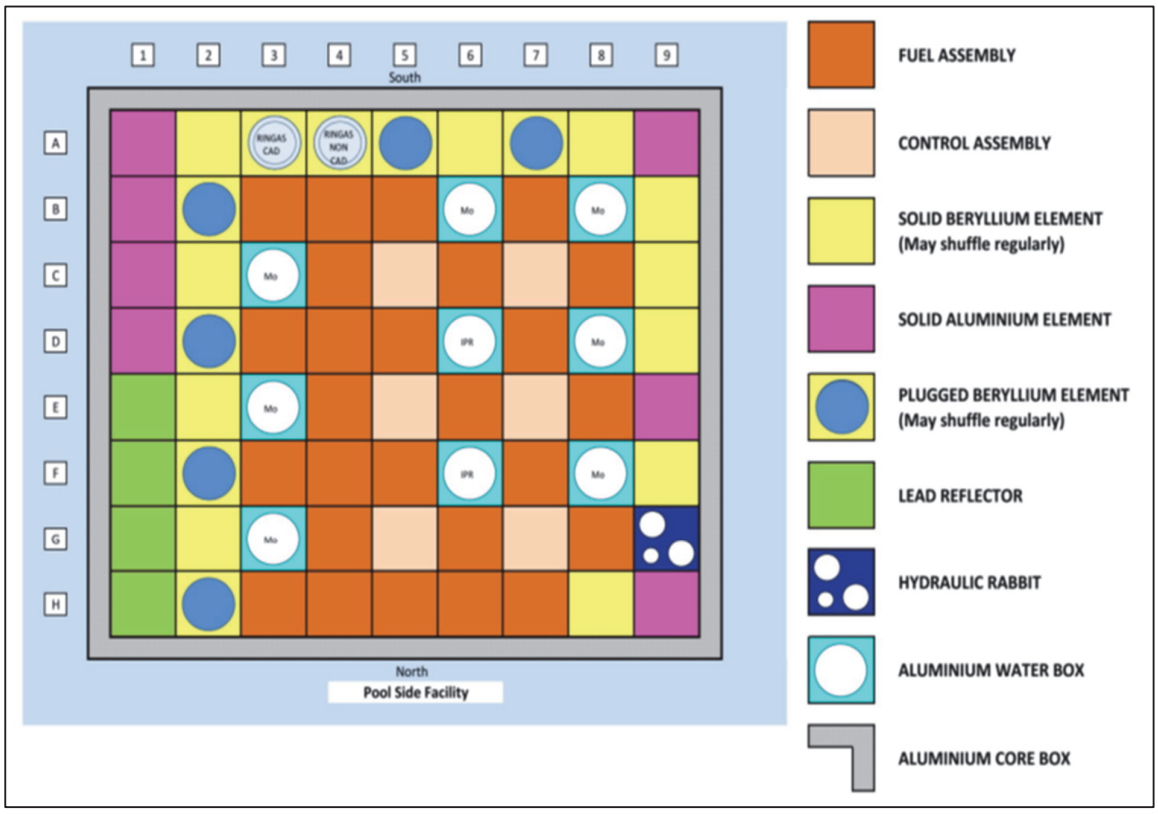


Figure 4-1: Layout of the core of the research and isotope production reactor that produces ^{99}Mo in target plates, via fission

There are 26 fuel assemblies and 6 control assemblies in the core. Each control assembly has a fuel-follower, attached to the bottom of the control assembly section by means of a coupler-piece. Beryllium reflector elements, as well as aluminium reflector elements, are used as neutron reflectors. As many as 7 in-core irradiation positions are available for the placement of target plate assemblies for the production of ^{99}Mo by fission.

A more detailed presentation of the fuel assemblies (but not the target plate assemblies[17]) used in this isotope production reactor, is given in Annexure A on page 216.

[17] Reason: protection of corporate IT.

4.3 Irradiation of target plates in the research reactor

Power-levels: Target plate assemblies

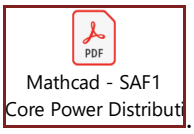
A target plate assembly contains 7 target plates and will be referred to as a TP_7 assembly. TP assemblies are licensed to be irradiated for up to 200 hours at a fission power of no more than 25 kW per individual TP, i.e. a combined fission power of $7 \times 25\ \text{kW} = 175\ \text{kW}$ per TP_7 assembly. Calculations with an MCNP6.2 calculation model of the isotope production reactor, using the following FMESH tally to calculate fission power[18],

```
fc944 Fission energy released in the FAs, CA_FFs and TPs
fmesh944:n geom   = xyz
           type   = flux
           factor = 1.5666E18
           origin = -19.275  -28.35  -56.0
           imesh  = -11.565  -03.855  +03.855  +11.565  +19.275  +26.985
           jmesh  = -20.250  -12.150  -04.050  +04.050  +12.150  +20.250  +28.350
           kmesh  = +29.685
           out    = ij
           emesh  = 6.25e-7  1.0  20.0
fm944     -1  0  -6  -8    $
```

indicates that the fission power P_{TP_7} in a TP_7 assembly will typically lie between

$$80\ \text{kW} < P_{TP_7} < 120\ \text{kW}$$

with an average TP_7 fission power that ranges between 95 kW and 105 kW, as is seen in the following analysis of the fission powers P_{TP_7} calculated by MCNP using the above FMESH tally:



In the previous paragraph, the term fission power was used to distinguish the power produced by neutron-driven fission, from additional contributions such as gamma-heating and neutron heating as well as the contribution of the radioactive decay of fission products and the activation product ^{28}Al, which is formed at high activities in research reactors, with their aluminium-based metallurgy.

It is important to note that the MCNP model of the reactor core is for a "snapshot core". While the reactor is operating, the fuel is depleted continually, and this is compensated for by slowly moving the 6 control assemblies (CAs) out of the active core height, while bringing the fuel-follower assemblies

[18] Mr Lesego Moloko from Necsa's Radiation and Reactor Theory (RRT) Section developed this MCNP tally.

(FFAs) attached to the bottom of each control assembly, into the active core height. The code MCNP executes billions of times slower than real-time so that the code can only work with a "snapshot in time" core configuration of fuel composition, target plate composition and vertical positioning of CAs and FFAs. Every such MCNP calculation runs for approximately 5 to 7 days on an 18-core processor workstation. In several years of running MCNP simulations, analysts have never encountered a TP_7 power above 130 kW. The average mass of ^{235}U which the TP supplier could load into a single target plate was in the order of 3.6 grams, and TP_7 assemblies with a fissile isotope mass-loadings in this range will typically not exceed 115 kW fission power in the specific IPR. If, in future, an alternative TP supplier can manage to consistently load an average ^{235}U mass of e.g. of 4.3 g of ^{235}U per TP, the P_{TP_7} fission power may edge closer to e.g. 135 kW. For the design-basis case, which strives to be conservative-realistic, the TP_7 assembly fission power was set at

$$P_{TP_7} = 140 \text{ kW}.$$

The reason for selecting a design-basis P_{TP_7} fission power level that is higher than the present average, is as follows. The higher the TP power, the more fission will occur and the higher the activity of fission products in the TPs will be, and therefore also in the radioactive waste. Using a conservative value for the target plate fission power will lead to conservative source terms for the intermediate-level liquid (radioactive) waste (ILLW). This will lead to the aimed-for degree of conservatism in calculated dose rates and on-site storage times, for ILLW in concrete drum waste packages.

Irradiation time: Target plate assemblies

In operational practice, radionuclide production target plates are irradiated in the research reactor for irradiation times in the range $\boxed{120 \text{ h} \leq T_{irr} \leq 196 \text{ h}}$, but the maximum allowed irradiation time,

$$T_{irr} = 200 \text{ h}$$

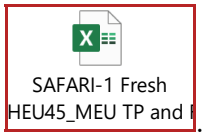
will be used as design-basis irradiation time because it will produce the highest source terms.

4.4 Elemental and isotopic composition of LEU_{20} target plates (TP_LEU_{20})

Composition 4-1 is an embedded EXCEL spreadsheet holding information about the Initial Heavy Metal (IHM) content and aluminium-alloy compositions in LEU_{20} target plates, as presently specified to the operator of the research reactor by the overseas supplier of the target plates. Every batch of TPs comes along with its materials specification sheet, and the information below represents an average over approximately 4 years of TP batches. The supplier of the TPs and associated material

specifications will remain anonymous, and original documentation related to material composition cannot be reproduced here. The spreadsheet is embedded below.

Composition 4-1: Spreadsheet with information about the Initial /Heavy Metal (IHM) content and aluminium-alloy compositions in LEU_{20} target plates



In the spreadsheet on Composition 4-1, the unusual term "meat" is used. This refers to the middle layer at the centre of an individual TP or fuel plate. The "meat" layer contains a U-Al alloy dispersed in an Al matrix using powder metallurgy and hot-rolling. The meat section is covered by cladding, which used an Al-alloy with circa 2.8 % magnesium, for better performance in contact with water. The Al-alloy in the meat is essentially pure Al along with unavoidable trace elements. The Al-alloy of the cladding is an Al-Mg alloy, i.e. a so-called 5-series Al-alloy; these alloys have outstanding underwater performance.

4.5 LEU_{20} target plates: Uranium vector and mass-loading

The uranium mass fraction vector (MFV) of fresh LEU_{20} TPs was taken as

$$MFV_{TP_{LEU20}} = \begin{pmatrix} MF(^{234}\mathrm{U}) \\ MF(^{235}\mathrm{U}) \\ MF(^{236}\mathrm{U}) \\ MF(^{238}\mathrm{U}) \end{pmatrix} = \begin{pmatrix} 0.194 \\ 19.75 \\ 0.216 \\ 79.84 \end{pmatrix} \%$$

based on TP specifications and supplier records (Van Rooyen, 2018b).

The normal, average uranium (i.e. IHM) mass-loading in a LEU_{20} TP_7 assembly is

$$M\left(IHM_{TP7_{LEU20}}\right) = 130.25 \text{ g}$$

also based on supplier records (Van Rooyen, 2018b). This amounts to the following nominal, average IHM isotopic vector, i.e. mass vector (MV) of uranium isotopes present per TP7_LEU_{20} assembly:

$$MV_{TP7_{LEU20}} = \begin{pmatrix} M(^{234}\mathrm{U}) \\ M(^{235}\mathrm{U}) \\ M(^{236}\mathrm{U}) \\ M(^{238}\mathrm{U}) \end{pmatrix} = \begin{pmatrix} 0.2527 \\ 25.724 \\ 0.2813 \\ 103.991 \end{pmatrix} \mathrm{g}.$$

The above mass vector was used in generating the material composition data for SCALE calculation models — refer to Annexure B on page 222.

4.6 Burnup of the IHM in the target plates

Under the above design-basis irradiation conditions, namely a fission power of 140 kW per TP_7 assembly and an irradiation time of 200 h, the burnup of initial ^{235}U mass in the design-basis LEU_{20} target plates, calculates to approximately 6 % using a SCALE 6.2.4. ORIGEN calculation model. This ORIGEN calculation model uses F33 1-group burnup-dependent cross-section sets generated during a preparatory step, using the SCALE 6.2.4 transport-depletion system T6-DEPL. The design-basis TP_7 assembly's energy production via fission amounts to

$$\begin{aligned} E_{TP_7} &= 140\ \mathrm{kW} \times 200\ \mathrm{h} \\ &= 1.17\ \mathrm{MWD}. \end{aligned}$$

With an average of 130.25 g of total IHM present in one TP_7 assembly, of which 25.724 g is ^{235}U, the burnup calculates to

$$BU_{TP} = 9.0\ \frac{\mathrm{GWD}}{\mathrm{tonne_IHM}}.$$

Expressed in terms of the Initial Fissile Heavy Metal (IFHM) mass of only the fissile isotope ^{235}U, the burnup calculates to

$$BU_{TP} = 45.4\ \frac{\mathrm{GWD}}{\mathrm{tonne_IFHM}}.$$

The design-basis BURN power of a TP_7 assembly is 140 kW per 130.25 g IHM, which calculates to

$$\begin{aligned} P_{BURN} &= \frac{140\ \mathrm{kW}}{130.25\ \mathrm{g}} \\ &= 1075\,\frac{\mathrm{MW}}{\mathrm{tonne}}. \end{aligned} \tag{4-1}$$

The SCALE code ORIGEN reads the BURN power in the unit MW/tonne, i.e. the result in Eq. (4-1) serves as input for one of ORIGEN's BURNDATA input parameters.

4.7 Nuclear fission

4.7.1 The energetic driving force behind nuclear fission: Binding energy per nucleon

The binding energy per nucleon is lower in heavy nuclei such as the fissile and fissionable isotopes of e.g. thorium, uranium and plutonium, compared to nuclei such as isotopes of e.g. molybdenum, cæsium and iodine, which are situated closer to the peak of the curve of $BE(A)$, i.e. binding energy per nucleon, shown in Figure 4-2. At the very peak of this curve, one encounters isotopes of Fe and Ni, notably ^{56}Fe.

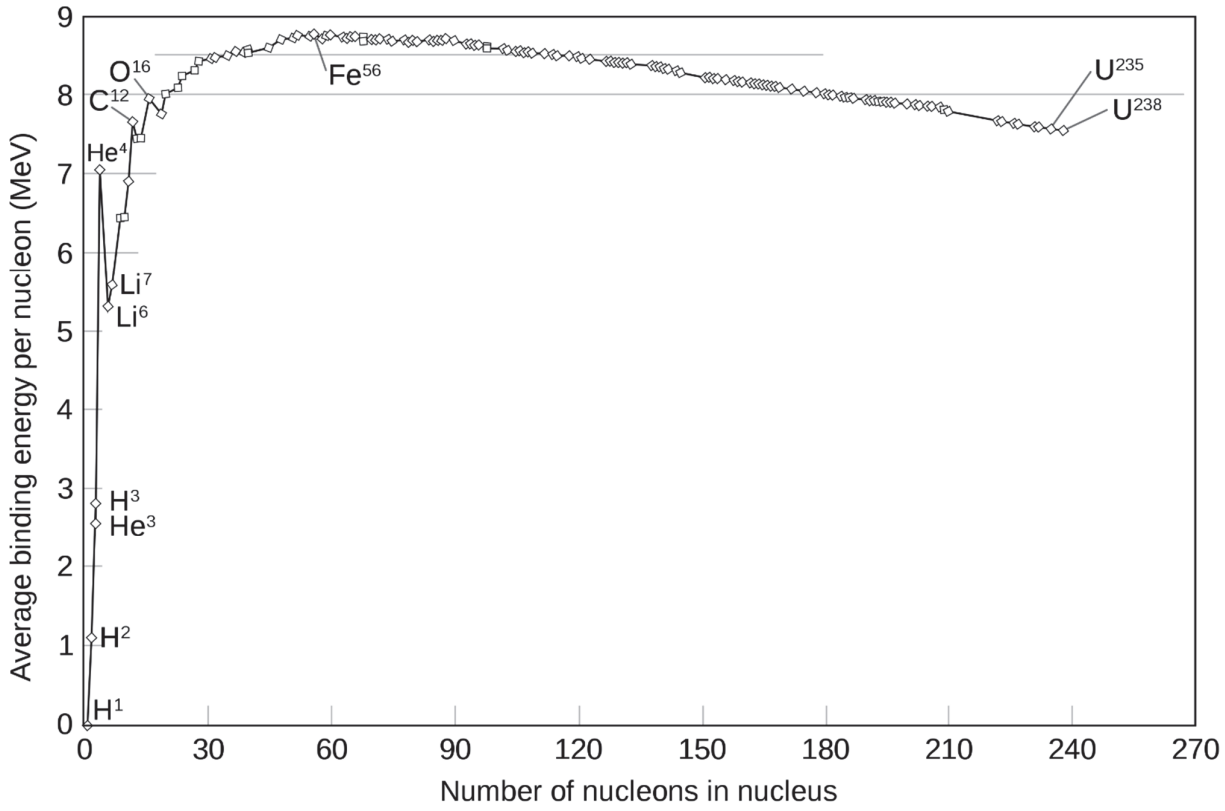


Figure 4-2: The curve of binding energy per nucleon, *BE(A)*, is seen to peak in the region of ^{56}Fe, where it is significantly higher than for heavy nuclei such as ^{235}U and ^{238}U

A significant amount of energy (more than 200 MeV) is released when nuclear fission of heavy nuclei such as ^{235}U, ^{238}U, or ^{239}Pu occurs. The reason is that the binding energy per nucleon, $BE(A)$ steadily

decreases from $A \approx 56$ (Fe) to $A \approx 238$ (uranium). If the heavy nucleus ^{235}U fissions, the fission fragments will have higher binding energies than the "oversized and overweight" fissioning nuclide, and this energy difference will be released. This energy change, ΔE, is more than 1 million times larger than the energy changes encountered in typical chemical reactions. As a result, the "burning" of uranium fuel delivers an energy density per unit mass of fuel that is more than 1 million times higher than the corresponding $\frac{\text{energy}}{\text{fuel mass}}$ ratio observed for the combustion of carbon and hydrocarbon fuels. The energetic driving force that underlies the fission of heavy nuclei, is the higher binding energies $BE(A)$ per nucleon, of isotopes in the atomic mass number domain $90 \leq A \leq 140$ of fission products, compared to $BE(A)\ \forall\ A \geq\ 230$, i.e. fissioning actinide nuclei.

4.7.2 Fission cross-sections: Fissile vs fissionable isotopes

The energy dependence of the cross-sections $\sigma_f(E)$ for the neutron-induced fission of the 2 uranium isotopes, ^{235}U and ^{238}U, are illustrated in Figure 4-3. (The cross-section data was taken from ENDF/B-8.0 (Brown *et al.*, 2018; Conlin *et al.*, 2018) via the JANIS-4.1 GUI, which can be accessed at

http://www.oecd-nea.org/janis/webstart/.

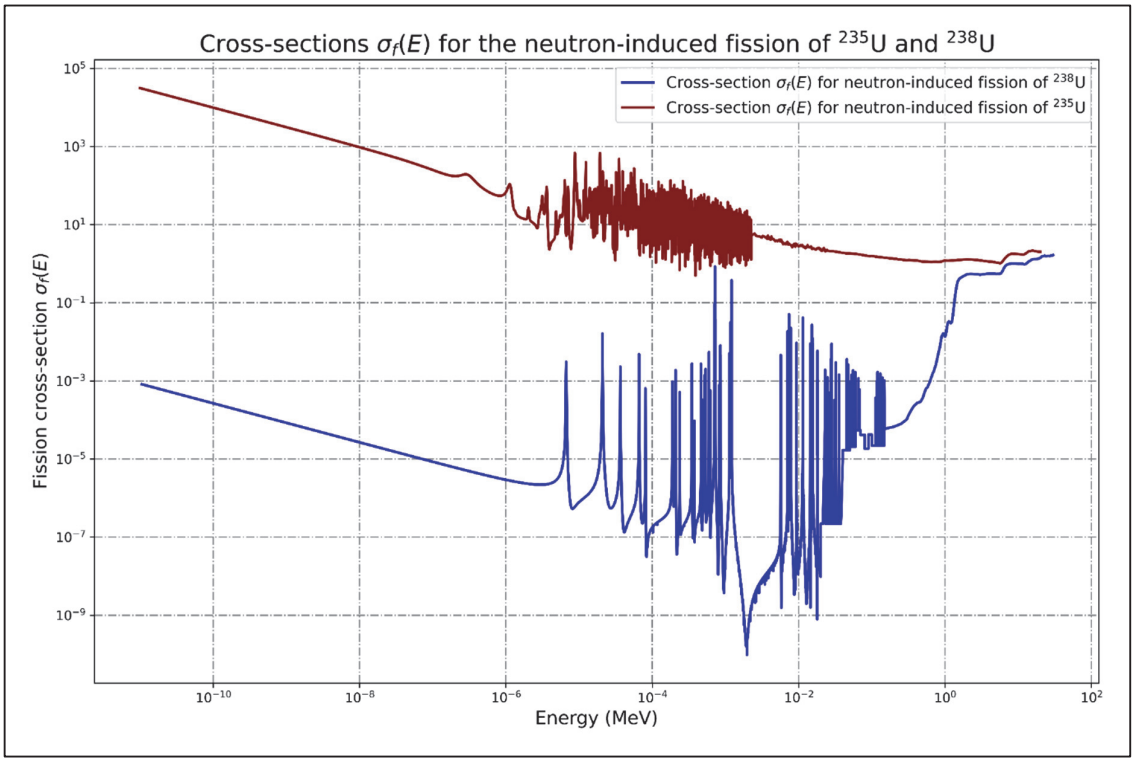


Figure 4-3: Cross-sections for the neutron-induced fission of ^{235}U and ^{238}U

From Figure 4-3 it is evident that ^{235}U is a **fissile** isotope, whereas ^{238}U is a fissionable isotope — the cross-section for the neutron-induced fission $\sigma_f(E)$ of ^{235}U is very high at thermal neutron energies, while that of ^{238}U only becomes non-negligible at approximately $E_n \geq$ 1.3 MeV.

The nuclear fission of a fissile isotope is initiated by an incident thermal neutron. In the case of the neutron-induced fission of ^{235}U, the target nucleus absorbs the incident slow neutron to form the compound nucleus, ^{236}U*, in an excited nuclear energy state (denoted by the superscripted symbol $*$). The absorbed neutron's binding energy (circa 7 MeV) as well as practically all its kinetic energy, is added to the internal excitation energy of the compound nucleus that is formed. In the case at hand, the ^{236}U* compound nucleus enters a cyclic prolate[19]-oblate shape-oscillation, and eventually overshoots the prolate (rugby-ball) shape, takes a dumbbell shape and then fissions into 2 fission fragments. The fission process is illustrated in the animation of Figure 4-4[20].

[19] A prolate (elongated) spheroid is shaped like a rugby ball; an oblate (flattened) spheroid is shaped like "flat" pumpkins.

[20] To be able to see the animation, the reader must use a post-2018 version of MS WORD.



Figure 4-4: Animation of the fission of the ^{235}U nucleus

In the animation of Figure 4-4, a thermal neutron is captured by the ^{235}U nucleus, a compound nucleus $^{236}U^{*}$ forms. The compound nucleus, formed after neutron absorption, is very unstable, with a lifetime of approximately 10^{-14} s. The "nuclear fluid" of the excited, large compound nucleus undergoes large oscillatory shape-deformations, because the repulsive Coulomb force in such a large, highly excited nucleus is very destabilising; in such nuclei, the short-ranged strong nuclear interaction "struggles" to keep the violently oscillating nucleus "in one piece". The shape-deformation oscillations are from an oblate spheroid (pumpkin shape) to a prolate spheroid (cigar) shape. If the compound nucleus is sufficiently excited, it will, during one such "oblate spheroid to prolate spheroid" oscillation, "overshoot" the prolate (cigar) shape and deform into an elongated dumbbell shape, the 2 ends of which then repel each other strongly via long-ranged Coulomb repulsion between positive charges. The attractive strong nuclear interaction, being very short-ranged, is no longer able to hold the 2 dumbbell ends together. The 2 dumbbell-shaped "blobs" scission asunder within approximately 10^{-20} seconds into 2 positively charged nuclear fragments, which repel each other with such tremendous Coulombic repulsion that many of their orbital electrons are torn off as a result of the fierce acceleration of these 2 fission fragments. Two highly positively charged *fission fragments* are thus formed. The (usually 2) fission fragments are highly excited and excessively rich in neutrons, so that neutrons will evaporate from the accelerating and accelerated fission fragments. The Coulomb barrier prevents charged particles from evaporating from the fission fragments; only neutrons can evaporate, because they are electrically neutral. The near-instantaneously released scission neutrons and evaporation neutrons are called *prompt* fission neutrons (PFNs).

The initial *fission fragments* are highly unstable and decay to a succession of *fission products.* During the scission and fragment-acceleration phases of fission, an average of around $\nu \approx 2.5$ neutrons are released for the neutron-induced fission of ^{235}U. This parameter, ν, is known as the average fission neutron yield or multiplicity. Additionally, β^--electrons and γ-photons are emitted. The nuclear fission reaction of ^{235}U is written as in equation (4-2).

$$ {}^{1}_{0}n + {}^{235}_{92}U \rightarrow ({}^{236}_{92}U)^* \rightarrow {}^{A}_{Z}X + {}^{A'}_{Z'}Y + \nu({}^{1}_{0}n) + \text{Energy} \tag{4-2} $$

where:

${}^{1}_{0}n$	=	Incident neutron, thermal
${}^{235}_{92}$U	=	Fissile target nucleus
$({}^{236}_{92}\text{U})^*$	=	Compound nucleus in excited state
${}^{A}_{Z}X + {}^{A'}_{Z'}Y$	=	Two fission fragments
$\nu({}^{1}_{0}n)$	=	Number of fission neutrons released; usually between 2 and 3

On average, thermal neutron-induced fission of ^{235}U releases 200 MeV of recoverable energy per fission event (Lamarsh & Baratta, 2017). Most of this energy is present in the high initial velocity of the fission fragments — the potential energy of the electrostatic repulsion between the positively charged fission fragments is converted to the kinetic energy of the accelerated fission fragments, which is subsequently converted to atomic vibrational energy, i.e. heat.

4.7.3 Neutron spectrum in the fissile layer on the irradiated target plates

When the fissile nucleus of ^{235}U undergoes nuclear fission, prompt fission neutrons (PFNs) are emitted with the energy spectrum shown in Figure 4-5. For prompt neutron emissions, the neutron emission spectrum $Q_{\text{PFN}}(E)$ can be quite accurately approximated by a Watt formula. For PFN emission by ^{235}U, the well-known Watt formula with coefficients, as specified in the MCNP6.2 manual (Werner, 2017),

$$ Q(E) = 0.439616 \exp\left(\frac{-E}{0.988}\right) \sinh\sqrt{2.249E} $$

is typically used. The Watt formula was derived from a neutron evaporation model (Watt, 1952).

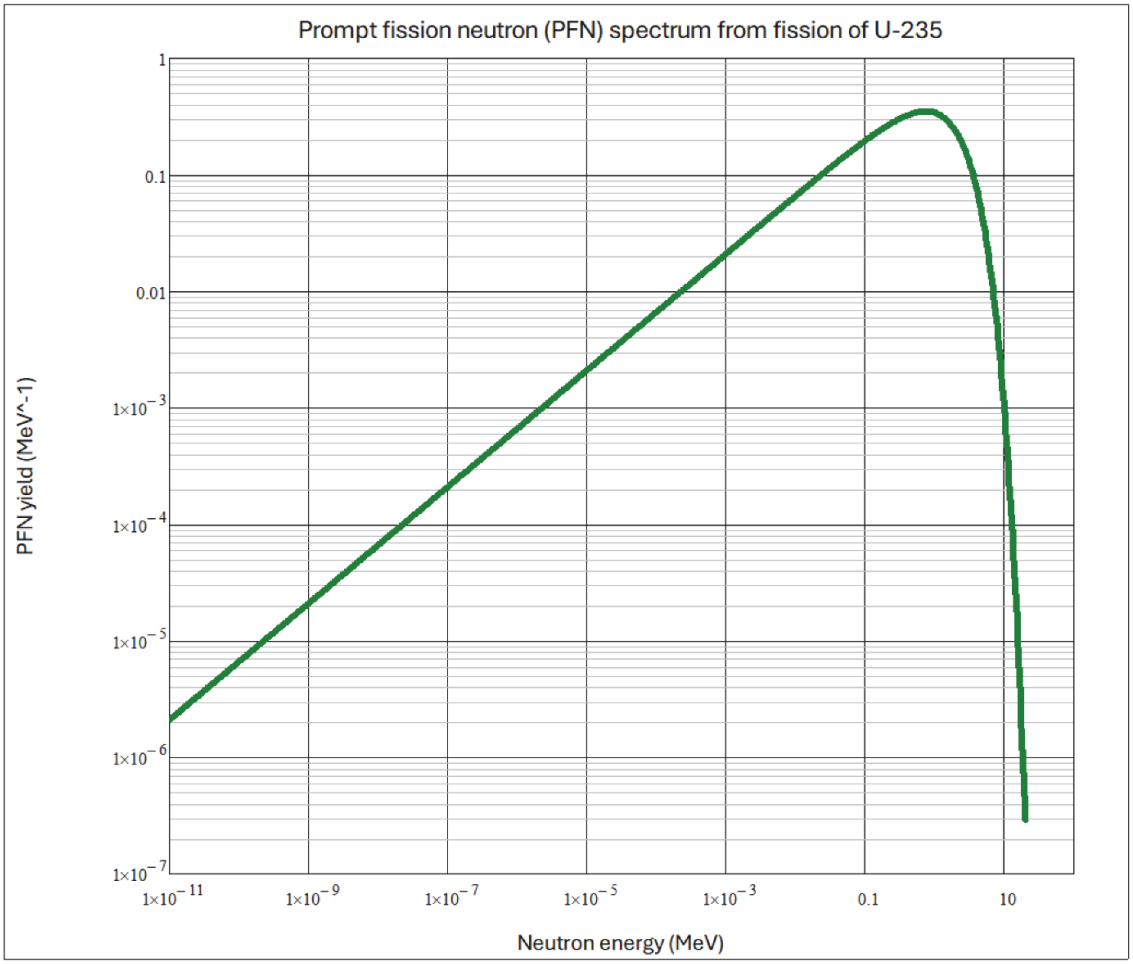


Figure 4-5: Energy spectrum of prompt fission neutrons emitted when 235U undergoes neutron-induced fission

The neutron energy spectrum inside the target plates was calculated using an MCNP6.2 calculation model using ENDF/B-8.0 cross-section data, and is shown in Figure 4-6.

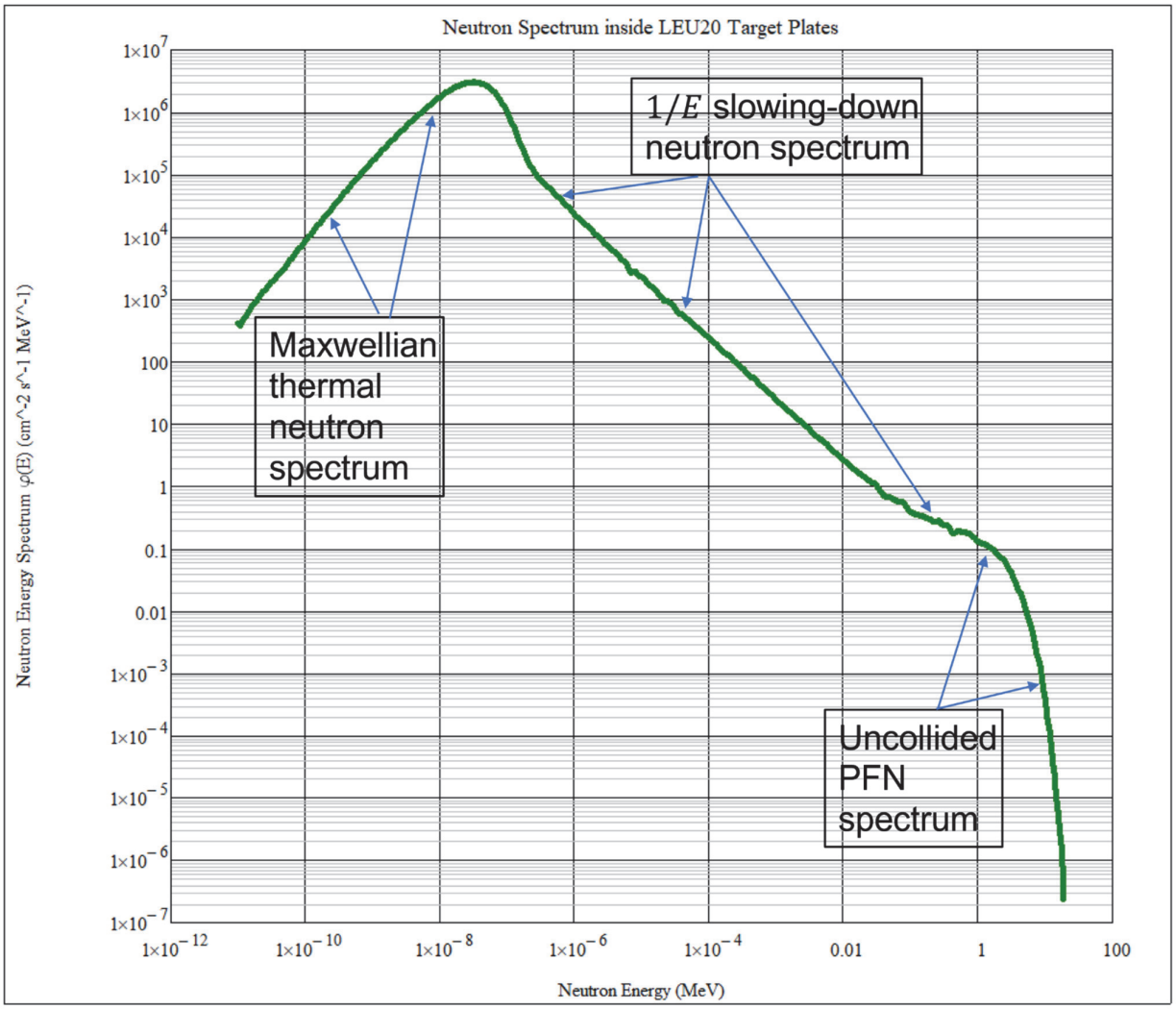


Figure 4-6: The neutron energy spectrum inside the target plates

What is observed on the RHS of Figure 4-6 is an uncollided portion of the original PFN spectrum seen in Figure 4-5. To the left of this is the characteristic slowing-down spectrum of neutrons in media such as water, where the dominant scattering isotope is ^{1}H. The slowing-down part of the spectrum has the mathematical form $\varphi_n(E) \propto 1/E$ and displays as a straight line on a log-log axial system as used in Figure 4-6. To the left of the slowing-down spectral component is the spectrum of the thermalised neutrons that have entered into thermal equilibrium with the medium they are moving in.

4.8 Fission products produced by fission

4.8.1 Fission product yield

The yield $Y_{FP}(A)$ of the fission products (FPs) for the thermal neutron-induced fission of ^{235}U, as a function of the mass number A of the fission products, is shown in Figure 4-7; this graph was produced by using the JANIS-4.0 GUI (Soppera *et al.*, 2013) to access ENDF/B-7.1 nuclear data, and porting fission yield data to plotting software.

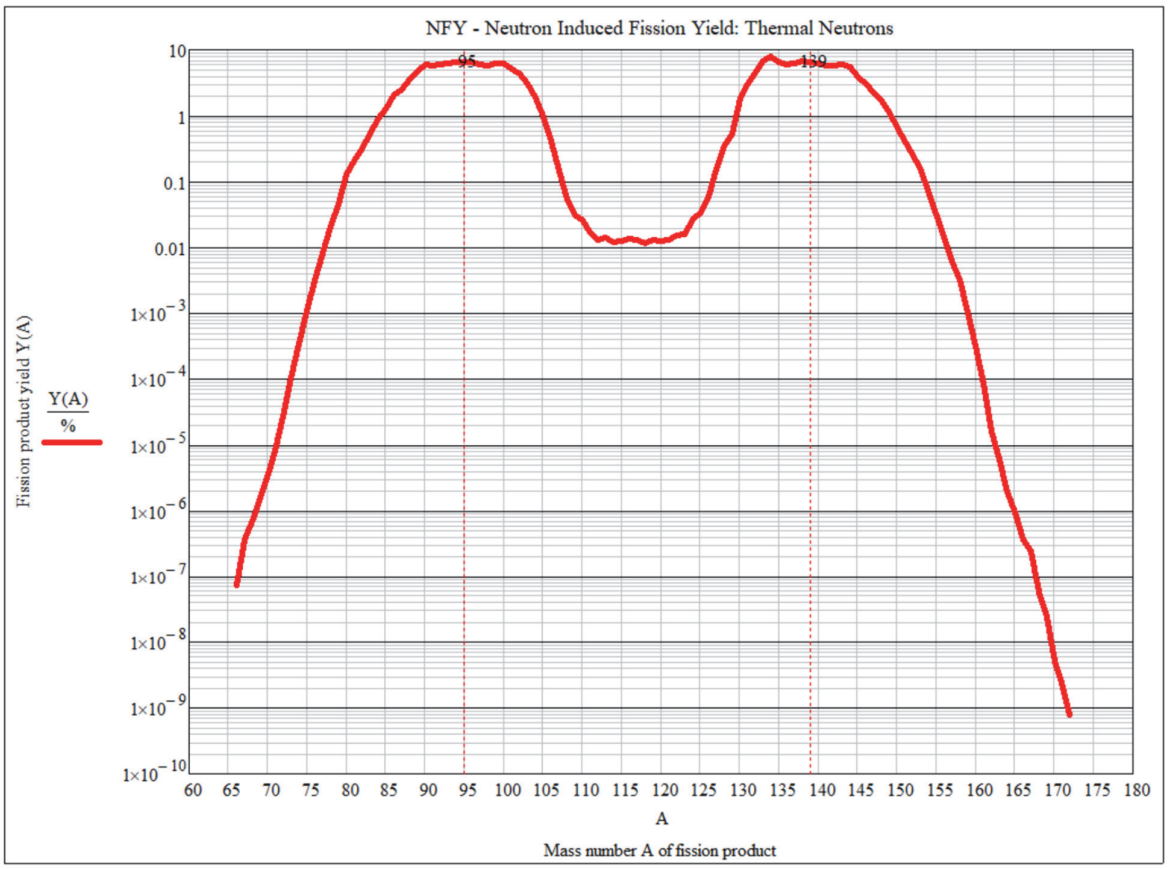


Figure 4-7: The fission product yields when the fissile isotope ^{235}U is fissioned by thermal neutrons

The fission-product yield curve $Y_{\mathrm{FP}}(A)$ seen in Figure 4-7 (and Figure 4-8) is colloquially known as the "M"-curve or the "twin-hump camel" curve, based on the 2 broad peaks or humps. The lower mass-number group of fission products have notable yields over the range are from

$$80 \leq A \leq 107,$$

whereas the heavy mass-number group has a broad peak for

$$127 \leq A \leq 155.$$

The medical radionuclide ^{99}Mo falls in the lower-energy peak of $Y_{FP}(A)$ while the medical radionuclide ^{131}I is located in the higher-energy peak of $Y_{FP}(A)$.

The twin peaks seen in Figure 4-7, which has a logarithmic scale on the vertical axis, are more accurately perceived when plotted with a linear scale for the vertical axis — see Figure 4-8.

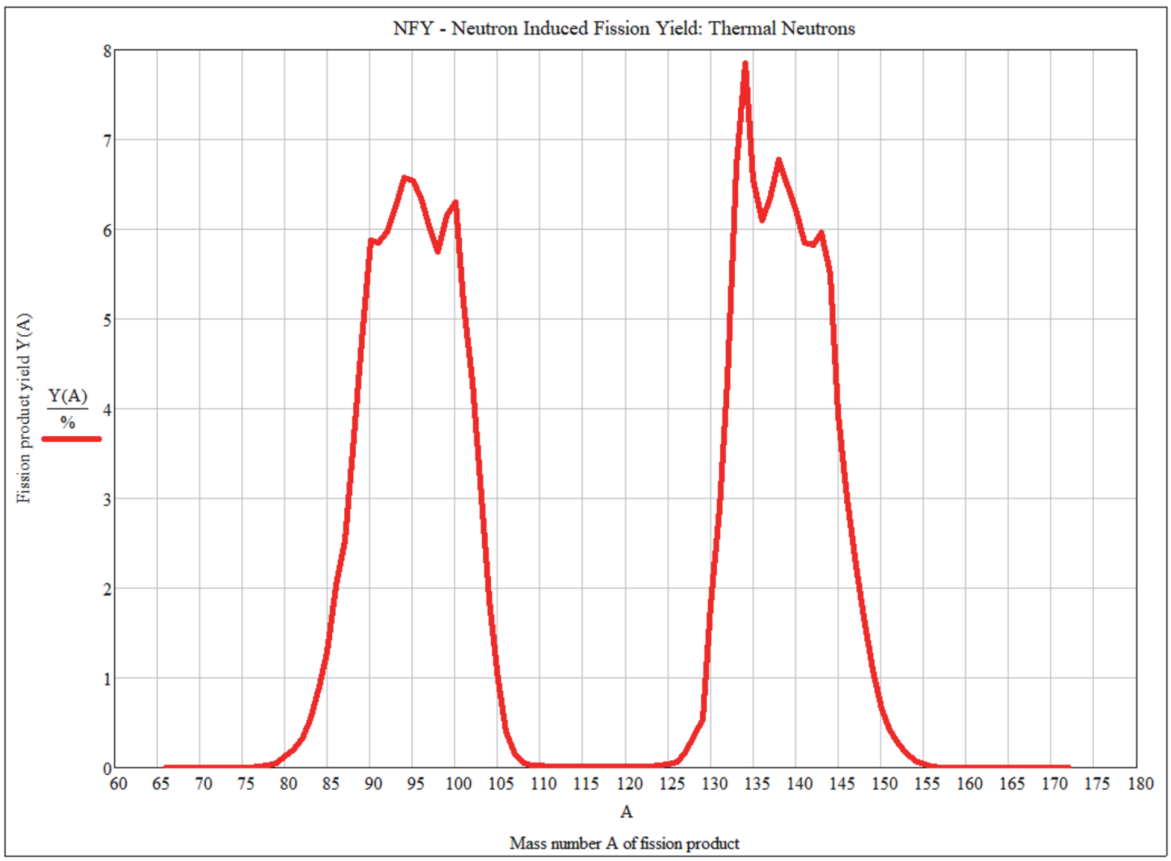


Figure 4-8: Fission-product yields $Y_{FP}(A)$ as a function of the mass number of the fission products, for thermal neutron-induced fission of ^{235}U

4.8.2 Understanding the radioactivity of fission fragments and fission products

Figure 4-9 presents a colour-coded chart of the nuclides (Soppera *et al.*, 2013).

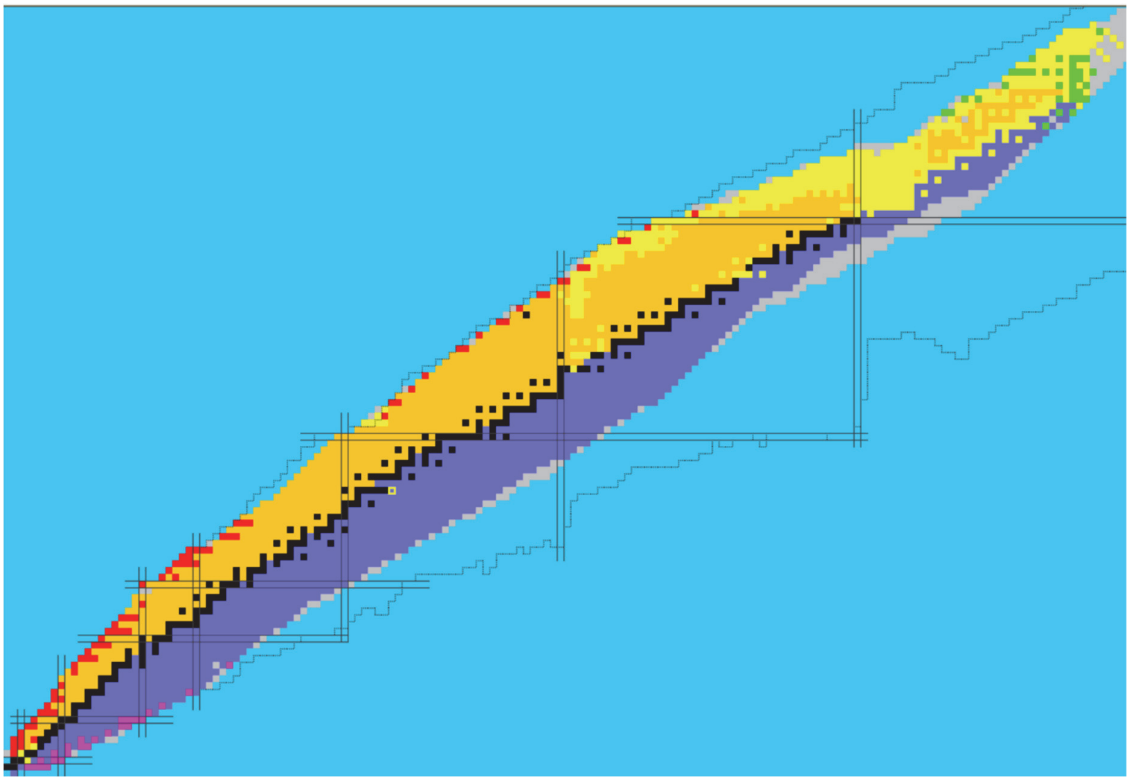


Figure 4-9: A colour-coded chart of the nuclides

Legend:

- **Proton drip-line**
- **Neutron-poor nuclei that transition via β^+ and EC**
- **α-particle emitting nuclei**
- **Stable nuclei**
- **Neutron-rich nuclei that transition via β^-**
- **Neutron drip-line**
- **Spontaneously fissioning heavy nuclei**
- **Short-lived nuclides with unknown properties**

Let $BE(Z,A)$ denote the binding energy ("BE") in a nucleus with atomic number Z and mass number A. The higher the value of $BE(Z,A)$, the more stable an isotope is bound. Conversely, the lower $\frac{1}{BE(Z,A)}$ is, the most tightly bound and stable nuclides will have the lowest $\frac{1}{BE(Z,A)}$ values. If a 3D plot of the chart of the nuclides is made, with every isotope's $\frac{1}{BE(Z,A)}$ parameter, i.e. the reciprocal of the binding energy per nucleon, plotted on the vertical z-axis, the zig-zag black line of β-stability seen in Figure 4-9 can be visualised as the "valley of β-stability"[21] , as seen in Figure 4-10. The higher the

[21] See e.g. https://en.wikipedia.org/wiki/Valley_of_stability.

binding energy per nucleon $BE(Z,A)$, the lower the 3D vertical height of the isotope in Figure 4-10. The highest $BE(Z,A)$ is observed in the immediate vicinity of the $^{56}_{26}$Fe nucleus, which lies at the vertical minimum of the valley of β-stability.

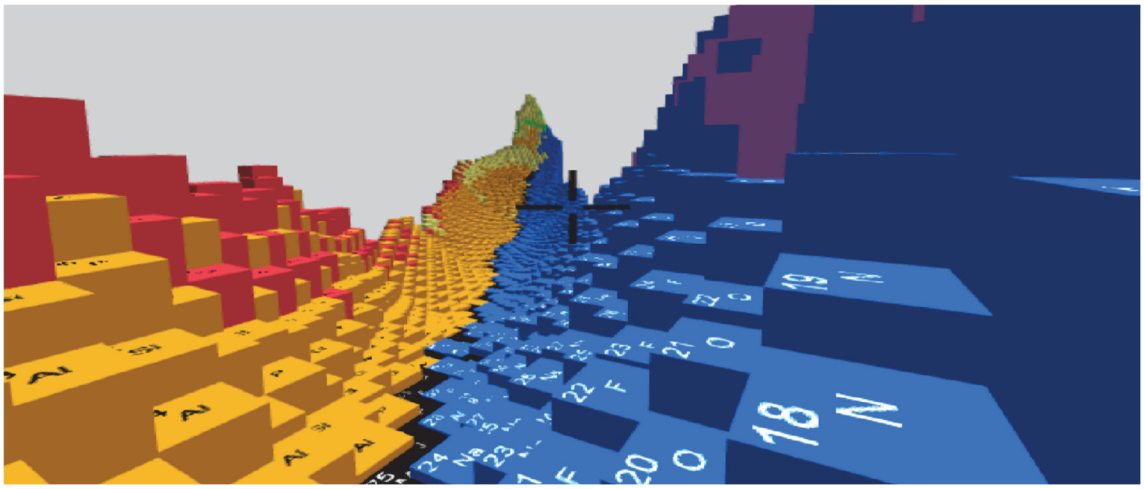


Figure 4-10: A 3D plot of the chart of the nuclides, showing the "valley of β-stability" amidst the surrounding "hills of β-instability"[22]; in the far distance, the steep peak of α-instability can be discerned

Legend:

- **Proton drip-line**
- **Neutron-poor nuclei that transition via β^+ and EC**
- **Stable nuclei**
- **Neutron-rich nuclei that transition via β^-**
- **Spontaneously fissioning heavy nuclei**
- **Neutron drip-line**
- **α-particle emitting radionuclei**

The proton drip-line is encountered when nuclei are so excessively neutron-poor, i.e. proton-rich, that they would spontaneously eject protons; the neutron drip-line is where nuclei are so excessively neutron-rich that they would spontaneously eject neutrons. Delayed fission neutrons may be emitted by fission fragments located towards the neutron drip-line.

[22] This diagram was generated using Nucleus-Win 2.1, developed at the Atomic Mass Data Centre (AMDC) in France (https://www.csnsm.in2p3.fr). Most of the activities of this organisation has since been relocated to China.

An animation[23] of the concept "valley of β-stability" is presented in Figure 4-11. As in Figure 4-10, the decreasing nuclear stability of nuclides that lie further and further from the valley of stability against β-transition, is displayed as steeply ascending mountainous slopes. (Click inside the animation to play it.)



Figure 4-11: Animation of the concept "valley of β-stability"

Concerning Figure 4-10, one can state that isotopes located on the neutron-rich side of the valley of β-stability (colour-coded blue and purple) are unstable because they have excessively high $\frac{\text{neutron}}{\text{proton}}$ ratios.

The reason for the intense radioactivity of fission products will now be developed. The ^{235}U nucleus has a $\frac{\text{neutron}}{\text{proton}}$ ratio of

$$\frac{N}{Z} = \frac{235 - 92}{92} \approx 1.55$$

whereas a stable nucleus with $A \approx 140$ (typical of high-mass fission fragments) requires a ratio $\frac{\text{neutron}}{\text{proton}}$ in the range

$$\frac{N}{Z} \approx 1.40;$$

a stable nucleus with $A \approx 90$ (typical of low-mass fission fragments) requires a ratio $\frac{\text{neutron}}{\text{proton}}$ in the range

[23] Note: This animation may not play in versions of MS Office older than Office-2019.

$$\frac{N}{Z} \approx 1.25.$$

However, when ^{235}U fissions, the fission fragments will have a $\frac{\text{neutron}}{\text{proton}}$ ratio

$$\frac{N}{Z} \geq 1.5$$

which means that fission fragments have a very large *neutron excess*. This neutron excess makes the fission fragments highly unstable, i.e. radioactive; in Figure 4-10 these fission fragments will lie high up on the blue side of the slope/cliff, very far from the valley of β-stability. Most fission fragments are extremely unstable as a result of the large neutron excess in their nuclei, and therefore transition quickly to a large ensemble of fission products, which in turn transition step by step, via β^- transitions, in their quest to reach the valley of β-stability.

4.9 Evolution of activities of radionuclides during and after target plate irradiation

When fission of a nucleus of ^{235}U takes place, fission products are formed with yields that accord with the function $Y_{FP}(A)$ reproduced in Figure 4-8 on page 141. All the fission products are excessively neutron-rich and therefore unstable against β^- transition. The latter transition leads to the disappearance of a neutron and the appearance of a proton, a β^- electron and an anti-neutrino $\overline{\nu}$ in its place.

It is necessary to use accurate codes with access to large databases of nuclear transitions, branching ratios and half-lives to follow the isotopic evolution of fissile material that had undergone fission, such as fissile target plates used to produce ^{99}Mo and ^{131}I. A suitable code for this purpose is ORIGEN in SCALE 6.2.4, which uses ENDF/B-7.1 nuclear data, which includes nuclear transition data such as branching and half-lives.

A SCALE 6.2.4 ORIGEN calculation model of the irradiation and subsequent "cooling" (i.e. isotopic evolution) of a TP_7 assembly was developed, and is embedded here; to open it, double-click the icon:



The time-dependent evolution of the activities of the medical radionuclides ^{99}Mo and ^{131}I as well as the principal long-term waste radionuclide, ^{137}Cs, was quantified using the above ORIGEN model; results are presented in Figure 4-12. The time-dependence of the activities $A(^{99}\text{Mo})$, $A(^{131}\text{I})$ and $A(^{137}\text{Cs})$ during in-core irradiation as well as after discharge, are shown.

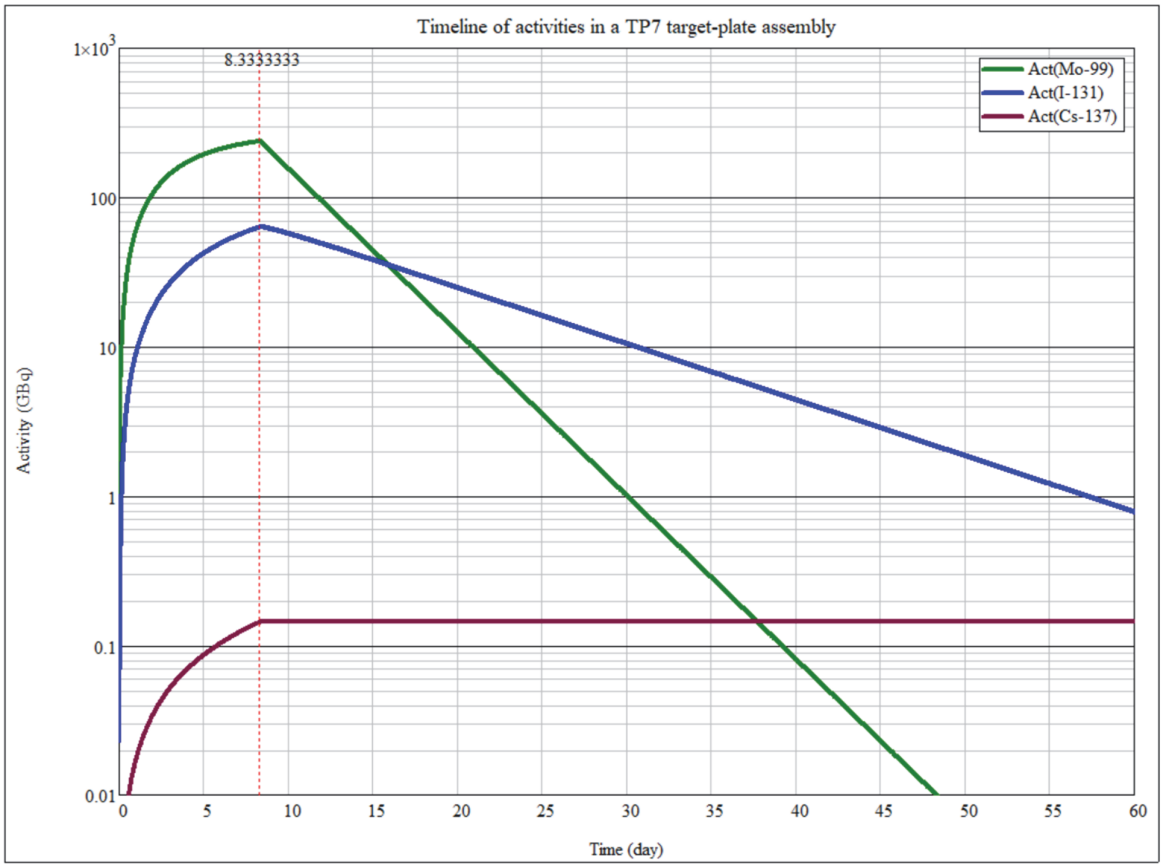


Figure 4-12: Activities of the radionuclides ^{99}Mo, ^{131}I and ^{137}Cs in the modelled process mass, as a function of time; the initial irradiation phase has a duration of 200 h, i.e. 8.333 days

The vertical dotted red line in Figure 4-12 signifies the time when the TP_7 assembly is removed, i.e. discharged, from the isotope production reactor. In the calculation model behind Figure 4-12, the target plates are not chemically processed, in order to show the unperturbed isotopic evolution. The activity of ^{99}Mo steadily grows in over the 200 h, i.e. 8.333 days of irradiation. The activity of ^{99}Mo grows in as follows in a TP_7 assembly. At $T_{irr} = 50$ h, the activity is $A(^{99}\text{Mo}) \approx 111$ TBq. At $T_{irr} = 100$ h, the activity is $A(^{99}\text{Mo}) \approx 177$ TBq. At $T_{irr} = 150$ h, the activity is $A(^{99}\text{Mo}) \approx 215$ TBq. At $T_{irr} = 200$ h, the predicted activity is $A(^{99}\text{Mo}) \approx 238$ TBq. The rate at which $A(^{99}\text{Mo})$ increases as a function of irradiation time, flattens during irradiation and is

approaching a plateau at $T_{irr} = 200$ h, i.e. it is clear why irradiation periods above the latter value carry an insignificant additional product-yield benefit and are therefore not pursued. After removal from the reactor, the target plates produce a high heating power and must therefore be allowed to cool down for between 16 and 23 hours before they are transferred from the reactor building to the hotcell complex for chemical processing (Van Rooyen & Adetula, 2018). A typical activity yield, $A(^{99}\text{Mo})$, at the end of the chemical processing step, is approximately 160 TBq per TP_7 assembly. Figure 4-12 shows that the product activity $A(^{99}\text{Mo})$ falls rapidly after irradiation, i.e. it is vital to deliver the ^{99}Mo-$^{99\text{m}}\text{Tc}$ generators to clinics within less than a few days. The activity of ^{131}I, which has a longer half-life, falls less rapidly. In contrast to the medically useful product nuclides, the activity of the principal waste nuclide in the ILLW, ^{137}Cs, survives above the unconditional clearance level for close to 6 centuries, and dictates that the waste disposal package for ILLW has to be designed to immobilise the waste for as long as 600 years.

4.10 Three waste streams from fission-based production of ^{99}Mo

4.10.1 Target plate dissolution and chemical processing

After irradiation in the reactor, the highly radioactive irradiated target plates with their valuable cargo of ^{99}Mo and ^{131}I are dissolved in a 6-molar NaOH (sodium hydroxide) alkaline solution to extract molybdenum and iodine. The isotopic purity of fission-based ^{99}Mo is nearly 100 %, i.e. it is sought-after, high specific activity (HSA) ^{99}Mo. In contrast, the isotopic purity of activation-produced and accelerator-produced ^{99}Mo is disastrously low — this explains the market's preference for fission-produced ^{99}Mo, despite the formidable radioactive waste "baggage" with which the fission-based production process burdens human civilisation.

The target plate dissolution process results in gaseous, liquid and solid radioactive waste streams.

4.10.2 Solid residue from irradiated target plates

The solid uranic residue (SR) formed by the chemical processing of irradiated target plates (ITPs) for the production of $(n,f)^{99}\text{Mo}$, is classified as HLW because a 2-litre canister of SR will typically contain between 200 g and 300 g of U-235 as well as approximately a kilogram of ^{238}U, and also approximately 1 g of plutonium isotopes (Van Rooyen, 2017, 2018c, 2019e). This SR-ITPs is stored in large concrete-walled hot-cells for a minimum of 2 years before the heating power from radioactive

transitions subsides to below the acceptance criterion for storage in vertical stainless-steel pipes in shallow boreholes, where it is placed in long-term storage (Van Rooyen, 2019e). The present study is not concerned with the characterisation or storage of this solid waste.

4.10.3 Intermediate-level liquid (radioactive) waste (ILLW)

The intermediate-level liquid radioactive waste (ILLW) from the production of $(n,f)^{99}\mathrm{Mo}$, only contains trace amounts of actinides, and the initial "cooldown storage" period is only 3 months, i.e. 6 to 7 times shorter than for the SR-ITPs, which is classified as HLW. Because the liquid radioactive waste has a high initial $\frac{\text{activity}}{\text{mass}}$ level and is dominated by $^{137}\mathrm{Cs}$, which has a relatively long half-life of $T_{½} = 30.08064$ years (Soppera *et al.*, 2013), it is classified as ILW. This waste stream is operationally dealt with as LILW-SL, because (1) the half-life of $^{137}\mathrm{Cs}$ is not much larger than 30 years and (2) the activities of longer-lived radionuclides are low and below exemption levels. After circa 2 years of on-site interim storage, the ILLW$[(n,f)^{99}\mathrm{Mo}]$ waste packages will typically meet acceptance criteria for road transport and final disposal.

4.10.4 Future economic values of radioactive waste from fission-produced ^{99}Mo

The ILLW produced from the $^{99}\mathrm{Mo}$ production process, is utterly devoid of any present or future commercial value. In contrast, the enriched uranium content of the solid residue holds significant potential future value (Van Rooyen, 2018b). It is therefore placed in long-term storage (LTS) in stainless-steel containment vessels in shallow boreholes, for possible future retrieval and recovery in support of medical radioisotope production (Van Rooyen, 2019e).

4.10.5 Gaseous radioactive waste from fission-produced ^{99}Mo

During chemical processing for the extraction of $^{99}\mathrm{Mo}$ and $^{131}\mathrm{I}$, gaseous radionuclides escape the solute; these are then retained as long as practicable in holdup tanks from which they are slowly vented through gigantic activated-charcoal beds, which adsorb a significant fraction of the noble gas xenon. The release of radioactive gases to the environment is maintained well below acceptance criteria for exempt waste (EW). Practically all these radioactive gases from $(n,f)^{99}\mathrm{Mo}$ production are nuclides of the noble gases krypton and xenon, i.e. so-called radio-kryptons and radio-xenons. It is imperative to retain as much as possible of, especially, xenon radionuclides because a sudden release of a large

activity of radio-xenons can be mistaken as a radiological signature of the detonation of a nuclear weapon (Saey, 2009; Saey *et al.*, 2013).

The SCALE 6.2.4 ORIGEN calculation model mentioned in §4.9 on page 145 was used to quantify the gaseous radioactive release per irradiated TP_7 assembly; results are summarised in Table 4-1.

Table 4-1: Inventory of radioactive noble gases in one irradiated TP_7 assembly, quantified 7 days after end-of-irradiation

Isotope	Activity at T=10 d (Bq)
Xe-133	8.04E+13
Xe-133m	6.94E+11
Xe-131m	3.66E+11
Kr-85	2.31E+10
Xe-135	1.14E+07
Xe-129m	1.66E+04
Kr-83m	8.60E+02
Xe-135m	6.06E+02
Xe-127	1.38E+01

The total mass of the above gaseous radionuclides is only 0.27 g, so that good adsorption of the noble gas xenon on large charcoal filter beds inside large stainless-steel tanks, can be achieved.

Operational releases of radioactive noble gases are not notably biologically hazardous, because they are not metabolically active, so that their absorption and retention in plants and animals are extremely low.

4.11 Production, cementation and drumming of intermediate-level liquid waste (ILLW)

In the production of $(n,f)^{99}$Mo, the main source of intermediate-level liquid (radioactive) waste (ILLW) arises from the target plate dissolver step and the filtration process. The liquid from the primary separation process between the solid and liquid streams is processed to remove molybdenum and iodine, because valuable medical isotopes of these elements are present. The resulting liquid waste is classified as Intermediate-Level Waste (ILW). It contains all the fission products and activation products that select the liquid waste stream pathway, as well as inevitable traces of α-particle emitting

actinides. These α-emitters do not constitute any acute external radiation hazard, but are important from the perspective of whether the waste will pass the waste acceptance criteria set by radioactive waste disposal institutes for near-surface trench disposal.

Target plates undergo alkaline digestion in a strong aqueous solution of NaOH (sodium hydroxide). Some chemical species precipitate while others stay in solution. Filtration separates the two waste streams. The solid uranic waste is placed in 2-litre stainless-steel 304L canisters (Van Rooyen, 2019e), while the liquid waste resulting from the dissolution of the TPs is initially accumulated in highly corrosion-resistant 40-litre SS-316L tanks. The dissolution of one TP requires just below 0.75 litres of 6-molar NaOH dissolved in water, so that the liquid effluent from the alkaline digestion of 42 TPs in total, can be readily accommodated in one 40-litre holdup tank. The design-basis number of ITPs per 40-litre holdup tank is therefore 42. From the day when the liquid waste of the last of the 42 TPs enters the 40-litre tank, 90 days are counted before the liquid waste is cemented. The entire content of one 40-litre holdup tank is agitated to ensure good mixing and then cemented and transferred into one 100-litre stainless steel drum inside one large concrete radioactive waste disposal drum. In other words, one concrete waste drum holds the cemented ILLW from 42 LEU_{20} ITPs for a design-basis irradiation time of $T_{irr} = 200$ h and a design-basis fission power of 140 kW per TP_7 assembly — this is the design-basis source term (DBST) per concrete drum.

The cementation method that is used to immobilise the liquid radioactive waste, mixes the ILLW with vermiculite and ordinary Portland cement (OPC) powder, and then pumps it into the stainless-steel drum inside the larger concrete drum, where the cementitious material hardens to an immobilising matrix. Vermiculite is a hydrated {magnesium-iron-aluminium-silicate} mineral. Vermiculite is expanded ("exfoliated") by heating the crude flaky mineral. The exfoliated or expanded granules are many times greater in volume than before heating and is lightweight, incombustible, compressible, highly moisture-absorbent, and chemically non-reactive i.e. inert. Exfoliated vermiculite particles have a high cation exchange capacity, i.e. they will adsorb and chemically immobilise radioactive cations of Cs^+ present in the liquid waste stream. The cement serves as a binder-hardener and immobiliser. Because the ILLW originates in a process that uses 6-molar NaOH, the resulting cement matrix will be high in alkalinity.

While the cement-vermiculite-ILLW mixture is still a wet slurry, it is transferred into 100-litre stainless-steel drums inside the central cavity of large concrete drums. The thick concrete wall of the drum must provide radiation shielding during handling, storage in the facility's "decay yard" and

during road transport to the national radioactive waste disposal site, where the drums will be buried in trenches.

The concrete drums have fixed dimensions. Radioactive waste disposal institutes typically charge a set price per radioactive waste drum, so that the more activity that can be concentrated inside a single drum, while still meeting the dose-rate waste acceptance criterion on the outer surface of the drum, the less the ratio $\frac{\textbf{Disposal Cost}}{\textbf{Activity}}$ will be. At present, the liquid radioactive waste from almost exactly 42 TPs consistently passes into one concrete drum, the immediate benefit of a better shielding concrete will be that the licensed operator will be able to ship the drums to the waste repository significantly sooner, i.e. the required cooling time to reach the radiological acceptance criteria for transport to the disposal facility will be shorter. This translates to a lower inventory of drums in interim on-site storage. In the future, it may become possible to concentrate the liquid radioactive waste via a volume reduction method, and to cement the waste of e.g., $10 \times 42 = 420$ ITPs into one concrete drum. When this is done, the improved shielding factor afforded by the use of high-density shielding concrete, will be particularly valuable, potentially leading to e.g. a 10-fold reduction in the number of drums required for disposal.

The large concrete drums with cemented, immobilised ILLW are sent to a national disposal site for radioactive waste.

4.12 Specific research objectives

4.12.1 Introduction

In §1.9 and §1.11 (page 48), the initial research goals/objectives were formulated in general and qualitative terms. Specific gaps in existing literature were identified during the course of the literature review, and are outlined in § 3.5.24 (page 124). The general research goals along with the identified gaps, are now turned into more detailed research objectives. The research objectives will now be numbered and formulated more specifically. Individual research objectives act as stepping-stones for achieving the overall research goal.

4.12.2 Problem statement

Fissile target plates with the composition specified in Composition 4-1 on page 81 undergo irradiation in the core of a 20 MW isotope production reactor, at a design-basis fission power of 140 kW per TP_7

assembly, for a design-basis irradiation time of 200 hours. The irradiated target plates are dissolved and the liquid waste (~35 litres) from the dissolution of 42 irradiated target plates is stored for 90 days in a holdup tank and then cemented with ordinary Portland cement powder plus exfoliated vermiculite; the cementitious slurry is transferred into stainless-steel drums inside large concrete drums. These large drums are stored on a concrete slab in on-site interim storage. The dose rates inside this "decay yard" must be within limits, to allow Radiation Protection staff to take routine dose rate readings, and to allow forklift operators to move drums as needed. The peak dose rate at the fenced-off perimeter of the decay yard, may not exceed the generically accepted public-area dose rate constraint of 1 μSv/h. The waste drums are only allowed to be shipped to the national radioactive waste disposal site when constraints on the (1) contact dose rate (CDR) and the (2) Transport Index (TI) are met. These radiological constraints are specified by the IAEA transport regulations (IAEA, 2018), and echoed in regulatory licences for the transport of radioactive materials as well as in the waste acceptance criteria (WAC) of radioactive waste disposal institutes. Packages of radioactive waste may be transported when $CDR < 2$ mSv/h. The constraint on the Transport Index (TI), namely $TI \leq 10$, implies that the peak dose rate at a distance of 1 m from the outer surface of a radioactive waste drum, must be below 0.1 mSv/h before road transport will be permitted. It is, therefore, necessary to identify affordable, strong and durable concrete types with good radiation shielding properties, for the cemented ILLW radioactive waste packages.

4.12.3 General research goals

To (1) maintain radiation levels within and on the periphery of the "decay yard" As Low As Reasonably Achievable (ALARA) and (2) be able to ship the drums as soon as possible after they had been filled with cemented ILLW, and (3) to be able to load the high-activity liquid waste from the chemical processing of 42 irradiated target plates into one drum, the shielding factor presented by the concrete drum, i.e. the drum's ability to shield the ionising photons emitted by the cemented radioactive content, should be maximised. Every drum has a fixed lateral wall thickness of 31.6 cm of concrete, and nominal concrete thicknesses of 30 cm to the top and bottom of the embedded stainless steel drum containing the cemented waste matrix. The dose rate reduction achieved with this material thickness must be maximised, by selecting an affordable and durable concrete type having good shielding performance. For practical and economic reasons, the drum material must be concrete, and four candidate concrete types will be investigated: (1) ordinary concrete, (2) magnetite concrete, (3) hematite concrete and (4) barite concrete. The research aim is to quantify the shielding factors

$SF = \frac{1}{DAF}$ which can be achieved by the use of the above 4 types of concrete for the manufacture of concrete shielding drums for the storage, transport and disposal of cemented liquid radioactive waste generated from a fission-based ^{99}Mo production process. The shielding factors for the 4 shielding concrete compositions must be quantified and the concrete types must be ranked by their shielding abilities. A shielding wall around the decay yard must be designed, if necessary. Economic considerations must also be taken into account, i.e. the recommended concrete type must be available and affordable. The concrete drums will be buried in shallow trenches, and it is necessary to establish a radiologically safe burial depth.

4.12.4 Specific research objectives

The formulation below uses the concepts dose attenuation factor (DAF) and shielding factor (SF), which were defined in § 2.2 which starts on page 55. The concept NBDR, i.e. the natural background dose rate is also used.

To reach the research goals, the following specific research objectives (designated as RO_i) will be pursued.

RO_1 Formulate the radiation attenuation physics principles for making a shielding structure with a specified, fixed thickness, as effective as possible for the attenuation of ionising photons in the energy range below circa 8 MeV[24].

RO_2 Present a literature review of the classification, clearance criteria, characterisation, immobilisation, transport and disposal of radioactive waste, with particular attention to the performance of high-density shielding concretes for concrete waste disposal drums. Identify existing gaps; address and fill these gaps.

RO_3 Develop SCALE 6.2.4 ORIGEN calculation models of target plates for $(n, f)^{99}$Mo production, undergoing irradiation in a research reactor, to quantify the radionuclide content and radiation emission characteristics of intermediate-level liquid (radioactive) waste (ILLW).

[24] Note by supervisor TJvR: At incident photon energies above circa 8 MeV, a non-trivial yield of neutrons can be produced via (γ, n) interactions, so that the optimisation of radiation shielding against incident ionising photons becomes more complex.

RO_4 Develop MCNP calculation models for a single, stand-alone concrete drum containing the design-basis source-terms at a number of discrete decay times T_{cool} that span the time period

$$90 \text{ days} \leq T_{cool} \leq 10 \text{ yr}.$$

Calculate the contact dose-rate (CDR) on the outer surface of the drum, as well as at the TI distance of 1 m from the lateral outer surface of the drum, for 5 different drum materials ("DM"):

DM_1 Drum material: Air (case NoShield).

DM_2 Drum material: Ordinary concrete (ORD-CRT).

DM_3 Drum material: Magnetite concrete (MAG-CRT).

DM_4 Drum material: Hematite concrete (HEM-CRT).

DM_5 Drum material: Barite concrete (BAR-CRT).

RO_5 Given the international dose rate constraints for the transportability of packages of radioactive material (refer to § 3.5.23 on page 123), use the computed dose rates to determine how long the drums will have to be stored in on-site interim storage in the "decay yard", for each of the drum materials DM_i listed above, before road transport to the disposal facility can commence.

RO_6 For a single, stand-alone drum, express the shielding factor SF of every drum material, i.e. concrete composition, relative to air (i.e. case NoShield).

RO_7 For a single, stand-alone drum, express the dose attenuation factor of each of the 3 high-density shielding concretes, relative to that of ordinary concrete.

RO_8 Develop MCNP calculation models for a rectangular, square-pitched array of $5 \times 11 = 55$ concrete drums standing on a concrete slab in a "decay yard". Assume that each drum contains an identical design-basis source term, which had been quantified for a number of discrete decay times. Calculate the average dose rate at the fence around the decay yard, for 5 different drum materials (DM_i) as specified above. The design-basis distance between the fence and the outer face of the closest drum array was set at 5.5 m.

RO_9 For the array of drums in the decay yard, express the shielding factor of every drum material, i.e. concrete composition, relative to air (i.e. case NoShield).

RO10 For the array of drums in the decay yard, express the shielding factor of every high-density shielding concrete, relative to that of ordinary concrete.

RO11 If the average dose rate at the fence of the decay yard is above acceptance criteria for public-access areas, design a radiation shielding wall around the decay yard. The wall material must be ordinary concrete. Find a wall height and thickness that provide satisfactory shielding performance.

RO12 The burial depth of the concrete drums with cemented ILLW depend on many factors, also the prevention of future human intrusion after the closure of the waste repository in the distant future. In this work, the required burial depth will be calculated from a radiological perspective, namely the need to maintain transmitted surface dose rates below one-tenth of the natural background dose rate (NBDR). This means that the burial depth of the drums must ensure that the presence of the underground drums may add only a trivial and negligible additional dose rate $\Delta\dot{D}$ to the natural level of the surface dose rate. Symbolically, this requirement is

$$\frac{\Delta\dot{D}}{NBDR} \leq 10\%$$

which calculates to

$$\Delta\dot{D} \leq 0.01\ \mu\text{Sv/h}$$

because $NBDR \approx 0.1\ \mu\text{Sv/h}$.

RO13 Quantify the tenth-value thicknesses (TVTs) for the high-density shielding concretes magnetite concrete hematite concrete and barite concrete as shielding materials against the radiation emissions by the radionuclides ^{60}Co, ^{137}Cs and ^{192}Ir, to add additional useful quantitative information to Table 2-3 on page 71.

The overarching research objective is to establish technical knowledge, conceptual clarity and a set of high-fidelity calculation models for high-fidelity code systems, for the characterisation, immobilisation, shielding, storage, transport and disposal of the ILLW from fission-produced radio-nuclides.

5. Calculation models and results

5.1 Process timeline: ILLW from fission-^{99}Mo production

The process timeline for the ILLW that results from the production of $(n, f)^{99}\mathrm{Mo}$, is summarised in Table 5-1.

Table 5-1: Process timeline for high-activity[25] liquid waste stream from the production of fission-based ^{99}Mo

Step	Time at beginning of step	Process
1	$T = 0$	Begin in-core irradiation of $6 \times \mathrm{LEU}_{20}$ TP_7 assemblies at a total neutronic fission power of $6 \times 140\ \mathrm{kW} = 0.84\ \mathrm{MW}$, for $T_{irr} = 200$ h
Reset time in ORIGEN model to zero		
2	$T = 0$	Discharge and then cool the 42 ITPs for circa 18 to 24 hours to allow the heating power to drop to a manageable level for a transfer from the reactor building to the isotope production hotcell complex
3	$T = 18$ h	Begin alkaline digestion of the TPs in a 6-molar solution of NaOH in water. This is also called target plate dissolution. All noble gases escape
4	$T = 20$ h	Separate the liquid radioactive waste from the solid residue by filtration. All noble gases escape
5	$T = 24$ h	7 days elapse until the 40-litre SS-316L tank is full with ILLW from a total of 42 ITPs
6	$T = 24\ \mathrm{h} + 7\ \mathrm{d} = 8\ \mathrm{d}$	Allow the ILLW in the 40-litre SS-316L holdup tank to "cool" for 90 days
7	$T = 8\ \mathrm{d} + 90\ \mathrm{d} = 98\ \mathrm{d}$	Cementation of ILLW with vermiculite; all noble gases escape. Next, the stainless-steel drum is sealed, i.e. noble gases no longer escape
8	$T = 98$ d	Store concrete drums containing cemented ILLW, in on-site interim storage, on a large, fenced, outdoor concrete slab known as the "decay yard"

[25] This is the naming convention used by the isotope production centre where the ILLW is produced, to distinguish this high-activity liquid waste from the low-activity liquid waste produced during the purification of e.g. molybdenum and iodine products.

5.2 Engineering specifications of tanks for ILLW and concrete drums for cemented ILLW

Tanks with an inner volume of 40 litres receive the intermediate-level liquid (radioactive) waste (ILLW) from target plate dissolution. These 40-litre SS-316L drums are located in the bottom compartment of the dissolver hot-cells. Each such drum is a rectangular drum with a height of 80 cm and equal side lengths of 22.5 cm. Above these drums, a horizontal layer of 100 mm Pb, supported by steel plates and beams, separates the "basement" section of the hotcell from the dissolver compartment of the hotcell. The lower part of the hotcell has a vertical Pb shielding wall thickness of 300 mm between the highly radioactive 40-litres ILLW holdup tanks and the Blue Area (where many people work), and vertical shielding wall thickness of 200 mm Pb on the other 3 sides. The top compartment of the dissolver-hotcell has a 250 mm Pb wall on the Blue Area side, and 150 mm Pb wall thicknesses on the 3 other sides.

The high-density concrete drums for the storage and disposal of cemented ILLW, are $z = 130$ cm high. Vertically, the inner cavity starts at $z \approx 32$ cm and ends at $z \approx 99$ cm, i.e. the cavity is approximately 67 cm high. The radius of the inner cavity is $R \approx 23$ cm, i.e. its ID is approximately 46 cm. In the inner cavity sits an embedded SS-304L drum with a capacity of $\sim$100 litres and a wall thickness of 3 mm. Directly after cementation, while still liquid, the cement-vermiculite ILLW slurry is pumped into the 100-litre SS drum inside the large concrete drum, where the cemented radioactive waste subsequently hardens. The thickness of the concrete wall of the drum is approximately 32 cm to the sides, bottom and top.

5.3 Calculation models: SCALE TRITON T6-DEPL and ORIGEN

To characterise the content of the ILLW, it is necessary to follow the evolution of the $[N_i, A_i(t)]$ nuclide activity matrix throughout the irradiation of the 42 LEU TPs which are eventually dissolved in the dissolver-hotcell, to fill one 40-litre ILLW tank.

Research objective RO_3, formulated on page 153, involves the adaptation of existing SCALE ORIGEN calculation models to enable the quantification of the radionuclide content $[N_i, A_i(t)]$ and radiation emissions $[E_g, Y_g(t)]$ from intermediate-level liquid (radioactive) waste (ILLW).

A calculation model developed in the SCALE 6.2.4 calculation sequence TRITON T6-DEPL, calculates the time-dependent F33 1-group reaction cross-sections for subsequent use by the SCALE

code ORIGEN. This up-front transport-depletion calculation takes approximately 7 days on a fast 2021 model PC. This SCALE TRITON T6-DEPL calculation model is treated in Annexure B which starts on page 222. This step prepares a set of F33 1-group, problem-dependent reaction cross-sections for subsequent use by the burnup code ORIGEN.

Next, a SCALE 6.2.4 ORIGEN calculation model for the irradiation of 42 LEU_{20} individual target plates (i.e. $6 \times TP_7$ assemblies), was developed adapted to calculate the radionuclide content $[N_i, A_i(t)]$ of the ~35 litres of ILLW. Such an ORIGEN calculation completes within ~15 minutes, i.e. much faster than the SCALE TRITON transport-depletion (T-DEPL) calculation. ORIGEN reads the pre-calculated F33 burnup-dependent 1-group cross-section library that had been generated over several days by the initial lengthy, preparatory 252-group TRITON T6-DEPL calculation. As a result of using pre-calculated, 1-group cross-sections, the code ORIGEN can produce its results remarkably quickly. The ORIGEN calculation model quantifies the radiological content of intermediate-level liquid waste, i.e. the $[N_i, A_i(t)]$-matrix; this ORIGEN model is discussed in Annexure B which starts on page 222. Using ENDF/B-7.1 radiation emission data, ORIGEN uses its calculated $[N_i; A_i(t)]$ matrices to quantify {Energy, Yield} matrices, i.e. $\left[E_g; Y_g(t)\right]$ matrices of the spectral detail of photon emission by the radioactive waste. These $(N; A)$ and $(E; Y)$ matrices jointly represent what is commonly referred to as the "source term(s)".

5.4 Partitioning of chemical species between the solid and liquid radioactive waste streams during the chemical processing of ITPs

This technical topic is presented in § B.4.4 on page 235.

5.5 Liquid radioactive waste from (n,f)^{99}Mo production: Activity and dominant radionuclides

5.5.1 Radionuclide inventory per concrete waste drum, after 1 yr, 5 yrs and 10 yrs

Table 5-2 presents the nuclide-activity matrix of the radionuclides with the highest activities in the liquid radioactive waste from processed irradiated target plates, evaluated at 1-year, 5-years and 10-years post-irradiation. A colour-coding convention is employed to guide the eye. (Note that the SCALE 6.2.4 code ORIGEN does not hyphenate nuclide names, and that these nuclide names are therefore reported as such (i.e. without hyphens) in Table 5-2).

Table 5-2: Radionuclides having the highest activities in the ILLW from chemically processed irradiated fissile target plates, evaluated at cooling times of 1 yr, 5 yrs and 10 yrs

Nuclide	Act(T=1yr) (Bq)		Nuclide	Act(T=5yr) (Bq)		Nuclide	Act(T=10yr) (Bq)
Pr144	5.95E+12		Cs137	7.39E+11		Cs137	6.58E+11
Ce144	5.95E+12		Pm147	7.07E+11		Ba137m	6.23E+11
Y91	2.60E+12		Ba137m	7.00E+11		Pm147	1.89E+11
Pm147	2.04E+12		Pr144	1.70E+11		Y90	6.68E+10
Nb95	1.47E+12		Ce144	1.70E+11		Sr90	6.68E+10
Cs137	8.10E+11		Y90	7.53E+10		H3	9.89E+09
Ba137m	7.67E+11		Sr90	7.53E+10		Pr144	2.00E+09
Zr95	7.18E+11		Rh106	2.00E+10		Ce144	2.00E+09
Rh106	3.05E+11		Ru106	2.00E+10		Sb125	1.95E+09
Ru106	3.05E+11		H3	1.31E+10		Eu155	1.35E+09
Sr89	2.91E+11		Sb125	6.85E+09		Sm151	1.33E+09
Ce141	2.58E+11		Eu155	2.80E+09		Rh106	6.64E+08
Ru103	2.36E+11		Cs134	1.69E+09		Ru106	6.64E+08
Rh103m	2.34E+11		Te125m	1.68E+09		Te125m	4.77E+08
Y90	8.29E+10		Pr144m	1.63E+09		Cs134	3.16E+08
Sr90	8.29E+10		Sm151	1.39E+09		Eu154	1.27E+08
Pr144m	5.68E+10		Fe55	2.44E+08		Tc99	1.10E+08
Te127m	2.53E+10		Eu154	1.90E+08		Eu152	9.21E+07
Te127	2.48E+10		Co60	1.50E+08		Co60	7.79E+07
Sb125	1.87E+10		Eu152	1.19E+08		Fe55	6.91E+07
H3	1.64E+10		Tc99	1.10E+08		Sn121m	3.98E+07
Nb95m	8.22E+09		Sn121m	4.30E+07		Sn121	3.09E+07
Cs134	6.49E+09		Sn121	3.34E+07		Pr144m	1.91E+07
Te129m	5.02E+09		Sn119m	1.96E+07		Cd113m	5.41E+06
Eu155	5.02E+09		Cd113m	6.92E+06		C14	3.71E+06
Te125m	4.39E+09		C14	3.71E+06		Zr93	1.91E+06
Te129	3.17E+09		Ag110m	3.59E+06		Ni63	1.01E+06
Sm151	1.43E+09		Mn54	2.86E+06		Cs135	8.54E+05
Sn123	1.39E+09		Te127m	2.33E+06		Nb93m	6.39E+05
Fe55	6.71E+08		Te127	2.29E+06		Sn126	5.23E+05
Sn119m	6.21E+08		Zr93	1.91E+06		Sb126m	5.23E+05
Eu154	2.62E+08		Zn65	1.14E+06		Sn119m	2.60E+05
Co60	2.54E+08		Ni63	1.05E+06		Se79	1.28E+05
Ag110m	2.07E+08		Cs135	8.54E+05		I129	1.22E+05
Pr143	1.77E+08		Sn123	5.48E+05		Sb126	7.32E+04
Cd115m	1.46E+08		Sn126	5.23E+05		Pd107	6.63E+04
Eu152	1.46E+08		Sb126m	5.23E+05		Mn54	4.94E+04

Nuclide	Act(T=1yr) (Bq)		Nuclide	Act(T=5yr) (Bq)		Nuclide	Act(T=10yr) (Bq)
Tc99	1.10E+08		Gd153	3.67E+05		Ag108m	2.84E+04
Mn54	7.33E+07		Nb93m	3.46E+05		Ag110m	2.26E+04
Zn65	7.27E+07		Nb95	2.14E+05		Ni59	6.81E+03
Pm148m	6.27E+07		Se79	1.28E+05		Zn65	6.38E+03
W185	5.24E+07		I129	1.22E+05		Ag108	2.47E+03
Sn121m	4.58E+07		Zr95	9.71E+04		Gd153	1.90E+03
La140	4.18E+07		Y91	7.91E+04		Pm146	1.71E+03
Ba140	3.63E+07		Sb126	7.32E+04		Pm145	1.62E+03
Sn121	3.56E+07		Pd107	6.63E+04		Tb157	1.48E+03
Y89m	2.81E+07		Ag110	4.88E+04		Ag109m	1.32E+03
Gd153	2.48E+07		Ag108m	2.86E+04		Cd109	1.32E+03
Cr51	1.36E+07		Ag109m	2.05E+04		Tm171	8.11E+02
Sb124	9.69E+06		Cd109	2.05E+04		Mo93	6.98E+02
Cd113m	8.42E+06		Ni59	6.81E+03		Rh102m	4.81E+02
Co58	6.74E+06		Tm171	4.93E+03		Ho166m	3.70E+02
Fe59	5.94E+06		Pm146	3.20E+03		Ag110	3.07E+02
W181	5.70E+06		Ag108	2.49E+03		Rb87	2.02E+02
Nd147	4.45E+06		Pm145	1.91E+03		Sm147	5.63E+01
Re188	3.93E+06		Tb157	1.55E+03		Sn123	3.04E+01
W188	3.89E+06		W181	1.34E+03		Sm145	2.95E+01
C14	3.72E+06		Sm145	1.22E+03		Eu150	2.89E+01
Pm148	3.03E+06		Rh102m	1.21E+03		Te127m	2.11E+01
Ag110	2.82E+06		Co57	1.16E+03		Ca41	2.07E+01
Zr93	1.91E+06		Nb95m	1.11E+03		Te127	2.07E+01
Eu156	1.37E+06		Mo93	6.99E+02		Tb158	1.53E+01
Ni63	1.08E+06		Sr89	5.75E+02		Pu239	1.50E+01
Cs135	8.54E+05		Ho166m	3.71E+02		Nb94	1.25E+01
Tb160	7.80E+05		V49	3.15E+02		Co57	1.10E+01
Sn126	5.23E+05		Ca45	2.06E+02			
Sb126m	5.23E+05		Rb87	2.02E+02			
Sc46	4.30E+05		Rh102	9.65E+01			
Ag109m	1.84E+05		W185	7.29E+01			
Cd109	1.84E+05		Dy159	5.61E+01			
In113m	1.74E+05		Sm147	4.35E+01			
Sn113	1.74E+05		Eu150	3.18E+01			
Cs136	1.60E+05		Ce139	2.65E+01			
Rb86	1.47E+05		In113m	2.63E+01			
Se79	1.28E+05		Sn113	2.63E+01			
I129	1.22E+05		Ca41	2.07E+01			
Ca45	1.04E+05		Tb158	1.56E+01			

Nuclide	Act(T=1yr) (Bq)		Nuclide	Act(T=5yr) (Bq)		Nuclide	Act(T=10yr) (Bq)
Sb126	7.85E+04		Pu239	1.50E+01			
Pd107	6.63E+04		Nb94	1.25E+01			
Dy159	6.24E+04		Pu241	1.04E+01			
Nb93m	6.20E+04						
Co57	4.84E+04						
Ce139	4.16E+04						
Xe131m	3.99E+04						
Ag108m	2.88E+04						
Sm145	2.40E+04						
Tm171	2.09E+04						
Ba136m	1.77E+04						
In115m	1.55E+04						
Rh102	1.23E+04						
I131	1.09E+04						
Ni59	6.81E+03						
V49	6.77E+03						
Pm146	5.29E+03						
Te123m	4.79E+03						
Y88	4.02E+03						
Rh102m	2.55E+03						
Ag108	2.51E+03						
Rb84	1.95E+03						
Tb157	1.61E+03						
Sn125	1.43E+03						
Pm145	9.77E+02						
Sn117m	8.26E+02						
Mo93	6.99E+02						
Rb83	5.30E+02						
Kr83m	3.94E+02						
Ho166m	3.72E+02						
Ta182	3.24E+02						
Tm170	3.12E+02						
Rb87	2.02E+02						
Gd151	1.32E+02						
In114m	1.20E+02						
In114	1.16E+02						

In Table 5-2 it is evident that, at $T_{cool} = 5$ yr, ^{137}Cs and its progeny nuclide, ^{137m}Ba, have the highest activities in the cemented liquid radioactive waste. The activities of ^{137}Cs and its progeny nuclide, ^{137m}Ba, are well in the lead at $T_{cool} = 10$ yr. The radionuclide ^{137}Cs belongs to the nutrient-analogue

element Cs, so that it is important to immobilise the liquid waste well, to prevent these isotopes from leaking into the environment, where they could potentially enter into the food chain. The element cæsium mimics the nutrient mineral K (potassium), which is an important electrolyte that is widely distributed in plants and the bodies of mammals.

5.5.2 The long hauliers: Radionuclide inventory per concrete drum, after 10^4 years

Table 5-3 presents the nuclide-activity matrix of the radionuclides having the highest activities in the liquid radioactive waste from processed irradiated target plates, evaluated at a time of 10^4 years after the end-of-irradiation. These can be called the long-haulier radionuclides.

Table 5-3: Long-haulier radionuclides in the ILLW — {Nuclide; Activity} matrix after 10^4 years

Radionuclide	Act(T=1.0E4 yr) (Bq)
Tc-99	1.06E+08
Zr-93	1.90E+06
Nb-93m	1.85E+06
C-14	1.10E+06
Cs-135	8.52E+05
Sn-126	5.07E+05
Sb-126m	5.07E+05
Se-79	1.25E+05
I-129	1.22E+05
Sb-126	7.10E+04
Pd-107	6.63E+04
Ni-59	6.21E+03
Rb-87	2.02E+02
Mo-93	1.24E+02
Sm-147	6.10E+01
Ca-41	1.93E+01

The radionuclides in Table 5-3 have very long half-lives, which means that they have low levels of nuclear instability. It is therefore found that they emit only low yields of low-energy ionising radiation. Their radiological hazard levels are low, and their clearance levels are generally high.

5.5.3 Graphic summary: Isotopic evolution of activity per drum

Figure 5-1 shows how the total activity of all the radionuclides in cemented liquid waste from the production of $(n, f)^{99}$Mo, as well as the combined activity of ^{137}Cs plus ^{137m}Ba in this process waste, varies with time, over the first 1000 years, measured from the initial production date of the waste. These values were calculated with the SCALE-6.2.4 ORIGEN calculation model.

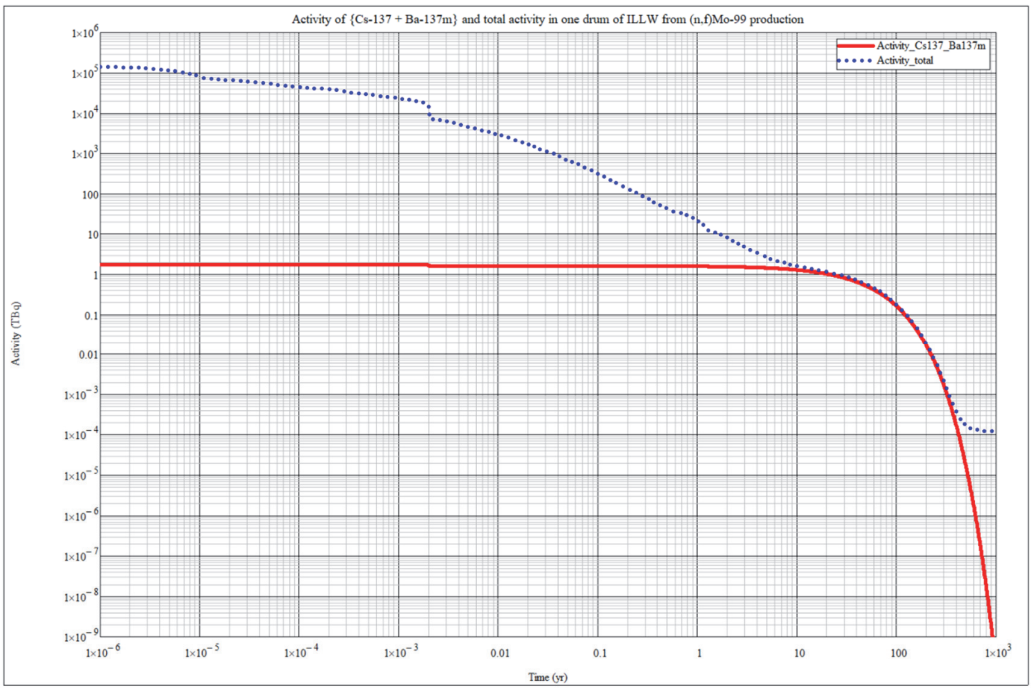


Figure 5-1: The total activity of all the radionuclides in the liquid radioactive waste from fission-produced ^{99}Mo, as well as the combined activity of the radionuclide ^{137}Cs plus its progeny nuclide, ^{137m}Ba, as a function of cooling time

Figure 5-1 indicates that, as from a cooling time of circa 5 years, the radionuclide pair {^{137}Cs; ^{137m}Ba} becomes radiologically dominant in the cemented ILLW, until circa 400 yrs.

Figure 5-2 shows the combined activity of the radioactive pair, {^{137}Cs; ^{137m}Ba}, relative to the total activity of all radionuclides in the cemented ILLW, as a function of time.

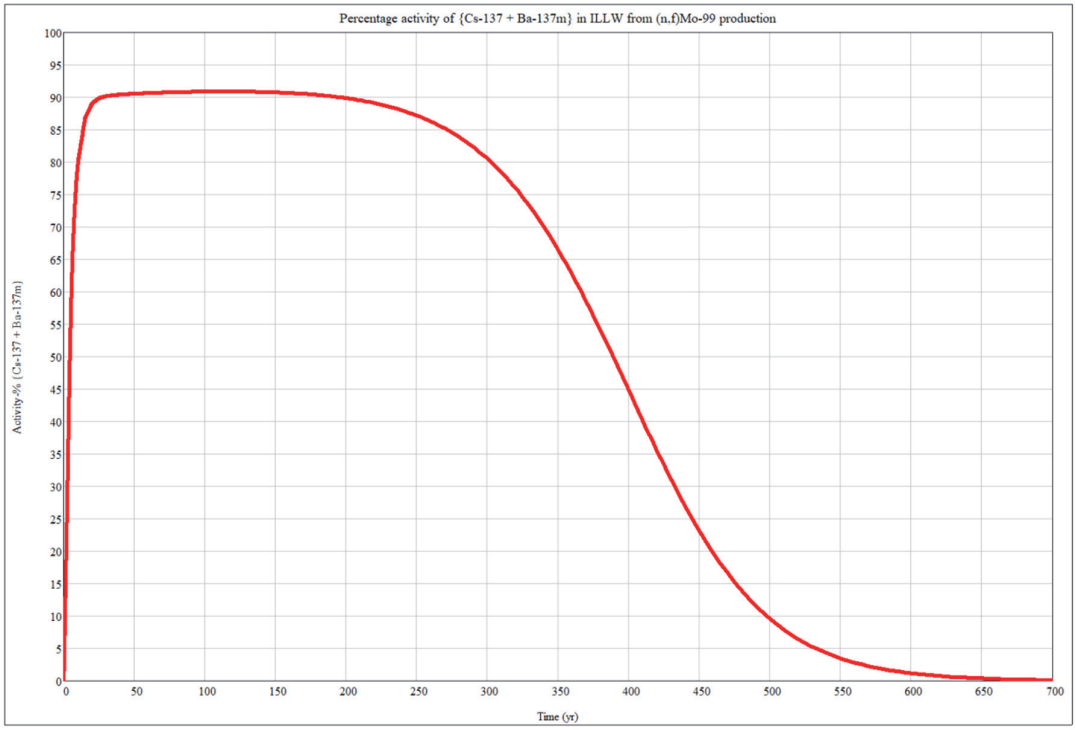


Figure 5-2: The combined activity of the radionuclide pair, ^{137}Cs and ^{137m}Ba, relative to the total activity of all radionuclides in the ILLW, as a function of time

In Figure 5-1 and Figure 5-2 it is evident that the radionuclide pair $\{^{137}\text{Cs}; ^{137m}\text{Ba}\}$ will dominate the activity in the ILLW from the production of $(n,f)^{99}$Mo, in the period from approximately 5 yrs to 400 yrs. The finding that $\{^{137}\text{Cs}; ^{137m}\text{Ba}\}$ becomes dominant within a few years, matches the operational experience of the waste producer and is also in harmony with published literature (IAEA, 1998).

5.6 Photon emission source term from ILLW from (n,f)^{99}Mo production

5.6.1 Energy spectrum

Photon emission spectra for the ILLW$[(n,f)^{99}\text{Mo}]$, is shown in Figure 5-3, at 5 distinct cooling times, measured from the time when the batch of TPs is discharged from the reactor: 90 days, 1 year, 5 years, 10 years and 100 years.

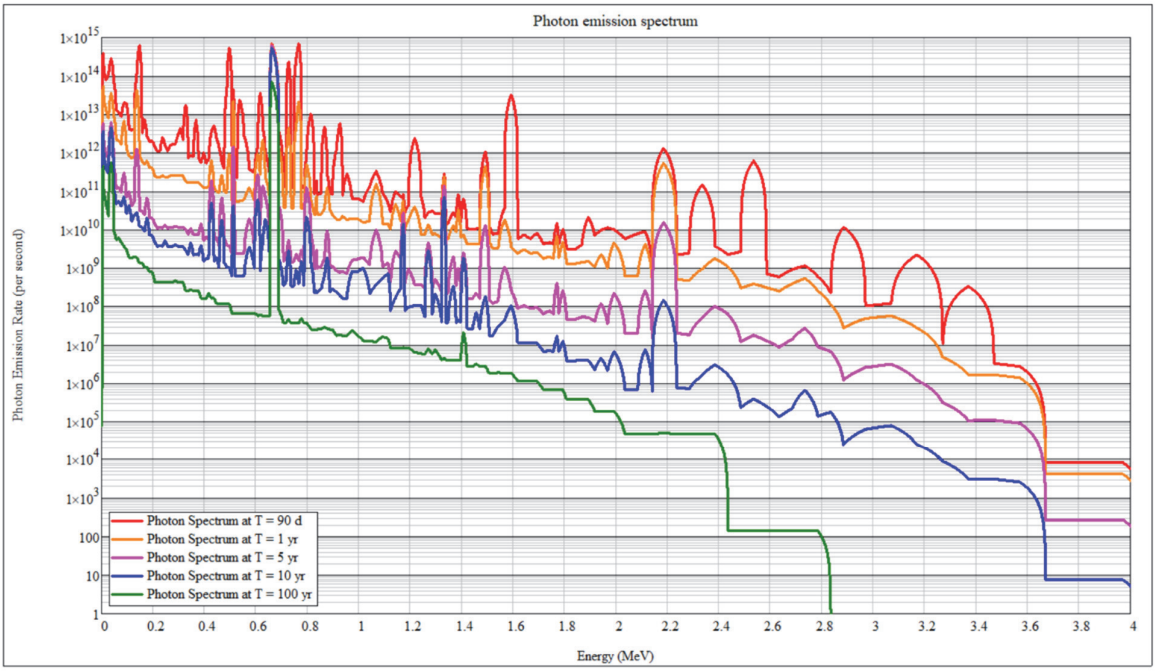


Figure 5-3: Photon emission spectra for liquid radioactive waste produced from the production of (n,f)^{99}Mo

In Figure 5-4 the photon emission spectra from ILLW[$(n,f)^{99}$Mo] is displayed on linear-linear scales, for decay times of 1 yr, 5 yrs and 10 yrs.

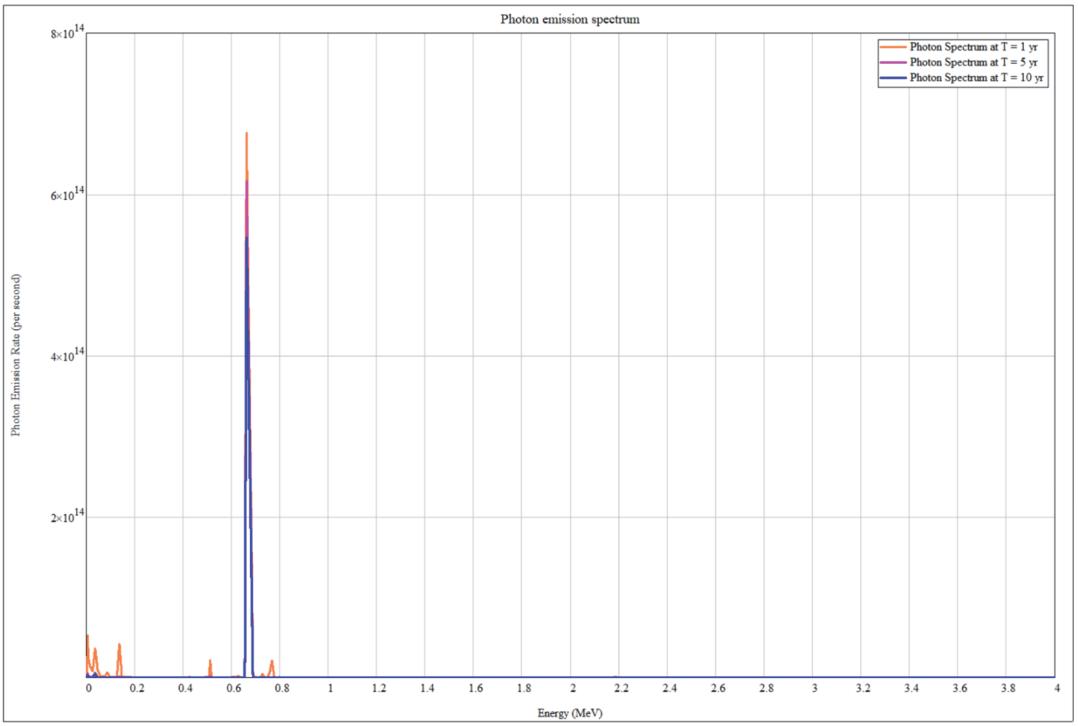


Figure 5-4: Photon emission spectra for liquid radioactive waste produced from the production of (n,f) ^{99}Mo, on linear-linear scales, for decay times of 1 yr, 5 yrs and 10 yrs

At the cooling times displayed in Figure 5-4, the prominence of the photon emission peak at $\boxed{E_\gamma = 0.661657 \text{ MeV}}$ is a distinguishing feature of the liquid radioactive waste; this photon peak is from the ^{137m}Ba progeny nuclide formed by its long-lived progenitor, ^{137}Cs (cf. (Soppera *et al.*, 2013)).

5.6.2 Lowering of the high energy component of the photon emission spectrum from ILLW

An investigation of Figure 5-3 indicates that a lower proportion of high energy ionising photons are emitted at longer decay times of the waste. This was investigated using numerical integration of linearly interpolated photon emission spectra. The calculational detail is embedded here 

(double-click to open) and results are summarised in Table 5-4.

Table 5-4: Percentage photons emitted at $E_\gamma \geq 1$ MeV in ILLW from fission-produced ^{99}Mo

Decay time	Percentage photons emitted at $E_\gamma \geq 1$ MeV
90 d	2.11

Decay time	Percentage photons emitted at $E_\gamma \geq 1$ MeV
1 yr	3.42E-1
5 yr	2.83E-2
10 yr	8.81E-3
100 yr	3.63E-4

It is clear from Table 5-4 that the relative magnitude of the high energy component in the emitted photon spectrum becomes lower and lower with the progression of time, as the radioactive waste decays. The reason is that, initially, the waste contains more short-lived, highly unstable radionuclides, which emit a higher proportion of high energy ionising photons. Over time, it is mainly longer-lived radionuclides that remain, and these usually emit lower energy ionising photons.

At lower photon energies, as is emitted at longer decay times, photo-electric absorption (PEA) of ionising photons is more important than Compton scattering (CS) as a photon-attenuation mechanism. According to Table 2-2 on page 64, the linear interaction coefficient for PEA increases as $\mu_{PEA} \propto Z^3$, whereas the linear interaction coefficient for CS is independent of Z and only depends on the mass-density ρ, as $\mu_{CS} \propto \rho$. Accordingly, it is expected that the improved performance of high-density shielding concretes, with their higher-Z elemental content such as Fe $(Z(\text{Fe}) = 26)$ and Ba $(Z(\text{Ba}) = 56)$, will be more pronounced at e.g. $T = 10$ yrs than at e.g. $T = 90$ days. This behaviour is prominently evident in the graphs in § 5.8 (starting on page 171) and § 5.11 (starting on page 187). The pattern that emerges in calculated results is explained in § 5.9 (page 183).

5.7 MCNP calculation models: Graphical representations

5.7.1 Calculation model: Single drum

Research objective RO_4 (page 154) concerns the development of an MCNP calculation model of single concrete drums manufactured from 4 distinct concrete materials and filled with cemented ILLW that had undergone a range of cooling times. Such a calculation model was developed, and the model description starts on page 239 in Annexure B. The present section presents a graphical journey showcasing facets of the MCNP model of stand-alone drums. All graphics presented in this section (§ 5.7) were generated directly from the MCNP model using the MCNP geometry plotter (LANL, 2018).

A side-view of the large concrete drum holding the cemented ILLW is displayed in Figure 5-5.

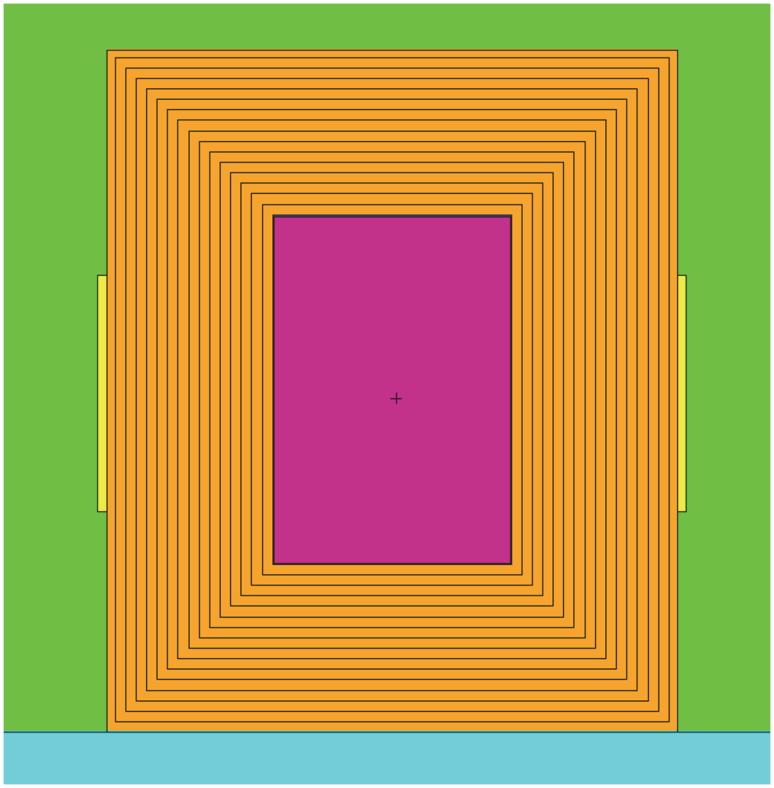


Figure 5-5: Side-view of a large high-density concrete drum containing cemented ILLW

Legend:

Cemented liquid radioactive waste
Concrete drum wall
Concrete floor slab
Air
TEM Detector

The "segmentation" of the concrete, as seen in Figure 5-5, is the result of it being subdivided into 16 concentric shells with a thickness of approximately 2 cm per shell, to facilitate a very simple form of variance reduction in the Monte Carlo radiation transport calculation, namely population control by cell-importance biasing.

Figure 5-6 is a top view of a stand-alone concrete drum filled with radioactive waste. Around the drum are 2 circumferential calculational detectors, filled with TEM[26] — one contact-detector to measure the

[26] Note by study supervisor TJvR: TEM is an initialism for tissue-equivalent material. The volume-averaged chemical composition of the human body, as documented in https://en.wikipedia.org/wiki/Composition_of_the_human_body, was used to define the material TEM in MCNP models. This material is used to fill calculational detector volumes, specifically when F6 energy absorption tallies are used in MCNP calculation models. This ensures a detector response that will closely correspond to the energy absorption properties of the human body.

contact dose-rate (CDR) and one detector at a distance of 1 m from the outside surface of the drum, to measure the Transport Index (TI).

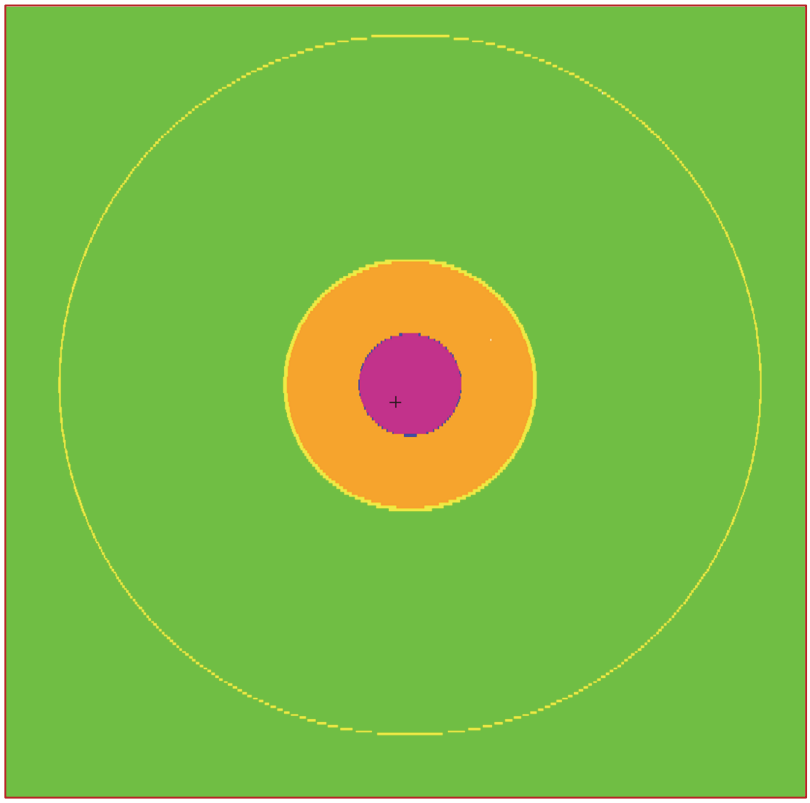


Figure 5-6: Top view of a concrete drum filled with radioactive waste, with 2 circumferential calculational detectors — one for the calculation of the contact dose rate (CDR) and the other to calculate the TI

Legend:

	Cemented liquid radioactive waste
	Concrete drum wall
	Air
	TEM Detector

The circumferential calculational TEM detectors seen in Figure 5-6 are both belt-line detectors, as can be seen in Figure 5-5. The term "belt-line" means that the detectors do not cover the full height of the drum, but only the central vertical range, where transmitted dose-rates will be highest. This enables these detectors to quantify good estimates of peak dose rates.

5.7.2 Calculation model: Drum array in the "decay yard"

Research objective RO_8 (page 154) stipulates the development of an MCNP calculation model of a large, rectangular array of concrete drums manufactured from 4 distinct concrete materials and filled with cemented ILLW that had undergone a range of cooling times. This drum array stands on a concrete slab in the "decay yard" which is surrounded by a perimeter fence. Such a calculation model was developed, and its description starts on page 261 in Annexure B.

Figure 5-7 shows the rectangular array of $5 \times 11 = 55$ concrete radioactive waste drums; each drum is filled with cemented liquid radioactive waste. Drums are arrayed in a square pitch on a concrete slab in a "decay yard". Around the decay yard stretches a fence, which is represented by a calculational detector that quantifies the dose rate at the fence position. The nearest distance between the drums and the fence is 5.5 m. The calculational detector is filled with low-density TEM; its width is 10 cm while its height is 200 cm. This calculational detector serves to quantify the average dose rate that will be incurred by people standing along the perimeter fence. No attempt is made to measure the peak dose-rate at the fence; fence dose-rates (FDRs) are averages over the entire perimeter TEM detector.

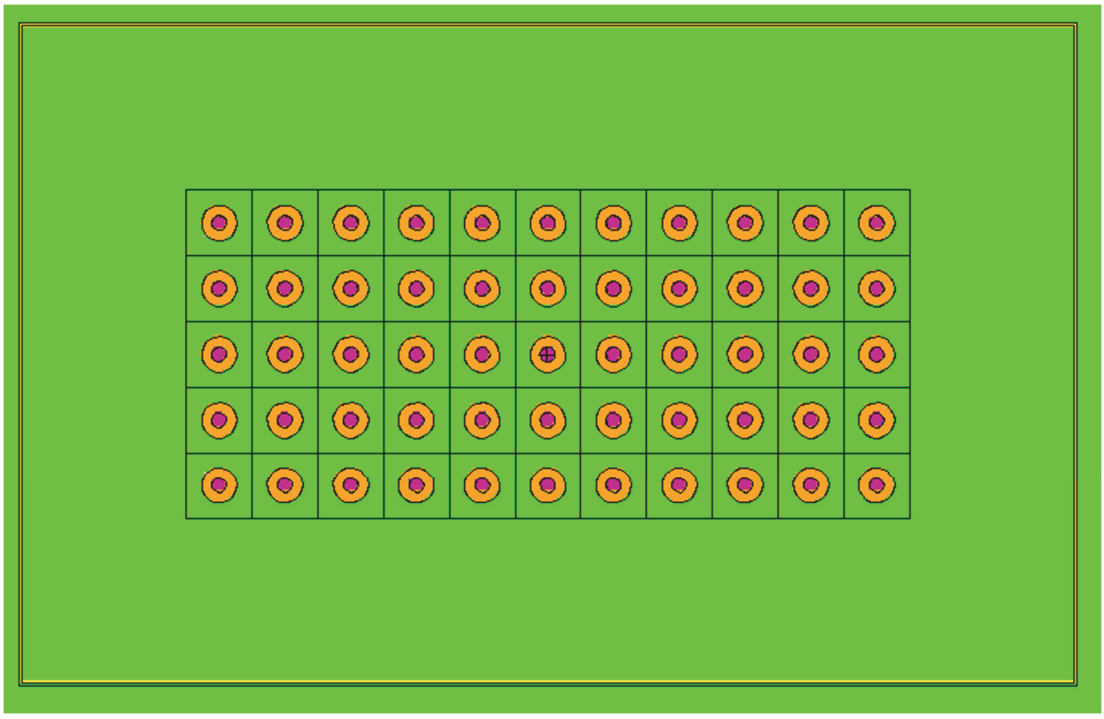
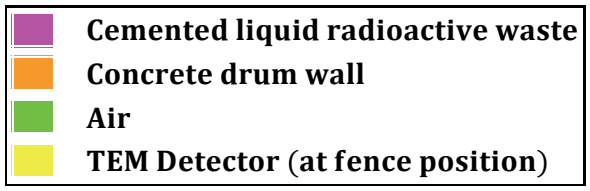


Figure 5-7: Array of 5 × 11 = 55 concrete drums filled with cemented liquid radioactive waste, arrayed on a concrete slab in a "decay yard"

Legend:



5.8 Calculated dose rates for a single, stand-alone concrete drum containing cemented ILLW from (n,f) ^{99}Mo production

5.8.1 Design of the computational experiment

To quantify the efficacy of the concrete drums as radiation shields for the ionising radiation emitted by ILLW, it is necessary to calculate the dose rates for the reference case of no shielding, as well as the dose rates for the use of 4 types of concrete as drum material: (1) Ordinary concrete (ORD-CRT), (2) Magnetite concrete (MAG-CRT), (3) Hematite concrete (HEM-CRT) and (4) Barite concrete (BAR-CRT).

In the presentation of the results of the analysis of the shielding of cemented ILLW, a colour-coding convention will be used to guide the eye. This convention is summarised in Table 5-5.

Table 5-5: Colour-coding convention used to guide the eye in the presentation of the shielding abilities of ordinary concrete (ORD-CRT), magnetite concrete (MAG-CRT), hematite concrete (HEM-CRT) and barite concrete (BAR-CRT)

Concrete type	Abbreviation	Colour-coding
No shielding	NoShield	
Ordinary concrete	ORD-CRT	
Magnetite concrete	MAG-CRT	
Hematite concrete	HEM-CRT	
Barite concrete	BAR-CRT	

5.8.2 Dose rates for case NoShield (single drum)

Research objective RO_6 on page 154 states that the shielding factor provided by different drum materials, must be quantified over a range of radioactive waste decay times, relative to the case of no shielding (case NoShield).

In the MCNP calculation models, the "no concrete shielding" configuration i.e. case NoShield, is easily modelled by simply adding e.g. a suffix E-6 to the mass-density of the drum's concrete in the cell cards of the MCNP input. This lowers the mass-density of the concrete by a factor 1.0E6 and renders the concrete less dense than air, i.e. it enables the modelling of "case NoShield" with minimal user effort. The results of the dose rate calculations for a single, stand-alone drum with no shielding effect, are listed in Table 5-6.

In Table 5-6 and many subsequent tables where dose rates and shielding factors are reported, the variable T_cool refers to the period of cooling time measured from the discharge of the batch of 42 irradiated target plates from the reactor. In view of the 90-day holdup period in the holdup tanks, this means that the time specification $T_{cool} = 90$ days refers to the time directly after cementation of the ILLW.

Table 5-6: Dose rates in the complete absence of shielding concrete, calculated for one stand-alone drum containing ILLW from an (n,f)^{99}Mo production process

Case: No Shielding		
T_cool (yr)	**Contact DR (Sv/h)**	**DR at 1m (Sv/h)**
0.25	3.379E+00	4.788E-01
1.00	3.158E-01	4.481E-02
2.00	1.759E-01	2.493E-02
3.00	1.283E-01	1.819E-02
4.00	1.064E-01	1.509E-02
5.00	9.565E-02	1.356E-02
10.00	7.865E-02	1.115E-02

All dose rates recorded in Table 5-6 are prohibitively high — the contact dose rate is more than 30 million times higher than the average natural background dose rate (NBDR) on the surface of the earth. The dose rate at 1 m from the (virtual) outer surface of the drum is more than 4.5 million times higher than the NBDR. It is therefore vital that an efficacious and affordable concrete shielding material be used for the drum. In other words, there it is imperative that the 100-litre stainless-steel drums containing the radioactive waste, be embedded inside thick concrete outer drums, so that the thick body of the outer concrete can perform the required vital shielding function.

5.8.3 Dose rates for case ORD-CRT (case 1drum)

Table 5-7 summarises the calculated dose rates for a single, stand-alone ordinary concrete (ORD-CRT) drum. The shielding factor is relative to case NoShield.

Table 5-7: Concrete drums for ILLW from an (n,f)^{99}Mo production process: Dose rates for ordinary concrete (ORD-CRT)

Case: Drum is Ordinary Concrete (ORD-CRT)				
T_cool (yr)	**Contact DR (Sv/h)**	**DR at 1m (Sv/h)**	**Shielding factor: CDR**	**Shielding factor: DR at 1 m**
0.25	5.412E-02	7.448E-03	62	64
1.00	4.134E-03	5.615E-04	76	80
2.00	2.240E-03	3.036E-04	79	82
3.00	1.619E-03	2.192E-04	79	83
4.00	1.337E-03	1.810E-04	80	83
5.00	1.200E-03	1.624E-04	80	84
10.00	9.849E-04	1.333E-04	80	84

The last 2 columns of Table 5-7 list the shielding factors presented by ordinary concrete drums. It is seen that the 32 cm thick ordinary concrete drum wall will lower transmitted dose-rates by a factor of 64 to 84 relative to the NoShield reference case. This range of DAF values is better than no shielding, yet simply not good enough — the mass-density ρ or ordinary concrete is low at $\rho = 2.3$ g cm^{-3}, and, furthermore, the atomic numbers Z of the main constituents of ordinary concrete are too low — $Z(O) = 8$ and $Z(Si) = 14$. The dose rate at 1 m from the drum is still more than a factor 1200 times higher than the NBDR, even after $T_{cool} = 10$ yr.

Research objective RO_5 on page 154 states that the abilities of different concrete materials to make drums transportable without having to wait excessively long, have to be quantified. Conclusions about the transportability of drums will be drawn after the presentation of the results.

A drum becomes transportable — from the waste producer to that national radioactive waste disposal facility — when the contact dose-rate dips below 2.0E-3 Sv/h, i.e. 2 mSv/h. This is documented and referenced in § 3.5.23 on page 123. Table 5-7 shows that ordinary concrete drums filled with cemented ILLW will have to be stored on-site for approximately 3 years before the contact dose rate will be low enough to allow their transportation to the national radioactive waste disposal site. However, in § 5.8.8

on page 178, it is seen that the TI of ordinary concrete drums will dictate a required on-site storage time of approximately 15 years before the drums will become radiologically eligible for road transport. Such a prolonged storage period will expose the concrete to 15 years of alternating frost, sunshine and rain which would lead to all the concrete deterioration mechanisms identified in § 3.5.9 on page 104. The long storage period required for ORD-CRT drums may lead to extensive concrete deterioration. The conclusion is that the use of ordinary concrete is not a viable option for the ILLW waste drums.

5.8.4 Dose rates for case MAG-CRT (case 1drum)

The drum's shielding cannot be made thicker, but a better shielding material can be selected. The first improved concrete material over ordinary concrete (ORD-CRT) that will be investigated, is magnetite concrete (MAG-CRT). Magnetite is a grade of iron ore that can be used to produce concrete that contains between circa 30 % and 40 % Fe by mass and has a mass-density around 3.20 g cm^{-3}. Dose rates calculated for ILLW in a magnetite concrete drum, are summarised in Table 5-8. The shielding factors are relative to case NoShield.

Table 5-8: Concrete drums for ILLW from an (n,f) ^{99}Mo production process: Radiological performance of magnetite concrete (MAG-CRT) drums; shielding factors are relative to case NoShield

Case: Drum is Magnetite Concrete (MAG-CRT)				
T_cool (yr)	**Contact DR (Sv/h)**	**DR at 1m (Sv/h)**	**Shielding factor: CDR**	**Shielding factor: DR at 1 m (TI)**
0.25	1.007E-02	1.439E-03	336	333
1.00	6.158E-04	8.661E-05	513	517
2.00	3.199E-04	4.482E-05	550	556
3.00	2.269E-04	3.175E-05	566	573
4.00	1.860E-04	2.601E-05	572	580
5.00	1.662E-04	2.323E-05	575	584
10.00	1.361E-04	1.902E-05	578	586

Table 5-8 shows that magnetite concrete is a significantly better shielding material than ordinary concrete. The dose rates are reduced by factors that range between 330 and 580, compared to the NoShield reference case.

A drum becomes transportable — from the waste producer to the national radioactive waste disposal facility — when (1) the contact dose-rate dips below 2 mSv/h and (2) $TI \leq 10$ (IAEA, 2018). Table 5-8 shows that magnetite concrete drums filled with cemented ILLW will have to be stored on-site for less than 1 year before they will qualify for transport to the final disposal site.

5.8.5 Dose rates for case HEM-CRT (case 1drum)

A concrete composition that represents a further improvement of shielding properties, will now be investigated: Hematite concrete (HEM-CRT). Hematite is high-grade iron ore that can be used to produce concrete that contains approximately 40 % to 50 % Fe by mass, and having a typical mass-density of 3.50 g cm^{-3}. Hematite ore usually has a reddish to purple colour, from which it derives its name — the Greek term for blood is *hema.* Dose rates calculated for a hematite concrete drum are summarised in Table 5-9. The shielding factor is relative to case NoShield.

Table 5-9: Concrete drums for ILLW from an (n,f) ^{99}Mo production process: Dose rates for hematite concrete (HEM-CRT)

Case: Drum is Hematite Concrete (HEM-CRT)				
T_cool (yr)	**Contact DR (Sv/h)**	**DR at 1m (Sv/h)**	**Shielding factor: CDR**	**Shielding factor: DR at 1 m**
0.25	7.268E-03	1.046E-03	465	458
1.00	4.201E-04	5.964E-05	752	751
2.00	2.153E-04	3.046E-05	817	818
3.00	1.518E-04	2.144E-05	845	848
4.00	1.241E-04	1.751E-05	858	862
5.00	1.108E-04	1.562E-05	863	868
10.00	9.062E-05	1.277E-05	868	873

Table 5-9 shows that hematite concrete is a better shielding material against ionising photons than magnetite concrete. The dose rates are reduced by factors that range between 455 and 870, compared to the NoShield reference case.

The twin reasons for the greater shielding ability of both magnetite and hematite concrete, compared to ordinary concrete, are that (1) they are denser than ordinary concrete and (2) also contain a high mass-% of Fe, for which the atomic number Z is 26.

A drum becomes transportable — from the waste producer to that national radioactive waste disposal facility — when the contact dose-rate dips below 2 mSv/h. Table 5-9 shows that hematite concrete drums filled with cemented ILLW will have to be stored on-site for less than 1 year before becoming eligible for transportation to a national radioactive waste disposal site.

5.8.6 Dose rates for case BAR-CRT (case 1drum)

Dose rates calculated for a barite concrete drum are summarised in Table 5-10. The shielding factor is relative to case NoShield.

Table 5-10: Concrete drums for ILLW from an (n,f)^{99}Mo production process: Dose rates for barite concrete (BAR-CRT)

Case: Drum is Barite Concrete (BAR-CRT)				
T_cool (yr)	**Contact DR (Sv/h)**	**DR at 1m (Sv/h)**	**Shielding factor: CDR**	**Shielding factor: DR at 1 m**
0.25	5.160E-03	7.878E-04	655	608
1.00	2.230E-04	3.437E-05	1416	1304
2.00	1.062E-04	1.637E-05	1657	1523
3.00	7.225E-05	1.118E-05	1776	1627
4.00	5.806E-05	8.986E-06	1833	1679
5.00	5.147E-05	7.969E-06	1858	1702
10.00	4.182E-05	6.476E-06	1881	1722

Table 5-10 shows that barite concrete is a better shielding material against ionising photons than hematite concrete. The dose rates are reduced by factors that range between approximately 600 and 1700, compared to the NoShield reference case.

A drum becomes transportable — from the waste producer to that national radioactive waste disposal facility — when the contact dose-rate drops below 2 mSv/h. Table 5-10 shows that barite concrete drums filled with cemented ILLW will have to be stored on-site for considerably less than 1 year before becoming eligible for transportation to a national radioactive waste disposal site.

Whether barite or hematite concrete will be the shielding material of choice, depends on (1) local availability, (2) cost as well as (3) the mechanical properties of the concrete. There are no barite mines in Southern Africa, while we do have hematite ore available (Netshiozwi, 2002). (In some countries

in the northern hemisphere, most hematite ore deposits were depleted during World War II and the first 2 decades of the subsequent Cold War.)

5.8.7 Shielding performance of MAG-CRT, HEM-CRT and BAR-CRT relative to ORD-CRT (stand-alone drum)

Research objective RO_7 on page 154 states that the shielding factor provided by the 3 high-density shielding concretes, must be compared to the shielding performance of ordinary concrete.

The improved quantitative markers of performance of (1) magnetite, (2) hematite and (3) barite concretes relative to ordinary concrete, are summarised in Table 5-11 (contact dose-rate) and Table 5-12 (Transport Index (TI)).

Table 5-11: The improved photon shielding performance of (1) magnetite concrete (MAG-CRT), (2) hematite concrete (HEM-CRT) and (3) barite concrete (BAR-CRT), relative to ordinary concrete (ORD-CRT) as material for a drum containing ILLW from (n,f)^{99}Mo production, i.t.o. contact dose rates (CDRs)

DAF Improvement of Heavier Concretes Relative to Lighter Concretes: Contact Dose-Rate (CDR)						
T_cool (yr)	CDR_ORD / CDR_MAG	CDR_ORD / CDR_HEM	CDR_ORD / CDR_BAR	CDR_MAG / CDR_HEM	CDR_MAG / CDR_BAR	CDR_HEM / CDR_BAR
0.25	5.4	7.4	10.5	1.4	2.0	1.4
1.00	6.7	9.8	18.5	1.5	2.8	1.9
2.00	7.0	10.4	21.1	1.5	3.0	2.0
3.00	7.1	10.7	22.4	1.5	3.1	2.1
4.00	7.2	10.8	23.0	1.5	3.2	2.1
5.00	7.2	10.8	23.3	1.5	3.2	2.2
10.00	7.2	10.9	23.6	1.5	3.3	2.2

Table 5-12: The improved photon shielding performance of (1) magnetite concrete (MAG-CRT), (2) hematite concrete (HEM-CRT) and (3) barite concrete (BAR-CRT), relative to ordinary concrete (ORD-CRT) as material for a drum containing ILLW from (n,f)^{99}Mo production, i.t.o. Transport Index (TI)

DAF Improvement of Heavier Concretes Relative to Lighter Concretes: Dose-Rate at 1m (DR1m)						
T_cool (yr)	DR_TI_ORD/ DR_TI_MAG	DR_TI_ORD/ DR_TI_HEM	DR_TI_ORD/ DR_TI_BAR	DR_TI_MAG/ DR_TI_HEM	DR_TI_MAG/ DR_TI_BAR	DR_TI_HEM/ DR_TI_BAR
0.25	5.2	7.1	9.5	1.4	1.8	1.3
1.00	6.5	9.4	16.3	1.5	2.5	1.7

DAF Improvement of Heavier Concretes Relative to Lighter Concretes: Dose-Rate at 1m (DR1m)						
T_cool (yr)	DR_TI_ORD/ DR_TI_MAG	DR_TI_ORD/ DR_TI_HEM	DR_TI_ORD/ DR_TI_BAR	DR_TI_MAG/ DR_TI_HEM	DR_TI_MAG/ DR_TI_BAR	DR_TI_HEM/ DR_TI_BAR
2.00	6.8	10.0	18.5	1.5	2.7	1.9
3.00	6.9	10.2	19.6	1.5	2.8	1.9
4.00	7.0	10.3	20.1	1.5	2.9	1.9
5.00	7.0	10.4	20.4	1.5	2.9	2.0
10.00	7.0	10.4	20.6	1.5	2.9	2.0

From both Table 5-11 and Table 5-12 the following quantitative improvements can be seen for the use of either of the 3 investigated high-density shielding concretes in a stand-alone drum:

1. The shielding performance of a MAG-CRT drum is 5.2 to 7.2 times better than that of an ORD-CRT drum.

2. The shielding performance of a HEM-CRT drum is 7.1 to 10.9 times better than that of an ORD-CRT drum.

3. The shielding performance of a BAR-CRT drum is 9.5 to 23.6 times better than that of an ORD-CRT drum.

4. The shielding performance of a HEM-CRT drum is 1.4 to 1.5 times better than that of a MAG-CRT drum.

5. The shielding performance of a BAR-CRT drum is 1.8 to 3.3 times better than that of a MAG-CRT drum.

6. The shielding performance of a BAR-CRT drum is 1.3 to 2.2 times better than that of a HEM-CRT drum.

The conclusion is that the best shielding performance is observed with barite concrete while hematite concrete is second best.

5.8.8 Transportability of individual drums in terms of radiological criteria

Research objective RO_5 on page 154 states that the abilities of different concrete materials to make drums transportable without having to wait excessively long, have to be quantified.

Figure 5-8 graphs the contact dose-rates (CDRs) as a function of elapsed time. Drums become transportable when the contact dose-rate (CDR) dips below 2 mSv/h. It is clear that, based on the contact dose-rate, MAG-CRT, HEM-CRT and BAR-CRT drums are transportable after less than 1 year, whereas ORD-CRT drums only become transportable after approximately 2.5 years.

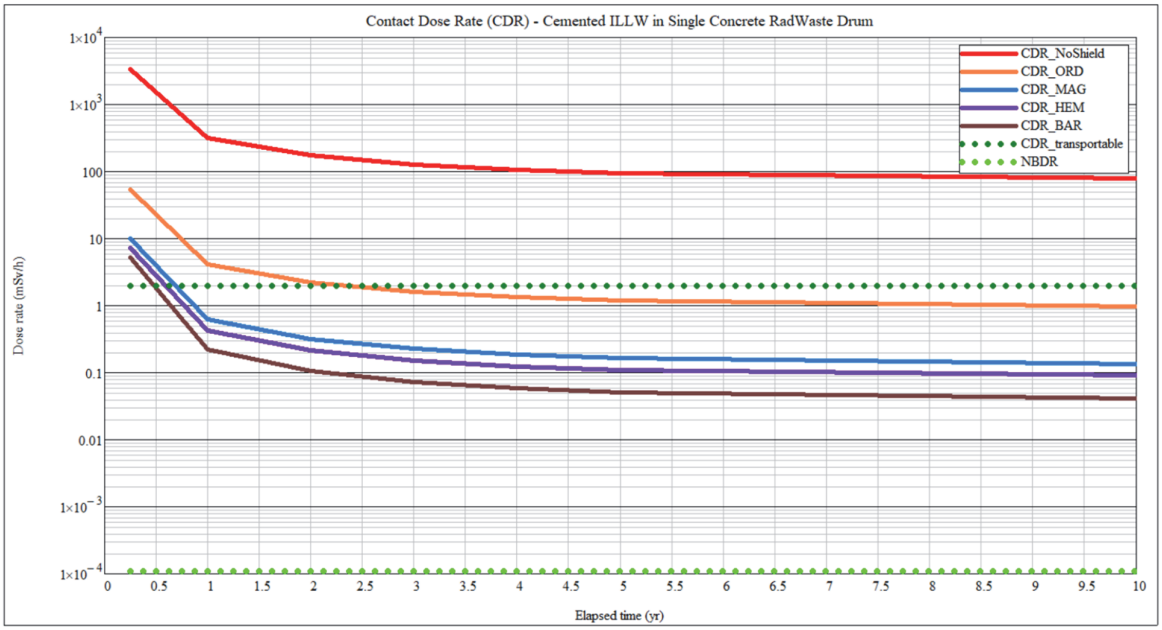


Figure 5-8: Contact dose-rates on an individual concrete drum containing cemented ILLW, as a function of elapsed time

Another criterion for transportability of packages of radioactive material, is the Transport Index (TI), which is the dose rate at 1 m from the outer surface of the drum, expressed in multiples of 10 μSv h^{-1}. The TI values for the drums are plotted in Figure 5-9 as a function of elapsed time.

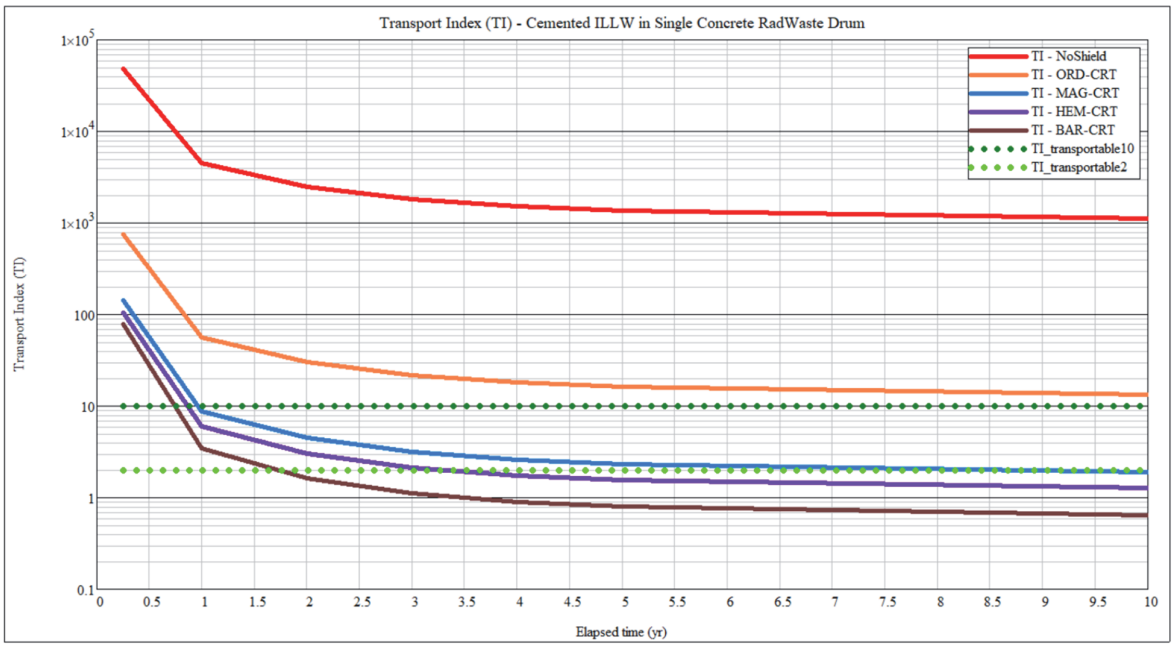


Figure 5-9: Transport Index (TI) for the concrete drums containing cemented ILLW, as a function of elapsed time

From the perspective of the Transport Index (TI), a package of radioactive material becomes transportable by road or rail once its TI dips below 10, and transportable by aircraft when its TI drops below 2. In Figure 5-9 it is seen that an ORD-CRT drum still has $TI > 10$ after an elapsed time of 10 yr, whereas a HEM-CRT drum has $TI < 10$ after 10 months. Figure 5-9 indicates that the use of ORD-CRT may lead to an operational disaster because drums will only become transportable ($TI < 10$) to the disposal site after approximately 15 years. As mentioned in § 5.8.3 on page 173, this will open the door to all the concrete deterioration mechanisms identified in § 3.5.9 (page 104). The conclusion is that the use of ordinary concrete is not a viable option for the ILLW waste drums — the shielding factor of ORD-CRT is too low for ILLW.

5.8.9 Shielding factors achieved with different concrete types

Figure 5-10 shows the *shielding factors* of the different concrete types, as a function of elapsed time. Here we have defined the quantity shielding factor (SF) as $SF = \frac{DR_{NS}}{DR_{WS}}$ (refer to § 2.2 starting on page 55). A shielding factor of e.g. 250 means that the shield is able to reduce the transmitted dose-rate by a factor 250 (relative to a reference case).

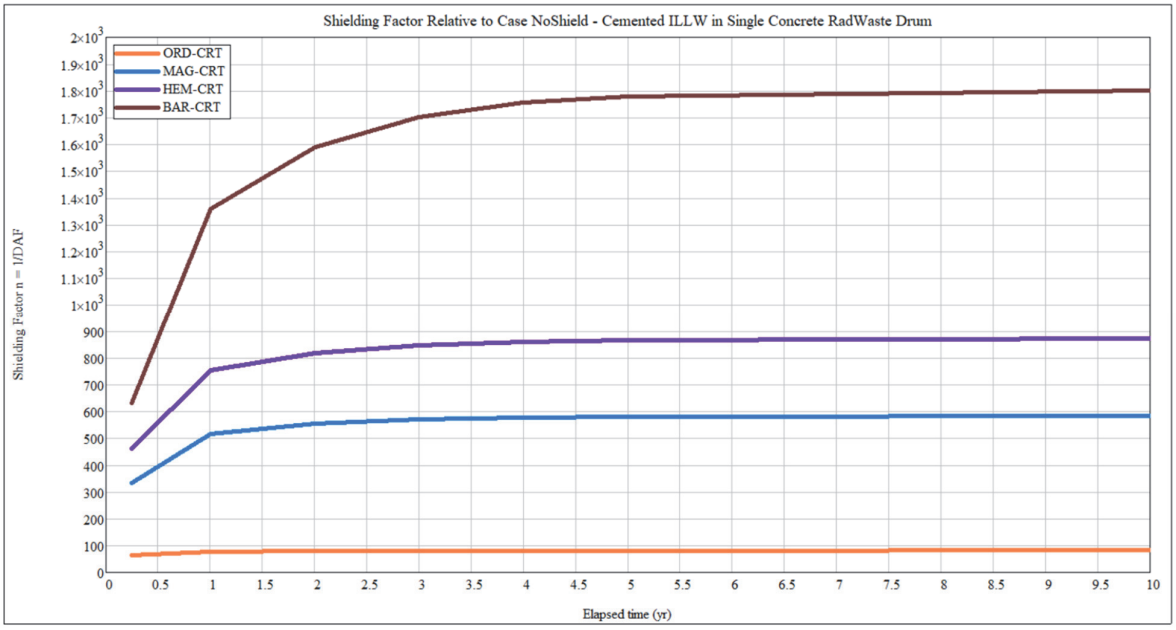


Figure 5-10: Shielding factor for different concrete drum materials, as a function of elapsed time, relative to the case of no shielding material

Figure 5-10 shows that the shielding factor is by far the best for BAR-CRT ($SF \approx 1800$ for 10-year old ILLW) and worst for ORD-CRT ($SF \approx 80$ for 10-year old ILLW). HEM-CRT is, as always, a viable and affordable option ($SF \approx 870$ for 10-year old ILLW), while the performance of MAG-CRT ($SF \approx 580$ for 10-year old ILLW) is intermediate between that of ORD-CRT and HEM-CRT.

Figure 5-11 shows the ratios $\left(\frac{SF_{MAG}}{SF_{ORD}}\right)$, $\left(\frac{SF_{HEM}}{SF_{ORD}}\right)$ and $\left(\frac{SF_{BAR}}{SF_{ORD}}\right)$ as a function of T_{cool}. In other words, it shows how many times better the high-density shielding concretes — MAG-CRT, HEM-CRT and BAR-CRT — perform, compared to the worst-performing shielding concrete, i.e. ORD-CRT.

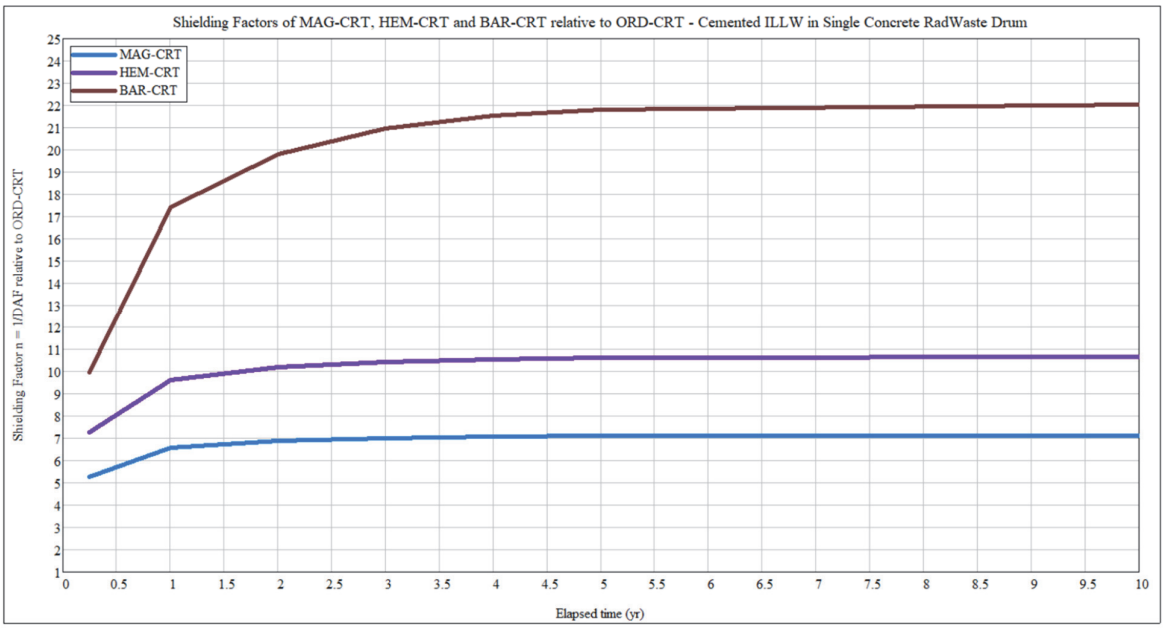


Figure 5-11: The shielding factors achieved with BAR-CRT, HEM-CRT and MAG-CRT, relative to ORD-CRT, at discrete cooling times of the cemented ILLW from ^{99}Mo production by a fission process

The interpretation of Figure 5-11 is straight-forward, e.g.:

1. At $T_{cool} = 1$ yr, BAR-CRT shields its radioactive content approximately 17 times better than ORD-CRT.

2. At $T_{cool} = 1$ yr, HEM-CRT shields its radioactive content approximately 9.5 times better than ORD-CRT.

3. At $T_{cool} = 1$ yr, MAG-CRT shields its radioactive content approximately 6.5 times better than ORD-CRT.

4. At $T_{cool} = 10$ yr, BAR-CRT shields its radioactive content approximately 22 times better than ORD-CRT.

5. At $T_{cool} = 10$ yr, HEM-CRT shields its radioactive content approximately 10.5 times better than ORD-CRT.

6. At $T_{cool} = 10$ yr, MAG-CRT shields its radioactive content approximately 7.0 times better than ORD-CRT.

The relative merit of using BAR-CRT is seen to increase with time, reaching a plateau at $T_{cool} \approx 5$ yrs. At that time, the shielding efficacy of BAR-CRT is a factor 2 times higher than that of HEM-CRT.

5.9 Improved performance of high-density shielding concretes at longer decay times

A trend that is clear in all reported results, tabular and graphic, is that the concrete shielding becomes more effective as the cemented radioactive content in the concrete drum material ages. The reason is that, as a general guideline with reasonably good validity, short-lived radionuclides are very unstable and therefore emit more energetic ionising radiation than longer-lived radionuclides, which are less unstable and usually emit lower energy ionising radiation. As the cemented ILLW ages, the activities of the shorter-lined radionuclides dwindle relative to that of the longer-lived radioisotopes and the average energy of emitted photons, $E_{av}(t)$, decreases as a function of time, t. This trend of the emitted photon spectrum becoming softer as t increases, i.e. $\boxed{E_{av}(t \rightarrow) \downarrow}$ is reported in Table 5-4 in § 5.6.2 on page 166. At cooling times beyond $T_{cool} \approx 2$ yrs, energies of emitted photons are found to shift into the energy range where PEA (photo-electric absorption) is important, and where the average Z-number of the constituent atoms in the concrete becomes more important than the mass-density ρ of the concrete. The linear attenuation coefficient μ for PEA depends as $\mu_{PEA} \propto \rho Z^3$, as shown in Table 2-2 on page 64. The Z-number for the chemical element Ba is $Z_{Ba} = 56$, which is much higher than that of Fe, which is $Z_{Fe} = 26$, so that the linear attenuation coefficient μ of Ba for the attenuation of ionising photons via PEA, is

$$\frac{(56)^3}{(26)^3} \approx 10$$

times more favourable relative to that of the element Fe. It is found that BAR-CRT becomes much better than the other concrete types, at $T_{cool} \geq 1$ yr, whereas it is only marginally better than HEM-CRT at $T_{cool} = 0.25$ yr (around 90 days, i.e. directly following cementation).

5.10 Depth dose curves for different concrete compositions

In this section, depth dose curves for 1-year old cemented ILLW in concrete drums, are presented for the 4 concrete types under investigation. The ILLW is assumed to be 1 year old.

In the calculation models used to generate the results reported in Figure 5-12 and Figure 5-13, the cementation matrix stretches to $R = 22.5$ cm, the stainless-steel wall of the inner drum to $R = 22.8$ cm and the concrete later to $R = 55$ cm.

Figure 5-12 presents the calculated depth dose curves[27], for cemented ILLW in concrete drums having the 4 concrete compositions under assessment.

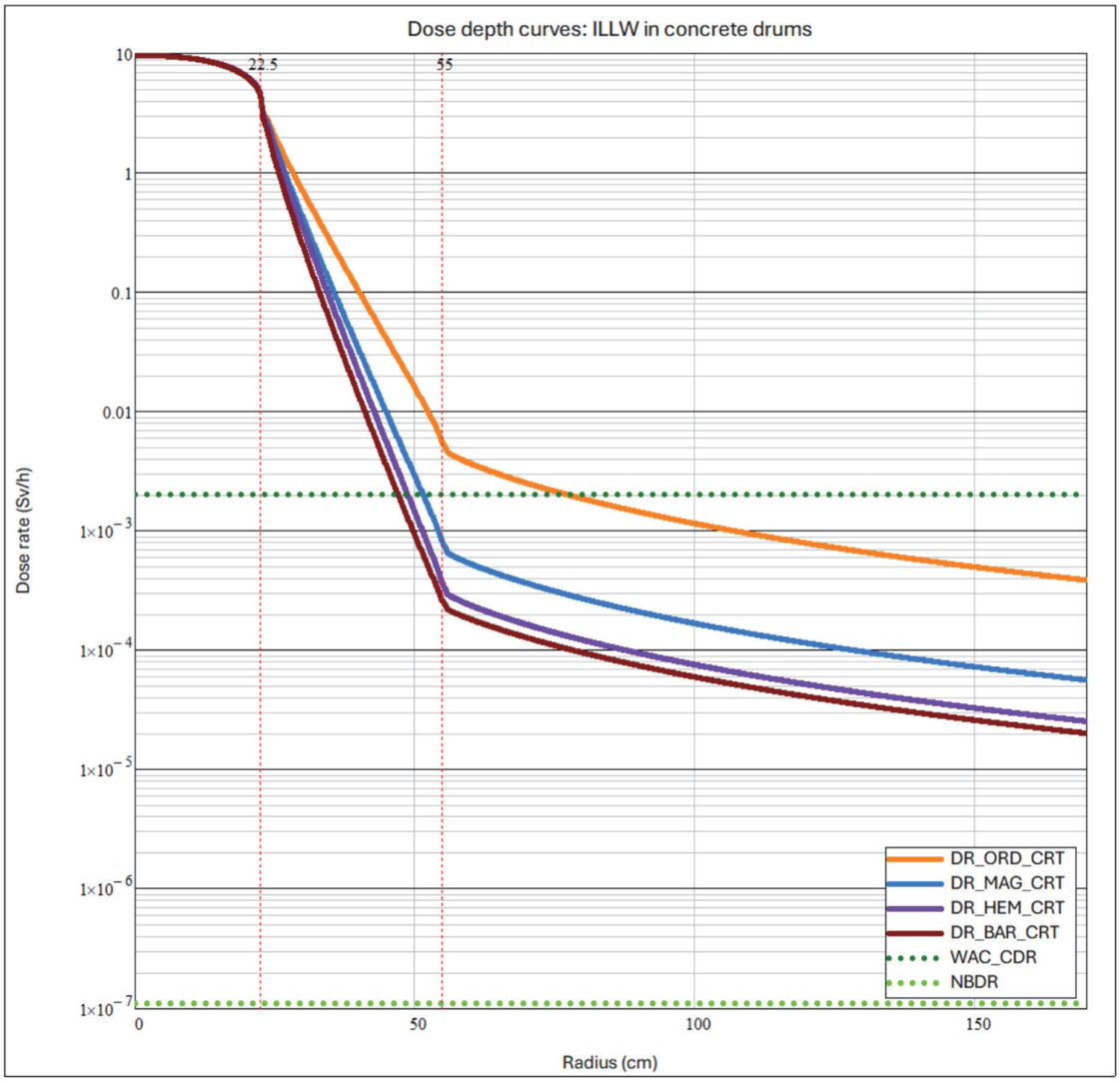


Figure 5-12: Dose rates as a function of the radius, for cemented ILLW in concrete drums with 4 different compositions

[27] Note: "Depth dose curve" is a standard term used in e.g. radiotherapy.

Inside the cementation matrix, dose rates are as high as 10 Sv/h, i.e. in the range where it will cause eventual death for an irradiation time of less than 1 hour. The 3 mm of stainless-steel causes a notable lowering of the dose rate, but the use of larger thicknesses will be prohibitively expensive. The dose depth curves for hematite and barite concrete are steeper than for ordinary concrete. As always, magnetite concrete displays intermediate shielding performance. The lowering of the dose rate through air is not a function of material attenuation, but of geometric attenuation. The dotted dark-green line showing the waste acceptance criterion (WAC) on the contact dose rate (CDR) indicates that, at $T_{cool} =$ 1 yr, all 3 high-density shielding concretes will meet the WAC on contact dose rate (CDR), whereas the ordinary concrete will fail to meet this WAC. The horizontal light green dotted line (seen at the bottom of the plot) indicates the NBDR. The substantial vertical gap between the dose depth curves and this NBDR reference line, shows that the drum always remains "radiologically formidable", even with the use of the best available shielding concrete.

Figure 5-13 shows the radial dependence of the dose rate ratios $\frac{\dot{D}_{OC}(r)}{\dot{D}_{BC}(r)}$ and $\frac{\dot{D}_{OC}(r)}{\dot{D}_{HC}(r)}$ inside and around drums of BAR-CRT and HEM-CRT. In the above ratios, OC signifies ordinary concrete, BC signifies barite concrete and HC signifies hematite concrete.

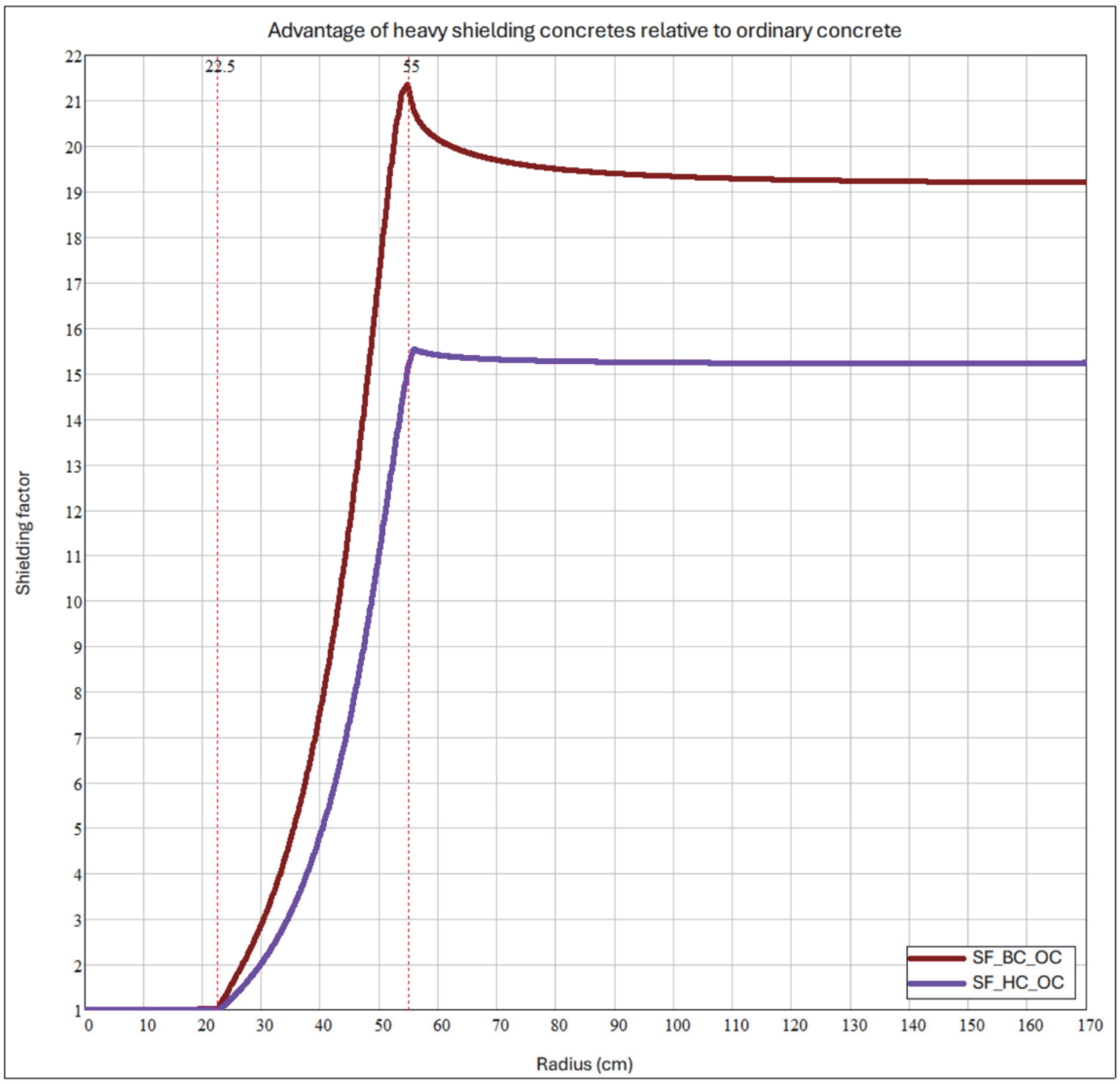


Figure 5-13: Radial dependence of the shielding factors of BAR-CRT and HEM-CRT relative to ORD-CRT, inside and around BAR-CRT and HEM-CRT drums containing cemented ILLW

Figure 5-13 confirms that, at $T_{cool} = 1$ yr, the use of barite concrete leads to a transmitted dose rate that is 19 to 20 times lower than is achieved with an ordinary concrete drum. For hematite concrete, the relative shielding factor for the transmitted dose rate is just above 15. Inside the barite concrete material, a significant amount of photo-electric absorption and Compton scattering "dams up" the photons; beyond the outer surface of the drum, this backscattering effect disappears because air is more than 3 decimal orders of magnitude less dense than concretes, so that the $\frac{\dot{D}_{OC}(r)}{\dot{D}_{BC}(r)}$ curve "dips" and then stabilises. In the case of lighter concretes this backscattering effect is less pronounced than for BAR-CRT.

5.11 Calculated dose rates at the fence around the "decay yard" for an array of 5 × 11 = 55 drums containing cemented ILLW from (n,f)^{99}Mo production

For the array of drums in the "decay yard", an array size of $5 \times 11 = 55$ drums was modelled, and the dose rate was evaluated at the boundary fence around the terrain — refer to Figure 5-7 on page 170. The results of the dose rate calculations for the array of 55 drums, are listed in Table 5-13. The shielding factors *SF* reported in Table 5-13 are the relative shielding factors for ORD-CRT, MAG-CRT, HEM-CRT and BAR-CRT relative to the reference case NoShield, i.e. using only "bare" 3 mm thick, 100-litre stainless-steel drums filled with cemented ILLW, with no concrete.

Table 5-13: Calculated average dose rates at the perimeter fence around an array of 5 × 11 = 55 drums in a "decay yard"

Case: Drum is zero-density concrete (case NoShield)		Case: Drum is Ordinary Concrete (ORD-CRT)		Case: Drum is Magnetite Concrete (MAG-CRT)		Case: Drum is Hematite Concrete (HEM-CRT)		Case: Drum is Barite Concrete (BAR-CRT)	
T_{cool} (yr)	Fence DR (Sv/h)	Fence DR (Sv/h)	SF	Fence DR (Sv/h)	SF	Fence DR (Sv/h)	SF	Fence DR (Sv/h)	SF
0.25	2.982E-01	2.637E-03	113	5.009E-04	595	3.587E-04	831	2.727E-04	1094
1.00	2.789E-02	1.997E-04	140	3.022E-05	923	2.046E-05	1363	1.173E-05	2377
2.00	1.553E-02	1.085E-04	143	1.549E-05	1003	1.043E-05	1489	5.632E-06	2758
3.00	1.132E-02	7.821E-05	145	1.089E-05	1040	7.171E-06	1579	3.774E-06	3000
4.00	9.394E-03	6.450E-05	146	8.930E-06	1052	5.845E-06	1607	3.075E-06	3055
5.00	8.444E-03	5.785E-05	146	7.977E-06	1059	5.229E-06	1615	2.738E-06	3085
10.00	6.943E-03	4.755E-05	146	6.529E-06	1063	4.253E-06	1633	2.214E-06	3136

From Table 5-13, the following quantitative improvements can be seen for the use of shielding concretes, from the viewpoint of the average dose rate at the fence around the decay yard, relative to the case of an array of unshielded, "bare" stainless-steel drums:

1. The shielding performance of an ORD-CRT drum is approximately 110 to 145 times better than that of *not* placing the cemented ILLW inside concrete shielding drums (case NoShield).

2. The shielding performance of a MAG-CRT drum is approximately 590 to 1060 times better than that of *not* placing the cemented ILLW inside concrete shielding drums (case NoShield).

3. The shielding performance of a HEM-CRT drum is approximately 830 to 1630 times better than that of *not* placing the cemented ILLW inside concrete shielding drums (case NoShield).

4. The shielding performance of a BAR-CRT drum is approximately 1090 to 3130 times better than that of *not* placing the cemented ILLW inside concrete shielding drums (case NoShield). With the dose rate at the fence around the decay yard used as the metric-of-merit, the relative merits of using the 3 types of high-density concrete, relative to using ordinary concrete, are summarised in Table 5-14. This table as well as Table 5-15 uses the abbreviation FDR which means "Fence Dose-Rate" i.e. the average dose rate at the fence around the modelled "decay yard" with its array of $5 \times 11 = 55$ concrete drums with cemented ILLW.

Table 5-14: The relative merit of using the 3 types of high-density concrete, relative to using ordinary concrete, for 55 drums arrayed in the decay yard

T_{cool} (yr)	FDR_ORD/ FDR_MAG	FDR_ORD/ FDR_HEM	FDR_ORD/ FDR_BAR
0.25	5.3	7.4	9.7
1.00	6.6	9.8	17.0
2.00	7.0	10.4	19.3
3.00	7.2	10.9	20.7
4.00	7.2	11.0	21.0
5.00	7.3	11.1	21.1
10.00	7.3	11.2	21.5

Still using the dose rate at the fence around the decay yard used as the metric-of-merit, the relative merits of using high-grade heavy concretes, relative to lower-grade heavy concretes, are summarised in Table 5-15.

Table 5-15: The relative merits of using high-grade heavy concretes, relative to lower-grade heavy concretes, for 55 drums arrayed in the decay yard

T_cool (yr)	FDR_MAG/ FDR_HEM	FDR_MAG/ FDR_BAR	FDR_HEM/ FDR_BAR
0.25	1.4	1.8	1.3
1.00	1.5	2.6	1.7
2.00	1.5	2.8	1.9
3.00	1.5	2.9	1.9
4.00	1.5	2.9	1.9
5.00	1.5	2.9	1.9
10.00	1.5	2.9	1.9

For a large array of drums containing cemented ILLW, the following conclusions about the proper selection of concrete type for the shielding drums, follow from Table 5-14 and Table 5-15, when the

dose rate at the fence around the decay yard where the drums are arrayed in a square pitch, is used as a metric of the relative merit of shielding concretes for the drums.

1. Improvements in lowering the dose rate at the fence follow the same pattern of concrete material dependence as is seen with the lowering of the CDR and TI of a single, stand-alone drum.

2. The longer the cooling time, the higher the dose rate reduction achieved by using superior-grade high-density shielding concrete (e.g. HEM-CRT or BAR-CRT) becomes, relative to using lower-grade heavy concrete drums (MAG-CRT) — refer to § 5.9 on page 183 for an explanation.

3. The use of magnetite concrete (MAG-CRT) as drum material, leads to perimeter dose rates between 5.3 and 7.3 times lower than is achieved by using ordinary concrete (ORD-CRT) as drum material.

4. The use of hematite concrete (HEM-CRT) as drum material, leads to perimeter dose rates between 7.4 and 11.2 times lower than is achieved by using ordinary concrete (ORD-CRT) as drum material.

5. The use of barite concrete (BAR-CRT) as drum material, leads to perimeter dose-rates between 9.7 and 21.5 times lower than is achieved by using ordinary concrete (ORD-CRT) as drum material.

6. The use of barite concrete leads to perimeter dose-rates that are between 1.8 and 2.9 times better than is achieved with the use of magnetite (MAG-CRT) concrete.

7. The use of barite concrete leads to perimeter dose-rates that are between 1.3 and 1.9 times better than is achieved with the use of hematite (HEM-CRT) concrete.

Figure 5-14 displays dose rates at the perimeter fence around the array of $5 \times 11 = 55$ concrete drums containing cemented ILLW$[(n,f)^{99}\mathrm{Mo}]$, for different shielding concrete types, as a function of the decay time of the ILLW. The 2 dotted green lines are reference lines to guide the eye with the interpretation of the plotted dose rate values. The dotted green reference line at $1\ \mu\mathrm{Sv/h}$ indicates the dose rate at which the radiological classification of an area, as well as access control and signposting,

typically becomes mandatory. The reference line at 0.11 µSv/h represents the average natural background dose rate on the surface of the earth, i.e. the NBDR.

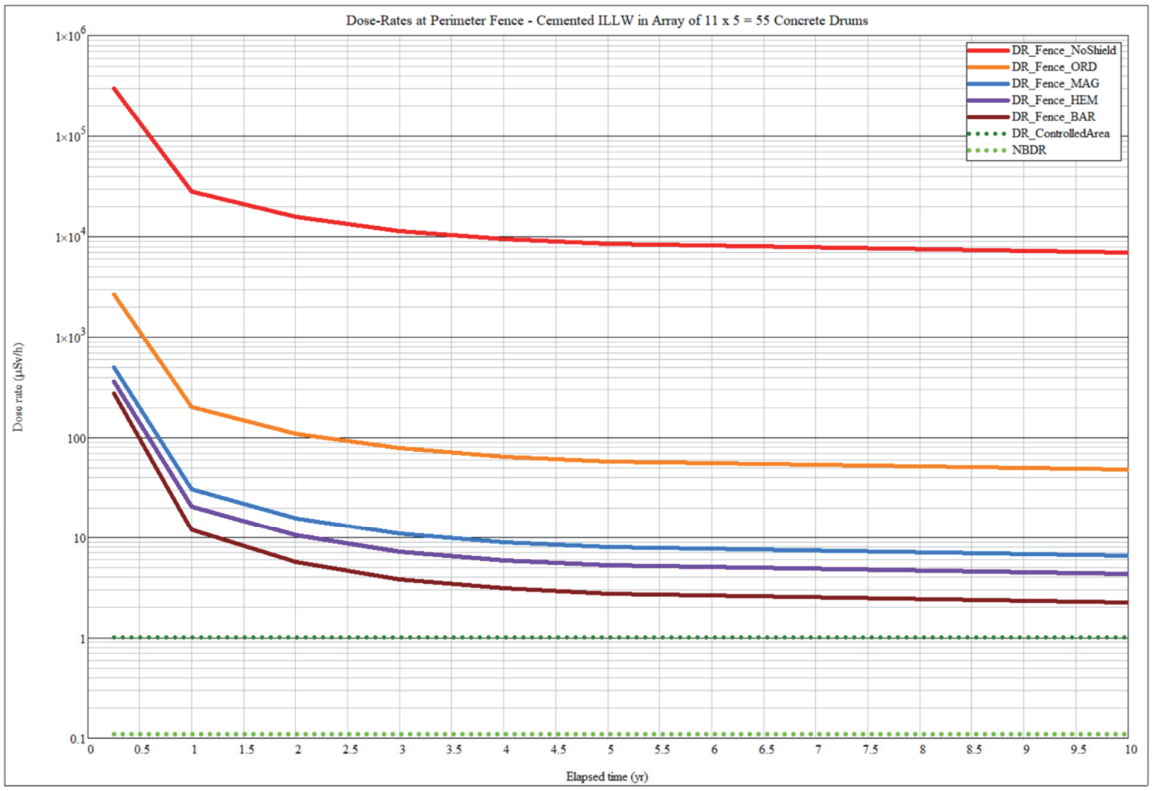


Figure 5-14: Dose rates at the perimeter fence around an array of 5×11=55 concrete drums containing cemented ILLW from the fission-based production of ^{99}Mo, for distinct concrete types, as a function of the decay time of the ILLW

Figure 5-14 shows that the perimeter of the decay yard is not radiologically safe, even when the drums are manufactured from hematite or barite concrete. Inspection of the dose rate at the perimeter of the storage area, for freshly cemented drums (i.e. at the elapsed time of 90 days, which is close to 0.25 years) indicates that an additional shielding factor of circa 100 would be required to ensure that the dose rate at the perimeter of the decay yard is at or below the radiological zoning criteria that would require access control. Increasing the separation distance between the drums and the perimeter fence to a value above circa 20 m would shrink the usable storage space in the decay yard to an impractically low value. A better solution would be to construct a shielding wall all around the decay yard. This solution is pursued in § 5.12 starting on page 193.

Figure 5-15 shows the time-dependence of the shielding factors provided by 4 types of concrete, for the array of 55 concrete drums filled with ILLW in the decay yard. Dose rates are evaluated at the site perimeter fence — see Figure 5-7 on page 170 for a graphic of the drums in the fenced decay yard. In Figure 5-15 the shielding factors are expressed as ratios relative to the dose rate for the case of no shielding (case NoShield), e.g. unshielded, steel-walled 100-litre drums filled with cemented ILLW.

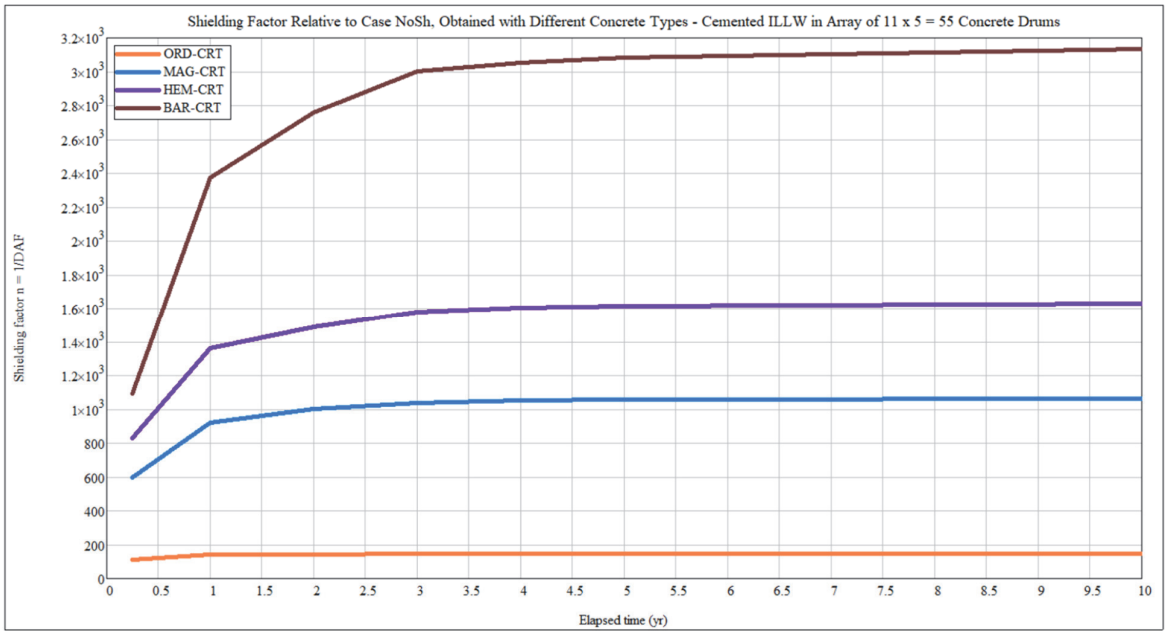


Figure 5-15: Shielding factors, evaluated at the perimeter fence around a 5×11=55 array of concrete drums containing cemented ILLW, as a function of elapsed time — shielding ability of 4 concrete types relative to the reference case of NoShield — no shielding

Figure 5-15 clearly indicates that BAR-CRT is a superior shielding material — it lowers the dose rate at the site perimeter by as much as a factor 3100 relative to case NoShield. The next best concrete material is HEM-CRT — the shielding performance of a HEM-CRT drum is as much as 1630 times better than that of using "bare" steel drums. The shielding performance of a MAG-CRT drum is as much as 1060 times better than case NoShield, while the shielding factor obtained with ORD-CRT drums is only 110 to 145 times better than that of case NoShield. ORD-CRT is a mediocre shielding material, while HEM-CRT and, especially BAR-CRT, are notably superior to ORD-CRT in their abilities to lower dose rates.

Relative shielding factors, evaluated at the perimeter fence around a $5 \times 11 = 55$ array of concrete drums, are shown in Figure 5-16, which displays the shielding ability of MAG-CRT, HEM-CRT and BAR-CRT relative to ORD-CRT drums containing cemented ILLW, as a function of elapsed time.

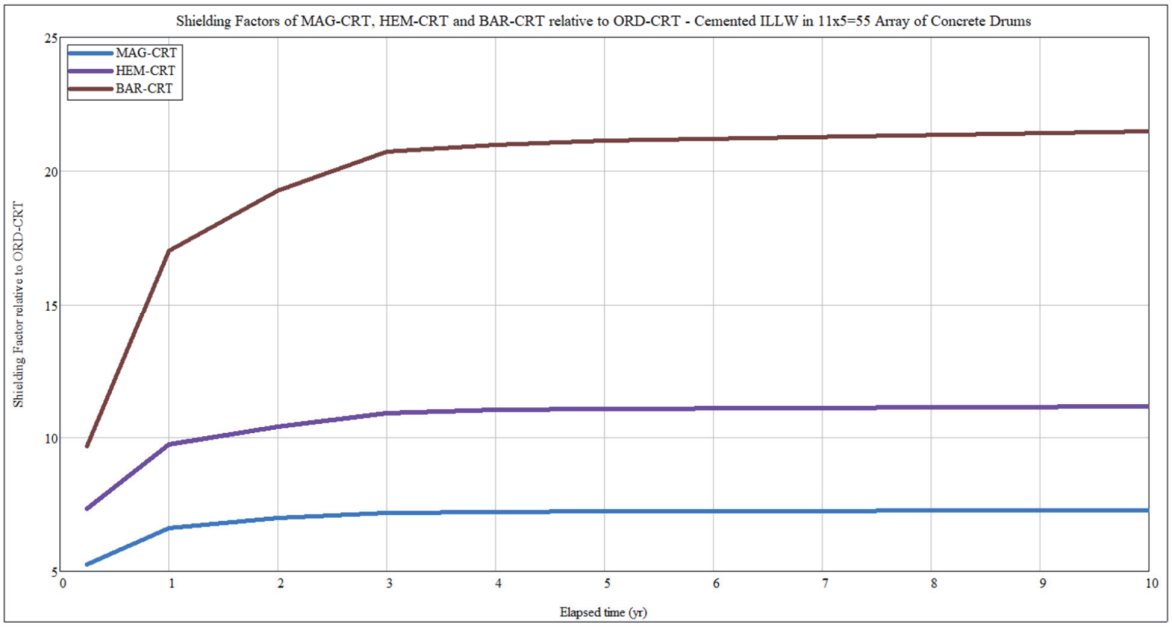


Figure 5-16: Relative shielding factors, evaluated at the perimeter fence around a 5×11=55 array of concrete drums containing cemented ILLW, as a function of elapsed time — shielding ability of MAG-CRT, HEM-CRT and BAR-CRT relative to ORD-CRT

Figure 5-16 shows that using HEM-CRT leads to perimeter dose-rates up to 11 times lower than is achieved with the use of ORD; using BAR-CRT leads to perimeter dose-rates up to 21 times lower than is achieved with the use of ORD-CRT. Again, it is seen that ORD-CRT is an underperforming shielding material, whereas HEM-CRT and, especially BAR-CRT, are significantly superior shielding materials for cemented ILLW. It is also noteworthy that the superiority of HEM-CRT and BAR-CRT relative to ORD-CRT increases with the elapse of time. The reason for this consistently observed phenomenon is explained in § 5.9 on page 183.

Figure 5-17 shows the shielding factors obtained with the use of BAR-CRT relative to the use of MAG-CRT and HEM-CRT.

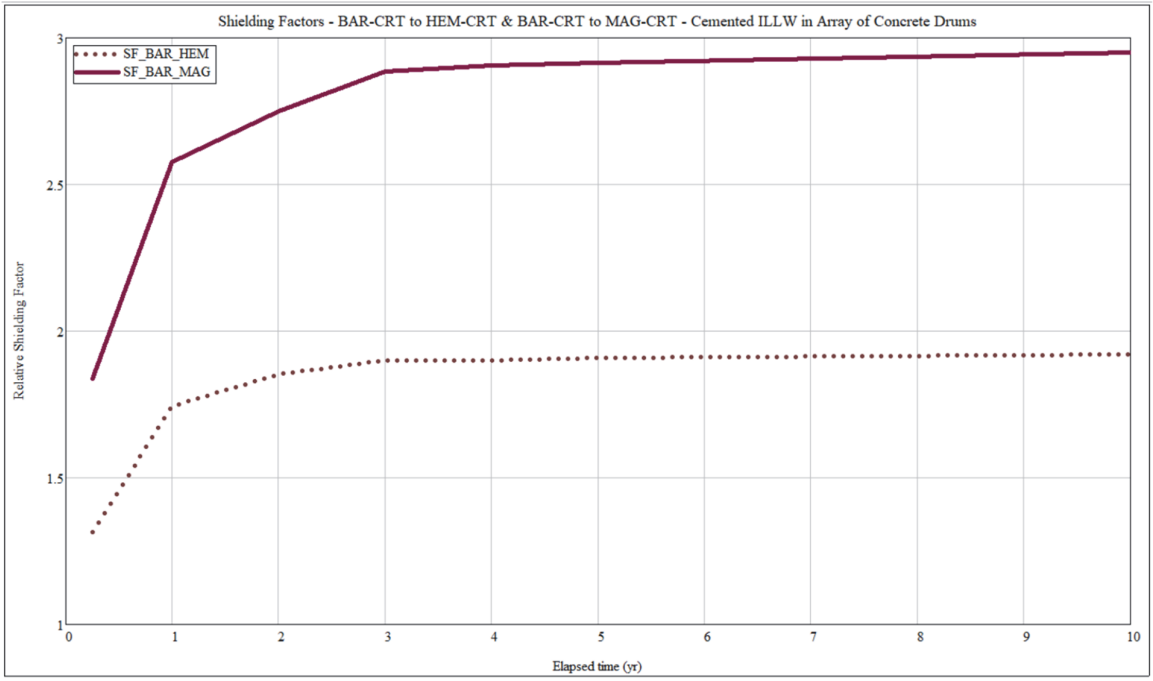


Figure 5-17: Relative shielding factors, evaluated at the perimeter fence around a 5×11=55 array of concrete drums containing cemented ILLW, as a function of elapsed time — shielding ability of BAR-CRT relative to MAG-CRT and HEM-CRT

From Figure 5-17 it is seen that the use of BAR-CRT drums lowers perimeter dose-rates up to 2.9 times better than MAG-CRT drums and up to 1.9 times better than HEM-CRT drums.

In all the graphs of shielding factors, it is observed that the relative dose rate reduction advantage of BAR-CRT over other concrete types, and of HEM-CRT over ORD-CRT, become larger at longer cooling times of the radioactive waste. The reason(s) are explained in § 5.9 on page 183.

5.12 Contour plots of the dose-rate fields around single and multiple concrete drums containing cemented ILLW

The dose-rate field through and around a single concrete drum filled with radioactive waste, is plotted in Figure 5-18. The drum rests on a large concrete floor slab.

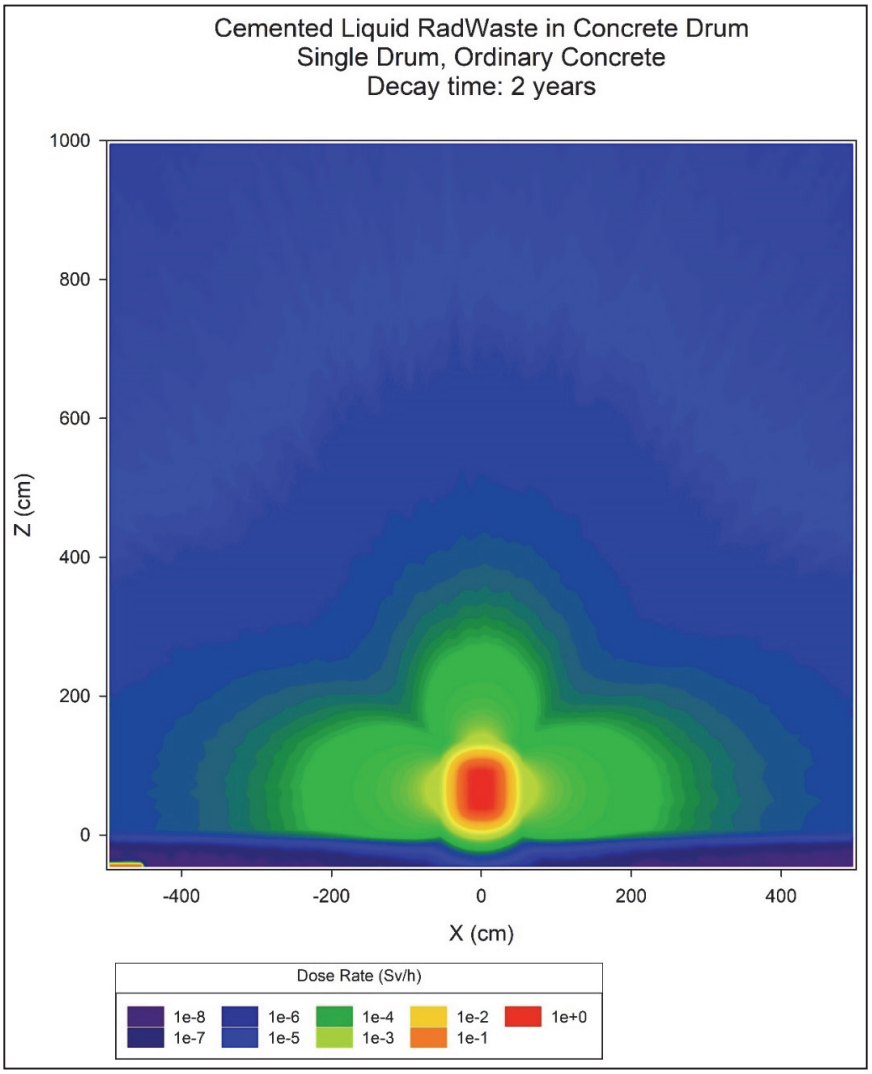


Figure 5-18: Dose-rate field through and a single drum filled with radioactive waste, which rests on a large concrete slab

The dose-rate field in the decay yard, where an array of $5 \times 11 = 55$ ordinary concrete drums with cemented ILW are stored, is shown in Figure 5-19.

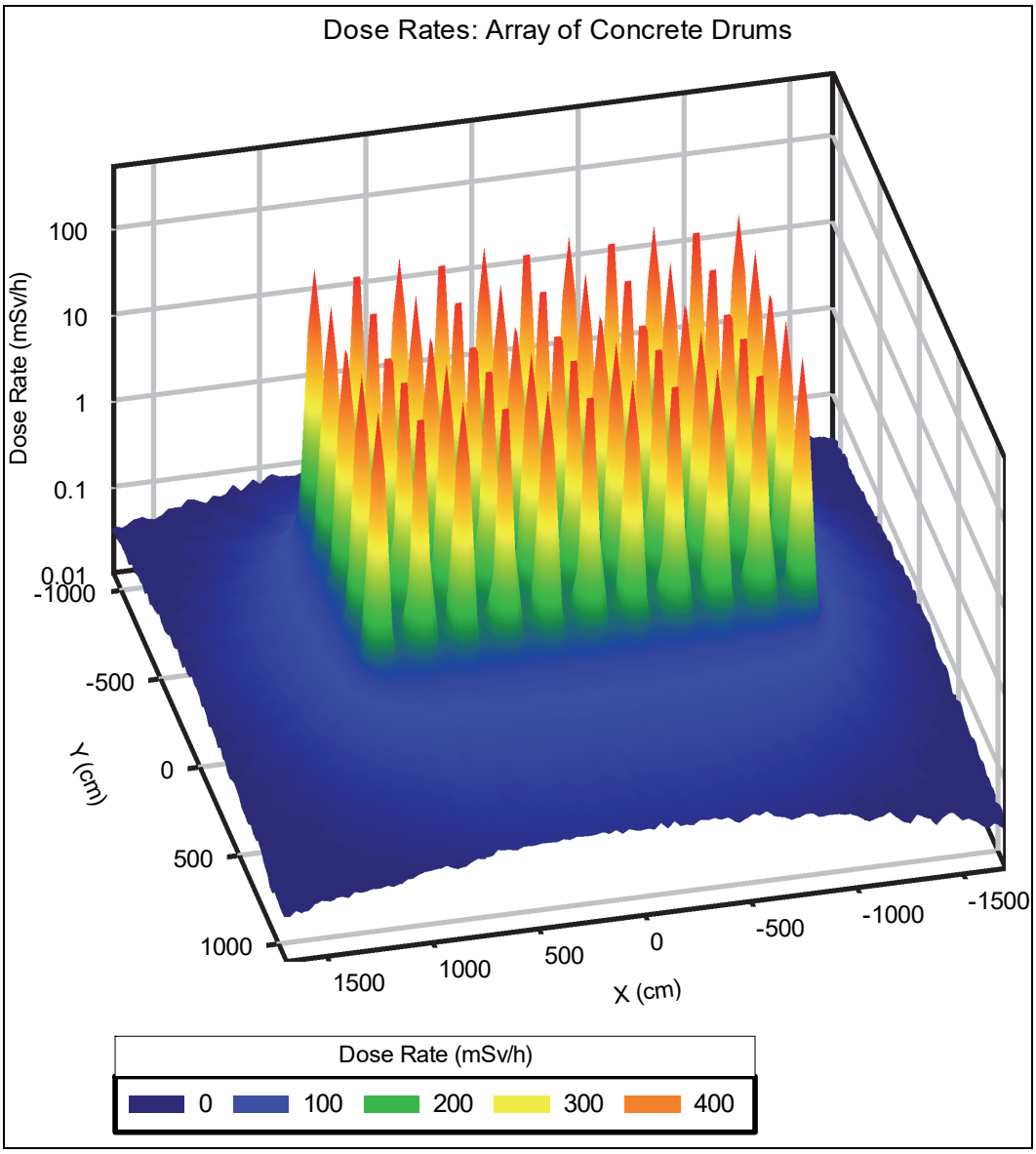


Figure 5-19: Dose-rate for the "decay yard" where an array of 11×5 drums is stored

Note that Figure 5-19 is not quantitatively informative, but rather serves as a "sanity-check", i.e. a qualitative verification of the realism of the MCNP calculation model. There is a distinct radiological "hotspot" at the centre of every drum, which verifies the soundness of the MCNP model.

Figure 5-20 shows the dose-rate field $\dot{D}(x, y)$ in the decay yard when cemented ILLW is placed in a 21×5 array of unshielded 100-litre stainless-steel drums. The logarithmic vertical scale acts to "blunt" high dose rate peaks and shows greater detail about $\dot{D}(x, y)$ further away from the drums. The lateral dose rate field extends further on the "long side" (21 drums) of the array than on the short side

(5 drums). Note that the tick labels on the x-axis and y-axis do not represent physical distance and are unitless numbers generated by the data visualisation software.

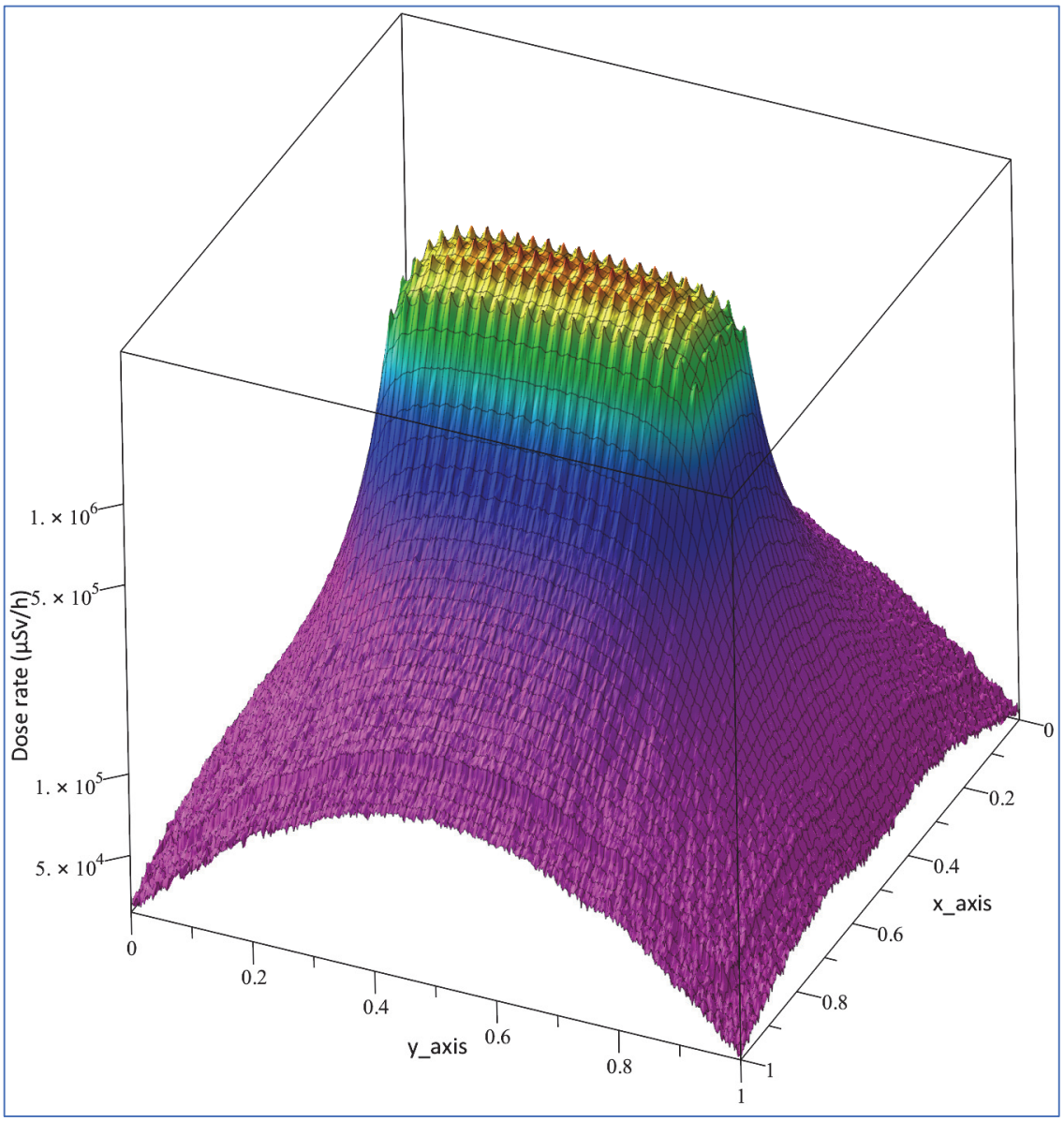


Figure 5-20: Dose rates in the decay yard when cemented ILLW is placed in a 21×5 array of unshielded 100-litre stainless-steel drums

5.13 Investigation of the shielding effect of a concrete shielding wall of different thicknesses, around the decay yard

Research objective RO_{II} on page 155 states that a shielding wall around the perimeter of the decay yard where ILLW drums are stored before transport to the disposal facility, must be designed if necessary.

From Figure 5-14 on page 190, it is evident that dose rates at the perimeter fence of the decay yard will easily exceed the limiting value of 1 μSv/h. If the ambient dose rate in an area exceeds the above constraint, the area must be placed under radiological signposting and access control. Because it would be disruptive to close existing roads and prevent people from walking close to the decay yard, a better solution would be to construct a shielding wall around the perimeter of the storage area.

An investigation about the shielding effect of an ordinary concrete wall around the decay yard, was performed. Wall heights of 240 cm and 270 cm, and wall thicknesses between 40 cm and 60 cm, were modelled. A judgement was made that a wall height higher than 270 cm would not be acceptable from a terrain planning perspective, because it would give the area a "prison atmosphere". A series of MCNP calculation models were developed and a RAR archive file containing the model inputs are embedded in Calculation model 5-1[28]. The source term was taken to be ILLW at a decay time of 1 year.

Calculation model 5-1: Concrete wall around decay yard for concrete drums filled with $ILLW[(n,f)^{99}Mo]$



An important consideration in the design of shielding walls around radioactive material, where a shielding roof structure is thin, or entirely absent, is skyshine. Skyshine refers to scattered photons from, mainly, Compton scattering of ionising photons with electrons in the atoms in air. The downward moving component in skyshine can be likened to a "rain" of ionising radiation that descends from

[28] The above archive file is opened by double-clicking it; a prerequisite is that the archive package WINRAR must be downloaded from the URL https://www.win-rar.com and installed on the user's PC. Once uncompressed in a suitable folder, the individual MCNP model files should be opened using text editors such as NotePad++ or VS CODE.

above. In the case of the decay yard, drums can initially have contact dose rates as high as 2 mSv/h (i.e. more than 10^4 times above natural background levels), and there is no shielding roof, i.e. skyshine will be a certainty.

Figure 5-21 is a contour plot of an y-z view of dose rates $\dot{D}(y,z)$ in the decay yard, when a 270 cm high and 60 cm thick ordinary concrete shielding wall is placed along the entire periphery.

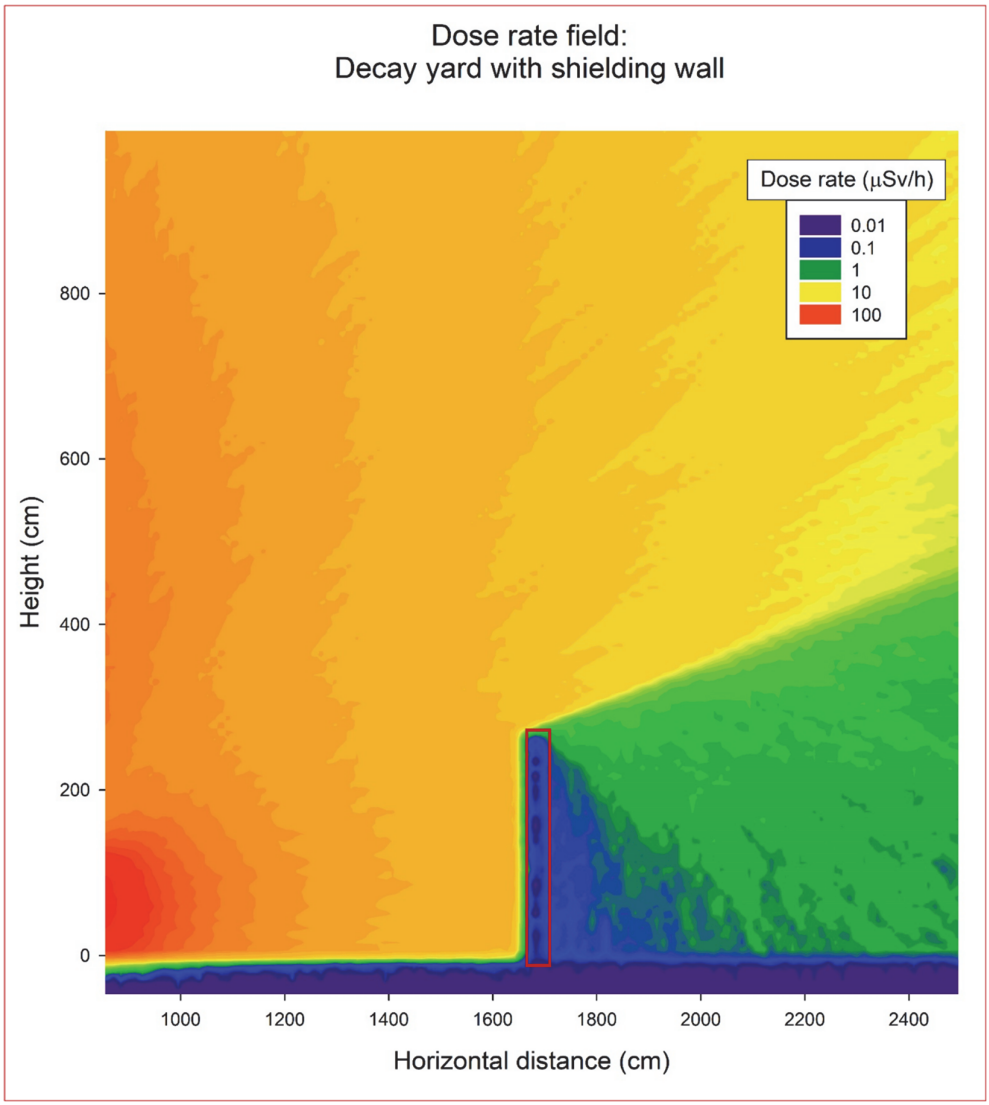


Figure 5-21: Contour plot of the shielding effect of a shielding wall around the perimeter of the decay yard — the wall is 270 cm high and 60 cm thick.

In Figure 5-21, the area where the array of concrete drums stands, is in the bottom left-hand corner; the high dose rate is recognised by the intense red colour. Unmistakable evidence of skyshine is

observed in the contour plot — skyshine radiation "rains down from above" on the right-hand side of the shielding wall (the wall is marked with a red outline). This observation implies that making the wall thicker and thicker will, at some point, become pointless, because skyshine will cross the wall from above. Skyshine entering the zone of human occupancy beyond the wall by "raining down from above", represents a radiation exposure pathway that bypasses the shielding effect of the wall on the line-of-sight transmitted dose rate. A "law of diminishing returns" will therefore be encountered as the wall is made thicker and thicker, and a limit will be reached where thicker walls become radiologically pointless and uneconomical.

The effect of the skyshine phenomenon observed in Figure 5-21 on dose rates beyond the shielding wall, is visualised in Figure 5-22 for perimeter ordinary concrete walls that are 240 cm high and have thicknesses of either 40 cm or 50 cm.

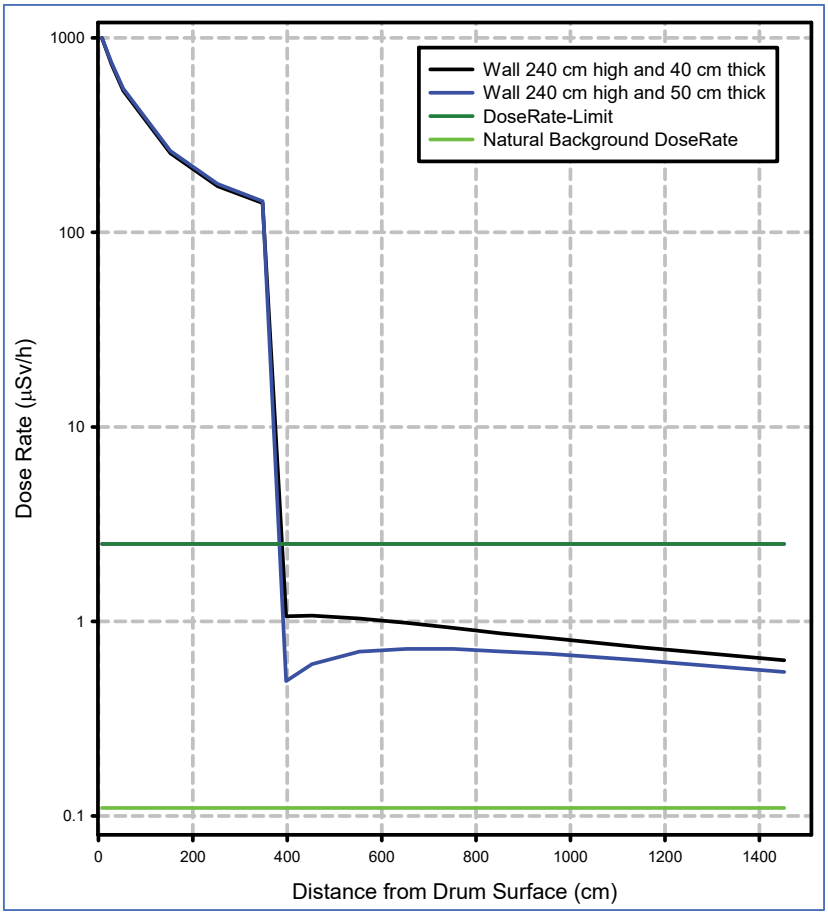


Figure 5-22: Influence of skyshine on dose rates beyond a 240 cm high perimeter shielding wall around the decay yard, for 2 wall thicknesses

From Figure 5-22 a judgement can be made that one will not gain any significant radiological advantage by making the wall thicker than 50 cm. Skyshine photons "raining down from above" make it pointless to increase the thickness of the shielding wall around the decay yard where drums of ILLW are stored, beyond the above thickness.

Figure 5-21 and Figure 5-22 show that there is a low dose-rate region in the "shadow" just outside the shielding wall, but that skyshine will cause dose rates beyond the wall to "creep back" as the bystander moves away from the wall. For a wall with a height of 240 cm and a thickness of 50 cm, the dose rate is highest when the person stands 2 m to 4 m away from the wall. For shielding walls thicker than 50 cm, the above-mentioned shadow and skyshine effects cause it to be safer to stand right against the outside of the perimeter wall, than to stand e.g. 4 m away from the wall's outer surface.

The 50 cm thick ordinary concrete shielding wall around the decay yard is able to reduce dose rates beyond the wall periphery by as much as 2 decimal orders of magnitude. It is judged that a wall thickness around 50 cm would be nearly optimal from a cost-benefit perspective. Designing the wall thicker than 60 cm is not recommended, as a result of the important contribution of skyshine to the dose rate field beyond the wall.

Figure 5-23 is a 3-D plot that shows how a shielding wall around the periphery of the decay yard, lowers dose rates beyond the wall.

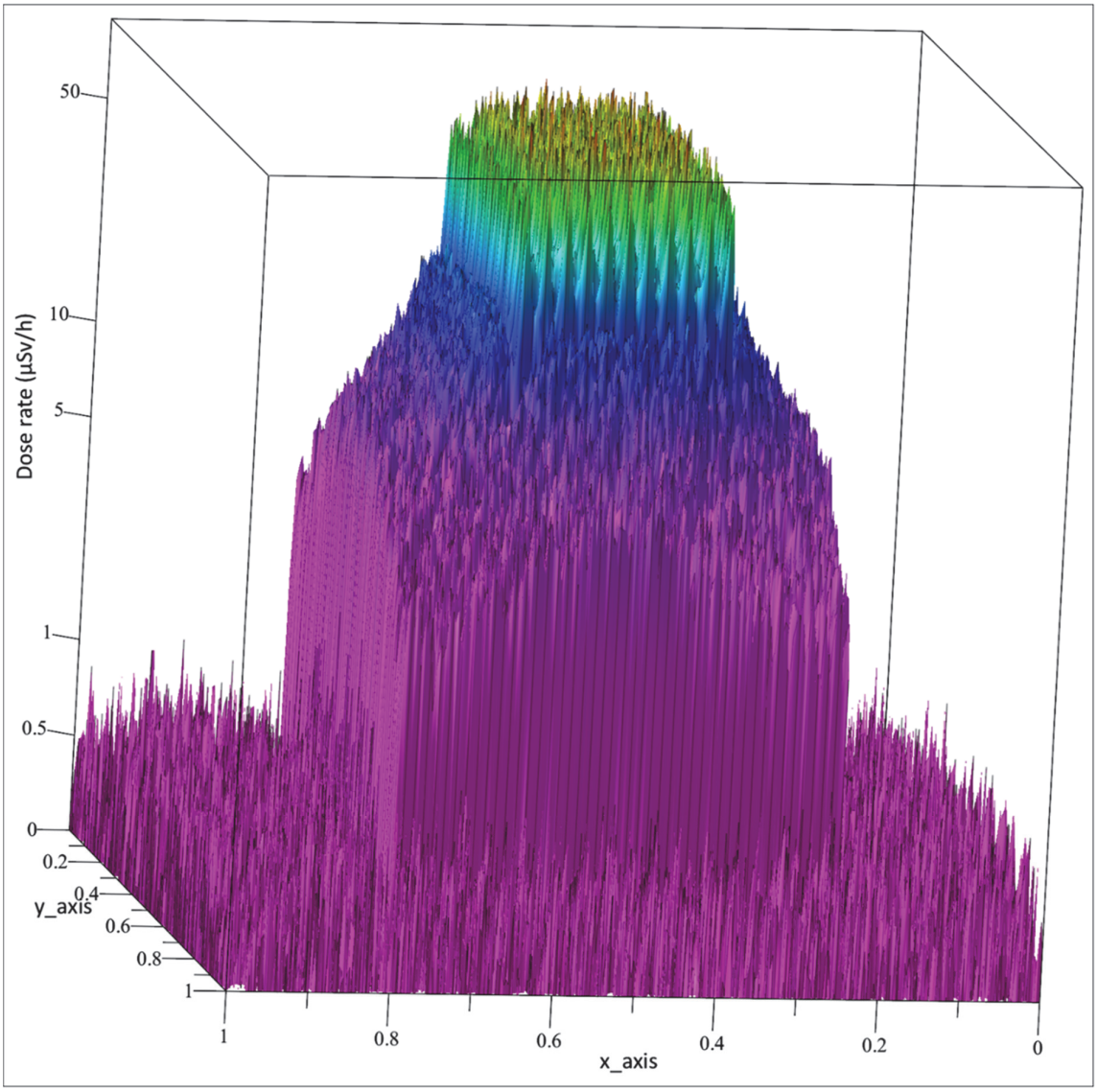


Figure 5-23: Ability of a shielding wall around the periphery of the decay yard, to lower dose rates

The sharp vertical drop in dose rates from circa 10 µSv/h to circa 0.2 µSv/h seen in Figure 5-23 shows the shielding effect of a 50 cm thick concrete wall. In contrast, Figure 5-20 (page 196) shows dose rates when a shielding wall around the periphery of the storage area, is absent. (Note: Unfortunately the Maple-2021 software used to produce Figure 5-23, appears to amplify statistical uncertainties in calculated results.)

Below is an embedded visualisation of skyshine, generated from an MCNP simulation; the video is launched by double-clicking its icon:



If the shielding factor achieved with a wall that is 240 cm high and 40 cm thick is taken as a baseline, the dose rate reduction factors obtained with the same wall height and a 60 cm thick wall appears to be less than 3 %, if the maximum dose rate in the vertical zone of human occupancy on the far side of the wall is used for comparison. For a wall that is 270 cm thick, the shielding factor appears[29] around 6% better for a 40 cm thick wall and 8% better for a 270 cm thick wall. There appears to be more value in making the shieling wall higher than in making it thicker. This is expected given the directionality of the skyshine photons that surmount the wall. Making the wall higher than 270 cm may meet resistance because it may give the area a prison atmosphere.

The final design recommendation for a perimeter shielding wall around the decay yard is that the minimum wall height should be ~240 cm and the maximum height ~270 cm, while the thickness should not be less than ~40 cm and not more than ~50 cm.

5.14 Required burial depth of concrete drums holding ILLW, in trenches at the disposal site

5.14.1 Research objective RO_{12}

Research objective RO_{12} is the quantification of the required burial depth for concrete drums containing ILLW, to reduce the transmitted dose rate on the surface of the landscape to $\frac{1}{10} \times$ NBDR, i.e. a value 10% of the natural background dose rate. The average value of the natural background dose rate (NBDR) is just above 1.0E-7 Sv/h, so that the above constraint on the surface dose rate above a trench filled with radioactive waste drums, calculates to 1.0E-8 Sv/h.

[29] The term "appear" is used on purpose because statistical error estimates for this scenario range between 6 % and 12 %, for 4000-minute long MCNP runs. No firm quantitative conclusions could be reached, given the time constraints for the research.

5.14.2 MCNP calculation model: Trench filled with buried drums

An MCNP calculation model was developed for a trench that contains $11 \times 11 \times 3 = 363$ concrete radioactive waste drums, of the waste form and drum design studied in this work. The drums are stacked in 3 vertical layers in the z-direction, with 11 drums in the x-direction and 11 drums in the y-direction. The stacking order is a square-pitched array. The nearest spacing between adjacent drums is below 1 cm. Each drum is filled with the design-basis source term for ILLW at the decay time $T = 1$ yr — the earliest possible age at which the drums will arrive at the final disposal site. The drum material is assumed to be magnetite concrete — this adds a degree of realistic conservatism to the calculation, because the Fe content of this concrete type, as well as its mass-density, are both lower than that of the preferred drum material, namely hematite concrete. The lateral soil, the underlying soil/rock as well as the soil overburden were assumed to all have an elemental composition that is completely dominated by SiO_2 (silicon dioxide), and its bulk density was taken as a conservative-realistic $\rho = 1.3$ g cm^{-3}. It should be noted that calculated dose rates for clay soil and sandy soil will be quite similar, because clay is an aluminium oxide while sand is an oxide of silicon; the atomic numbers of Si and Al, and therefore their photon attenuation characteristics, are very similar, because $Z(\mathrm{Al}) = 13$ and $Z(\mathrm{Si}) = 14$.

5.14.3 MCNP-generated plots of calculation models: Trench filled with buried drums

Figure 5-24 shows a side-view of the $11 \times 11 \times 3$ array of concrete drums buried in a trench at a disposal site. The MCNP plotter was used to generate pictures of the modelled geometry of the drums in trench geometry[30].

[30] Note that Figure 5-24 and most other graphics in this work must be viewed in full colour to be meaningful; a grey-tone printout will be incomprehensible.

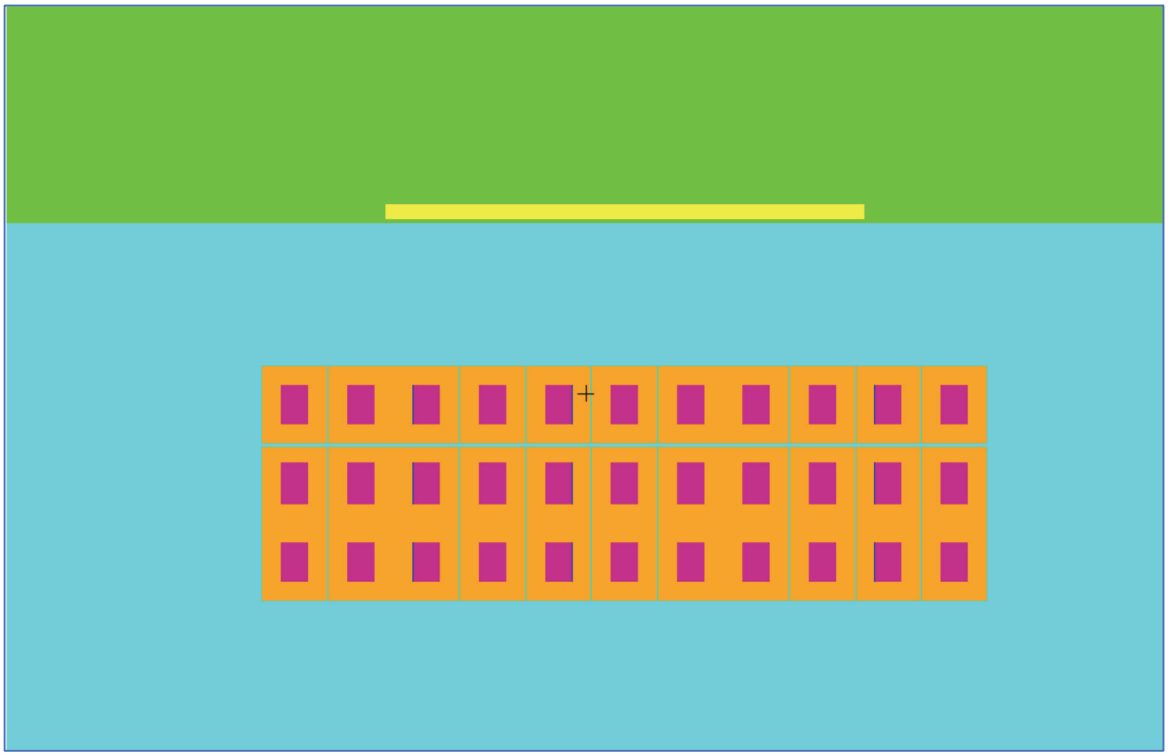
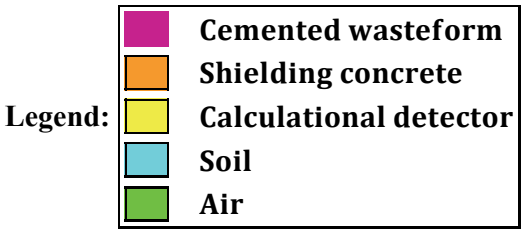


Figure 5-24: An MCNP geometry plot of the side-view (i.e. x-z view) of an 11×11×3 square-pitched array of radioactive waste drums buried in a trench at a disposal site; the modelled thickness of the soil overburden in this diagram is 2.35 m



A top view of the drums in the trench is presented in Figure 5-25.

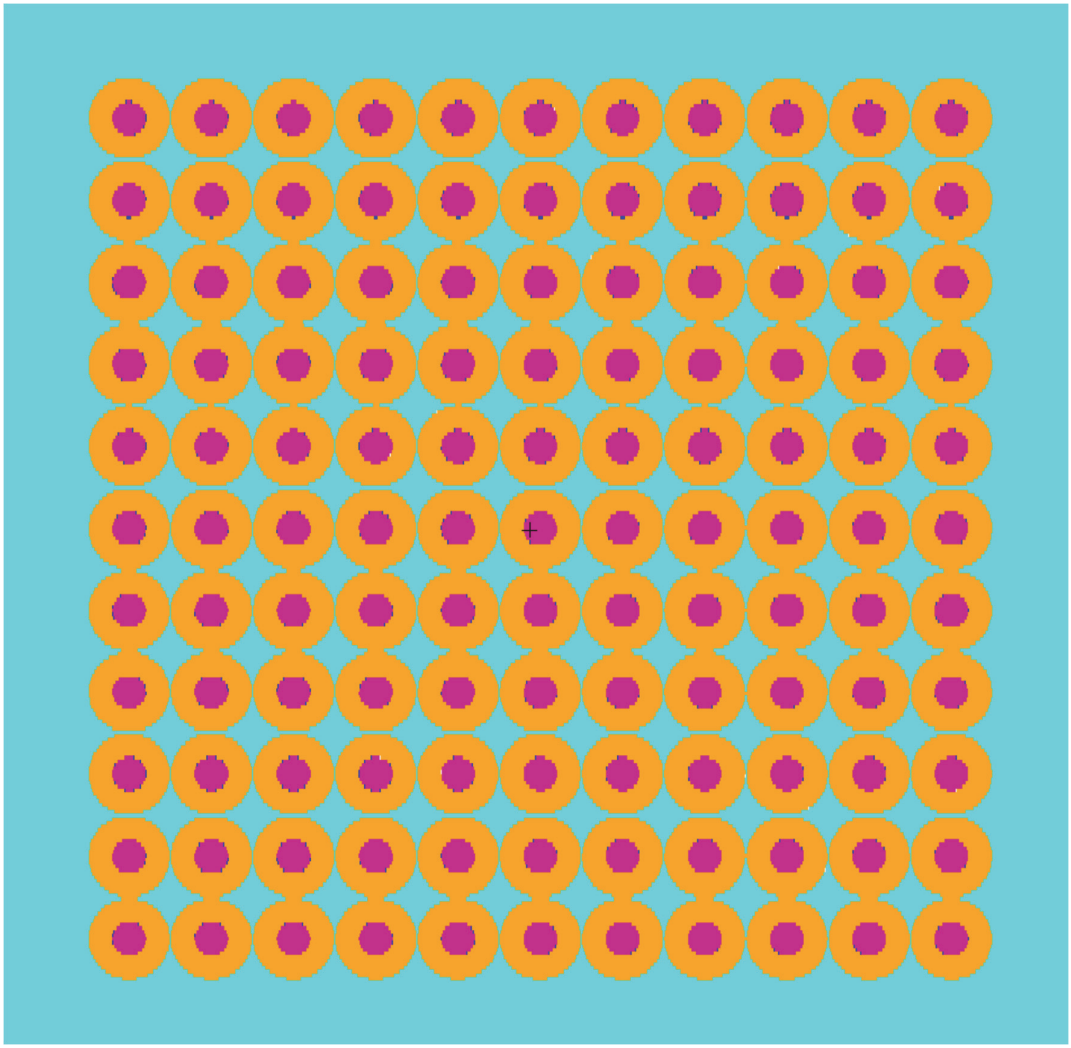
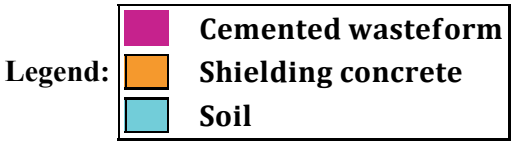


Figure 5-25: A top view (i.e. x-y view) of 11×11 concrete drums filled with radioactive waste, in a trench at a disposal site



5.14.4 Results of dose rate calculations: concrete drums with radioactive waste buried in a trench at a disposal site

Results of dose rate calculations for the concrete drums containing radioactive waste, buried in a trench at a disposal site, in an $11 \times 11 \times 3$ array are presented below.

Figure 5-26 shows a side-view (i.e. an xz plot) of the dose rates in and around the 3 stacked layers of radioactive waste drums buried in the trench.

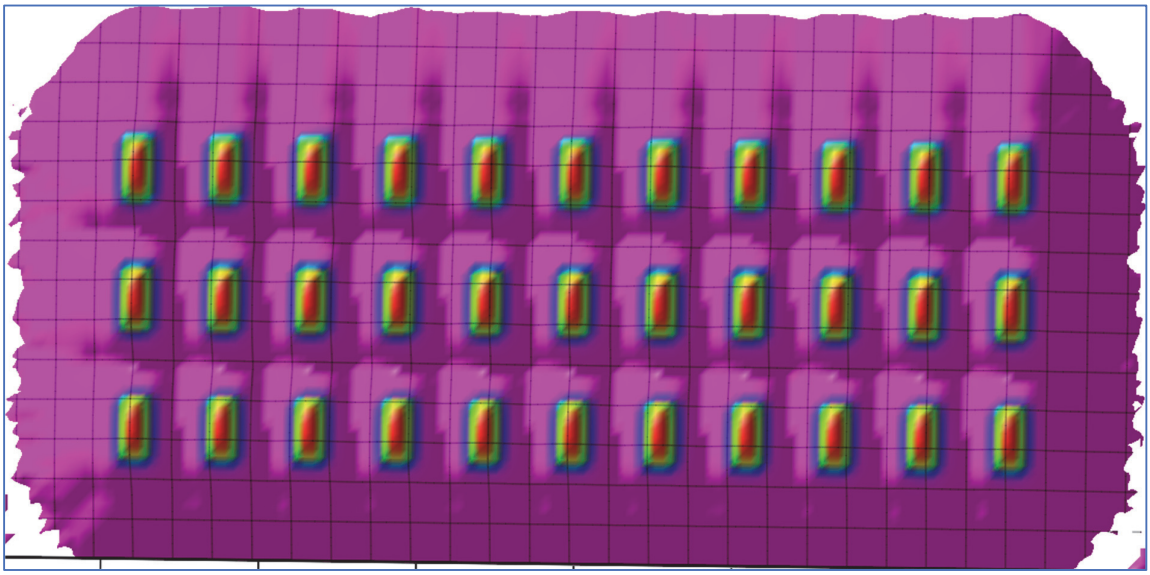


Figure 5-26: Side-view (x-z plot) of dose rates around waste drums buried in a trench (logarithmic dose-rate axis)

Figure 5-27 displays the same data as Figure 5-26, now with a linear axis for the dose rate, and observed at a slight angle.

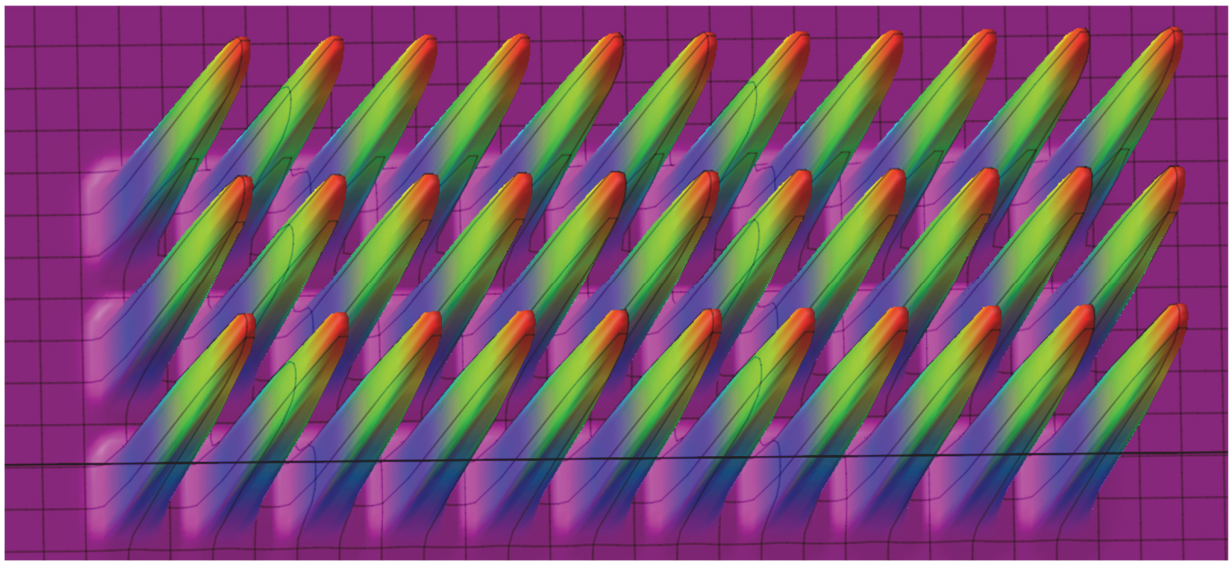


Figure 5-27 Side-view (x-z plot) of dose rates around waste drums buried in a trench (linear dose-rate axis)

Figure 5-26 and Figure 5-27 are not quantitatively informative, but serve as qualitative, visual validations of the calculation model — the peaks in the dose-rate field coincide exactly with the

physical placement of the underground drums. Validation checks of this nature are also termed "sanity checks".

Quantitatively useful results are presented in Figure 5-28, which shows how dose rates on the ground surface vary as a function of the thickness of the layer of soil between the top of the topmost row of buried drums, and the soil surface[31].

[31] Comment by study supervisor TJvR: The oscillatory nature of the curve in Figure 5-28 has to do with statistical fluctuations in the calculated results (below 3 %) as well as the display of linearly interpolated values on a logarithmic vertical axis.

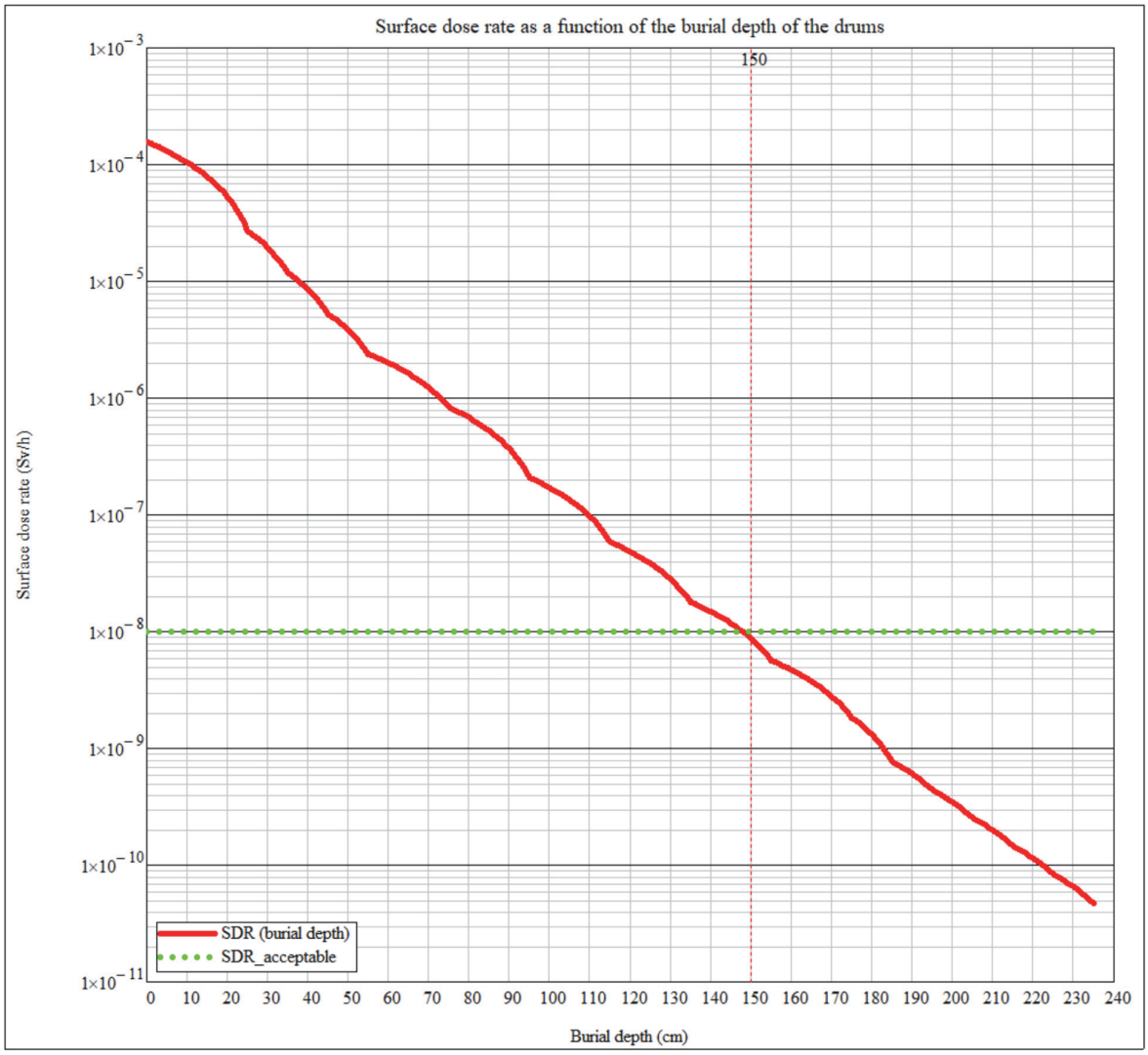


Figure 5-28: Dependence of the surface dose rate directly above buried radioactive waste drums, on the thickness of soil covering to topmost row of underground drums; there are 11×11×3 = 363 radioactive waste drums in the trench, each drum filled with the design-basis source term at a decay time of 1 year

Figure 5-28 indicates that, from a radiation shielding perspective, the required thickness of the layer of soil above the drums must be at least 150 cm. With this thickness of soil overburden covering the drums, the peak dose rate on the soil surface will be approximately 10^{-8} Sv/h, which is below 10% of the prevailing NBDR. This criterion means that the added dose rate attributable to the presence of the disposed drums will have a somewhat smaller magnitude than the typical 1σ standard deviation on the NBDR, when the latter is sampled over a terrain that spans several hectares. Other safety considerations also influence the decision on how deep the drums have to be buried. One issue is e.g.

the likelihood of human intrusion after the closure and abandonment of the site in the distant future, as well as the possibility that wind erosion can lower the effective burial depth of the drums, over time. These factors may e.g. dictate a preferred burial depth of e.g. 200 cm or even 250 cm as well as the use of hard, compacted clay for the uppermost 50 cm of the soil overburden, to minimise the rate of potential wind erosion of top-soil.

5.14.5 Documentation of calculation model and results: Drums with radioactive waste, buried in a trench

All calculation models and results related to the calculation of dose rates inside and above the trench, are consolidated into one RAR archive file, which is embedded below as Calculation model 5-2.

Calculation model 5-2: Trench with 363 concrete drums containing cemented intermediate level liquid (radioactive) waste (ILLW)



The above archive file is opened by double-clicking it; a prerequisite is that the archive package WINRAR must be downloaded from the URL **https://www.win-rar.com** and installed on the user's PC. Once uncompressed in a suitable folder, the individual MCNP model files should be opened using text editors such as NotePad++ or VS CODE.

5.15 Tenth-value thickness (TVT) values for high-density shielding concretes

5.15.1 Additional TVT information

Table 2-3 on page 71 contains no tenth-value thickness (TVT) values for the high-density shielding concretes magnetite concrete, hematite concrete and barite concrete. To deliver the results related to research objective RO_{13}, as formulated on page 155, these TVT values have been quantified during this work, and are summarised in Table 5-16, along with previously calculated TVT values for other shielding materials. Being more comprehensive, Table 5-16 therefore replaces the less detailed Table 2-3.

Table 5-16: Tenth-value thickness (TVT) for combinations of radionuclides and shielding materials; TVT values for 3 high-density shielding concrete formulations are included

Material	Mass-density ρ ($\mathrm{g\ cm^{-3}}$)	Tenth-value thickness for radionuclide (cm)		
		^{60}Co	^{137}Cs	^{192}Ir
Tungsten-alloy $\begin{Bmatrix}\mathrm{W} & 94\ \% \\ \mathrm{Ni} & 3\ \% \\ \mathrm{Cu} & 3\ \%\end{Bmatrix}$	17.4	2.5	1.4	1.7
Lead-alloy $\begin{Bmatrix}\mathrm{Pb} & 95\ \% \\ \mathrm{Sb} & 4\ \% \\ \mathrm{Sn} & 1\ \%\end{Bmatrix}$	11.0	3.7	1.9	2.0
Iron (Fe)	7.85	6.0	4.2	4.0
Aluminium (Al)	2.70	17.1	12.3	11.3
Ordinary concrete	2.30	19.4	13.9	12.8
Magnetite concrete	3.2	14.0	10.1	9.5
Hematite concrete	3.5	12.9	9.2	8.8
Barite concrete	3.4	13.2	8.9	8.7

The practical use of the information in Table 5-16 will now be demonstrated.

Example 1

At an industrial irradiator facility using a ^{60}Co source, the dose rate in a specific area is found to be up to 1000 times too high. Hematite concrete shielding blocks are available for stacking a shielding wall. For the shielding of ^{60}Co, the TVT of HEM-CRT is circa 13 cm, i.e. a thickness of $3 \times 13 = 39$ cm of hematite concrete will decrease the transmitted dose rate by the required shielding factor of

$$SF = 1000 = 10^3.$$

In practice, stackable concrete shielding blocks have widths of 20 cm, which means that a shielding thickness of 40 cm will be used.

5.15.2 Explanation of the apparent anomaly in calculated TVT values for the shielding of ^{60}Co by hematite and barite concrete

For the shielding of the radionuclide ^{60}Co, Table 5-16 shows no advantage for barite concrete relative to hematite concrete, whereas results reported in many tables and graphs in this chapter showed a non-

negligible dose-rate reduction advantage of BAR-CRT over HEM-CRT for the shielding of intermediate-level liquid (radioactive) waste (ILLW). The answer to this apparent contradiction and enigma is found in Table 2-2 on page 64 — the radionuclide ^{60}Co, for which BAR-CRT does not outperform HEM-CR in Table 5-16, emits its most intense γ-photons in the energy range where Compton scattering (CS) dominates photon attenuation and where PEA is unimportant; from Table 2-2 it is known that the linear interaction coefficient μ for CS is proportional to the mass-density ρ but independent of the atomic number Z. Because the mass-density ρ of barite concrete is not higher than that of hematite concrete, the use of BAR-CRT holds no advantage relative to the use of HEM-CRT in the approximate energy range $0.8\ \text{MeV} < E_\gamma < 1.5\ \text{MeV}$, where CS dominates and ^{60}Co radiated its most intense γ-photons. However, Figure 5-3 on page 165 shows that the ILLW from $(n,f)^{99}$Mo production emits the overwhelming majority of its γ-photons at $E_\gamma < 0.8$ MeV. In the photon energy regions where pair production (PP) and photo-electric absorption (PEA) dominate, the linear interaction coefficient $\mu(Z,E)$ is a monotonically rising function of the atomic number Z of the shielding material. This means that barite concrete (high-Z) will perform better relative to hematite concrete (average Z) for collections of many radionuclides having diverse emission energies, as encountered in typical radioactive waste packages, than would appear from taking only the ^{60}Co column in Table 5-16 at face value. In the energy range where PEA dominates, BAR-CRT performs much better than HEM-CRT.

6. Summary and conclusions

6.1 Meeting of research objectives

All the research objectives listed in § 4.12 (starting on page 151), were answered by the use of calculation models, which are discussed in § 5.3 (page 157), § 5.7 (page 167), § 5.8 (page 171), § 5.11 (page 187) and § 5.12 (page 193), along with a presentation of results. Additional, technical descriptions of selected aspects of codes and computational models have been presented in Annexure B (starting on page 222).

6.2 Statistical validity of results

The statistical validity of results is discussed in the subsection "Statistical validity of computed dose rates" on page 258 in Annexure B. It is shown that the results and conclusions are statistically valid. The null-hypothesis, as formulated on page 50, is rejected and the alternate hypothesis, namely that high-density shielding concretes will have a far higher ability than ordinary concrete to lower transmitted dose-rates outside concrete drums filled with ILLW, is accepted.

6.3 Verification and validation of results

This study is presented in a facility-agnostic format and therefore no attempt is made to compare calculated dose rates to measured dose rates. (The study supervisor (TJvR) has performed extensive previous work dealing with radioactive waste from (n, f) ^{99}Mo production (Van Rooyen, 2009, 2019b) and computed results in the present work are deemed accurate.)

6.4 Concrete type(s) to be used for drums housing cemented liquid radioactive waste from a fission-based ^{99}Mo production process

6.4.1 Ordinary concrete: a mediocre shielding material

A clear result of this investigation is that both hematite and barite concrete, will deliver a significantly better shielding drum compared to ordinary concrete, which is a mediocre shielding material against ionising photons. Packaging the significantly radioactive ILLW in ordinary concrete will be a singularly poor decision from an ALARA perspective because the material has decidedly inferior dose attenuation characteristics, as repeatedly came to light during this investigation.

A clear result of this investigation is that both hematite and barite concrete will deliver a far better shielding drum compared to ordinary concrete, which is a rather mediocre shielding material against ionising photons.

6.4.2 Magnetite concrete: an unnecessary choice in SA

In parts of the world where hematite iron ore reserves are depleted or absent, it makes sense to use magnetite iron ore for manufacturing high-density shielding concrete. However, the Fe content in magnetite is lower than in hematite, and the long-term oxidation stability of hematite is also better than that of magnetite — see footnote 13 on page 109. In South Africa, there are abundant hematite iron ore reserves, and there is no need to resort to the use of magnetite coarse and fine aggregates. The shielding ability of hematite concrete consistently outperforms that of magnetite concrete, for radiation sources dominated by photon emission.

6.4.3 Best selection: Barite concrete or hematite concrete?

As a shielding material for the attenuation of ionising photons, barite concrete performs better than hematite concrete. The following factors may, nevertheless, make hematite concrete the most practical choice in South Africa:

1. There are significant regional hematite iron ore deposits (Netshiozwi, 2002).

2. There is little if any nearby barite ore deposits; the material may have to be imported from e.g. China — see e.g. http://www.chinabarite.com/.

3. Hematite coarse and fine aggregate containing a minimum of 60 % Fe by mass, is a relatively affordable material choice with the benefit of an established local supply chain.

4. The concrete drum manufacturer presently used by the nuclear industry in SA, has considerable experience in manufacturing hematite concrete drums that are acceptably tough and durable. Switching to an untested aggregate such as barite, will require a long qualification and licensing campaign. The most prudent option will be to abide by a hematite shielding concrete technology.

6.5 Importance and applicability of this study

This work will be of interest to organisations that produce the radionuclide ^{99}Mo using fission-based processes, and therefore have to characterise, immobilise, shield, store, transport and dispose of the radioactive wastes associated with this production route.

In South Africa, this work will be of direct interest to organisations such as Necsa, NTP, the National Nuclear Regulator (NNR) and the National Radioactive Waste Disposal Institute (NRWDI).

This manuscript can be used at any of the above organisations as a foundation for the development of training material regarding the characterisation, immobilisation, shielding, storage, transport and disposal (CISSTD) of ILLW[$(n,f)^{99}$Mo] in particular, and all Low and Intermediate Level (radioactive) Waste in general.

6.6 Potential further work in the field of the characterisation, immobilisation, shielding, storage, transport and disposal of radioactive waste

Many radioactive waste streams have source terms that are difficult to predict using only codes and calculation models. At PWR NPPs, ion-exchange resins and filters in the chemical and volume control system (CVCS) are used to remove contaminants, including radionuclides, from the reactor coolant system (RCS), but the nuclide-activity matrix, i.e. $(N_i; A_i)$ radioisotope inventory matrix per unit mass of resin and filter material, depends on many complex and unpredictable factors such as whether there are leaking fuel rods present in a given fuel cycle, as well as the primary coolant chemistry regime that is followed. The radionuclide content of ion-exchange resins and filters therefore has to be characterised using a variety of experimental measurement techniques, including γ-spectrometry. If a representative $(N_i; A_i)$ radioisotope activity inventory per unit volume of ion-exchange resin and filters can be formulated, the analysis presented in this study can be applied to intermediate-level radioactive waste (ILW) produced from the operation of a PWR. The shielding factors that will be obtained for the above PWR related waste stream, can then be determined for drums manufactured of the same four concrete types analysed in the present study. The dimensions of the large concrete drums supplied to (1) the producer of ILLW[$(n,f)^{99}$Mo] and (2) the PWR power plant in South Africa, are identical. Some notable radionuclides that will be encountered in PWR RCS ion exchange resins and filters, include ^{60}Co, ^{137}Cs, ^{54}Mn, ^{110m}Ag, ^{55}Fe, ^{58}Co and ^{65}Zn (Kamaruzaman *et al.*, 2018). Monte Carlo

calculations will lead to the quantification of a quantitatively different but qualitatively similar set of shielding factors $SF(m_{CRT}, t_d)$ for the different concrete materials m_{CRT}, at discrete decay times t_d.

One of the few source terms that can, like the source term for ILLW$[(n,f)^{99}\mathrm{Mo}]$, be characterised without having to rely almost exclusively on empirical radioanalytical measurements, is that of solid residue from irradiated target plates used to produce ^{99}Mo, i.e. SRITP$[(n,f)^{99}\mathrm{Mo}]$. The SCALE ORIGEN calculation models for these two waste streams (liquid and solid) are, proverbially, "98%" identical and a similar approach that uses very similar calculation models, can be used to determine accurate source terms for SRITP$[(n,f)^{99}\mathrm{Mo}]$. These source terms can then be used in a set of MCNP calculation models to produce a comprehensive radiological safety case for the long-term storage (LTS) of SRITP$[(n,f)^{99}\mathrm{Mo}]$ inside sealed stainless-steel pipes in shallow boreholes. The ORIGEN calculation model will also quantify the uranium and plutonium vectors in the solid residue, which will provide information useful to the possible recovery of valuable fissile isotopes from the uranic solid residue.

Annexure A:

The isotope production reactor and the target plate assemblies for fission-based radionuclide production

A.1 Reactor core layout

The core layout of the core of the MTR is shown in Figure 6-1.

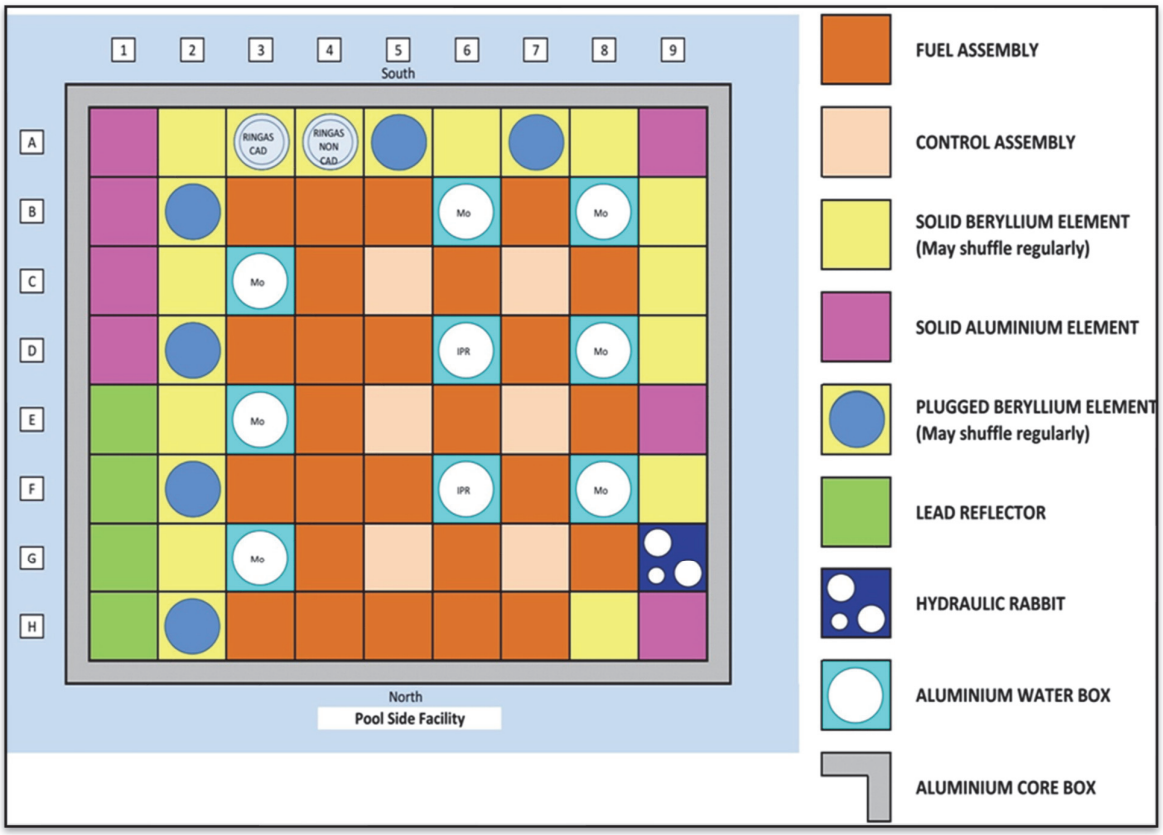


Figure 6-1: Top view of the core layout of the MTR

In Figure 6-1 it is seen that the reactor core contains 26 fuel assemblies and 6 control assemblies, and that 3 sides of the core are reflected by a combination of beryllium and aluminium reflector elements. There are a number of irradiation positions for isotope production.

A.2 Core and fuel parameters

Table 6-1 summarises some key parameters of the reactor core and fuel, as used from 1965 to the present (Moloko, 2011).

Table 6-1: Some key parameters of the isotope production reactor used to produce ^{99}Mo via a fission process

Parameter	**LEU$_{20}$ Core**
Number of control assemblies, with fuel-followers	6
Fuel type	U_3Si_2-Al
Uranium enrichment (mass-%)	19.75
Number of fuel plates per fuel assembly	19
Number of fuel plates per fuel-follower assembly	15
Total uranium in alloy of "meat" section in fuel plates (mass-%)	74-79
Mass of ^{235}U per FA (g)	340 ±6.7
Mass of ^{235}U per fuel-follower assembly (g)	230 ±5.3
Fuel "meat" thickness (cm)	0.0508
Fuel cladding thickness (cm)	0.0384
Fuel-follower "meat" thickness (cm)	0.0508
Fuel-follower cladding thickness (cm)	0.0384
Nominal inlet water temperature (℃)	40.0
Nominal outlet water temperature (℃)	47.2

The detailed designs of fuel assemblies and target plates are treated in (Zamonsky, 2019).

A.3 Fuel assemblies

The fuel assemblies used in the isotope production reactor under assessment are plate-type MTR fuel assemblies with 19 plates each. The fuel plates consist of a "meat" i.e. core section of uranium-silicide-aluminium (U_3Si_2-Al) powder dispersoid, enclosed in aluminium-alloy cladding. Figure 6-2 shows an x-y view of a fuel plate.

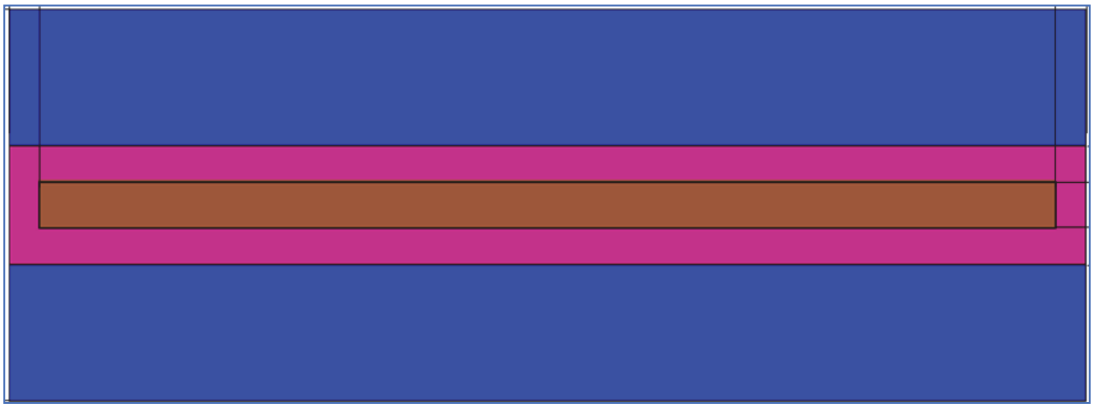


Figure 6-2: Single fuel plate in a fuel assembly used in the IPR

Legend:

Aluminium cladding
LEU_{20} U_3Si_2 dispersoid in Al, as meat or core of fuel plate
Water

An x-y section of a research reactor fuel assembly is shown in Figure 6-3; note that component dimensions have been deliberately deleted.

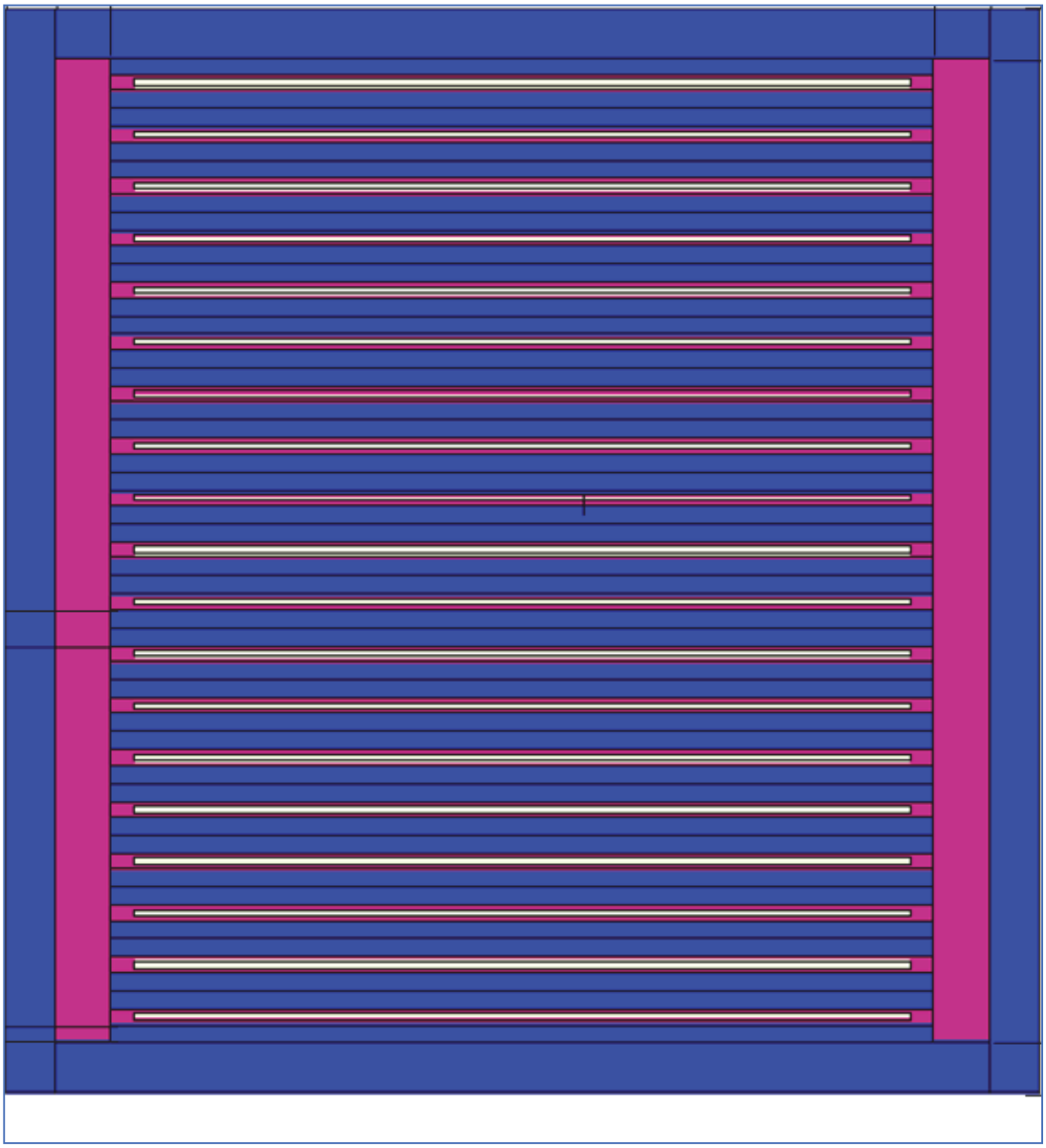


Figure 6-3: An x-y view at the active part of a fuel assembly used in the IPR

Legend:

	Aluminium
	LEU_{20} U_3Si_2 dispersoid in Al, as meat or core of fuel plates
	Water

The axial model of the fuel assembly is shown in Figure 6-4. Note that Figure 6-2, Figure 6-3 as well as Figure 6-4 were generated using the MCNP geometry plotter.

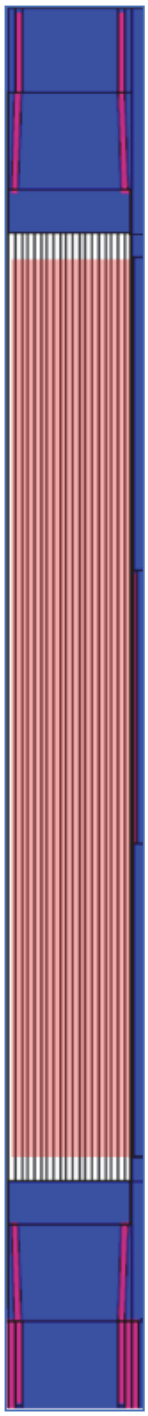


Figure 6-4: Axial view of a fuel assembly in the IPR

Legend:

- **Aluminium**
- **Inactive part of fuel plates**
- **Active, uranium-bearing part of fuel plates**
- **Water**

Figure 6-5 shows some photographs of a typical fuel assembly used in the MTR.



Figure 6-5: Photos of a fuel assembly for the MTR

The LHS of Figure 6-5 is an axial view of a fuel assembly that shows the top and bottom adaptors. On the RHS a close-up of the top adaptor of the fuel assembly shows the individual plates as well as the structural support comb along the centre.

A.4 Target plate (TP) assemblies for radionuclide production

In order to protect commercial IP (intellectual property), no information about the engineering specifications of TPs is presented in this work.

Annexure B:
Calculation models: SCALE T6-DEPL, SCALE ORIGEN and MCNP6

(Note: This chapter is very technical and leans quite heavily on input provided by the study supervisor, TJvR.)

B.1 Calculation models

Two SCALE calculation models were developed prior to this study and were used for this study:

1. A SCALE 6.2.4 T6-DEPL model of a TP_7 target plate assembly surrounded by 8 fuel assemblies (Van Rooyen, 2018b).

2. SCALE 6.2.4 ORIGEN models of target plates (Van Rooyen, 2018b).

The MCNP models of (1) a single radioactive waste drum and (2) an array of radioactive waste drums, were developed during the course of this work, with continual guidance by the study supervisor.

B.2 Transport-depletion (T-DEPL): Neutron transport and burnup/depletion calculation sequences in the SCALE system

The code ORIGEN in the SCALE 6.2.4 system (Ade & Betzler, 2016; Jessee *et al.*, 2017; ORNL, 2020; Rearden & Jessee, 2020) was used as the mainstay for calculating the burnup and depletion of the fissile material in the target plates, as well as for modelling the elemental partitioning between chemical species that takes place during the chemical processing of the irradiated target plates. The SCALE computational system is developed at Oak Ridge National Laboratory (ORNL) in the USA under a quality management system and is internationally accepted by nuclear safety regulators. The code ORIGEN is able to calculate the isotopic evolution in irradiated nuclear material during irradiation and after discharge from nuclear reactors, in fast calculations that generally never exceed execution times of circa 15 minutes on a typical 2021 model PC. ORIGEN requires a problem-dependent F33 ORIGEN library of burnup-dependent 1-group reaction cross-sections. Pre-calculated F33 libraries for US power reactors such as PWRs and BWRs, are shipped along with SCALE 6.2.4, but this is not the case for isotope production reactors that employ plate-fuel and target plates.

To develop an F33 ORIGEN library for fast ORIGEN calculations of the isotopic content of irradiated nuclear material, Mr B.A. Adetula[32] developed the initial geometry facets of a SCALE-6.2.4 TRITON transport-depletion T6-DEPL calculation model for a TP_7 assembly surrounded by 8 reactor fuel assemblies. This original model was made more realistic (Van Rooyen, 2018b) by adding 20 cm of water at the vertical top and bottom of the model, to account for neutron moderation and reflection in this water; COMPOSITION and BURNDATA parameters were also developed by Van Rooyen (2018b). This T6-DEPL model is embedded in Calculation model 6-1 on page 224 and its geometry can be viewed in Figure 6-6 on page 228.

The above calculation model was executed to produce a set of burnup-dependent 1-group reaction-rate cross-sections in the F33 libraries, for LEU_{20} target plates.

The average i.e. 1-group effective cross-section $\langle\sigma\rangle$ for the irradiation of a nuclide having a cross-section function $\sigma(E)$, by a neutron fluence-rate spectrum $\varphi(E)$, is given by Eq. (6-1)

$$\langle\sigma\rangle = \frac{\int \sigma(E)\,\varphi(E)dE}{\int \varphi(E)dE}. \qquad (6\text{-}1)$$

Mathematically, Eq. (6-1) is a real functional that maps 2 continuous real functions onto a real scalar value (Akhiezer & Glazman, 1993). The function $\varphi(E)$ acts as the weighting function for the calculation of the scalar value $\langle\sigma\rangle$ i.e. the 1-group flux-weighted cross-section, σ_{1g}. One-group cross-sections are used in the rate-equations that are solved by the code ORIGEN.

Above, we have referred to the TRITON transport-depletion calculation sequence in SCALE 6.2.4. The TRITON calculation sequence functions as follows: The basic repeated structure with its dimensions and initial material composition, is read and passed to CENTRM to calculate self-shielded 252-group multigroup cross-sections for use in the transport solver. A transport code (solver) such as XSDRN, NEWT or KENO-VI is next used to calculate a 252-group multigroup neutron fluence-rate distribution in the nuclear fuel material. Next, the burnup and depletion code ORIGEN calculates the altered composition of the material after a time-step. Next, Eq. (6-1)) is applied to calculate 1-group effective cross-section values for all rection cross-sections. The above sequence of (1) CENTRM, (2) the neutron transport solver and (3) ORIGEN is repeated, in a predictor-corrector methodology, to calculate a set of 1-group reaction cross-sections at every burnup i.e. fuel-evolution step. All these XS

[32] Mr Adetula developed the calculation model geometries at Necsa's Radiation and Reactor Theory (RRT) Section during 2017 and 2018.

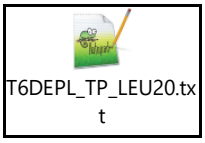
values are placed inside an F33 XS library for subsequent use by the code ORIGEN. The transport-depletion methodology is described in (DeHart & Petrie, 2004; Jessee *et al.*, 2017; Rearden & Jessee, 2020); the transport solver for SCALE 6.3 and beyond is described in (Davidson *et al.*, 2018). The numerical methods are elucidated in (Pusa, 2013) as well as (Pusa & Leppänen, 2013). In the transport solver, it is assumed that nuclide concentrations are invariant over a given time-step, and the neutron fluence-rate $\varphi(E)$ is computed for this time-step. The function $\varphi(E)$ is now used to solve Eq. (6-1) to compute a large number of quasi-static values of σ_{1g}, so that the rates of neutron-induced nuclear reactions, which are coefficients in the rate-equations for the irradiated material system, can be computed. The depletion code (ORIGEN) thus calculates an altered set of nuclide concentrations at the end of the time-step, assuming constant reaction rates — see e.g. (Pusa, 2013) and (Pusa & Leppänen, 2013).

The T6-DEPL calculation sequence in SCALE 6.2.4 is capable of modelling the exact 3-D detail of a TP_7 assembly located amidst 8 surrounding fuel assemblies in the isotope production reactor. The transport solver in the T6-DEPL calculation sequence is the Monte Carlo code KENO-6 and the depletion solver is the code ORIGEN.

B.3 SCALE 6.2.4 TRITON T6-DEPL calculation model for a LEU_{20} TP_7 target plate assembly

The SCALE 6.2.4 T6-DEPL calculation model for a TP_7 target plate assembly with LEU_{20}, as fissile material, is embedded in Calculation model 6-1. The embedded text file can be opened by double-clicking on it.

Calculation model 6-1: SCALE 6.2.4 T6-DEPL calculation model for a TP_7 target plate assembly with LEU_{20}, as fissile material



The purpose of Calculation model 6-1 is to generate F33 burnup-dependent 1-group cross-section sets for subsequent fast analyses using an ORIGEN calculation model.

Chosen parts of Calculation model 6-1 are now discussed. The first lines invoke the T6-DEPL SCALE calculation sequence and specifies the use of the 252-group neutron cross-section library, v7-252 which is based on ENDF/B-7.1 cross-section data. The parameter specification parm = (AddNux = 4, CENTRM) specifies 2 execution parameters. The parameter AddNux = 4 requests that 1-group cross-sections $\sigma(BU)$ must be calculated and added to the F33 ORIGEN library, for the maximum possible number of nuclide species. The parameter CENTRM requests that the most rigorously accurate cross-section resonance self-shielding treatment option that is available in SCALE 6.2 should be used. Next, the number of atoms per (barn×cm) of the initial compositions of the TP meat ("core"), the TP cladding, the FA cladding and the FA meat ("core") are specified, for isotopes and elements. These compositions were calculated during the project reported in (Van Rooyen, 2018b) which draws on the data in Composition 4-1 on page 131.

```
'SAFARI-1 TP7 LEU20 RIG - T-DEPL CALCULATIONS
=T6-DEPL parm= (AddNux=4, CENTRM)
TRITON-KENO6 T6-DEPL model of Safari-1 Target Plates
v7-252
read composition
' Mixture 1 = TP Meat/Core
 U-234       1   0   1.43339E-5      383   end
 U-235       1   0   1.45303E-3      383   end
 U-236       1   0   1.58239E-5      383   end
 U-238       1   0   5.79971E-3      383   end
 AL          1   0   4.75044E-2      383   end
 FE          1   0   1.63881E-5      383   end
 C           1   0   5.89251E-5      383   end
 N           1   0   4.13803E-5      383   end
 SI          1   0   1.08618E-5      383   end
 MG          1   0   1.25520E-5      383   end
 CR          1   0   5.86707E-6      383   end
 MN          1   0   5.55288E-6      383   end
 TI          1   0   6.37317E-6      383   end
 W           1   0   4.97818E-7      383   end
 CU          1   0   1.10416E-6      383   end
 ZN          1   0   5.59923E-7      383   end
 LI          1   0   4.38942E-6      383   end
 MO          1   0   1.33999E-7      383   end
 CO          1   0   4.80069E-8      383   end
 B           1   0   1.97617E-7      383   end
 CD          1   0   5.42750E-9      383   end
'
' Mixture 2 = TP Clad = FA Clad
 AL          2   0   5.82325E-2      378   end
```

```
 MG          2   0   1.87325E-3      378   end
 FE          2   0   7.57014E-5      378   end
 SI          2   0   9.26285E-5      378   end
 MN          2   0   2.95966E-5      378   end
 CR          2   0   6.25423E-6      378   end
 C           2   0   1.35374E-5      378   end
 CU          2   0   1.79112E-6      378   end
 TI          2   0   1.18890E-6      378   end
 NI          2   0   6.92573E-7      378   end
 ZN          2   0   3.48175E-7      378   end
 W           2   0   8.84448E-8      378   end
 B           2   0   1.50470E-6      378   end
 AG          2   0   1.50737E-7      378   end
 PB          2   0   2.35410E-8      378   end
 SN          2   0   2.05455E-8      378   end
 LI          2   0   2.33954E-7      378   end
 MO          2   0   1.69461E-8      378   end
 CO          2   0   2.75902E-8      378   end
 CD          2   0   1.44641E-8      378   end
 CA          2   0   4.05703E-8      378   end
 DY          2   0   1.00060E-8      378   end
 EU          2   0   1.06998E-8      378   end
 GD          2   0   1.03399E-8      378   end
 SM          2   0   1.08138E-8      378   end
 SB          2   0   1.33539E-9      378   end
'
' Mixture 3 = Water
 H2O         3  den=0.993     1.0    318   end
'
' Mixture 4 = FA Meat/Core
 U-234       4   0   1.22253E-5      383   end
 U-235       4   0   2.40420E-3      383   end
 U-236       4   0   1.21215E-5      383   end
 U-238       4   0   9.62154E-3      383   end
 SI          4   0   8.04050E-3      383   end
 AL          4   0   3.20244E-2      383   end
 FE          4   0   1.10434E-5      383   end
 C           4   0   3.97075E-5      383   end
 N           4   0   2.78847E-5      383   end
 MG          4   0   8.45836E-6      383   end
 CR          4   0   3.95360E-6      383   end
 MN          4   0   3.74189E-6      383   end
 TI          4   0   4.29465E-6      383   end
 W           4   0   3.35462E-7      383   end
 CU          4   0   7.44052E-7      383   end
 ZN          4   0   3.77312E-7      383   end
 LI          4   0   2.95787E-6      383   end
 MO          4   0   9.02968E-8      383   end
 CO          4   0   3.23501E-8      383   end
```

```
 B           4   0   1.33167E-7      383   end
 CD          4   0   3.65740E-9      383   end
end composition
```

The burn specification

```
read burndata
  power=1075   burn=10    nlib=60   down=0   end
end burndata
```

means that the average power per unit mass IHM in the TPs is 1075 MW per tonne initial uranium (i.e. Initial Heavy Metal) content, that a TP_7 assembly is irradiated for 10 days (i.e. 240 hours) at full power, and that 60 cross-section sets per 240-hour irradiation period is written to the ORIGEN F33 library, i.e. 1-group cross-sections are averaged over periods of

$$\frac{240 \text{ hours}}{60} = 4 \text{ hours}$$

to provide a library of burnup-dependent cross-sections. Note that this BURN specification is specifically used to prepare the F33 XS library, for later use by ORIGEN. The library is prepared for maximum irradiation times of 240 hours, whereas, in practice, TPs will not be irradiated for more than 200 hours. The strategy is to produce an F33 library that has "headroom" in the sense of containing data that will enable ORIGEN runs to answer questions such as "what product inventory can be achieved if TPs are irradiated to 220 hours?" In other words, the burnup domain covered by the F33 library is deliberately made slightly larger than necessary, in the interest of flexibility of application.

The burnup power specification $\boxed{\text{power} = 1075}$ for target plate irradiation has been calculated as Eq. (4-1) on page 132.

The SCALE TRITON T6-DEPL model was executed successfully (runtime: circa 7 days) and an ORIGEN F33 library of burnup-dependent cross-sections was produced; this ORIGEN F33 cross-section set enables the SCALE code ORIGEN to perform fast analyses for the isotopic evolution of the modelled type of target plate assembly, when irradiated in the modelled type of reactor.

(Note by study supervisor TJvR: In the SCALE system there is also a 56-group neutron cross-section library that can be used to produce an F33 library in under 30 hours, but the SCALE developers emphasise that this library is only fit for quick scoping investigations. It is also possible to use continuous cross-sections in the KENO-6 transport solver runs, but this will push the required runtime up by a factor as large as 10, i.e. towards 60 or 70 days, which is untenably slow. SCALE 6.2.4 codes are essentially unable to run in more than one processor core and thread, and obtaining faster results

using continuous cross-sections sets in multi-threaded calculations, will only become routinely possible once SCALE 6.3 is released (circa 2022). This ends the note by TJvR.)

Figure 6-6 presents a top view of the geometry modelled in Calculation model 6-1 (page 224), i.e. one central TP_7 assembly surrounded by 8 fuel assemblies in the isotope production reactor.

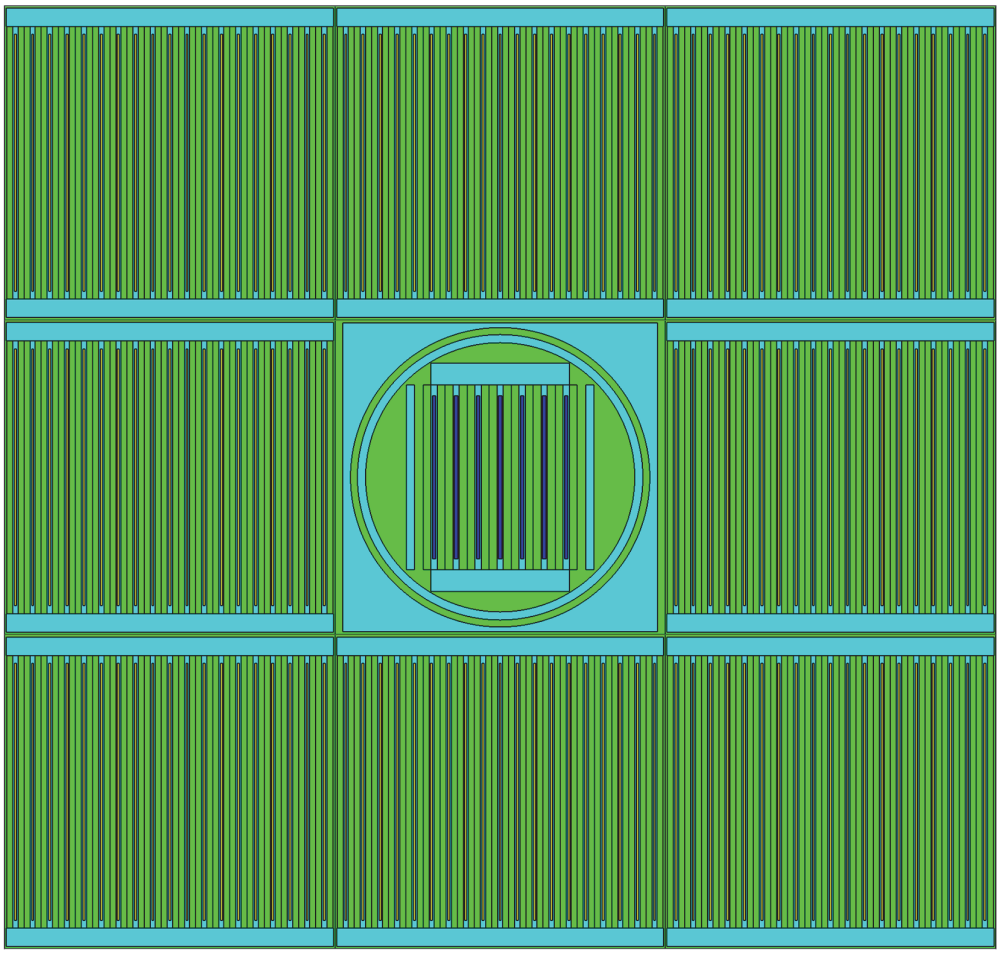


Figure 6-6: Top view of the geometry of the SCALE-6.2.4 TRITON T6-DEPL calculation model of one central target plate assembly, surrounded by 8 fuel assemblies in the reactor core

All 4 of the modelled system's lateral boundaries seen in Figure 6-6 have reflective, i.e. mirror boundary conditions for neutron transport.

Figure 6-7 shows a side-view of the TP_7 assembly surrounded by lateral fuel assemblies and water at the top and bottom.

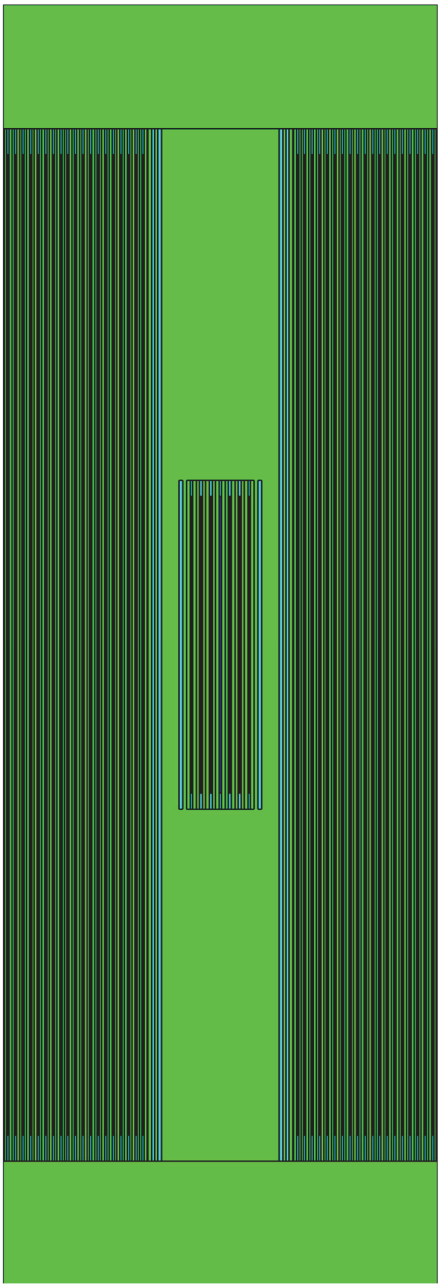


Figure 6-7: Side-view of a TP_7 target plate assembly surrounded by fuel assemblies; the active height of a target plate is only 18 cm whereas the active height of a FA is 59.37 cm

The top and bottom geometry boundaries that are seen in Figure 6-7 are vacuum boundaries, i.e. neutrons that traverse these boundaries are lost. The water layers at the top and bottom of Figure 6-7 are both 20 cm thick, which is adequate for arriving at an accurate $\varphi(E)$ neutron spectrum detail inside the fissile "meat" of the TPs, where Eq. (6-1) is applied to generate problem-specific, 1-group burnup-dependent F33 cross-sections $\sigma(BU)$.

B.4 SCALE 6.2.4 ORIGEN calculation model for the irradiation of 42 individual LEU_{20} target plates and the production of circa 35 litres of ILLW — intermediate-level liquid waste

B.4.1 The SCALE 6.2.4 code ORIGEN

The problem that is solved using the SCALE code ORIGEN, can be formulated as follows (Rearden & Jessee, 2020:5–9 – 5–18). When a collection of nuclides is placed in a neutron fluence-rate field $\varphi(E)$, the nuclides will undergo neutron-driven nuclear reactions such as fission and isotopic transmutation by neutron activation, followed by nuclear transitions (radioactive decay). A mathematical formulation of the process is presented in Eq. (6-2).

$$\frac{dN_i}{dt} = \sum_{j \neq i} \left(l_{ij}\lambda_j + f_{ij}\sigma_j\varphi \right) N_j(t) - (\lambda_i + \sigma_i\varphi)N_i(t) \tag{6-2}$$

where

N_i	=	number of nuclide i (atoms)
λ_i	=	transition constant of nuclide i
l_{ij}	=	fractional yield of nuclide i from the nuclear transition of radionuclide j
σ_i	=	spectrum-averaged removal cross-section for nuclide i (barn)
f_{ij}	=	fractional yield of nuclide i from neutron-induced removal of nuclide j
φ	=	1-group time-dependent neutron fluence − rate ($\mathrm{cm^{-2}s^{-1}}$)

Eq. (6-2) has no spatial dependence and must be interpreted as being spatially averaged over a system volume. The variable φ is the spatially averaged neutron fluence-rate, and all energy dependence of neutron interactions is embedded in the 1-group, fluence-weighted average cross-sections σ_i and reaction yields f_{ij}.

It is convenient to write Eq. (6-2) in matrix notation, as

$$\frac{d\vec{N}(t)}{dt} = \boldsymbol{A}\vec{N}(t), \tag{6-3}$$

where $\boldsymbol{A}$ is known as the "transition matrix". The representation of the transition matrix as

$$A = \boldsymbol{A}_\sigma\varphi + \boldsymbol{A}_\lambda,$$

where $\boldsymbol{A}_\sigma$ is the part of the transition matrix containing neutron-driven reaction terms, and $\boldsymbol{A}_\lambda$ is the part containing nuclear transition (i.e. "radioactive decay") terms, is convenient, because the numerical solution of this system of LODEs holds the (1) reaction cross-section and (2) fluence-rate terms constant over time-step n,

$$\frac{d\vec{N}(t)}{dt} = \left(\boldsymbol{A}_{\sigma,n}\varphi_n + \boldsymbol{A}_\lambda\right)\vec{N}(t), \tag{6-4}$$

which holds within the time-step $t_{n-1} \leq t \leq t_n$.

In all ORIGEN calculations reported in this work, the Chebyshev Rational Approximation Method (CRAM) was used for the numerical solution of Eq. (6-4). The accuracy of the CRAM solver is related to its order, with an order-16 solution having a truncation error of less than 0.01 % for all nuclides in most problems. ORIGEN is instructed to use the CRAM solver, via the statement

```
solver{
  type=CRAM
  opt{ order=16  substeps=32 }
}
```

The above options opt{ order = 16 substeps = 32 } represents the highest accuracy specification available for ORIGEN calculations in SCALE 6.2.4.

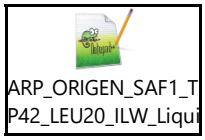
ORIGEN subdivides radioactive nuclides into 3 categories: Activation products (AP), fission products (FP) and actinides (AC).

B.4.2 The ORIGEN calculation model

The ORIGEN calculation model uses the F33 cross-section library produced by the TRITON T6-DEPL Transport-Depletion calculation of Calculation model 6-1 (see page 224). Alternating (1) CENTRM cross-section processing calculations, (2) KENO-6 transport calculations and (3) ORIGEN depletion calculations are performed to arrive at an F33 cross-section library that contains 60 sets of burnup-dependent 1-group reaction cross-sections for the isotopic evolution of target plates. The runtime of Calculation model 6-1 (page 224), is in the order of 7 days on a fast 2021 model PC. In contrast, an ORIGEN calculation typically executes in under 15 minutes.

The SCALE-6.2.4 ORIGEN calculation model for the irradiation of 42 LEU_{20} target plates and the subsequent chemical separation step that produces approximately 35 litres of ILLW — intermediate-level liquid waste — is embedded here as Calculation model 6-2.

Calculation model 6-2: SCALE-6.2.4 ORIGEN calculation model for the irradiation of 42 individual LEU_{20} target plates and the subsequent chemical separation



The embedded file can be opened by double-clicking it.

The ORIGEN calculation model for the target plate irradiation, chemical processing, separation of liquid waste and subsequent ageing of the ILLW, will now be discussed and explained in broad detail. The ORIGEN input begins with instructions to the ARP interface code about the name and content of the F33 burnup-dependent cross-section library produced previously by Calculation model 6-2.

```
=arp
'library name in "arpdata.txt" file
SAF1_TP_LEU20
'Fissile Isotope Enrichment Mass% for this fuel type
19.75
'Number of cycles
1
'Number of days per cycle
10
'Cycle-average specific power (MW/MTU_IHM)
1069
'Number of cross-section sets generated per cycle (NLIB):
60
'Moderator density (g/cc)
0.993
'Interpolated output ORIGEN library
ft33f001
end
```

The F33 library is named SAF1_TP_LEU20. The TPs contains 19.75 % enriched uranium as IHM, and the water coolant density is 0.993 g cm^{-2}. The F33 library was historically developed at a power

per unit mass of 1069 $\frac{\text{MW}}{\text{tonne_IHM}}$ (Van Rooyen, 2018b). In the F33 library, there are 60 cross-section sets, each one averaged over a specific burnup range.

In the discussion below, it is assumed that the reader has opened Calculation model 6-2 in a text editor.

In the `bounds` section of the ORIGEN model, the energy boundaries of the neutron, photon, electron and α-particle energy groups in which emitted spectra must be reported by ORIGEN, are specified.

BURN STEP 01 is named `case(IR_01)` ("irradiation step 01") and reads the cross-section data at position 1 of the F33 library file: `lib{ file = "ft33f001" pos = 1 }`. The first 4 hours of TP irradiation uses the XS data at `pos = 1` on the F33 library, as is specified by `time = { units = hours t = [ 1 2 3 4 ] }`. The 42 TPs are irradiated and undergo fission at a combined fission power of `power = [ 4R 0.840 ]` over 4 hours — the power per TP_7 assembly is 140 kW so that the power of 6 × TP_7 assemblies will be 840 kW, i.e. 0.84 MW. The initial material composition of the 42 TPs was prepared from Composition 4-1 on page 131 (Van Rooyen, 2018b) and is summarised in Table 6-2.

Table 6-2: Initial material composition of the 42 TPs

```
mat{
      units=grams
      iso=[ U234=1.51611   U235=154.34625  U236=1.68804  U238=623.94960
            Al=1460.523555
            Mg=25.24042405
            Fe=2.659063720
            Si=1.644113495
             C=0.416630713
            Cr=0.280372353
            Mn=0.271400372
            Ti=0.162839399
             N=0.148595864
            Cu=0.074579079
             W=0.051767590
            Zn=0.033083872
            Ni=0.022429953
            Li=0.014568018
             B=0.009982433
            Ag=0.008971981
            Mo=0.006841033
            Pb=0.002691594
```

```
            Co=0.002562596
            Sn=0.001345797
            Cd=0.001182502
            Ca=0.000897198
            Dy=0.000897198
            Eu=0.000897198
            Gd=0.000897198
            Sm=0.000897198
            Sb=8.97198E-05          ]
    }
```

In total, there are 50 BURN steps during which the isotopic content of the TPs evolves, mainly via neutron-induced fission, neutron activation and radioactive transition. During BURN step 2, the F33 cross-sections are read with the specification lib{ file = "ft33f001" pos = 2 }, etc., until BURN step 50, reads the F33 cross-sections with the following specification: lib{ file = "ft33f001" pos = 50 }. In other words, each BURN step reads the specific, pre-calculated, 1-group cross-section set for the TP burnup state that is relevant for the BURN step.

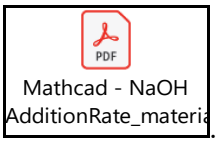
B.4.3 Material feed during the alkaline digestion of the ITPs

After the 50 irradiation steps, with each step lasting 4 hours, i.e. a total of 200 hours of in-core neutron irradiation, the TPs are discharged and cooled for 16 hours, in step case(DISCHARGE_COOL). Next follows the process step, case(DISSOLVE_TPS), which lasts 1 hour. The 42 TPs are dissolved in a 6-molar NaOH aqueous solution. The addition of the water and NaOH, along with traces of Na_2CO_3 (sodium carbonate) impurities, are modelled by the ORIGEN statement

```
    mat { previous=last
          units=grams
          % 33.5974 kg NaOH (with Na2CO3 carbonate impurities)
          plus 64.4 kg water per TP42 in 1 hr = 27.28 gram/s MAT FEED
          feed = [ Na = 1.60928
                   O  = 5.88624
                   H  = 0.67115
                   C  = 0.0160928   ]
    }
```

The specification mat { previous = last } states that the material input equals the exit-material from the previous process step. The additional feed statement specifies that specific elements are added at a given mass per second material feed rate. The numerical values for the material feed rate in the

above specification, were calculated using the methodology in the following embedded PDF file[33] (double-click the icon to open the document):



B.4.4 Partitioning of chemical species between solid and liquid waste streams: retained fractions during processing

In the design-basis case, the approximately 40 litres of ILLW in the SS-316L holdup tank contains the radionuclides from 42 LEU_{20} ITPs. During the dissolution of ITPs in the dissolver-hotcell, some chemical elements and, by implication, all their isotopes and radioisotopes, select the liquid pathway while other elements select the solid residue pathway. In SCALE ORIGEN calculation models, chemical affinities for the modelled process pathway can be quantified and expressed as **retained** factors for every chemical element in the Periodic Table.

In work spanning the years 2012 to 2018, the partition factors for the selection of the solid-residue pathway, were quantified as accurately as possible, based on measurements and known chemical behaviour in alkaline 6-molar NaOH aqueous solutions (Van Rooyen, 2012, 2017, 2019e). These partition factors are directly useful for the modelling of the source term selecting the liquid radioactive waste pathway. Let PF_e^L be the partition factor by which element e selects the liquid pathway; all partition factors are constrained to the domain $PF_e \in [0; 1]$. Let PF_e^{SR} be the partition factor by which element e selects the solid residue (SR) pathway. In the above references, PF_e^{SR} values were quantified by calibration against measured activities for a range of radionuclides sampled from SR-ITPs after 5 or more years of storage. The PF_e^L values are now simply

$$PF_e^L = (1 - PF_e^{SR})$$

except for the noble gases, for which $PF_e^L = 0$, because they are vented when the chemical processing is performed. In practice, a Factor of Safety (FoS) was incorporated into the liquid-phase partition fractions PF_e^L so as to construct a conservative yet realistic design-basis source term. This is conveniently performed in a spreadsheet, by multiplying the values PF_e^L by an FoS of e.g. 1.1 and capping the magnitudes of all chemical partition factors at 1.00. This leads to a conservative design-

[33] The MathCAD model was developed by the study supervisor TJvR.

basis source term (DBST); it is important that the DBST should (1) not underpredict the emission of ionising radiation, but (2) not overpredict it excessively.

In the code ORIGEN, the partition fractions are termed retained fractions. The retained fractions used for the different chemical elements in the ORIGEN calculation model, are summarised in Table 6-3.

Table 6-3: Retained fractions, i.e. partition fractions of chemical elements for the selection of the liquid waste pathway in the generation of ILLW from fission-produced ^{99}Mo

```
    processing{            % Element_id = fraction retained
      retained=[   H=1.00000
                  HE=0.00000
                  LI=0.50000
                  BE=0.10000
                   B=1.00000
                   C=0.90000
                   N=0.50000
                   O=1.00000
                   F=0.75000
                  NE=0.00000
                  NA=0.98000
                  MG=0.20000
                  AL=0.98000
                  SI=0.60000
                   P=0.60000
                   S=0.60000
                  CL=0.70000
                  AR=0.00000
                   K=0.70000
                  CA=0.20000
                  SC=0.20000
                  TI=0.30000
                   V=0.30000
                  CR=0.30000
                  MN=0.30000
                  FE=0.30000
                  CO=0.65000
                  NI=0.40000
                  CU=0.40000
                  ZN=0.40000
                  GA=0.40000
                  GE=0.40000
                  AS=0.30000
                  SE=0.20000
                  BR=0.95000
```

```
KR=0.00000
RB=0.90000
SR=0.10000
 Y=0.50000
ZR=0.10000
NB=0.20000
MO=0.90000
TC=0.90000
RU=0.30000
RH=0.65000
PD=0.65000
AG=0.50000
CD=0.50000
IN=0.50000
SN=0.50000
SB=0.40000
TE=0.45000
 I=0.90000
XE=0.00000
CS=0.95000
BA=0.25000
LA=0.40000
CE=0.40000
PR=0.50000
ND=0.90000
PM=0.10000
SM=0.10000
EU=0.25000
GD=0.40000
TB=0.20000
DY=0.40000
HO=0.40000
ER=0.40000
TM=0.40000
YB=0.40000
LU=0.40000
HF=0.40000
TA=0.40000
 W=0.40000
RE=0.30000
OS=0.30000
IR=0.30000
PT=0.30000
AU=0.00100
HG=0.20000
TL=0.20000
PB=0.10000
BI=0.10000
PO=0.10000
```

```
AT=0.10000
RN=0.01000
FR=1.00E-08
RA=1.00E-06
AC=1.00E-08
TH=1.00E-08
PA=1.00E-08
 U=1.00E-08
NP=1.00E-08
PU=1.00E-08
AM=1.00E-08
CM=1.00E-08
BK=1.00E-08
CF=1.00E-08
ES=1.00E-08
FM=1.00E-08
MD=1.00E-08
NO=1.00E-08
LR=1.00E-08      ]      }
```

The following examples serve to establish the correct interpretation of Table 6-3:

- 98 % of Na selects the liquid pathway.
- 20 % of Mg selects the liquid pathway.
- 30 % of Fe selects the liquid pathway.
- 95 % of Cs selects the liquid pathway.
- 25 % of Ba selects the liquid pathway.
- 1 ppm of Ra selects the liquid pathway.
- 10 ppb of U selects the liquid pathway.
- 10 ppb of Pu selects the liquid pathway.

Note by study supervisor, TJvR: The above retained mass fractions are not perfect, but represent the best currently available values. Chemistry specialists at the isotope production facility have stated that observed partition factors between liquid or solid waste streams, fluctuate significantly between production runs. One reason is that the raw material, $NaOH$, which is used for the alkaline digestion of irradiated target plates, contain unpredictable levels of Na_2CO_3 (sodium carbonate) impurities, which cause different partition fractions to

be observed. If a bag of NaOH absorbs ambient moisture, some of the NaOH reacts with atmospheric CO_2 to form Na_2CO_3 (sodium carbonate) which then perturbs the chemical partition factors for the waste streams. This chemical process that converts hydroxides into carbonates, is known as carbonation.

B.5 The Monte Carlo method

B.5.1 Introduction

If one could determine the exact path each particle makes and energies it assumes while passing through a medium in its random-walk fashion, one could, in principle, calculate many useful quantities by averaging over a large number of individual particle histories so as to minimise the stochastic effects of the individual particle interactions. For example, the probability that a particle in a certain energy range will be absorbed in a certain volume could be estimated by computing the proportion of all particles, in the specific energy group, that terminates in the specified volume. This concept of using a large number of particle histories, each of which is random in nature, to estimate some average particle behaviour, is the essential feature of the Monte Carlo method.

In Monte Carlo calculations, the particle tracks or histories are generated by simulating the random nature of the particle interactions with the medium. To do this, one requires mathematical expressions for the probability relationships which govern the track length of an individual particle between interaction points, the choice of an interaction type at each such point, the choice of a new energy and a new direction if the interaction is of a scattering type, and the possible production of additional particles. These are all stochastic variables. One needs a complete understanding of the physics of the various processes a particle undergoes in its lifetime from the time it is born in the source until it is either absorbed or leaves the system under consideration, in order to make selections of the specific values for these variables.

Monte Carlo methods are used in radiation transport applications such as shielding & detector response analysis & dosimetry. Monte Carlo refers to a statistical method wherein expected characteristics of particles (e.g. particle fluence) are estimated by sampling a large number of individual particle histories whose trajectories are simulated by a digital computer.

The fundamental advantage of Monte Carlo techniques over deterministic techniques (i.e. numerical solutions to the Boltzmann transport equation (BTE)), is that Monte Carlo techniques more accurately

represent the geometry and the nuclear data than deterministic techniques. Deterministic techniques require reasonably simple geometries for the numerical technique to work, and use the multigroup approximation to cross-section data. Monte Carlo techniques can handle complex geometries and continuous cross-section data (as well as simple geometry and multigroup data). The disadvantage of the Monte Carlo technique is that it is statistical in nature and does not provide an exact solution to the problem. All results represent estimates with associated uncertainties. Also, Monte Carlo techniques can be quite time-consuming on a computer if small uncertainties are required.

The relationship between Monte Carlo techniques and deterministic techniques is: deterministic techniques provide a highly exact solution to a significantly simplified approximation of the problem, while Monte Carlo techniques provide an approximate solution to a highly exact representation of the problem.

When a neutron, e.g., traverses a material, it interacts with the constituent atoms of that material. These processes occur statistically in nature, with the probability of occurrence determined by a cross-section. Nobody can predict exactly how far one particle will travel in a material before interacting; however, one can predict the distribution of flight distances that a large number of those particles will have prior to their first interaction. Using "random" numbers, the digital computer can generate a statistical history of the life of each particle—a random walk analysis. That is, an individual particle may experience many scattering interactions before finally being absorbed or leaking from the system. Random numbers—a set of numbers which have no pattern and are sampled uniformly between 0 and 1, are used at each interaction to determine which process (fission, elastic scattering, etc.) occurs., how much energy is lost, what is the new direction of the particle (in the event of scattering), or how many neutrons are created in a fission event. The life of the particle begins at birth—either from an external (fixed) source of from a fission event, and ends with absorption or with a scattering event that moves the particle outside the region of interest. The events that occur during a particle's life, are tabulated and become the history of that particle. Because a single particle is not representative of the system, a number of histories must be evaluated to accurately describe what occurs.

B.5.2 Examples of Monte Carlo processes

A sequence of random numbers $0 < R_i < 1$ is used to produce a random distribution of quantities that simulate the problem at hand:

S_1 Determine the initial position where the neutron is emitted.

S_2 Use a random number to select the energy E of an emitted particle, based on the energy spectrum $Q(E)$ of particle emission.

S_3 Use the next random number(s) to sample the direction cosine(s) of the particle's direction of movement.

S_4 Use the next random number to determine the location of the next collision site (the distance travelled depends on the total cross-section $\mu_t(E)$ of the material medium at the particle energy E.

S_5 Check the new position to determine whether the particle has escaped (leaked) from the system. If it has, add 1 to the total leaked and go to step S_1 & start another history with another particle. If not, go to step S_6.

S_6 Determine which type of interaction occurred at the new position, based on the next random number. Each type of interaction has an associated cross-section that determines the probability of occurrence:

- If the interaction is scattering, then determine the new energy of the neutron after scattering using the next random number. Then go to step S_3 and continue to follow the particle, i.e. determine the direction in which the scattered particle moves.
- If the interaction is absorption, go to step S_1 and start a new source particle in the system.

S_7 When a given set of histories has been completed — enough to provide acceptable statistical precision — evaluate the tally.

B.5.3 Monte Carlo sampling techniques for discrete stochastic variables

The way in which a random number between 0 and 1 is used to select an event from a discrete probability distribution is best explained by example. The illustrative, simplifying assumption is made that, in the energy range of interest, there are only 3 possible photon interaction mechanisms: photo-electric absorption, Compton scattering and pair production. Consider the selection of whether a photon of a given energy will interact by the photoelectric effect (PEE), Compton scattering (CS) or pair production (PP) in a particular collision. The probabilities of the three available modes of interaction are defined as

$$\begin{aligned} p_1 &= \left(\frac{\mu_{PEA}}{\mu_t}\right) \\ p_2 &= \left(\frac{\mu_{CS}}{\mu_t}\right) \\ p_3 &= \left(\frac{\mu_{PP}}{\mu_t}\right) \end{aligned} \quad (5)$$

where $\mu_t = \mu_{PEA} + \mu_{CS} + \mu_{PP}$. The discrete probability density function is normalised, because

$$\sum_{i=1}^{N} p_i = 1 \quad (6)$$

where N is the number of interaction options (in the above example, $N = 3$).

Suppose that, at a given photon energy, $\mu_{PEA} = 0.324\ \text{cm}^{-1}$, $\mu_{CS} = 0.987\ \text{cm}^{-1}$ and $\mu_{PP} = 0.137\ \text{cm}^{-1}$. This means that

$$\begin{aligned} p_1 &= 0.22376 \\ p_2 &= 0.68163 \\ p_3 &= 0.09461 \end{aligned}$$

The index 1 denotes photoelectric absorption, the index 2 denotes Compton scattering and the index 3 denotes pair production; the reaction type is uniquely referenced by its discrete, integer index.

The discrete probabilities may be represented as shown in Figure 8. Here the black bar denotes interaction type 1, i.e. photo-electric absorption; the red bar denotes interaction type 2, i.e. Compton scattering, while the green bar denotes interaction type 3, i.e. pair production.

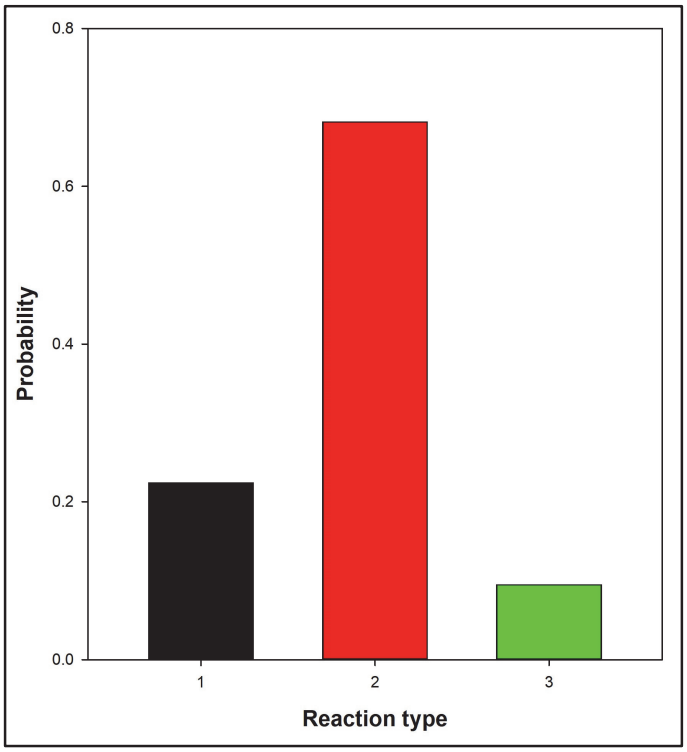


Figure 8: Probabilities of photon interaction types

Let us now define the cumulative probability distribution,

$$P_J = \sum_{i=1}^{j} p_i \text{ for j} \leq \text{N} \qquad (7)$$

which gives the probability that interaction type i is less than or equal to than j. In the above example,

$$\begin{array}{lll} P_1 = p_1 & = & 0.22376 \\ P_2 = p_1 + p_2 & = & 0.90539 \\ P_3 = p_1 + p_2 + p_3 & = & 1.00000 \end{array}.$$

The above cumulative probability distribution is illustrated in Figure 9. As in Figure 8, the black bar denotes interaction type 1, i.e. photo-electric absorption; the red bar denotes interaction type 2, i.e. Compton scattering, while the green bar denotes interaction type 3, i.e. pair production.

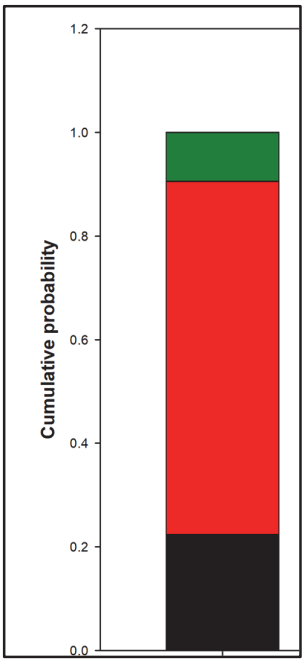


Figure 9: Normalised cumulative probability distribution function for photon interaction type at a given incident photon energy

The interaction selection process now happens as follows, at the particular photon energy where the above linear interaction coefficients hold true:

Generate a random number r between 0 and 1.

- If $\boxed{r \leq 0.22376}$, then select photo-electric absorption as the interaction type.
- If $\boxed{0.22376 < r \leq 0.90539}$, then select Compton scattering as interaction type.
- Finally, if $\boxed{0.90539 < r \leq 1.0}$ then select pair production as interaction type.

The summation (in general: integration) of the normalised probability density function yields a normalised cumulative probability distribution function which has values in the interval $[0; 1]$.

Because the random number r is uniformly distributed on the unit interval $[0; 1]$, each type of interaction is sampled with probability p_1, p_2, or p_3. In a large number of samples, Compton scattering would, e.g., be selected in circa 68 % of the cases, photo-electric absorption in circa 22 % and pair production in circa 9.5%. The smaller the number of samples, the greater the degree of statistical fluctuations would be.

B.5.4 Extension to continuous probability density functions

The above example can be extended to continuous probability density distributions. Consider a continuous probability density function (pdf), say $f(x)$. By definition, the probability of finding the variable x between x and $x + dx$, is the infinitesimal area $f(x)\,dx$. Accordingly, the probability that a randomly selected value of x is between x_1 and x_2, is given by the area under $f(x)$ bounded by x_1 and x_2:

$$P\{x_1 < x \leq x_2\} = \int_{x_1}^{x_2} dx\, f(x). \tag{8}$$

Let us now assume that x may be any value between the limits a and b, either of which may be $-\infty$ or $+\infty$, respectively. Corresponding to $f(x)$, there is a cumulative probability distribution $F(x)$, defined by

$$F(x) = \int_{a}^{x} dx'\, f(x'). \tag{9}$$

The probability that the randomly selected value of x is less than x_1, $P\{x < x_1\}$, is thus given by $F(x_1)$. It is easily seen that the function $F(x)$ is monotonically increasing with x if $f(x)$ is a normalised probability density function between a and b, with $F(a) = 0$ and $F(b) = 1$. We see that F presents a mapping from the interval $[a; b]$ to $[0; 1]$. Likewise, the inverse cumulative probability density function F^{-1} will be a mapping from the probability internal $[0; 1]$ to the interval $[a; b]$ where the variable x has to be sampled.

In other words, to correctly sample the variable x, determine the normalised probability density function $f(x)$ from physics principles. This defines the normalised cumulative probability density function $F(x)$ as well as the normalised inverse cumulative probability density function $F^{-1}(x)$. Now, a random number on the interval $[0; 1]$ is generated using a random number generating algorithm; the corresponding sampled value of the variable x is given by $x = F^{-1}(r)$. This sampling process is repeated many thousands of times in order to achieve acceptable statistical results.

B.6 How the code MCNP is used to calculate dose rates around packages of radioactive material

The first step in the use of the code MCNP6 to calculate the dose rate field inside and around packages of radioactive material, is to specify the geometry and material composition of the system to high accuracy, in an MCNP ***calculation model.*** The code needs to know the spatial location of matter in space, which can be expresses mathematically as $N_i(\vec{\boldsymbol{x}})$, where N_i denotes the number density of nuclide i as a function of the spatial vector $\vec{\boldsymbol{x}}$. The need to specify $N_i(\vec{\boldsymbol{x}})$ is seen by referring to the Boltzmann transport equation (BTE). A key function of the calculation model is to specify the spatial distribution of matter, to the radiation transport code.

B.6.5 Operator form of the Boltzmann transport equation (BTE)

It must be stressed that a Monte Carlo code such as MCNP does not "solve" the BTE numerically, but rather models the stochastics of the very physical processes that led to the derivation of the mathematical formulation of the BTE. This "equivalence" between a stochastic code and the BTE, means that one can use the mathematical form of the BTE to conceptualise Monte Carlo simulation codes, specifically their user-input specifications.

In operator notation, the time-independent or steady-state Boltzmann transport equation, which is an integro-differential equation, is written as Eq. (10),

$$\mathbb{B}\psi = Q \tag{10}$$

where the linear Boltzmann transport operator $\mathbb{B}$ is, in its simplest form (for non-fissioning systems), given by Eq. (11),

$$\mathbb{B} \equiv \vec{\boldsymbol{\nabla}} \cdot \hat{\boldsymbol{\Omega}} + \mu_t(\vec{\boldsymbol{x}}, E) - \int_0^{\infty} dE' \int_{\hat{\boldsymbol{\Omega}}} d\hat{\boldsymbol{\Omega}}\, \mu_s\left(\vec{\boldsymbol{x}}, E' \to E, \hat{\boldsymbol{\Omega}}' \to \hat{\boldsymbol{\Omega}}\right). \tag{11}$$

The function Q in Eqs. (10) and (11) is known as the source-term of the BTE. If there are non-zero terms in Q that are independent of the solution, ψ, of the BTE, then $\mathbb{B}\psi = Q$ is an inhomogeneous operator equation, with the source-term Q "driving" the system. In the BTO, the variable $\hat{\boldsymbol{\Omega}}$ denotes the direction of movement of a radiation particle, μ is the linear interaction coefficient, μ_t is the total linear interaction coefficient, μ_s is the linear interaction coefficient for scattering transfer from an

initial energy to a final energy and from an initial direction to a final direction, $\vec{x}$ is the spatial position of the particle and E its energy. More detailed information about the BTE and its interpretation can be found in Henry (1975).

B.6.6 Deterministic and stochastic radiation transport codes

For real-life radiation sources and material configurations, the BTE, $\boxed{\mathbb{B}\psi = Q}$ has to be solved by computer codes running on powerful digital computers. Two general categories of such radiation transport codes exist:

- Deterministic codes solve a spatially discretised, multigroup approximation of the BTE iteratively until convergence of the directional fluence-rate solution ψ is achieved. The scalar fluence rate, φ, is arrived at by integrating ψ over all directions $\widehat{\boldsymbol{\Omega}}$; the scalar fluence rate φ is used to quantify, e.g., dose rates.

- Monte Carlo simulations simulate the stochastic nature of radiation transport by sampling cumulative probability density functions via the generation of, typically, millions of pseudo-random numbers which are, in turn, generated by a suitable numerical algorithm. The scalar fluence-rate solution, φ, in tallied regions of space is evaluated in order to quantify e.g. dose rates.

B.6.7 MCNP calculation models: Overview

The code user develops a *calculation model,* which serves as user input to the code. The code MCNP reads the *calculation model*, which is an ASCII text file containing many keywords and numbers, in which the user specifies radiation emission (the source term), the identities and spatial positions of materials, as well as tallies, i.e. the quantities to be calculated.

The nuclear cross-section data used by MCNP6.2 (LANL, 2018) spans many GBs of nuclear data files, which are either shipped with the code or downloaded by the user and then made available to the code by editing code's XSDIR ("cross-section directory") file, which resides in the DATA folder.

An important concept in understanding the input to MCNP, is that several terms in the BTE contain linear interaction coefficients μ, also known as "macroscopic cross-sections" with the common alternate symbol, Σ. The linear interaction coefficient μ is defined as

$$\mu(\vec{x}, E) = \sum_i N_i(\vec{x})\,\sigma_i(E) \tag{12}$$

where $N_i(\vec{x})$ denotes the number-density of nuclide i as a function of the spatial vector $\vec{x}$, and $\sigma_i(E)$ is the energy-dependent cross-section or "microscopic cross-section" of nuclide i. The user specifies isotopic or elemental identities as ZAID numbers. Low-energy photon-electron transport is independent of the exact isotope, and depends only on the elemental, chemical identities, because radiation interactions are atomic as opposed to nuclear in nature, i.e. the interactions involve atomic electrons and not the strong nuclear interactions which characterise neutron interactions with nuclei. For these transported particles (MODE P E) materials are specified by ZAID numbers $1000 \times Z$, where Z is the atomic number. The element oxygen ($Z(\mathrm{O}) = 8$) is e.g. specified by the ZAID of $1000 \times 8 = 8000$. When nuclear interactions such as (γ, n) reactions become possible, it becomes necessary to specify the isotopic composition of materials to MCNP, and ZAID numbers are specified as $ZAID = 1000 \times Z + A$ while the MODE specification must e.g. become (MODE N P E). When the code MCNP is executed, values of $\sigma_i(E)$ are read from extensive nuclear data compilations available to the code, as an automatic background process, while the user has to explicitly specify $N_i(\vec{x})$., i.e. the spatial positions of different materials. Typically, the majority of the specification statements in an MCNP calculation model deals with the user's specification of the identities i and the 3D spatial location $N_i(\vec{x})$ of all nuclides i, within the system of interest. The specification of $N_i(\vec{x})$ is spread over all three subdivisions of an MCNP6 calculation model — the surface cards[34], cell cards and the material cards.

A typical dose rate calculation using MCNP6 conceptually deals with the steady-state BTE, i.e. not the time-dependent BTE.

An investigation of the terms of the Boltzmann transport operator, $\mathbb{B}\psi = Q$, makes it clear what input information the user has to specify to the code MCNP.

[34] Note by study supervisor, TJvR: Technically, the surface cards are the second part of an MCNP input, yet they have to be developed first, because the cell-cards (section 1 of an MCNP input) are entirely dependent of the surface definitions.

1. The term $\boxed{\vec{\nabla} \cdot \hat{\Omega}}$ is known as the ballistic[35] term or streaming term in the BTE; it represents the laws of the transport of radiation in the absence of matter (i.e. in a classical vacuum) and requires no user input.

2. The term $\boxed{\mu_t(\vec{x}, E)}$ is known as the outscattering term in the BTE; the variable μ_t represents a sum over all nuclides, $N_i(\vec{x})$ in the 3D spatial system, i.e. the user has to specify the identity i and the spatial position of every nuclide in the system. (The energy-dependence of the cross-sections is read from the circa 40+ GByte of nuclear data that ships with MCNP6, but this is an automated background process). The physical interpretation of this term is that *any* (hence the total cross-section) interaction at spatial position $\vec{x}$ will remove a neutron travelling in the infinitesimally small cone of directions $d\hat{\Omega}$ around $\hat{\Omega}$, and in the infinitesimally small energy-band dE around E, to a direction of travel and an energy outside this domain of phase-space.

3. The term $\mu_s(\vec{x}, E' \rightarrow E, \hat{\Omega}' \rightarrow \hat{\Omega})$ is known as the in-scattering integral of the BTE; it is also a linear interaction coefficient (i.e. a macroscopic cross-section), and therefore requires exactly the same user-supplied information as necessitated by the total linear interaction coefficient term, μ_t, as discussed above — namely the specification of $N_i(\vec{x})$ where N_i is the number density of every isotope of interest, inside the spatial volume of interest, i.e. the spatial "radiation transport theatre". This term deals with the ability of matter to scatter neutrons moving in other directions, and having other energies, into the infinitesimally small cone of directions $d\hat{\Omega}$ around $\hat{\Omega}$, and into the infinitesimally small energy-band dE around E, at the infinitesimally small spatial cell $d\vec{x}$ around $\vec{x}$.

4. The term $\boxed{Q(\vec{x}, E, \hat{\Omega})}$ requires the user to specify the spatial location (variable: $\vec{x}$), energy spectrum (variable: E) and directionality (variable: $\hat{\Omega}$) of all "fixed sources", i.e. sources that do not depend on the fluence rate. In the case of radionuclide sources, radiation emission is isotropic so that only the spatial position and energy spectra of emitted ionising radiation are specified.

In summary: By analysing the Boltzmann Transport Equation (BTE) it becomes clear that, in an MCNP6 calculation model, the identities and spatial locations $N_i(\vec{x})$ of all nuclides i, as well as the

[35] Note by study supervisor, TJvR: The Greek grammatical root β-λ, i.e. B-L, is found in Greek verbs and nouns dealing with objects that are thrown and then move through the air. Examples of English words based on the Greek root β-λ, include ball and ballistic.

spatial placement and energy spectrum of all fixed sources $Q(\vec{x}, E, \hat{\Omega})$ have to be defined. The balance of a typical n MCNP input is composed of tally definitions (i.e. output requests) along with a handful of "housekeeping" cards.

The above discussion has now presented the background needed to interpret a simple MCNP6 calculation model for radioactive waste in a concrete drum. The calculation model is reproduced in Calculation model 3.

Calculation model 3: Calculation model to determine the contact dose rate and the Transport Index (TI) for concrete drum containing ILLW

```
ILLW 100L 42LEU-ITPS @ COOLING, INSIDE CRT DRUM
c Cell Cards:
01  01   -1.5       -01                          imp:p=1    $ CEMENTED LW IN DRUM
02  02   -7.85      -02  +01                     imp:p=1    $ STEEL DRUM WALL
03  11   -2.30      -03  +02                     imp:p=1    $ Concrete Drum Wall
c
04  03   -0.01      -04  +03                     imp:p=1    $ TEM DET Contact DR
06  03   -0.10      -06  +05                     imp:p=1    $ TEM DETECTOR @ 1M from DRUM
c
07  11   -2.30      -07                          imp:p=1    $ ORD-CONCRETE FLOOR SLAB
c
08  04   -1.2E-3    -99  +03  +04  #06  +07      imp:p=1    $ AIR SURROUND
99  00                   +99                     imp:p=0    $ EXTERNAL VOID
c ===========================================================================

c ===========================================================================
c Surface Cards:
01   RCC   0  0  32.2         0   0  066.0        022.5
02   RCC   0  0  32           0   0  066.6        022.7
03   RCC   0  0  00           0   0  130.0        054.3
04   RCC   0  0  42.0         0   0  045.0        056.0
c
05   RCC   0  0  42.0         0   0  045.0        153.0
06   RCC   0  0  42.0         0   0  045.0        154.0
c
07   RPP  -3000  +3000       -3000  +3000        -50    +00      $ Concrete Slab
c
99   RPP  -3000  +3000       -3000  +3000        -50  +9000      $ Air surround
c ===========================================================================

c ===========================================================================
c Data Cards:
c
mode  P
c
sdef   POS  = 0  0  30
       par  = P
       erg  = D22
       x    = D1
       y    = D2
       z    = D3
```

```
       cell = 1
       eff  = 1.0E-3
       wgt  = 6.276E+11
c
c
si1 H    -30    +30
sp1 D  0     1
c
si2 H   -30     +30
sp2 D  0     1
si3 H    +0    +100
sp3 D  0     1
c
c =====
c
c      Energy           ST_10yr
#      SI22             SP22
       a                D
       0.000            0.0000
       9.99900e-04      0.0000
       1.00000e-03      5.085222E+08
       1.70000e-03      1.674200E+07
       3.40000e-03      4.008050E+10
       5.40000e-03      3.809000E+12
       7.40000e-03      1.137600E+12
       ⋮                  ⋮
       1.47700e+01      0.000000E+00
       1.48700e+01      0.000000E+00
       1.49700e+01      0.000000E+00
       1.50000e+01      0.000000E+00
       1.60700e+01      0.000000E+00
       2.00000e+01      0.000000E+00
c
c =====
c
c Material: Cemented LW - 55% Portland Cement + 20% Vermiculite + 20% Water + 5% NaOH
m01     1000     -2.794
        8000     -50.061
       11000     -3.282
       12000     -2.736
       13000     -1.455
       14000     -11.30
       19000     -0.457
       20000    -26.336
       26000     -1.575
c
c SS-304L:
m02     6000     -00.03
        7000     -00.07
       14000     -00.60
       15000     -00.03
       16000     -00.02
       24000     -19.00
       25000     -01.70
       26000     -68.55
       28000     -10.00
c
c TEM for Photon Problems (Wikipaedia):
```

```
m03     1000       -9.98774E+00
        3000       -9.98774E-06
        4000       -5.13655E-08
        5000       -2.56828E-05
        6000       -2.28291E+01
        7000       -2.56828E+00
        8000       -6.13533E+01
        ⋮              ⋮
       83000       -7.13410E-07
       90000       -1.42682E-07
       92000       -1.42682E-07
c
c Air with 1% water (Photon-Electron TPT at Low Energies):
m04     1000    -1.12003E-01    $ H  in Air
        2000    -6.93003E-05    $ He in Air
        6000    -1.26990E-02    $ C in Air
        7000    -7.47157E+01    $ N in Air
        8000    -2.38908E+01    $ O in Air
       10000    -1.18801E-03    $ Ne in Air
       18000    -1.26721E+00    $ Ar in Air
       36000    -2.97001E-04    $ Kr in Air
       54000    -3.96002E-05    $ Xe in Air
c
c US-NRC REGULATORY CONCRETE; mass-density = 2.30 g/cc
m11    1000     -1.0     $ H  in NRC Regulatory Concrete
       8000     -53.2    $ O  in NRC Regulatory Concrete
       11000    -2.9     $ Na in NRC Regulatory Concrete
       13000    -3.4     $ AL in NRC Regulatory Concrete
       14000    -33.7    $ Si in NRC Regulatory Concrete
       20000    -4.4     $ Ca in NRC Regulatory Concrete
       26000    -1.4     $ Fe in NRC Regulatory Concrete
c
c Magnetite Concrete (rho = 3.2 g/cc)
m12    1000       -0.4113
       8000       -44.550
       12000      -1.1416
       13000      -3.8486
       14000      -6.6751
       16000      -0.1415
       20000      -5.1259
       22000      -0.9331
       23000      -0.3115
       24000      -0.1201
       25000      -0.2085
       26000      -36.528
c
c Hematite Concrete  (rho = 3.5 g/cc)
m13    1000        -0.3113
       8000       -33.0504
       12000       -0.9338
       13000       -2.3486
       14000       -2.5750
       16000       -0.1415
       20000       -7.1024
       22000       -5.4329
       23000       -0.3113
       24000       -0.1698
       25000       -0.1981
```

```
       26000      -47.4250
c
c Barytes Concrete (rho = 3.4 g/cc)
m14    1000       -00.448
       8000       -31.127
       11000      -00.119
       12000      -00.193
       13000      -00.423
       14000      -01.720
       16000      -10.993
       19000      -00.133
       20000      -07.662
       26000      -00.112
       56000      -47.072
c
c
f116:p   1  2  3  4  6
fm116    5.767836E-7
c
f126:p   4  6
fm126    5.767836E-7
c
PRDMP  -111   -117   0   100   1E6
CTME   1000
c ===================================================================
```

The surface cards

```
01   RCC   0  0  32.2          0   0  066.0         022.5
02   RCC   0  0  32            0   0  066.6         022.7
03   RCC   0  0  00            0   0  130.0         054.3
04   RCC   0  0  42.0          0   0  045.0         056.0
c
05   RCC   0  0  42.0          0   0  045.0         153.0
06   RCC   0  0  42.0          0   0  045.0         154.0
c
07   RPP  -3000  +3000       -3000  +3000        -50    +00      $ Concrete Slab
c
99   RPP  -3000  +3000       -3000  +3000        -50  +9000      $ Air surround
```

specify a radioactive waste matrix inside a steel drum inside a larger, outer concrete drum. Two detector material layers enable the quantification of the contact dose rate as well as the Transport Index (TI). The drum stands on a thick concrete slab and is surrounded by air.

The cell cards

```
01  01   -1.5        -01                          imp:p=1    $ CEMENTED LW IN DRUM
02  02   -7.85       -02  +01                     imp:p=1    $ STEEL DRUM WALL
03  11   -2.30       -03  +02                     imp:p=1    $ Concrete Drum Wall
c
04  03   -0.01       -04  +03                     imp:p=1    $ TEM DET Contact DR on Drum
06  03   -0.10       -06  +05                     imp:p=1    $ TEM DETECTOR @ 1M from DRUM
c
07  11   -2.30       -07                          imp:p=1    $ ORD-CONCRETE FLOOR SLAB
c
08  04   -1.2E-3     -99  +03  +04  #06  +07      imp:p=1    $ AIR SURROUND
```

```
99  00                    +99                    imp:p=0    $ EXTERNAL VOID
```

specify the spatial location of material between given surfaces. The 2nd number from the LHS in every line refers to the material number in the material cards. The 3rd (negative) number from the LHS in every line specifies the mass-density of the material.

Cell card 1,

```
01  01   -1.5       -01                    imp:p=1    $ CEMENTED LW IN DRUM
```

states that cell 1 contains material 1, i.e. "Cemented LW - 55% Portland Cement + 20% Vermiculite + 20% Water + 5% NaOH". The mass-density of material 1 is $1.5\ \mathrm{g\ cm^{-3}}$; all space inside surface 1, i.e. a right circular cylinder (RCC), is filled with this material. The importance of photon transport in this cell is 1.

Cell card 2,

```
02  02   -7.85      -02  +01                imp:p=1    $ STEEL DRUM WALL
```

states that cell 2 contains material 2, i.e. the material specified in material card M2, which is stainless steel of type 304-L. The mass-density of material 2 (stainless steel) is $7.85\mathrm{g\ cm^{-3}}$; the intersection of all space that is inside surface 2 but outside surface 1, is filled with SS-304L. The importance of photon transport in cell 2 is 1.

The specification of the composition of materials to MCNP as in e.g.

```
m01     1000     -2.794
        8000     -50.061
       11000     -3.282
       12000     -2.736
       13000     -1.455
       14000     -11.30
       19000     -0.457
       20000    -26.336
       26000     -1.575
```

uses ZAID i.e. ZA-ID identifiers of elements and not of isotope, because only atomic interactions and not nuclear reactions, are at stake in the low-energy photon transport simulation required by the ILLW source term. The negative number following the ZAID is the mass-fraction or mass-percentage of the element Z in the material; a positive number would denote a number-of-atoms fraction.

Next, we consider the statement `MODE P` at the start of the data card section of the MCNP calculation model. This simply means that only photon transport is considered in the model.

The photon source term specifies on of the photon emission spectra seen in Figure 5-3 on page 165:

```
sdef   POS  = 0  0  30
       par  = P
       erg  = D22
       x    = D1
       y    = D2
       z    = D3
       cell = 1
       eff  = 1.0E-3
       wgt  = 6.276E+11
c
c
si1 H    -30    +30
sp1 D  0     1
c
si2 H   -30     +30
sp2 D  0     1
si3 H    +0    +100
sp3 D  0     1
c
c =====
c
c      Energy           ST_10yr
#      SI22             SP22
       a                D
       0.000            0.0000
       9.99900e-04      0.0000
       1.00000e-03      5.085222E+08
       1.70000e-03      1.674200E+07
       3.40000e-03      4.008050E+10
       5.40000e-03      3.809000E+12
       7.40000e-03      1.137600E+12
         ⋮                ⋮
       1.47700e+01      0.000000E+00
       1.48700e+01      0.000000E+00
       1.49700e+01      0.000000E+00
       1.50000e+01      0.000000E+00
       1.60700e+01      0.000000E+00
       2.00000e+01      0.000000E+00
c
```

Source photons (par = P) are randomly generated at (x, y, z) points inside a 60 cm × 60 cm × 100 cm cubic volume with origin $(x, y, z) = (0,0,30)$, but then only source-points inside cell 1, are accepted in accordance with the criterion $\boxed{\text{CELL} = 1}$; this is called cell-rejection. Cell-rejection allows one to specify a simple rectangular sweep-volume by using cartesian spatial source distributions D1, D2 and D3. The energy spectrum of the source photons is specified in distribution D22.

The specification $\boxed{\text{wgt} = 6.276\text{E}11}$ means that a total of 6.276E11 source particles is generated inside the source volume of the radioactive waste; the above value of the MCNP keyword parameter **wgt** was computed using the SCALE 6.2.4 code ORIGEN.

The "housekeeping card"

```
CTME   1000
```

specifies that the simulation must run for 1000 minutes. On a PC with e.g. 12 to 15 available threads for multi-threading, this means that the real execution time will be around a factor 10 times less than the specified 1000 minutes.

The MCNP tally specification

```
f126:p   4  6
fm126    5.767836E-7
```

states that the energy deposition rate in cells 4 and 6 must be quantified. Cell 4 represents the volume in which the contact dose rate (CDR) must be quantified, while cell 6 represents the tally volume in which the dose rate on which the transport index (TI) of the package is based, must be known. Tally numbers ending with the number 6 is MCNP's way of requesting the rate of energy deposition. The tally multiplication factor 5.767836E-7 in the correcponding FM card is a unit conversion factor that must be used to ensure that the tally is evaluated in the desired dose rate units, namely Gy/h: $\left(\frac{\text{MeV/g s}}{\text{Gy/h}}\right) = 5.767836\text{E-}7$. By default, MCNP6 evaluates energy deposition rates in the units $\left(\frac{\text{MeV}}{\text{g s}}\right)$. In order to ensure that energy deposition rate results are expressed in Gy/h, the above tally multiplication factor (TMF) has to be specified in the FM card corresponding to the type-6 tally.

B.7 MCNP calculation model: Single concrete drum with cemented liquid radioactive waste

B.7.1 The code MCNP

Until approximately 1980, theoreticians were focused on deriving equations that describe reality. This methodology was fruitful but also turned out to have severe limitations, and the emphasis has since shifted towards computational simulations[36].

The Monte Carlo method is a statistical technique that is capable of simulating a mathematical or physical experiment on a computer. In mathematics, it can provide the expectation value of functions and evaluate integrals; in science and engineering, it is capable of simulating complex problems which

[36] Comment by study supervisor TJvR: see e.g. two lectures by Stephen Wolfram: https://www.youtube.com/watch?v=qoDZKlcdPNM&t=25s and https://www.youtube.com/watch?v=pMfrRFNCKhE.

are comprised of various random processes with known or assumed probability density functions. To be able to simulate the random process which involves sampling from a probability function for an event, the Monte Carlo method uses random numbers or pseudo-random numbers. Just like any statistical process, the Monte Carlo method requires repetition to achieve a small relative uncertainty. Variance reduction methods can be used to enable the Monte Carlo simulation to converge faster.

MCNP is a general-purpose Monte Carlo N-Particle code that can be used for neutron, photon, electron or coupled neutron/photon/electron transport. Specific areas of application include e.g. radiation protection and dosimetry, radiation shielding, nuclear criticality safety, fission reactor analyses and decommissioning of nuclear facilities. The code treats an arbitrary three-dimensional configuration of materials in geometric cells. Pointwise radiation interaction cross-section data in ACE format are used. For the transport of ionising photons, MCNP6 accounts for incoherent and coherent scattering, the possibility of fluorescent emission after photo-electric absorption, absorption in pair production with local emission of annihilation radiation, and bremsstrahlung.

Important standard features that make MCNP versatile and easy to use include keyword-driven (1) geometry & materials specification language, (2) source description language; (3) geometry and output tally plotters; numerous variance reduction techniques; a flexible tally structure; and an extensive collection of cross-section data.

All MCNP calculations of dose rates in this work, used a very simple variance reduction scheme known as population control via cell-importance biasing. A simple example is e.g. seen in the following cell cards:

```
11  14   -3.40      -11  +02                    imp:p=1    $ Concrete Drum Wall
12  14   -3.40      -12  +11                    imp:p=1    $ Concrete Drum Wall
13  14   -3.40      -13  +12                    imp:p=2    $ Concrete Drum Wall
14  14   -3.40      -14  +13                    imp:p=4    $ Concrete Drum Wall
15  14   -3.40      -15  +14                    imp:p=6    $ Concrete Drum Wall
16  14   -3.40      -16  +15                    imp:p=8    $ Concrete Drum Wall
17  14   -3.40      -17  +16                    imp:p=10   $ Concrete Drum Wall
18  14   -3.40      -18  +17                    imp:p=15   $ Concrete Drum Wall
19  14   -3.40      -19  +18                    imp:p=20   $ Concrete Drum Wall
20  14   -3.40      -20  +19                    imp:p=25   $ Concrete Drum Wall
21  14   -3.40      -21  +20                    imp:p=30   $ Concrete Drum Wall
22  14   -3.40      -22  +21                    imp:p=40   $ Concrete Drum Wall
23  14   -3.40      -23  +22                    imp:p=50   $ Concrete Drum Wall
24  14   -3.40      -24  +23                    imp:p=60   $ Concrete Drum Wall
25  14   -3.40      -25  +24                    imp:p=80   $ Concrete Drum Wall
26  14   -3.40      -26  +25                    imp:p=90   $ Concrete Drum Wall
```

To guide the eye, the cell-importance biasing parameters are in red. The above biasing scheme "biases space to encourage particle transport out of the drum, from the interior towards its surface". In

technical terms, the concrete around the cemented radioactive waste is subdivided in nested shells, and cell importances are made higher in increments as one moves from the inside to the outside. This means that particles are split into multiple particles as they move outward, but that a fraction of particles snuffed out when they move deeper into the concrete, away from the spatial region of interest.

The version of MCNP used in this study, was MCNP6.2 (LANL, 2018).

B.7.2 Statistical validity of computed dose rates

MCNP calculation models were run with runtimes and variance reduction schemes that were adequate to keep the Monte Carlo standard deviation of all calculated results well below 0.20 %. A typical result for calculated dose rates for a typical drum, is e.g.

```
cell  35
                  4.18193E-05 0.0012
cell  42
                  6.47554E-06 0.0014
```

The above result means that the highest reported 1σ relative standard deviation for calculated dose rates, is 0.14 %. With dose rates outside a typical HEM-CRT drum being in the order of 10 times lower than for a typical ORD-CRT drum, the dose rate reduction achieved with the use of high-density shielding concretes are in the order of 90 % (see e.g. Table 5-11 on page 177) whereas the 1σ relative standard deviation of all computed results is below 0.2 %. In some research projects, where an effect is debatable, formal techniques of inferential statistics such as a p-value test have to be used to make certain that an effect is a real, trustworthy "signal" and not just statistical "noise". However, in the case of the dose rates computed with MCNP6 in this research work, the effect size (magnitude of dose rate reduction) is huge, and the signal-to-noise ratio is overwhelmingly large (often exceeding a factor of 1000). There is therefore no need to employ inferential statistics methods to formally demonstrate the validity of the overall finding. One may state categorically that the use of high-density shielding concretes in drums holding ILLW, will drive down transmitted dose-rates by significant factors.

B.7.3 MCNP calculation model: Single concrete drum

The set of MCNP6 calculation models used to calculate the dose rate field around a single concrete drum filled with cemented liquid waste, is embedded in Calculation model 6-4 as a RAR file.

Calculation model 6-4: MCNP6 calculation models used to calculate the dose-rate field around a single concrete drum filled with cemented liquid waste



The above archive file is opened by double-clicking it; a prerequisite is that the archive package WINRAR must be downloaded from the URL **https://www.win-rar.com** and installed on the user's PC. Once uncompressed in a suitable folder, the individual MCNP model files should be opened using text editors such as NotePad++ or VS CODE.

The MCNP model describes a concrete drum placed on a large concrete slab. The cemented radioactive waste matrix at the centre of the large drum has a radius of 22.5 cm and stretches vertically from $z = 32.2$ cm to $z = (32.2\text{ cm} + 66\text{ cm}) = 98.2$ cm. The cemented ILLW is surrounded by a 3 mm steel shell, which is in turn nested in an enveloping large concrete drum with a lateral wall thickness of $54.3\text{ cm} - 22.7\text{ cm} = 31.6$ cm. Outside the central waistline (or "belt-line") of the outer surface of the concrete drum, there is a calculational TEM detector, with a wall thickness of $56.0\text{ cm} - 54.3\text{ cm} = 1.7$ cm, which represents a human hand touching the drum, in order to be able to calculate a good estimate of the maximum contact dose-rate (CDR) on the outer surface of the drum. The maximum contact dose-rate (CDR) on the outer surface of the concrete drum filled with radioactive waste, must be below 2 mSv/h, i.e. 2.0E-3 Sv/h, for the drum to be legally transportable, according to the IAEA's transport regulations (IAEA, 2018). At a separation distance of 100 cm from the drum wall, there is a 1 cm thick calculation detector (also located as a circumferential belt-line), to calculate the dose rate at 1 m from the drum, which is used to quantify the "Transport Index" or TI of the package of radioactive material. Packages of radioactive material may be transported if $TI \leq 10$ (IAEA, 2018), which is equivalent to the requirement that the 1-metre peak dose-rate from the surface of the package must be at or below 0.1 mSv/h.

The surface cards in the MCNP calculation model represent the surfaces in the modelled geometry. The MCNP cell cards use these surfaces to uniquely define all of space as belonging to distinct and unique material cells, each filled with a material having a specified composition and mass-density.

After the cell cards and the surface cards, the data cards follow as the third section of an MCNP input. The specification MODE P states that only photons are transported. The SDEF card specifies the

Source Definition. The source particles are photons: `PAR = P`. Some of the source term specifications represent technicalities of how the spatial Monte Carlo sampling of source points are done. We will only focus on the line `ERG = D22` which states that the emitted source-photons have energy distribution number 22, i.e. D22. This photon source spectrum $Q_\gamma(E)$ is displayed in Figure 5-3 on page 165, and is communicated to MCNP via the vertically formatted `SI22 SP22` matrix, which is seen below. (To save space, a long list of numbers related to the source term has been hidden, just under the position of the red text "Hidden text". To make hidden text visible, toggle the



Show/Hide button in the "Home" domain of the menu ribbon of MS WORD.)

```
c Data Cards:
mode P
c
SDEF   POS  = 0  0  30
       PAR  = P
       ERG  = D22
       X    = D1
       Y    = D2
       Z    = D3
       CELL = 1
       EFF  = 1.0E-3
       WGT  = 3.727E+13
c
si1 H    -30    +30
sp1 D  0     1
c
si2 H   -30     +30
sp2 D  0     1
c
si3 H    +0    +100
sp3 D  0     1
c
c =====
c
c      Energy           ST_0.25yr
#      SI22             SP22
       A                D
Hidden text
```

The materials for the 4 concrete types have been discussed in § 2.4.4 starting on page 77, and this topic requires no further explanation.

The MCNP housekeeping card, CTME 2000, states that the MCNP6.2 Monte Carlo simulation should run for the equivalent of 2000 minutes on a single-core processor. On an 8-core processor that can run $2 \times 8 = 16$ execution threads, the 2000 prescribed minutes of MCNP6.2 execution, maps to roughly 200 minutes real execution time, which is an "affordable" time i.t.o. project completion.

B.8 MCNP calculation model: Array of 11 x 5 concrete drums in the "decay-yard"

The MCNP calculation model for an array of $5 \times 11 = 55$ concrete drums containing cemented ILLW, arranged on a large concrete slab in the "decay yard", is embedded as Calculation model 6-5.

Calculation model 6-5: MCNP calculation model for an array of $11 \times 5 = 55$ concrete drums containing cemented ILLW



The above archive file is opened by double-clicking it; a prerequisite is that the archive package WINRAR must be downloaded from the URL **https://www.win-rar.com** and installed on the user's PC. Once uncompressed in a suitable folder, the individual MCNP model files should be opened using text editors such as NotePad++ or VS CODE.

The MCNP calculation models of the drum array were used to calculate dose rates at the fence of the decay yard where the cemented liquid waste drums are allowed to cool off for a waiting period, before being shipped to the national repository for radioactive waste disposal. The geometry of the modelled array of $5 \times 11 = 55$ drums is shown in Figure 5-7 on page 170. Dose rates are tallied at the "fence" around the rectangular "decay yard" border in Figure 5-7 on page 170. In the MCNP model, the "fence" is a 180 cm high calculation detector filled with tissue-equivalent material; it represents people standing at the fence of the decay yard.

Selected parts of the MCNP calculational model for the array of concrete drums are now discussed block-by-block.

The first topic is that the model uses the repeated structure capability of MCNP, which involves the concepts U (Universe), LAT (lattice) and FILL to define a repeated structure. In essence, one complete

drum with its square air-volume "unit-cell" is defined. This is repeated in an infinite lattice, which is then "cut" using a cookie-cutter surface card, to define a finite 11 x 5 array.

```
ILLW 100L 42LEU-ITPS @ T_cool, INSIDE CRT DRUM, 5×11=55 DRUM ARRAY
c Cell Cards:
c M11 = ORD CRT; rho = 2.30 g/cc
c M12 = MAG CRT; rho = 3.20 g/cc
c M13 = HEM CRT; rho = 3.40 g/cc
c M14 = BAR CRT; rho = 3.40 g/cc
c
01  1   -1.5       -1                    u=1   IMP:P=1   $ CEMENTED LW IN DRUM
02  2   -7.85      -2  +1                u=1   IMP:P=1   $ MILD STEEL DRUM WALL
03  13  -3.40      -3  +2                u=1   IMP:P=1   $ Concrete Drum Wall
04  4   -1.2E-3        +3                u=1   IMP:P=1   $ Infinite air around drum
05  0             -10    lat=1  fill=1  u=2   IMP:P=1   $ Infinite lattice of drums
c
11  0             -11           fill=2        IMP:P=1   $ Finite Array of 11 x 5 drums
c
21  11  -2.30     -21                         IMP:P=1   $ ORD-CRT FLOOR SLAB
23  3   -0.10     -23  +22                    IMP:P=1   $ TEM-DET at Fence
31  4   -1.2E-3   -99  +11 +21 #23            IMP:P=1   $ AIR SURROUND
c
99  0                 +99                     IMP:P=0   $ EXTERNAL VOID
```

In the source definition (SDEF), the following special repeated structure syntax restricts photon emission to the cemented ILLW volume inside each of the 55 drums in the array.

```
c Restrict photon emission to the fuel pins in the 5 fuel assemblies, using cell-
rejection
SI51 L  (1<5[-5:5 -2:2 0:0]<11)
SP51 D  1.00  54R          $ 5x11=55 = 1 + 54 Drums in Drum Array in Decay Yard
```

The following mesh tally requests the quantification of the photon dose-rate in

$$130 \times 100 = 13{,}000$$

volumes (voxels). These values are then ported to a plotting package to construct a contour plot of the calculated dose-rates, allowing for the intuitive visualisation of results. The information obtained from the following mesh tally specification, is visualised in Figure 5-19 on page 195.

```
FC124 Mesh tally – photon dose-rate
FMESH124:p
       GEOM   = XYZ
       ORIGIN = -2000  -1500  +20
       TYPE   = FLUX
       FACTOR = 1.0
       OUT    = IJ    $ alternatives: COL or JK
       WGT    = 1.0
c
       IMESH =       +2000
       IINTS = 130
c
```

```
       JMESH =       +1500
       JINTS = 100
c
       KMESH =        +170
       KINTS = 1
c
c FRDRCF - NCS - Photons:
#      DE124            DF124
       1.00000E-3      2.88000E-11
       5.00000E-3      4.82400E-11
       6.00000E-3      5.97600E-11
       7.00000E-3      8.10000E-11
       8.00000E-3      1.20600E-10
       9.00000E-3      1.76400E-10
       1.00000E-2      2.46600E-10
       1.20000E-2      3.78000E-10
       1.30000E-2      4.39200E-10
       1.50000E-2      5.61600E-10
       1.70000E-2      6.51600E-10
       2.00000E-2      8.10000E-10
       2.50000E-2      9.90000E-10
       3.00000E-2      1.12320E-09
       4.00000E-2      1.26360E-09
       5.00000E-2      1.33200E-09
       6.00000E-2      1.40400E-09
       7.00000E-2      1.48680E-09
       8.00000E-2      1.59840E-09
       1.00000E-1      1.86840E-09
       1.50000E-1      2.69280E-09
       2.00000E-1      3.60000E-09
       3.00000E-1      5.43600E-09
       4.00000E-1      7.20000E-09
       5.00000E-1      8.89200E-09
       5.11000E-1      9.07200E-09
       6.00000E-1      1.04760E-08
       6.62000E-1      1.14120E-08
       8.00000E-1      1.34280E-08
       1.00000E+0      1.61640E-08
       1.11700         1.76400E-08
       1.33000         2.01240E-08
       1.50000         2.20320E-08
       2.00000         2.69280E-08
       3.00000         3.51000E-08
       4.00000         4.21200E-08
       5.00000         4.82400E-08
       6.00000         5.40000E-08
       6.12900         5.47200E-08
       8.00000         6.69600E-08
       1.00000E+1      7.95600E-08
       1.50000E+1      1.09440E-07
       2.00000E+1      1.37520E-07
```

The WGT value in the SDEF card for the calculation models for the drum array, is 55 times higher than the WGT value for the single-drum case, because there are $5 \times 11 = 55$ identical drums present in the drum array.

The (DE, DF)-matrix in Calculation model 6-5 on page 261, is a listing of the $(E_i, \Re_i)$-values of the blue line in the fluence-rate to dose-rate response function $\Re_\gamma(E)$ in Figure 6-10 which is based on (ICRU, 2020).

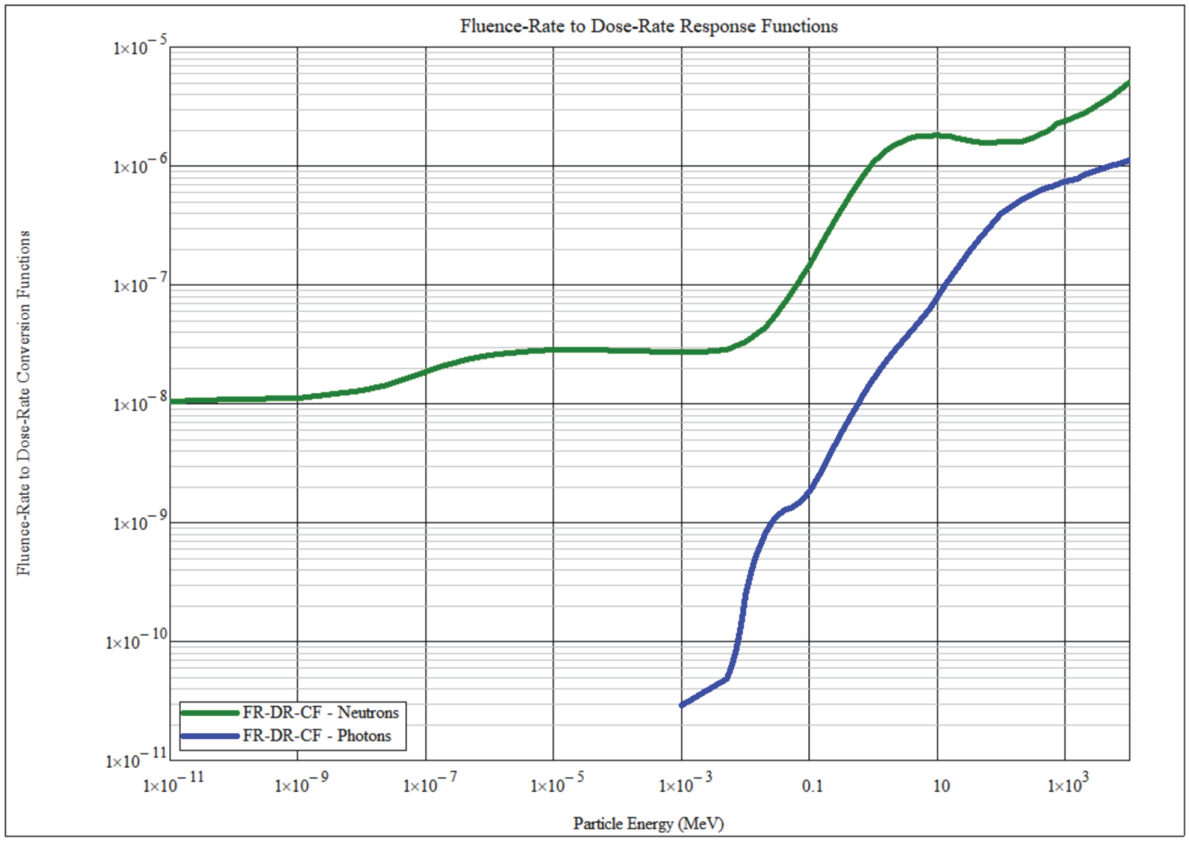


Figure 6-10: The fluence-rate to dose-rate response function R(E) for ionising photons (ICRU, 2020)

This concludes the explanation of the MCNP6 Calculation model 6-5 for the array of $5 \times 11 = 55$ drums holding ILLW.

Bibliography

Abdo, A.E.S., Kansouh, W.A. & Megahid, R.M. 2002. Investigation of Radiation Attenuation Properties for Baryte Concrete. *Japanese Journal of Applied Physics*. 41(12R):7512.

Abubakar, A.K., Zakari, Y.I., Sadiq, U. & Van Rooyen, T.J. 2014. Investigation of Neutron and Photon Shielding Prospects of Nigerian Magnetite Using the MCNPX Code. In: Abuja, Nigeria: Nigeria Atomic Energy Corporation, Abuja, Nigeria. https://inis.iaea.org/search/search.aspx?orig_q=RN:45088700.

Ade, B. & Betzler, B. 2016. ORIGEN Reactor Libraries.

Adetula, B.A. 2017. *SAFARI-1 LEU Spent Fuel Transfer Cask*. (RRT-SAFA-REP-17038). Pelindaba, Pretoria, South Africa: Radiation and Reactor Theory (RRT) Section, South African Nuclear Energy Corporation SOC Ltd. (Necsa).

Ahmad, M. 2011. Molybdenum-99/Technetium-99m Management: Race Against Time. *Annals of Nuclear Medicine*. 25(9):677–679.

Ahmad, M., Vandegrift, G. & Cristini, P. 2014. Molybdenum-99 (99Mo): Past, Present, and Future. *Science and Technology of Nuclear Installations*. 2014:839369.

Akhiezer, N.I. & Glazman, I.M. 1993. *Theory of Linear Operations in Hilbert Space*. Dover Publications.

Akkurt, I., Basyigit, C., Kilincarslan, S., Mavi, B. & Akkurt, A. 2006. Radiation shielding of concretes containing different aggregates. *Cement and concrete composites*. 28(2):153–157.

Akkurt, I., Akyıldırım, H., Mavi, B., Kilincarslan, S. & Basyigit, C. 2010. Radiation shielding of concrete containing zeolite. *Radiation Measurements*. 45(7):827–830.

Atkins, M. & Glasser, F.P. 1992. Application of Portland Cement-Based Materials to Radioactive Waste Immobilization. *Waste management*. 12(2–3):105–131.

Bart, F., Cau-dit-Coumes, C., Frizon, F. & Lorente, S. eds. 2012. *Cement-Based Materials for Nuclear Waste Storage*. 2013th ed. Springer.

Bashter, I.I., Abdo, A.E.-S. & Abdel-Azim, M.S. 1997. Magnetite ores with steel or basalt for concrete radiation shielding. *Japanese journal of applied physics*. 36(6R):3692.

Basyigit, C., Uysal, V., Kilinçarslan, Ş., Mavi, B., Günoğlu, K., … Akkaş, A. 2011. Investigating radiation shielding properties of different mineral origin heavyweight concretes. In: Vol. 1400. *AIP conference proceedings*. American Institute of Physics. pp. 232–235.

Borai, E.H., Harjula, R. & Paajanen, A. 2009. Efficient Removal of Cesium from Low-Level Radioactive Liquid Waste Using Natural and Impregnated Zeolite Minerals. *Journal of Hazardous Materials*. 172(1):416–422.

Brown, D.A., Chadwick, M.B., Capote, R., Kahler, A.C., Trkov, A., … Dunn, M. 2018. ENDF/B-VIII.0: The 8th Major Release of the Nuclear Reaction Data Library with CIELO-Project

Cross Sections, New Standards and Thermal Scattering Data. *Nuclear Data Sheets*. 148:1–142.

Brown, M.A., Johnson, N., Gelis, A.V., Stika, M., Servis, A.G., … Tkac, P. 2021. Recovery of high specific activity molybdenum-99 from accelerator-induced fission on low-enriched uranium for technetium-99m generators. *Scientific Reports*. 11(1):13292.

Cau-dit-Coumes, C. 2013. Alternative Binders to Ordinary Portland Cement for Radwaste Solidification and Stabilization. *Cement-Based Materials for Nuclear Waste Storage*. 171–191.

Cau-dit-Coumes, C. 2014. Cement Stabilization / Solidification of Low- and Intermediate-Level Radioactive Wastes Research Centers Form the French Atomic Energy Commission for Industry Units Based. 1–45.

Cau-dit-Coumes, C., Courtois, S., Peysson, S., Ambroise, J. & Pera, J. 2009. Calcium sulfoaluminate cement blended with OPC: A potential binder to encapsulate low-level radioactive slurries of complex chemistry. *Cement and Concrete Research*. 39(9):740–747.

Collier, N.C., Milestone, N.B., Gordon, L.E. & Ko, S.C. 2014. Suitability of a Supersulfated Cement for Nuclear Waste Immobilisation. *Journal of Nuclear Materials*. 452(1–3):457–464.

Conlin, J.L., Haeck, W., Neudecker, D., Parsons, K.D. & White, M.C. 2018. *Release of ENDF/B-8.0-Based ACE Data Files for MCNP*. (LA-UR-18-24034). USA: Nuclear Data Team, XCP-5, Los Alamos National Laboratory (LANL).

Davidson, G.G., Pandya, T.M., Johnson, S.R., Evans, T.M., Isotalo, A.E., … Wieselquist, W.A. 2018. Nuclide depletion capabilities in the Shift Monte Carlo code. *Annals of Nuclear Energy*. 114:259–276.

De Freitas, R.M. & Al-Tabbaa, A. 2013. Development of Low-pH Cements for Immobilisation of Intermediate Level Radioactive Waste: Achievements and Challenges. In: Vol. 1. *Proceedings of the International Conference on Radioactive Waste Management and Environmental Remediation, ICEM*.

DeHart, M.D. & Petrie, L.M. 2004. A radioisotope depletion method using Monte Carlo transport with variance reduction and error propagation. *Transactions, Chicago, American Nuclear Society*.

Drace, Z. & Ojovan, M.I. 2011. Cementitious Materials for Radioactive Waste Management within IAEA Coordinated Research Project. In: Vol. 54983. *International Conference on Radioactive Waste Management and Environmental Remediation*. pp. 5–13.

Drace, Z., Mele, I., Ojovan, M.I. & Rahman, R.O.A. 2012. Overview of research activities on cementitious materials for radioactive waste management. *MRS Online Proceedings Library*. 1475(1):253–264.

Eckelman, W.C. 2009. Unparalleled Contribution of Technetium-99m to Medicine Over 5 Decades. *JACC: Cardiovascular Imaging*. 2(3):364–368.

Elliott, A.T. 1994. Radionuclide generators. In: *Textbook of Radiopharmacy: Theory and practice*. Gordon and Breach, Singapore. pp. 19.

Evans, N.D.M. 2008. Binding Mechanisms of Radionuclides to Cement. *Cement and Concrete Research*. 38(4):543–553.

Fllaoui, A., Ghamad, Y., Zoubir, B., Ayaz, Z.A., El Morabiti, A. & Amayoud, H. 2016. Validation of a new design of tellurium dioxide-irradiated target. *Nuclear Engineering and Technology*. 48(5):1273–1279.

Freiesleben, H. 2013. Final Disposal of Radioactive Waste. *EPJ Web of Conferences*. 54:01006.

GE Healthcare. 2014. *GE Healthcare Announces FDA Approval to Supply Technetium 99m Generators*. https://www.businesswire.com/news/home/20140530005046/en/GE-Healthcare-Announces-FDA-Approval-Supply-Technetium Date of access: 12 Feb. 2020.

Geddes, D.A., Ke, X., Bernal, S.A., Hayes, M. & Provis, J.L. 2018. Metakaolin-Based Geopolymers for Nuclear Waste Encapsulation. In: F. Martirena, A. Favier, & K. Scrivener, eds. Vol. 16. *Calcined Clays for Sustainable Concrete*. Dordrecht: Springer, Netherlands. pp. 183–188. http://link.springer.com/10.1007/978-94-024-1207-9_29.

Gencel, O., Brostow, W., Ozel, C. & Filiz, M. 2010. Concretes Containing Hematite for Use as Shielding Barriers. *Journal of Material Science*. 16(3):249–256.

Glasser, F. 2011. Application of Inorganic Cements to the Conditioning and Immobilisation of Radioactive Wastes. In: *Handbook of Advanced Radioactive Waste Conditioning Technologies*. Elsevier. pp. 67–135.

Glasser, F.P. 2010. *Cements in Radioactive Waste Disposal*. Aberdeen, Scotland, UK: University of Aberdeen.

Gunoglu, K. & Akkurt, İ. 2021. Radiation shielding properties of concrete containing magnetite. *Progress in Nuclear Energy*. 137:103776.

Haffner, R., Miller, W.H. & Morris, S. 2019. Verification of I-131 yields from the neutron irradiation of tellurium. *Applied Radiation and Isotopes*. 151:52–61.

Henry, A.F. 1975. *Nuclear Reactor Analysis*. Vol. 4. MIT Press Cambridge, Massachusetts.

Hosan, I. 2018. Radioactive Waste Classification, Management and Environment. *Engineering International*. 5(2):53–62.

Hussain, A. & Al-Othmany, D. 2013. Treatment and Conditioning of Spent Ion Exchange Resin from Nuclear Power Plant. *Advances in Physics Theories and Applications*. 12.

IAEA. 1996. *Clearance Levels for Radionuclides in Solid Materials*. (IAEA-TECDOC-855). Vienna, Austria: International Atomic Energy Agency (IAEA).

IAEA. 1998. *Management of Radioactive Waste from 99Mo Production*. (IAEA-TECDOC-1051). Vienna, Austria: International Atomic Energy Agency (IAEA).

IAEA. 2001. *Generic Models for Use in Assessing the Impact of Discharges of Radioactive Substances to the Environment*. (Safety Reports Series No. 19). Vienna, Austria: International Atomic Energy Agency (IAEA). https://www.iaea.org/publications/6024/generic-models-for-use-in-assessing-the-impact-of-discharges-of-radioactive-substances-to-the-environment.

IAEA. 2003. *Manual for Reactor Produced Radioisotopes*. (IAEA TECDOC 1340). Vienna, Austria: International Atomic Energy Agency (IAEA). http://www.isotopes.gov/outreach/reports/Reactor_Isotopes.pdf.

IAEA. 2006. *Development of Specifications for Radioactive Waste Packages*. (IAEA-TECDOC-1515). Vienna, Austria: International Atomic Energy Agency (IAEA). https://www.iaea.org/publications/7571/development-of-specifications-for-radioactive-waste-packages.

IAEA. 2009a. *Classification of Radioactive Waste for protecting people and the environment*. (General Safety Guide GSG-1). Vienna, Austria: International Atomic Energy Agency (IAEA). http://www-ns.iaea.org/standards/.

IAEA. 2009b. *Predisposal Management of Radioactive Waste - General Safety Requirements Part 5*. Vienna, Austria: International Atomic Energy Agency (IAEA).

IAEA. 2011a. *Nuclear Security Recommendations on Nuclear and Other Radioactive Material Out of Regulatory Control*. (15). Vienna, Austria: International Atomic Energy Agency (IAEA).

IAEA. 2011b. *Research Reactors in Africa*. Vienna, Austria: International Atomic Energy Agency (IAEA).

IAEA. 2014a. *Radiation Protection and Safety of Radiation Sources: International Basic Safety Standards - General Safety Requirements Part 3 - GSR-3*. Vol. 3. (General Safety Requirements no. GSR Part 3). Vienna, Austria: International Atomic Energy Agency (IAEA).

IAEA. 2014b. *Near Surface Disposal Facilities for Radioactive Waste*. (Text SSG-29). Vienna, Austria: International Atomic Energy Agency (IAEA). https://www.iaea.org/publications/10567/near-surface-disposal-facilities-for-radioactive-waste.

IAEA. 2017. *Selection of Technical Solutions for the Management of Radioactive Waste.* (IAEA-TECDOC-1817). Vienna, Austria: International Atomic Energy Agency (IAEA). https://public.ebookcentral.proquest.com/choice/publicfullrecord.aspx?p=4921054.

IAEA. 2018. *Regulations for the Safe Transport of Radioactive Material (SSR-6)*. (SSR-6 (Rev. 1)). Vienna, Austria: International Atomic Energy Agency (IAEA). https://iopscience.iop.org/article/10.1088/0952-4746/18/3/026.

IAEA. 2019. *Strategy and Methodology for Radioactive Waste Characterization*. (IAEA-TECDOC-1537). Vienna, Austria: International Atomic Energy Agency (IAEA). https://www.iaea.org/publications/7655/strategy-and-methodology-for-radioactive-waste-characterization.

IAEA. 2020. *Design Principles and Approaches for Radioactive Waste Repositories*. (NW-T-1.27). Vienna, Austria: International Atomic Energy Agency (IAEA).

ICRP. 2007. *The 2007 Recommendations of the International Commission on 103*. Vol. 103. Elsevier.

ICRU. 2011. *Fundamental Quantities and Units for Ionizing Radiation*. (Journal of the ICRU Vol 11 No 1 (2011) Report 85). Bethesda, Maryland, USA: International Commission on Radiation Units and Measurements.

ICRU. 2020. *Operational Quantities for External Radiation Exposure*. (ICRU Report 95). Maryland, USA: International Commission on Radiation Units & Measurements (ICRU). 10.1177/1473669120966222.

Ionascu, L., Nicu, M., Turcanu, C., Dragolici, F., Rotarescu, G.H. & Hulubei, H. 2013. Chemical Composition of Radioactive Waste and the Mechanical Performance of Cemented Matrix. *Romanian Reports in Physics*. 65(4):1512–1518.

Jansen, D.R., Krijger, G.C., Kolar, Z.I., Zonnenberg, A.B. & Zeevaart, J.R. 2010. Targeted Radiotherapy of Bone Malignancies. *Current drug discovery technologies*. 7(4):233–246.

Jantzen, C.M., Lee, W.E. & Ojovan, M.I. 2013. Radioactive waste (RAW) conditioning, immobilization, and encapsulation processes and technologies: overview and advances. In: W.E. Lee, M.I. Ojovan, & C.M. Jantzen, eds. (Woodhead Publishing Series in Energy). *Radioactive Waste Management and Contaminated Site Clean-Up*. Woodhead Publishing. pp. 171–272.

Jessee, M.A., Ade, B. & Evans, T. 2017. Reactor Physics Capabilities in SCALE 6.2.

Kamaruzaman, N.S., Kessel, D.S. & Kim, C.L. 2018. Management of Spent Ion-Exchange Resins From Nuclear Power Plant by Blending Method. *Journal of the Nuclear Fuel Cycle and Waste Technology(JNFCWT)*. 16(1):65–82.

Kautsky, U., Saetre, P., Berglund, S., Jaeschke, B., Nordén, S., … Andersson, E. 2016. Impact of low and intermediate-level radioactive waste on humans and the environment over the next one hundred thousand years. *Journal of Environmental Radioactivity*. 151:395–403.

Kelley, D. 2017. Proven Technologies for the Solidification of Complex Liquid Radioactive Waste (LRW): Global Case Studies of Applications and Disposal Options. In: Vol. 57854. *International Conference on Nuclear Engineering*. American Society of Mechanical Engineers. pp. V007T10A002.

Kim, B., Lee, J., Kang, J. & Um, W. 2021. Development of geopolymer waste form for immobilization of radioactive borate waste. *Journal of Hazardous Materials*. 126402.

Knapp, F.F.R. & Mirzadeh, S. 1994. Continuing Important Role of Radionuclide Generator Systems for Nuclear Medicine. *European Journal of Nuclear Medicine*. 21(10):1151–1165.

Kot'átková, J., Zatloukal, J., Reiterman, P. & Kolář, K. 2017. Concrete and Cement Composites Used for Radioactive Waste Deposition. *Journal of Environmental Radioactivity*. 178:147–155.

Kozempel, J., Mokhodoeva, O. & Vlk, M. 2018. Progress in Targeted Alpha-Particle Therapy. What We Learned about Recoils Release from In Vivo Generators. *Molecules*. 23(3):581.

Lamarsh, J.R. & Baratta, A.J. 2017. *Introduction to Nuclear Engineering*. 4 edition ed. Hoboken, NJ: Pearson.

LANL. 2018. *RSICC Code Package CCC-850: MCNP6.2: Monte Carlo N–Particle Transport Code System Including MCNP6.2 and MCNPDATA Libraries*. Los Alamos, USA: LANL.

Laverov, N.P., Omel'yanenko, B.I., Yudintsev, S.V. & Stefanovsky, S.V. 2012. Confinement Matrices for Low- and Intermediate-Level Radioactive Waste. *Geology of Ore Deposits*. 54(1):1–16.

Lee, W.H., Cheng, T.W., Ding, Y.C., Lin, K.L., Tsao, S.W. & Huang, C.P. 2019. Geopolymer technology for the solidification of simulated ion exchange resins with radionuclides. *Journal of Environmental Management*. 235:19–27.

Lersow, M. & Waggitt, P. 2019. *Disposal of All Forms of Radioactive Waste and Residues: Long-Term Stable and Safe Storage in Geotechnical Environmental Structures*. 1st ed. 2020 edition ed. Springer.

Matsuyama, K., Okabe, H., Shimoda, C., Miyamoto, S., Kaneko, M., … Toyohara, M. 2017. Geopolymer Solidification of Intermediate Level Waste–17078.

Milestone, N.B. 2006. Reactions in Cement Encapsulated Nuclear Wastes: Need for Toolbox of Different Cement Types. *Advances in Applied Ceramics*. 105(1):13–20.

Mirzadeh, S., Mausner, L.F. & Garland, M.A. 2011. Reactor-Produced Medical Radionuclides. In: 2nd ed. (Springer Reference). *Handbook of Nuclear Chemistry*. Springer. pp. 1857–1902.

Moloko, L.E. 2011. Impact of Beryllium Reflector Ageing on SAFARI-1 Reactor Core Parameters. Potchefstroom, South Africa: North-West University. (MSc Dissertation).

Mushtaq, A., Iqbal, M. & Muhammad, A. 2009. Management of radioactive waste from molybdenum-99 production using low enriched uranium foil target and modified CINTICHEM process. *Journal of Radioanalytical and Nuclear Chemistry*. 281(3):379–392.

Nagasaki, S. & Nakayama, S. eds. 2015. *Radioactive Waste Engineering and Management*. 2015 edition ed. Springer.

NEA. 2016. *2016 Medical Isotope Supply Review: 99Mo/99mTc Market Demand and Production Capacity Projection 2016-2021*. (NEA/SEN/HLGMR(2016)2). Paris, France: Nuclear Energy Agency (NEA/OECD).

Netshiozwi, S.T. 2002. Origin of High-Grade Hematite Ores at Thabazimbi Mine, Limpopo Province, South Africa. Johannesburg, South Africa: University of Johannesburg (UJ). (Masters).

NISDF. 2017. *The UK Nuclear Industry Guide To: Clearance and Radiological Sentencing: Principles, Process and Practices.* Phoenix House, 18 King William Street, London EC4N 7BP: The Nuclear Institute (UK). https://www.nuclearinst.com/Publications Date of access: 20 Nov. 2019.

Ojovan, M.I. & Hyatt, N.C. eds. 2020. *Materials for Nuclear Waste Immobilization*. S.l.: Mdpi AG.

Ojovan, M.I. 2011. *Handbook of advanced radioactive waste conditioning technologies*. Elsevier.

Ojovan, M.I., Lee, W.E. & Kalmykov, S.N. 2019. *An Introduction to Nuclear Waste Immobilisation*. 3 edition ed. Elsevier.

ORNL. 2020. *SCALE: A Comprehensive Modelling and Simulation Suite for Nuclear Safety Analysis and Design, Version 6.2.4.* Radiation Safety Information Computational Center (RSICC), Oak Ridge National Laboratory, USA. http://rsicc.ornl.gov/.

Ouda, A.S. 2021. Preliminary investigation on gamma-ray attenuation of alkali-activated concrete waste based-geopolymer modified with pozzocrete fly-ash. *Progress in Nuclear Energy*. 134:103681.

PNNL. 2011. *Compendium of Material Composition Data for Radiation Transport Modeling*. (PNNL-15870 Rev. 1). Pacific Northwest National Laboratory.

Pusa, M. 2013. *Numerical Methods for Nuclear Fuel Burnup Calculations*. VTT Technical Research Centre of Finland: Aalto University.

Pusa, M. & Leppänen, J. 2013. Solving Linear Systems with Sparse Gaussian Elimination in the Chebyshev Rational Approximation Method. *Nuclear Science and Engineering*. 175(3):250–258.

Pusch, R. 2006. Clays and Nuclear Waste Management. *Developments in Clay Science*. 1:703–716.

Rahman, R.O.A., Rakhimov, R.Z., Rakhimova, N.R. & Ojovan, M.I. 2014. *Cementitious materials for nuclear waste immobilization*. John Wiley & Sons.

Raj, K., Prasad, K.K. & Bansal, N.K. 2006. Radioactive Waste Management Practices in India. *Nuclear Engineering and Design*. 236(7–8):914–930.

Rearden, B.T. & Jessee, M.A. 2020. *SCALE Code System Version 6.2.4 Reference Manual*. (Report ORNL/TM-2005/39). Office of Scientific and Technical Information (OSTI), PO Box 62, Oak Ridge, TN 37831, USA. https://www.ornl.gov/scale.

Saey, P.R. 2009. The influence of radiopharmaceutical isotope production on the global radioxenon background. *Journal of Environmental Radioactivity*. 100(5):396–406.

Saey, P.R.J., Ringbom, A., Bowyer, T.W., Zähringer, M., Auer, M., … Verboomen, B. 2013. Worldwide measurements of radioxenon background near isotope production facilities, a nuclear power plant and at remote sites: the “EU/JA-II” Project. *Journal of Radioanalytical and Nuclear Chemistry*. 296(2):1133–1142.

Saling, J. 2018. *Radioactive Waste Management*. 2nd edition ed. Routledge.

Sellin, P. & Leupin, O.X. 2013. Clay as an Engineered Barrier in Radioactive-Waste Management–a Review. *Clays and Clay Minerals*. 61(6):477–498.

Shams, T., Eftekhar, M. & Shirani, A. 2018. Investigation of gamma radiation attenuation in heavy concrete shields containing hematite and barite aggregates in multi-layered and mixed forms. *Construction and Building Materials*. 182:35–42.

Sharp, J.H., Hill, J., Milestone, N.B. & Miller, E.W. 2003. Cementitious Systems for Encapsualation of Intermediate Level Waste. In: *ASME 2003 9th International Conference on Radioactive Waste Management and Environmental Remediation*. American Society of Mechanical Engineers Digital Collection. pp. 1425–1433.

Shi, C. & Fernández-Jiménez, A. 2006. Stabilization/Solidification of Hazardous and Radioactive Wastes with Alkali-Activated Cements. *Journal of Hazardous Materials*. 137(3):1656–1663.

Shultis, J.K. & Faw, R.E. 2000. *Radiation Shielding*. La Grange Park, IL: American Nuclear Society (ANS).

Shultis, J.K. & Faw, R.E. 2005. Radiation Shielding Technology. *Health Physics*. 88(4):297–322.

Singh, N.B., Kumar, M. & Rai, S. 2020. Geopolymer cement and concrete: Properties. *Materials Today: Proceedings*. 29:743–748.

Škvára, F., Svoboda, P., Doležal, J., Bittnar, Z., Šmilauer, V., … Šulc, R. 2008. Geopolymer Concrete - an Ancient Material Too? *Ceramics- Silikáty*. 52(4):296–298.

Soppera, N., Bossant, M., Cabellos, O., Dupont, E. & Díez, C.J. 2013. *JANIS 4.0 JAva-based Nuclear Information System*. Paris, France: OECD Nuclear Energy Agency (NEA).

Stewart, M.W.A., Vance, E.R., Moricca, S.A., Brew, D.R., Cheung, C., … Bermudez, W. 2013. Immobilisation of Higher Activity Wastes from Nuclear Reactor Production of 99Mo. *Science and Technology of Nuclear Installations*. 2013:926026.

Sublet, J.-Ch., Eastwood, J.W., Morgan, J.G., Gilbert, M.R., Fleming, M. & Arter, W. 2017. FISPACT-II: An Advanced Simulation System for Activation, Transmutation and Material Modelling. *Nuclear Data Sheets*. 139:77–137.

Sukhanov, L.P. 2013. Methods and Production of Cementation Materials for Immobilisation into Waste Form. Research of Cementation Processes for Specific Liquid Radioactive Waste Streams of Radiochemical Plants.

Swift, P., Kinoshita, H., Collier, N.C. & Utton, C.A. 2013. Phosphate Modified Calcium Aluminate Cement for Radioactive Waste Encapsulation. *Advances in Applied Ceramics*. 112(1):1–8.

Tan, Q., Li, N., Xu, Z., Chen, X., Peng, X., … Yao, Z. 2019. Comparative performance of cement and metakaolin based-geopolymer blocks for strontium immobilization. *Journal of the Ceramic Society of Japan*. 127(1):44–49.

Tomar, B.S., Steinebach, O.M., Terpstra, B.E., Bode, P. & Wolterbeek, H.T. 2010. Studies on Production of High Specific Activity 99Mo and 90Y by Szilard-Chalmers Reaction. *Radiochimica Acta International journal for chemical aspects of nuclear science and technology*. 98(8):499–506.

Van der Merwe, N.J. 2017. *System for the Classification and Demarcation of Radiological Areas*. (Necsa SHEQ Instruction SHEQ-INS-8030). Pelindaba, Pretoria, South Africa: South African Nuclear Energy Corporation, Pty Ltd (Necsa).

Van Rooyen, T.J. 1992. *Kinematics and Dynamics of Compton Scattering*.

Van Rooyen, T.J. 2009. *Design of a Shielding Wall around the NTP Decay Yard for Radioactive Waste*. (RRT-SHLD-REP-09003). Pelindaba, Pretoria, South Africa: Radiation and Reactor Theory (RRT) Section, South African Nuclear Energy Corporation SOC Ltd. (Necsa).

Van Rooyen, T.J. 2011. *Doses Around the Concrete-Walled NTP Hotcells 2 and 3 in the Event of Criticality Accidents*. Pelindaba, South Africa: Radiation and Reactor Theory (RRT), South African Nuclear Energy Corporation (Necsa).

Van Rooyen, T.J. 2012. *Dose Rates Outside NTP Hotcell-2 Holding the Solid Radioactive Waste from 53760 Processed Moly-Production Target Plates*. (RRT-SHLD-REP-12003). Pelindaba, South Africa: Radiation and Reactor Theory (RRT), South African Nuclear Energy Corporation (Necsa).

Van Rooyen, T.J. 2017. *Activities, Heat Release Rates and Dose-Rates for Solid-Residue from Irradiated LEU and MEU Target-Plates, in LTS Containers*. (RRT-SHLD-REP-17003). Pelindaba, Pretoria, South Africa: Radiation and Reactor Theory (RRT) Section, South African Nuclear Energy Corporation SOC Ltd. (Necsa).

Van Rooyen, T.J. 2018a. *Lead-Glass Shielding Thicknesses Required to Achieve Dose-Rate Reduction Goals for the Cementation of Liquid Radioactive Waste at NTP*. (RRT-SHLD-REP-18001). Pelindaba, South Africa: Radiation and Reactor Theory (RRT), South African Nuclear Energy Corporation (Necsa).

Van Rooyen, T.J. 2018b. *Down-Blending Scoping Study for Using Uranium Recovered from HEU MTR Fuel, to Produce LEU Target-Plates for Medical Radio-Isotope Production*. (RRT-UDB-REP-18001 REV03). Pelindaba, Pretoria, South Africa: Radiation and Reactor Theory (RRT) Section, South African Nuclear Energy Corporation SOC Ltd. (Necsa).

Van Rooyen, T.J. 2018c. *Nuclear Criticality Safety Assessment for a Pipe-Storage Facility for LTS Containers Holding Uranic Solid-Residue from Processed Target-Plates*. (RRT-CRIT-REP-18002). Pelindaba, South Africa: Radiation and Reactor Theory (RRT), South African Nuclear Energy Corporation (Necsa).

Van Rooyen, T.J. 2019a. *Dependence of the Peak Dose-Rate Outside a Mausoleum Containing 3 Koeberg OSGs, on the Density of the Concrete*. (RRT-SHLD-REP-19007). Radiation and Reactor Theory (RRT) Section, Necsa, South Africa.

Van Rooyen, T.J. 2019b. *Effect of Shielding Material-Loss at the Edge of a NTP C5 Concrete Drum Containing Low-Density Radioactive Waste, on External Dose-Rates, Rev 02*. (RRT-NTP-REP-19001). Pelindaba, Pretoria, South Africa: Radiation and Reactor Theory (RRT) Section, South African Nuclear Energy Corporation SOC Ltd. (Necsa).

Van Rooyen, T.J. 2019c. *Calculation of Energy Deposition Rates and Dose-Rates for an Irradiated SAFARI-1 Fuel-Assembly in the Spent-Fuel Transport-Cask*. (RRT-SAFA-REP-17040 REV

03). Pelindaba, Pretoria, South Africa: Radiation and Reactor Theory (RRT) Section, South African Nuclear Energy Corporation SOC Ltd. (Necsa).

Van Rooyen, T.J. 2019d. *Koeberg Original Steam Generators (OSGs): Shielding Studies for On-Site Transient Storage*. (RRT-SHLD-REP-19004). Pelindaba, Pretoria, South Africa: Radiation and Reactor Theory (RRT) Section, South African Nuclear Energy Corporation SOC Ltd. (Necsa).

Van Rooyen, T.J. 2019e. *Dose-Rate Assessment for the Thabana Pipe-Store Holding LTS Containers with Solid-Residue from Irradiated Target-Plates*. (RRT-SHLD-REP-19001). Pelindaba, Pretoria, South Africa: Radiation and Reactor Theory (RRT) Section, South African Nuclear Energy Corporation SOC Ltd. (Necsa).

Van Rooyen, T.J. 2020a. *Theoretical Assessment of the Viability of a Necsa Patent for Utilising Atomic Recoil to Produce Radionuclides at Enhanced Specific Activities*. (RRT-NTP-REP-20003). Pelindaba, Pretoria, South Africa: Radiation and Reactor Theory (RRT) Section, South African Nuclear Energy Corporation SOC Ltd. (Necsa).

Van Rooyen, T.J. 2020b. *Transport of Irradiated Tellurium Dioxide in the NTP "ERIKA" Package — Activities, Dose-Rates and Heat Release Rates*. (RRT-NTP-REP-20001). Pelindaba, Pretoria, South Africa: Radiation and Reactor Theory (RRT) Section, South African Nuclear Energy Corporation SOC Ltd. (Necsa).

Van Rooyen, T.J. 2020c. *Transport and Shielding of Ionising Radiation*. Pelindaba, South Africa: Radiation and Reactor Theory (RRT), South African Nuclear Energy Corporation (Necsa).

Van Rooyen, T.J. & Adetula, B.A. 2018. *Dose-Rates, Doses and Energy Deposition Rates from Ten Irradiated Target-Plates in the Dalene Inner Container*. (RRT-SHLD-REP-18002). Pelindaba, Pretoria, South Africa: Radiation and Reactor Theory (RRT) Section, South African Nuclear Energy Corporation SOC Ltd. (Necsa).

Van So Le. 2014. *Generator Development: Up-to-Date Recovery Technologies for Increasing the Effectiveness of Utilisation*. *Science and Technology of Nuclear Installations*.

Watt, B.E. 1952. Energy spectrum of neutrons from thermal fission of U 235. *Physical Review*. 87(6):1037.

Wattal, P.K. 2013. Indian Programme on Radioactive Waste Management. *Sadhana*. 38(5):849–857.

Werner, C.J. 2017. *MCNP User's Manual - Code Version 6.2*. (LA-UR-17-29981). Los Alamos, USA: Los Alamos National Laboratory (LANL).

Xuequan, W., Sheng, Y., Xiaodong, S., Mingshu, T. & Liji, Y. 1991. Alkali-Activated Slag Cement Based Radioactive Waste Forms. *Cement and Concrete Research*. 21(1):16–20.

Yıldız, B., Erten, H. & Kış, M. 2011. Sorption behavior of Cs+ ion on clay minerals and zeolite in radioactive waste management: sorption kinetics and thermodynamics. *Journal of Radioanalytical and Nuclear Chemistry*. 288(2):475–483.

Yu, Q., Li, S., Li, H., Chai, X., Bi, X., … Ohnuki, T. 2019. Synthesis and characterization of Mn-slag based geopolymer for immobilization of Co. *Journal of Cleaner Production*. 234:97–104.

Zamonsky, O.M. 2019. *MCNP SAFARI-1 Calculation Model Description*. (RRT-SAFA-REP-13004 Rev 03). Pelindaba, Pretoria, South Africa: Radiation and Reactor Theory (RRT) Section, South African Nuclear Energy Corporation SOC Ltd. (Necsa).

Zhou, Q., Milestone, N.B. & Hayes, M. 2006. Alternative to Portland Cement for Waste Encapsulation—the Calcium Sulfoaluminate Cement System. *Journal of Hazardous Materials*. 136(1):120–129.

Zosin, A.P., Priimak, T.I. & Avsaragov, K.B. 1998. Geopolymer Materials Based on Magnesia-Iron Slags for Normalization and Storage of Radioactive Wastes. *Atomic Energy*. 85(1):510–514.